

## ABSTRACT

CHATTERJEE, KONY. Design and Evaluation of a Thermoelectric Heating/Cooling Fabric for On-Body Thermal Comfort (Under the direction of Dr. Tushar K. Ghosh).

The need for space cooling and heating – attributed to the increasing population and built environments, especially in warmer parts of the world – is expected to exact a tremendous toll on the environment.<sup>1</sup> Space cooling currently accounts for almost 20% of the total electricity used in buildings globally, and is the fastest-growing use of energy in buildings with the use nearly tripling between 1990 and 2016.<sup>2</sup> While in the US the recommended setpoint for indoor thermal regulation devices is between 21.5 – 24 °C (71 – 75 °F), an expansion of this setpoint range by even 1 °C can result in energy savings between 7 – 15%.<sup>3</sup> Additionally, depending on a variety of genetic and physiological factors, different people feel thermally comfortable at different temperature and hence a universal setpoint could be rendered meaningless.<sup>4-6</sup> In such a scenario, textiles present an accessible platform for the deployment of wearable heating/cooling modules for next-to-skin thermal comfort. Integration of thermal management into textiles can be achieved in two manners: (i) by incorporating materials or surfaces that can provide passive heating or cooling effects without the need for an external power source i.e. via phase change materials, moisture wicking textiles, thermally insulating fibers, and radiative cooling fabrics, and (ii) by using an external power source to provide active heating and cooling i.e. via Joule heating fabrics or thermoelectric heating and cooling fabrics. The opportunities and limitations of each of these approaches are discussed and a special emphasis is placed on the review of thermoelectric fabrics.

This research proposes that the Peltier effect observed in thermoelectric modules when an externally applied current can produce heating or cooling at the junction of two dissimilar semiconducting materials can be used as a noiseless, fluidless, small form factor cooling device to

provide on-body thermal comfort. By suggesting the use of carbon nanotube yarns that are selectively doped to produce n-type and p-type semiconductors, and then integrating them into a woven fabric structure, it is proposed that a cooling of 5 °C can be achieved by such a fabric. In-plane characterization of all three thermoelectric transport parameters – electrical conductivity, thermopower/Seebeck coefficient, and in-plane thermal conductivity is proposed so that the material performance can be accurately studied. Moreover, the incorporation of these materials into proposed fabric structure will also be optimized using theoretical calculations that combine the woven fabric geometry with thermoelectric cooling performance. Finally, the management of waste heat will also be theorized in this proposal, with suggestion for which waste heat management method is the most appropriate.

© Copyright 2021 by Kony Chatterjee

All Rights Reserved

Design and Evaluation of a Thermoelectric Heating/Cooling Fabric for On-Body Thermal  
Comfort

by  
Kony Chatterjee

A dissertation submitted to the Graduate Faculty of  
North Carolina State University  
in partial fulfillment of the  
requirements for the degree of  
Doctor of Philosophy

Fiber and Polymer Science

Raleigh, North Carolina  
2021

APPROVED BY:

---

Dr. Tushar K. Ghosh  
Committee Chair

---

Dr. Jun Liu

---

Dr. Joseph Tracy

---

Dr. Wei Gao

**DEDICATION**

To my parents, Ruby and Guru Chatterjee, and my advisor Dr. Tushar Ghosh.

## BIOGRAPHY

Kony Chatterjee was born in Dehradun, India to Ruby and Guru Chatterjee in the year 1993. She started her education at Riverdale Elementary School where she discovered her love for reading and writing. Throughout her education, she was fortunate to be taught by some of the best chemistry and mathematics teachers, first at Delhi Public School, Noida, then at Delhi Public School, Pune and finally at DAV Public School, Pune. She played competitive tennis for six years and represented her country before moving to Mumbai for her undergraduate studies. She obtained her Bachelor of Technology (B. Tech) degree in Fibers and Textile Processing Technology from Institute of Chemical Technology (ICT) in Mumbai in the year 2015. Her undergraduate experience at ICT nurtured her interests in textiles and materials science and encouraged her to enroll as a master's student at North Carolina State University's Wilson College of Textiles in Raleigh, North Carolina. She obtained her M.S. in Textile Engineering at Wilson College of Textiles in 2017 and continued her PhD in the Fiber and Polymer Science program, both under the tutelage of Dr. Tushar K. Ghosh.

## ACKNOWLEDGMENTS

When I started my research journey, I was completely unaware of the empowering nature of the scientific process and mentorship. Without them, I would have never been able to develop the self-confidence I have today, and this wouldn't have been possible without the excellent mentorship, support, guidance and education provided to me by my advisor, Dr. Tushar K. Ghosh, whom I thank profusely.

Thank you, Dr. Jun Liu for collaborating with me, guiding me and helping me understand my research in a more competent manner. I also thank my committee members Dr. Joseph Tracy and Dr. Wei Gao for their support and for serving as members on my committee. I have thoroughly enjoyed their classes during my graduate studies.

Without my friends Rina and Ishira, I would have never become an engineer and I want to thank them dearly for their friendship, no matter how many miles separate us. Thank you also to my dogs, Vladimir and Penny, and my cats Maldi and Kubrick who may never be able to read this but who support me with their unquestioning love expressed in a way only possible by pets.

Thank you, Ashish Kapoor, Jordan Tabor and Shuzhen Wei for your excellent feedback, support, and friendship as we work on our respective PhD programs, it means a lot to me.

Lastly, thank you to my parents – for their encouragement, patience, support, protection, and above all knowing how to balance all these responsibilities. They have kept me going through this process, and I am lucky to be the daughter of Ruby and Guru Chatterjee.

## TABLE OF CONTENTS

<b>LIST OF FIGURES .....</b>	<b>vii</b>
<b>LIST OF TABLES .....</b>	<b>xiv</b>
<b>1. INTRODUCTION .....</b>	<b>1</b>
<b>2. PART 1 LITERATURE REVIEW: TEXTILE-BASED THERMAL COMFORT SYSTEMS: CURRENT STATUS AND POTENTIAL SOLUTIONS.....</b>	<b>4</b>
2.1 Introduction.....	4
2.2 Active versus Passive Thermoregulation Systems .....	6
2.3 Passive Systems for Thermal Comfort .....	9
2.3.1 Phase Change Materials.....	9
2.3.2 Passive Heating in Textiles.....	12
2.3.3 Passive Cooling in Textiles.....	22
2.4 Active Systems for Thermal Comfort.....	31
2.4.1 Joule Heating .....	31
2.4.2 Thermoelectric Temperature Regulation .....	38
2.4.2.1 Principles of TE Materials and Devices.....	39
2.4.2.2 Flexible Thermoelectric Materials.....	42
2.4.2.2.1 Inorganic Thin Film Thermoelectric Materials.....	43
2.4.2.2.2 Organic Thermoelectric Materials .....	50
2.4.2.2.3 Organic-Inorganic Hybrid Thermoelectric Materials .....	62
2.5 Conclusions.....	64
<b>3. PART 2 DISSERTATION RESEARCH: ON-BODY COOLING USING YARN-BASED THERMOELECTRICS FOR SEAMLESS INTEGRATION INTO TEXTILES .....</b>	<b>66</b>
3.1 Introduction.....	67
3.2 In-Plane Thermoelectric Properties of Flexible and Room Temperature Doped Carbon Nanotube Films .....	73
3.2.1 Introduction.....	73
3.2.2 Sample Preparation .....	77
3.2.3 Measurements .....	78
3.2.3.1 Electrical Conductivity .....	78
3.2.3.2 Seebeck Coefficient .....	79
3.2.3.3 In-plane Thermal Conductivity.....	80

3.2.4 Results and Discussion .....	82
3.2.5 Conclusions.....	88
3.3 Design and Evaluation of a Woven Thermoelectric Heating/Cooling Fabric for On- Body Thermal Comfort.....	90
3.3.1 Introduction.....	90
3.3.2 Materials and Methods.....	92
3.3.2.1 TE Materials Characterization .....	92
3.3.2.2 Junction Fabrication.....	93
3.3.2.3 FabTEC Device Fabrication .....	94
3.3.3 Theory and Calculation.....	95
3.3.4 Results and Discussion .....	95
3.3.4.1 Single and Two Junction Characterization .....	95
3.3.4.2 Fabric TEC Characterization .....	98
3.3.4.3 FabTEC Modeling .....	101
3.3.4.4 Separation of Junctions via Fabric Weave Design .....	106
3.3.5 Conclusions.....	108
<b>4. CONCLUSIONS AND FUTURE OUTLOOK .....</b>	<b>110</b>
<b>5. REFERENCES.....</b>	<b>113</b>
<b>APPENDICES .....</b>	<b>151</b>
<b>Appendix A .....</b>	<b>152</b>
<b>Appendix B .....</b>	<b>155</b>

## LIST OF FIGURES

- Figure 1:** Concept of an ideal PTCS that includes active and passive components.<sup>8</sup> Passive components include IR cooling, phase change materials, thermal management/moisture wicking/directionally conducting fibers, and moisture/temperature actuator fibers or patches. Potential active components include fiber-based sensors, thermoelectric heating/cooling, resistive heating, and actuators for moisture/thermal management. Reproduced with permissions.<sup>8</sup> Copyright 2020, WILEY-VCH Verlag GmbH & Co. KGaA, Weinheim. .... 7
- Figure 2:** Typical differential scanning calorimetry (DSC) heating thermogram for PCM melting. During the phase change, the PCM material absorbs a large amount of latent heat from its surroundings. Reproduced with permissions.<sup>9</sup> Copyright 2007, Elsevier Ltd. .... 10
- Figure 3:** Feather structure of modern birds.<sup>129</sup> a) The feather shaft and feather vane. The vane contains barbs and barbules. b) Barbs branching from the feather shaft. c) Barbules are miniature beams branching from the barbs. Reproduced with permissions.<sup>129</sup> Copyright 2016, Acta Materialia Inc. Cross-sectional Scanning electron microscope (SEM) images melt spun polyester.<sup>130</sup> d) Round. e) Hollow-round. f) Trilobal. g) Hollow-trilobal. Reproduced with permissions.<sup>130</sup> Copyright 2006, Wiley Periodicals, Inc. .... 14
- Figure 4:** Biomimetic hollow core-shell fibers produced via free-spinning for thermal insulation.<sup>16</sup> a) A polar bear in its natural habitat. b) SEM image showing the hollow, foam-like structure of polar bear fur. c) SEM image of the core-shell structure of polar bear fur. d) Freeze-spinning method to produce biomimetic fibers, combines directional freezing with solution spinning. This process involves extrusion of silk fibroin solution from a syringe, followed by freezing as it passes through a cold copper ring. Thus formed porous structure is woven into a textile, as shown in figures e), f) and g). Reproduced with permissions.<sup>16</sup> Copyright 2018, WILEY-VCH Verlag GmbH & Co. KGaA, Weinheim. .... 20
- Figure 5:** Mechanical and thermal insulation performance of biomimetic hollow core-shell fibers inspired by polar bear hair.<sup>16</sup> a) SEM images showing the aligned cross-sections of fibers prepared at - 40°C, - 60°C, - 80°C, and - 100°C. b) SEM images of randomly aligned fiber cross-sections prepared at - 196 °C. c) Comparison of tensile strength and elongation with pore size shows that the random pores (1) have worse mechanical properties than aligned pores (2). d) Infrared images of fibers placed vertically on a heated stage at various temperatures, showing the temperature difference between the fibers and the stage. From left to right, the pore sizes of the fibers (in  $\mu\text{m}$ ) are: 85, 65, 45, 30 and 20, respectively. e) Absolute temperature difference ( $|\Delta T|$ ) between the stage and the fibers shows that smaller pore sizes have better thermal insulation. Reproduced with permissions.<sup>16</sup> Copyright 2018, WILEY-VCH Verlag GmbH & Co. KGaA, Weinheim. .... 21
- Figure 6:** Moisture transport and collection in nature. a) Peaks and troughs on the overwings of the desert beetle.<sup>197</sup> Scale bar = 10 mm. b) SEM image of the overwings with flattened hemispheres in a hexagonal array, like the superhydrophobic surface of a lotus leaf. Scale bar = 10  $\mu\text{m}$ . Reproduced with permissions.<sup>197</sup> Copyright 2001, Springer Nature. Directional adhesion of water on the superhydrophobic wings of a

butterfly.<sup>198</sup> c) Illustration showing arrows on the butterfly wings, indicating the radial-outward (RO) direction away from the body's central axis along which water droplets roll. d) SEM image shows lamellar stripes on the wings, stacked stepwise along the RO direction. Scale bar = 100 nm. Reproduced with permissions.<sup>198</sup>

Copyright 2007, The Royal Society of Chemistry. Fog collection system on the spine of the cactus plant.<sup>199</sup> e) SEM image of a single cactus spine consisting of three regions: (1) tip with oriented barbs, (2) middle with gradient grooves, and (3) base with hair-like structures called trichomes. The blue and yellow boxes indicate regions with wider and narrower grooves, respectively. Scale bar = 20  $\mu\text{m}$ . f) Mechanism of fog collection on the cactus, water droplet deposition on the barbs and spine (4), followed by collection on its tip (5), transportation on grooves (6), and absorption onto trichomes (7). Adapted with permissions.<sup>199</sup> Copyright 2012, Springer Nature.

**Figure 7:** Trilayered moisture wicking membrane with directional water transport for thermal comfort.<sup>18</sup> ..... 24

a) Schematic showing the moisture wicking process in the trilayered fabric. The outermost layer (blue) is composed of electrospun hydrolyzed polyacrylonitrile-SiO<sub>2</sub> (HPAN) fibers and facilitates capillary motion to pull out sweat. The middle layer (purple) is composed of hydrolyzed PU-PAN (PU-HPAN) fibers and acts as a transfer layer with progressive wettability. It guides the water from the inner to the outer layer, without allowing transfer in the opposite direction. The layer closest to the skin (orange) is hydrophobic PU membrane which allows anisotropic wettability thorough the thickness, allowing sweat to penetrate through the inner layer without spreading on the surface. b) SEM image of the cross-section of the trilayered membrane. c) A drop of water placed on the hydrophobic PU side of the trilayered membrane penetrates it almost instantaneously. d) A drop of water placed on the hydrophilic HPAN side spreads across its surface. e) and f) illustrate the mechanism of water transport through the layers, depending on whether the water is dropped from the PU side or the HPAN side, where the transport depends on the balance of hydrostatic pressure (HP), hydrophobic force (HF), and capillary force (CF<sub>1</sub>, CF<sub>2</sub>) felt by the water droplet. Reproduced with permissions.<sup>18</sup> Copyright 2018, WILEY-VCH Verlag GmbH & Co. KGaA, Weinheim.

**Figure 8:** Dual mode coated textile composed of nanoPE for radiative heating and cooling.<sup>68</sup> ..... 26

a) Dual mode textile composed of multiple layers of nanoPE, carbon and copper with each layer consisting of a porous structure to enable comfort. b) and c) Illustrate the mechanism of dual mode textile. In cooling mode (b) with the high emissivity layer facing outside and the thinner nanoPE layer facing towards the skin, there is larger heat transfer resulting in cooling. In the heating mode (c) when the low emissivity layer is facing outside with the thicker nanoPE towards the skin, heat transfer coefficient decreases, enabling heating. d) High emissivity layer with carbon coating, with e) showing the SEM image of this side. The rough surface and pores enable higher emissivity. f) Low emissivity layer with copper coating, with g) showing the SEM image of this layer with its optically smooth surface and nanopores for moisture and vapor permeability. Reproduced with permissions.<sup>68</sup> Copyright 2017, Creative Commons Attribution NonCommercial License (CC BY-NC). Woven and knitted nanoPE fabric for large-scale radiative cooling.<sup>20</sup> h)

- Schematic illustrating the various modes of cooling integrated into the fabric. With its high mid-IR transparency, it allows for radiative cooling from the human body, while remaining opaque to visible light. i) nanoPE microfibers were manufactured using a modified wet spinning process wherein a solution of paraffin oil and PE is extruded, and solidified, thereby phase separating to create nanopores. The paraffin oil is subsequently removed using methylene chloride, creating nanoPE fibers. j) SEM image of the cross-section and pores of the nanoPE fiber, with the inset showing a lower magnification SEM image of the fiber's cross-section. Reproduced with permissions.<sup>20</sup> Copyright 2018, Springer Nature. .... 29
- Figure 9:** Cotton fabric dip coated with AgNW dispersion to create a resistive heating fabric for personal thermal comfort.<sup>38</sup> a) Concept of the AgNW coated fabric that enables passive thermal radiation insulation coupled with active Joule heating. b) The cloth was cut into an S shape and placed on the palm, with the thermal image showing that the AgNW cloth can effectively block IR radiation from the human body, thereby showing a lower temperature. c) Different voltages are applied to a 1 inch X 1 inch AgNW-cotton fabric and the temperature change is measured. A 0.9 V applied voltage can induce a temperature change up to 38 °C. Reproduced with permissions.<sup>38</sup> Copyright 2015, American Chemical Society. CNT fibers integrated into woven fabric for Joule heating textiles.<sup>222</sup> d) CNTs are woven with cotton threads and copper wires to create Joule heating fabrics. The copper wires were used as conductors so that no other conductive paste or tape was needed. Scale bar, 6 cm. e) Heating textile at high and low magnifications. Scale bars are 3 mm and 25 mm for the left and right images. f) The fabric had a large heating area of 13 cm X 10 cm and showed an increase in saturation temperatures of 38 °C, 48 °C and 60 °C when the voltage is increased from 5 V, 7 V to 9 V. g) Thermal image of the heating textile at 9 V wrapped around the wrist. Reproduced with permissions.<sup>222</sup> Copyright 2017, WILEY-VCH Verlag GmbH & Co. KGaA, Weinheim. .... 33
- Figure 10:** Principals of TE devices.<sup>266</sup> (a) When flows through a TE junction, it can either heat or cool the junction depending on the direction of the current, known as the Peltier effect. (b) When an external thermal gradient is applied to the junction, electrical current is generated through the Seebeck effect. (c) Commercial TE generators consist of many n and p TE legs connected to form TE junctions electrically in series and thermally in parallel to enable higher power output and spread heat flow over a larger area. Reproduced with permissions.<sup>266</sup> Copyright The Author and 2008, American Association for the Advancement of Science. .... 40
- Figure 11:** Interdependence of various TE parameters that influence ZT of the material, illustrating the challenge of optimizing ZT.<sup>261</sup> Data of actual semiconducting single walled carbon nanotube (SWCNT) networks, from Ref [259]. Reproduced with permissions.<sup>261</sup> Copyright 2018 WILEY-VCH Verlag GmbH & Co. KGaA, Weinheim. .... 41
- Figure 12:** Crystal structure of Bi<sub>2</sub>Te<sub>3</sub>.<sup>296</sup> Reproduced with permissions.<sup>296</sup> Copyright 2019, Springer Nature Switzerland AG. .... 44
- Figure 13:** Woven-yarn TE fabrics.<sup>327</sup> a–f) Illustration (a–c) and photographs (d–f) of zigzag, garter, and plain-weave TE textiles, respectively. Scale bar = 2 mm. g–i) The output power per textile area and per TE couple as a function of applied thermal gradient ( $\Delta T$ ) for zigzag, garter, and plain-weave TE textiles, respectively.

- Reproduced with permissions.<sup>327</sup> Copyright 2016, 2016 WILEY-VCH Verlag GmbH & Co. KGaA, Weinheim. .... 45
- Figure 14:** Wearable TEC for localized cooling.<sup>336</sup> a-d) TEC modules fabricated with commercial p- and n-type Bi-Te with a) high fill factor (FF = 36%, aspect ratio, AR = 1.0), b) low FF (FF = 12%, AR = 1.0), c) ultra-low FF (FF = 5.2%, AR = 1.6), and d) commercial TEC module (FF = 28.4%, AR = 1.0). The black heat sink is anodized aluminum. e), f) Show transient temperature data from cooling the human body and in controlled environments, for the various TECs. The optimal currents are 1 A for high FF TEC (blue), 2.4 A for low FF TEC (black), and 2 A for ultra-low FF TEC (red). Ultra-low FF TEC generates the lowest cold side temperature and has the highest cooling. Reproduced with permissions.<sup>336</sup> Copyright 2019, Creative Commons Attribution 4.0 International License (CC-BY-4.0). Flexible TED for on-body cooling.<sup>34</sup> g) Wearable TE device (TED) integrated into a vest and arm band. h) TED consists of alloy pillars connected with flexible copper electrodes and silicone sheets. i) A 5 cm X 5 cm fabricated TED. j) TED design with low thermal conduction inside and high thermal conduction within the silicone sheets enables cooling without the use of a heat sink.  $T_{\text{air}}$  = ambient temperature,  $h_{\text{air}}$  = heat transfer coefficient between TED and air,  $T_{\text{h}}$  = temperature at the top of TED,  $G_{\text{TED}}$  = thermal conductance of TED,  $T_{\text{c}} = T_{\text{skin}}$  = temperature at the bottom of TED,  $Q_{\text{skin}}$  = human metabolic heat. k) Thermal regulation by TED under natural convection shows that the surface temperature of the silicone layer remained 26 °C in temperature range of 19 °C – 33 °C. l) With forced convection of 5 km h<sup>-1</sup> the ambient temperature range broadens to 15 °C – 36°C. Reproduced with permissions.<sup>34</sup> Copyright 2019, Creative Commons Attribution NonCommercial License 4.0 (CC-BY-NC). .... 49
- Figure 15:** (a) Polymeric semiconductors have  $\pi$ -conjugated cores that enable charge transport and side chains that can impart solution processability, charge carrier creation, and molecular assembly. (b) Ionization energy (HOMO) and electron affinity (LUMO) of polymeric semiconductors can be tuned via their molecular design. (c) Molecular structures of high-performance p and n-type OTEs. Adapted from Russ et al.<sup>262</sup> copyright 2016, The Authors. .... 51
- Figure 16:** Polymer TEG for human body heat harvesting.<sup>342</sup> a) Fabrication process for textile integrated TEG: 1. Burning holes through the knitted fabric, 2. Filling the holes by stencil printing p- (red) and n-type (blue) materials on both sides of the fabric, 3. Silver interconnects (light blue) are printed onto a heat transfer membrane (light gray) on both sides of the device, 4. Heat pressing interconnects onto both sides of the device using the heat transfer membrane. b) Wearable TEG integrated into knitted fabric consisting of 32 p- and n-type legs. Reproduced with permissions.<sup>342</sup> Copyright 2019 WILEY-VCH Verlag GmbH & Co. KGaA, Weinheim. .... 54
- Figure 17:** Part of a graphene sheet with chiral indices (n,m) corresponding to the SWCNT formed by rolling the sheet from (0,0) to (n,m) along the highlighted roll-up vector to form a cylinder.<sup>261</sup> Rolling up along the shaded blue area (indicated as roll-up vector) forms a (9, 4) SWCNT cylinder. White hexagons correspond to chiral indices that form semiconducting SWCNTs, gray hexagons to chiral indices that form metallic SWCNTs, and green hexagons to chiral indices that form

- semiconducting SWCNTs present in a typical batch of commercial sodium dodecylbenzenesulfonate (SDBS) dispersed SWCNTs produced by the high-pressure carbon monoxide (HiPCO) process. Reproduced with permission.<sup>261</sup> Copyright 2018, WILEY-VCH Verlag GmbH & Co. KGaA, Weinheim. .... 59
- Figure 18:** The concept of fabric integrated thermoelectric cooling (FabTEC) that enables next to skin heating and cooling in both indoor/outdoor and warm/cold conditions,. 66
- Figure 19:** Three-dimensional thermoelectric textiles (TET) for power generation.<sup>437</sup> (a) Schematic diagram of the TET with PEDOT:PSS/MWCNT yarns as p-type and PEI/MWCNT yarns as n-type legs and optical image showing the vertical arrangement of legs. (b) A TET sample measuring 8 cm X 9.3 cm. Reproduced with permissions.<sup>437</sup> Copyright 2020, The Royal Society of Chemistry. Woven yarn TE fabric with n- and p-type semiconductor sheaths ( $\text{Bi}_2\text{Te}_3$  and  $\text{Sb}_2\text{Te}_3$ , respectively) coated onto nanofibers and then twisted into flexible yarns.<sup>327</sup> (c)-(e) Illustrations of TE textiles made via zigzag, garter and plain weave structures, respectively. Reproduced with permissions.<sup>327</sup> Copyright 2016 WILEY-VCH Verlag GmbH & Co. KGaA, Weinheim. .... 68
- Figure 20:** (a) Simple fabrication of doped PEI-MWCNT film using a PEI-Ethanol solution of varying concentrations. SEM images of (b) pristine MWCNT film and (c) 5 wt.% PEI-Ethanol treated film shows a deposition of PEI on the surface of the MWCNTs. Scale bars for (b) and (c) are 10  $\mu\text{m}$ . .... 77
- Figure 21:** Electrical and thermoelectric properties of undoped MWCNT and n-type doped MWCNT/PEI films as PEI-Ethanol concentration increases from 0 wt.% to 20 wt.%. (a) Seebeck coefficient of pristine MWCNT film (p-type indicated by  $\square$ ) and doped MWCNT films (n-type indicated by  $\diamond$ ). (b) Seebeck coefficients of just n-type doped MWCNT/PEI films ( $\diamond$ ), representing the area highlighted in the box in (a). (c) Electrical conductivity ( $\circ$ ) increases as the amount of PEI increases. (d) Overall power factors ( $\triangle$ ) of the pristine MWCNT and doped MWCNT films, with a maximum power factor at 15 wt.% PEI calculated as  $521.67 \pm 69.33 \mu\text{W}/\text{mK}^2$ . .... 83
- Figure 22:** (a) CCD image of pump beam focused (20x, Gaussian beam spot radius = 2.95  $\mu\text{m}$ ) on microtomed MWCNT sample surface covered with 80 nm Al. (b) Data fitting for in-plane thermal conductivity of n-type 5-MWCNT/PEI (red) and p-type MWCNT (blue) calculated from the ratio of in-phase signal ( $V_{\text{in}}$ ) to the out-of-phase signal ( $V_{\text{out}}$ ). .... 86
- Figure 23:** (a) Open circuit Seebeck voltage of a single junction composed of a pristine MWCNT film (3 cm length X 1 cm width X 8.4  $\mu\text{m}$ ) as p-type leg and 5-MWCNT/PEI (3 cm length X 1 cm width X 10  $\mu\text{m}$ ) as n-type leg ( $\square$ ), as a function of applied thermal gradient. The measured Seebeck coefficient of a single junction is  $138.95 \pm 2.48 \mu\text{V}/\text{K}$ . (b) Air stability of n-type doped MWCNT/PEI films over 28 days with 5-MWCNT/PEI ( $\square$ ), 10-MWCNT/PEI ( $\circ$ ), 15-MWCNT/PEI ( $\triangle$ ), and 20-MWCNT/PEI ( $\nabla$ ). .... 87
- Figure 24:** Fabrication and characterization of single and double junction MWCNT devices. (a) The p-type and n-type MWCNT TE legs are cut into 10 mm X 2 mm strips with 1 mm X 1 mm Z-axis tape (shown in blue) attached to the ends. The p-type MWCNT interconnect is placed on the tape and attached firmly, with the copper wire being used as connectors to the power supply. (b) Single junction

configuration. (c) Two junction configuration with the legs connected as p-type MWCNT, n-type MWCNT and p-type MWCNT, forming a PN and an NP junction. Copper tape was used to secure the copper wire to form a more robust connection. (d) Cooling by the single junction shown in (b). (e) The average cooling gradient achieved by the single junction in (b) is further highlighted to show a cooling of 0.4 °C. (f) Voltage-current graph obtained from the DC power supply connected to the single junction shows that the device has an overall resistance of  $80.24 \pm 3.75 \Omega$ . (g) Heating and cooling above and below room temperature, respectively for the two junction setup shown in (c). (h) Thermal gradient achieved by the two junction setup shows a cooling of 1.1 °C and heating of 3 °C below and above room temperature, respectively. (i) Voltage-current graph obtained from DC power supply connected to the two junction system in (c) shows an overall resistance of  $150.52 \pm 6.24 \Omega$  of the system. .... 97

**Figure 25:** (a) Overall proposed FabTEC design with the grey and black yarns as the support yarns, yellow yarns as the interconnect, and the green and orange yarns as n-type and p-type yarns, respectively. The yarns are physically disconnected as indicated by the red crosses. The path of current is illustrated by the blue arrows. The repeat unit of the fabric is illustrated in the red box and (b). (c) The representative unit highlighted in (b) is fabricated into a woven configuration with transparent PET as support yarns and n- and p-type MWCNT films as flat yarns and interconnects. Disconnects are illustrated with red crosses. The 4 cm X 4 cm FabTEC demonstration fabric can be mounted on the wrist as shown on the right, with the ability to flex with the body. (d) Heating and cooling performance of the FabTEC as a function of time. Each current value is held for 60 seconds, and the experiment is stopped when the cold junction starts heating. The maximum cooling is 1.3 °C below room temperature (21 °C) and heating is 3 °C above room temperature. (e) Heating and cooling performances as a function of the applied current. (d) The voltage-current graph of the FabTEC shows an overall resistance of  $509 \pm 26 \Omega$ . .... 99

**Figure 26:** Variation in ZT of TE materials and resultant cooling density at different cooling gradients. (a) The electrical conductivity is increased and resultant ZT and its effect on cooling density is reported. (b) The Seebeck coefficient is increased to result in increasing ZT and resultant cooling density is reported. (c) Graph illustrates the region highlighted by the red, dashed box in (b), showing the region where cooling density is positive (i.e. there is cooling) and where it is negative (i.e. no cooling) at lower values of ZT..... 101

**Figure 27:** Influence of aspect ratio (AR) of the TE leg in each junction on the total cooling and cooling density of the FabTEC. (a) Increase in projected area of FabTEC as AR increases. (b) Decrease in cooling density with increasing AR for various cooling gradients. (c) Zoomed-in version of the graph in (b) which shows in greater detail the reduction in cooling density with increased AR at higher values of AR. (d) Total cooling (not considering the change in  $A_p$ ) as a function of AR. .. 103

**Figure 28:** Junction density and its influence on the overall cooling achieved by FabTEC at various current levels. Total cooling for (a) 1666 junctions/m<sup>2</sup> (30 ends/picks per inch), (b) 6666 junctions/m<sup>2</sup> (60 ends/picks per inch) and (c) 18518 junctions/m<sup>2</sup> (100 ends/picks per inch) of FabTEC. .... 105

<b>Figure 29:</b> Thermal management weave design for separation hot and cold junctions. (a) Repeat unit with two junctions on the face and back of FabTEC. (b) Proposed design that reduces crimp and imparts greater separation to the two junctions. (c) Junction separation as seen from the front view of the modified FabTEC.....	107
<b>Figure S30:</b> (a) Schematic diagram of the setup to measure Seebeck coefficient with the image in (b) showing the setup with the MWCNT film places across the hot and cold sides. While in (b) the temperature probe has been moved aside to show a better view of the film, during measurement the probe is placed on the film as in (a) to measure thermal gradient and Seebeck voltages on the same side of the film. ....	152
<b>Figure S31:</b> SEM images at 10000X magnification for (a) pristine MWCNT film and (b) 5-MWCNT/PEI film. Both scale bars are 5 $\mu\text{m}$ .....	152
<b>Figure S32:</b> Thickness variation as a function of concentration of PEI in ethanol. Table S1. Thermoelectric properties of pristine and n-type MWCNT films. ZT for the films is calculated by assuming that the thermal conductivities of the PEI doped films remain constant as the concentration varies from 5 to 20 wt.% PEI. ....	153
<b>Figure S33:</b> Comparison of $\kappa$ and PF for various reported TE materials containing CNTs (cited work indicated by $\square$ with red for p-type and blue for n-type). Data for the materials are from the cited sources: MWCNT-PANI, <sup>494</sup> MWCNT-PTh, <sup>506</sup> SWCNT-PEDOT:PSS, <sup>248</sup> SWCNT-PEI, <sup>255</sup> SWCNT, <sup>255</sup> MWCNT-PEI, <sup>437</sup> and MWCNT-PEDOT:PSS. <sup>437</sup> This work (indicated by $\star$ ) shows high PF with lower $\kappa$ than other reported materials. ....	154
<b>Figure S34:</b> FabTEC modeling for TE performance. (a) Overall fabric design with disconnects. (b) Repeat unit with symmetry. (c) Projected length in the XX' plane. (d) Projected length in the YY' plane. (e) Calculation of projected lengths..	155
<b>Figure S35:</b> Peltier cooling, resistive heating, and heat transfer within the TEC as a function of the AR for various cooling gradients.....	160
<b>Figure S36:</b> Peltier cooling, resistive heating and heat transfer within the FabTEC for 1666 junctions/m <sup>2</sup> density.....	163
<b>Figure S37:</b> Peltier cooling, resistive heating and heat transfer within the FabTEC for 6666 junctions/m <sup>2</sup> density.....	164
<b>Figure S38:</b> Peltier cooling, resistive heating and heat transfer within the FabTEC for 18518 junctions/m <sup>2</sup> density.....	165

**LIST OF TABLES**

<b>Table 1:</b> Seebeck coefficients, electrical conductivities and resultant power factors of flexible thermoelectric materials explored for FabTEC .....	74
<b>Table S2:</b> Overall TE performance of MWCNT materials.....	153
<b>Table S3:</b> Modeling Parameters for AR Effect on FabTEC Cooling Density .....	159

## 1. INTRODUCTION

The International Energy Agency has estimated that in 2018 air conditioners and electric fans to stay cool accounted for nearly 20% of the total electricity used in buildings around the world.<sup>2</sup> Without intervention, rising global populations and incomes – especially in warmer parts of the world – will put an even greater stress on the world's resources to provide space cooling. An interesting and innovative approach to this growing problem is by intervening at the personal level via textiles. By integrating user controllable and responsive heating/cooling systems into textiles, there is a chance to provide personalized on-body thermal comfort without heating and cooling the built environment. However, this must be done without sacrificing the inherent characteristics of textiles – breathability, comfort, flexibility and strength. Serendipitously, the hierarchical nature of the textile structure as it progresses from fiber to yarn to fabric (or directly from fiber to fabric) can provide multiple form factors and sizes where heating/cooling devices can directly be integrated.<sup>7</sup>

This dissertation is composed of a number of review and research papers, as well as supplementary information necessary to tie all of it together. Some of the papers are published and others are in different stages of publication. The dissertation is divided into two parts – **part 1 in Section 2** which provides a critical review of the current literature in textile-based thermal comfort, and **part 2 in Section 3** that proposes integration of active components into textiles to provide thermal comfort without sacrificing the inherent comfort, flexibility and strength of textiles.

The review in part 1 has been published in two different papers, with the publication titled “Smart Textile-Based Personal Thermal Comfort Systems: Current Status and Potential Solutions”<sup>8</sup>

covering the active and passive thermal comfort systems, and the publication titled “Thermoelectric Materials for Textile Applications” (In press, MDPI Molecules) containing the review of flexible thermoelectric systems for personal thermal comfort.

The review starts with a discussion of the broader environmental impact that our need for thermal comfort has had in Section 2.1. This is followed by a classification of the various approaches to creating personal thermal comfort systems (PTCS) within textiles into two types: passive PTCS (pPTCS) which do not need an external power source and can respond to the environment around them due to their inherent material/surface properties, and active PTCS (aPTCS) which need an external power source to operate, in Section 2.2. An ideal PTCS system consisting of sensors coupled with either pPTCS or aPTCS or both is also described, see *Figure 1*, and although sensors are not a focus of this review, such an ideal PTCS system could possibly allow thermal comfort to the wearer without user intervention. Various manners of deployment of pPTCS in textiles are discussed, including phase change materials in Section 2.3.1,<sup>9–13</sup> thermal management in textiles that reduces the amount of heat lost from the body using traditional methods such as interlinings<sup>14,15</sup> as well as more novel methods of creating unique fiber materials/shapes<sup>16</sup> and fabric structures<sup>17</sup> in Section 2.3.2, and passive cooling by allowing the body to more rapidly dissipate heat via techniques such as evaporative<sup>18</sup> and radiative cooling<sup>19,20</sup> in textiles in Section 2.3.3.

However, it is apparent that other than phase change materials, most pPTCS provide either heating or cooling not both. Further, even phase change materials themselves suffer from bulkiness and degradation in performance over time.<sup>21</sup> Finally, pPTCS are limited to the amount of temperature

gradient they can provide for comfort. Hence, there is a need to have powered aPTCS that can controllably deliver both heating and cooling and provide a larger range of thermal gradient. aPTCS can be implemented using a variety of technologies such as liquid cooling integrated into textiles,<sup>22–25</sup> electrocaloric cooling,<sup>26–28</sup> magnetocaloric cooling,<sup>29–32</sup> thermoelectric temperature regulation,<sup>33–37</sup> and Joule heating devices.<sup>38–45</sup> While Joule heating devices are easier to implement into textile structures and thermoelectrics (TEs) show potential for both heating and cooling, liquid cooling can be cumbersome and bulky, and magnetocaloric and electrocaloric cooling are emerging technologies existing mainly in flexible film form.<sup>34</sup> Additionally, TE cooling is well-studied and has the highest exergetic efficiency amongst the various methods of solid state cooling.<sup>46</sup> Thus, resistive or Joule heating fabrics are discussed in Section 2.4.1, followed by TE fabrics for temperature regulation in Section 2.4.2.

In part 2, dissertation research carried out for textile-based thermoelectric fabrics is presented, with Section 3.2 discussing the material selection and characterization process, and Section 3.3 discussing the design and evaluation of such a thermoelectric fabric. Section 3.2 has already been published under the title “In-plane Thermoelectric Properties of Flexible and Room Temperature Processable Doped Carbon Nanotube Films”<sup>47</sup> and Section 3.3 is in the process of submission to *Materials Today*. Hence, this document is divided into a review section that consists of two published papers, and the research results that consists of two publications as well.

## **2. PART 1 LITERATURE REVIEW: TEXTILE-BASED THERMAL COMFORT SYSTEMS: CURRENT STATUS AND POTENTIAL SOLUTIONS**

### **2.1 Introduction**

The global energy consumption grew by 2.3% between 2013 and 2017, the fastest pace in a decade.<sup>1,2,48</sup> Driven by the growth in population, household and commercial floor space, buildings account for about 40% of the energy consumption in the U.S. and Europe.<sup>49</sup> Similarly in China, buildings account for about 27% of total national energy use from 1999 to 2001, which is predicted to increase to about 35% in 2020.<sup>50</sup> Moreover, China's primary energy consumption from 1978 to 2015 grew annually by 5.6%, almost 3 times higher than that of the world during the same period.<sup>51</sup> In 2010, space heating dominated the residential and commercial buildings energy consumption globally, accounting for 32% and 33% of the total consumption.<sup>52</sup> Space cooling currently accounts for almost 20% of the total electricity used in buildings globally, and is the fastest-growing use of energy in buildings with the use nearly tripling between 1990 and 2016.<sup>2</sup> For obvious reasons, there is a growing concern about the unsustainable growth in energy consumption, especially for heating and cooling – mainly attributed to population migration to cities, decreasing household sizes, changes in lifestyle coupled with an increase in the number of built spaces due to urbanization, and the growing and ever present need for thermal comfort.<sup>2,53</sup> The way to moderate this demand and mitigate the potentially serious environmental consequences, is by introducing fundamental changes both at the building and individual levels. While at the building level, it is important to reduce the building operational energy load with better design and retrofitting to the level that it can be met through renewable sources of energy,<sup>54</sup> at the personal level, developing a thermoregulation systems that can provide heating/cooling for the space immediately surrounding the body would contribute immensely to energy

sustainability.<sup>55</sup> Although, the Standard 55 from the American Society of Heating, Refrigerating, and Air-Conditioning Engineers (ASHRAE) defines an indoor temperature set point between approximately 20°C and 23°C, extending this range by just 1-2°C can result in an annual energy savings of 7-45%.<sup>55</sup>

Therefore, there exists a tremendous opportunity to develop next-to-skin thermoregulatory systems, ideally, within textiles, termed as personal thermal comfort systems (PTCS). Textiles are an obvious choice not just due to their proximity to the skin, but also due to their conformable nature and their hierarchical structure that can allow incorporation of heating and cooling systems at the fiber, yarn, or fabric level. Additionally, by moving heating and cooling away from built environments to personally controlled systems, it would be possible to tailor thermal comfort requirements based on age, gender, location, and metabolism.

## 2.2 Active versus Passive Thermoregulation Systems

The cost of energy for space heating and cooling and its impact on environment should not be underestimated (*cf* Section 2.1). Globally, space heating and cooling account for over one-third of all energy consumed in buildings, rising to over 50% in cold climates.<sup>48</sup> PTCS could be a key component in the solution to this problem. Exposure to extreme hot or cold temperatures can negatively impact a person's performance, create life-threatening situations such as heat strokes or hypothermia, as well as negatively impact quality of life.<sup>56,57</sup> Moreover, factors such as gender,<sup>4</sup> age,<sup>5</sup> and physiology<sup>6</sup> can influence the experience or lack of thermal comfort, and hence moving temperature control away from the built environment to next-to-skin thermoregulation can have overall positive impacts.

PTCS can be implemented using active and/or passive systems. Active PTCS (aPTCS) enable personal thermoregulation with the aid of an external power source. Examples of aPTCS include Joule or resistive heating fabrics<sup>38,39,58–60</sup> and thermoelectric (TE) temperature regulators.<sup>33,61,62</sup> On the other hand, passive PTCS (pPTCS) require no external energy to operate and are able to regulate the micro-climate around skin due to intrinsic material properties or structural/morphological characteristics of the system itself. Such pPTCS can also enable personal thermal comfort via actuators that can respond to a stimulus from the body, such as temperature or moisture-triggered actuators.<sup>63–67</sup> Temperature and moisture are two important natural triggers already available in the human body and the environment, and hence are good candidates as stimulants. pPTCS also include radiative cooling textiles,<sup>19,20,68–70</sup> fibers with highly directional thermal conductivity,<sup>71,72</sup> phase change materials (PCMs) integrated into textiles,<sup>21,73</sup> and thermally insulating textiles.<sup>16,74,75</sup>

For integration into textiles, there are certain requirements that both aPTCS and pPTCS must fulfill: (i) mechanical and physical compatibility with textiles, i.e., flexibility, lightweight, and conformability such that they can be integrated into body-worn form factors,<sup>16</sup> (ii) low power requirements in case of aPTCS,<sup>58</sup> and (iii) stable and controllable temperature regulation in the relevant range.<sup>38</sup>

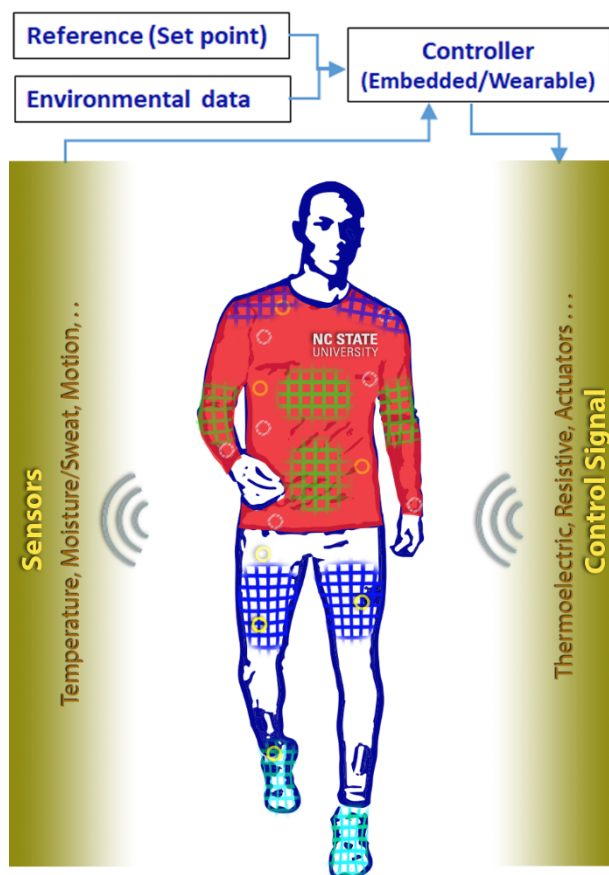


**Figure 1:** Concept of an ideal PTCS that includes active and passive components.<sup>8</sup> Passive components include IR cooling, phase change materials, thermal management/moisture wicking/directionally conducting fibers, and moisture/temperature actuator fibers or patches. Potential active components include fiber-based sensors, thermoelectric heating/cooling, resistive heating, and actuators for moisture/thermal management. Reproduced with permissions.<sup>8</sup> Copyright 2020, WILEY-VCH Verlag GmbH & Co. KGaA, Weinheim.

While an ideal PTCS should be autonomous, it should also allow the user to have direct control over their environment based on their own perception of comfort. The level of personal control should be independent of the building's temperature set point, to accommodate the individual's perception of thermal comfort. The autonomous PTCS should be able to sense and respond to the changes in environmental conditions around the wearer's body, as shown in *Figure 1*. In such a system, both active and passive components could be incorporated in the same clothing to complement each other. For example, the functionality of a thermoregulation textile containing only pPTCS such as moisture or temperature responsive actuators can be further expanded by incorporating aPTCS such as resistive heating elements into them. On the other hand, the system could potentially be composed solely of aPTCS: combining temperature and/or moisture sensors that can trigger TE heating and cooling fabrics depending on the sensors' assessment of the wearer's physiology and surroundings. Consequently, a truly "smart" textile, one that is a self-monitoring, adaptive, and responsive textile, can provide optimal thermal comfort to the wearer without the need for intervention.

Certain pPTCS are capable of providing such a form of adaptive thermal regulation, such as the dual mode heating and cooling garment developed by Hsu et al,<sup>68</sup> but most are limited to either cooling<sup>19,20</sup> or thermal insulation,<sup>16,74</sup> or are more specifically geared towards moisture management.<sup>76</sup> The following sections cover such systems beginning with pPTCS, and then continuing onto aPTCS.

## 2.3 Passive Systems for Thermal Comfort

Passive thermoregulatory textiles provide thermal comfort due to an inherent morphological/structural or material property of the textile. This includes textiles that can store and release latent heat energy using PCMs,<sup>9,21,56,73,77</sup> insulate the body from uncontrolled heat-loss by using multilayer structures,<sup>14,74</sup> possess unique fiber structures such as core-shell insulating fibers<sup>16</sup> and moisture-wicking textiles,<sup>18,78–81</sup> have directional thermal conductivity,<sup>72,82,83</sup> or regulate infrared (IR) radiation emitted by the human body,<sup>19,20,68</sup> or actuators that can alter structural porosity and moisture/vapor permeability in response to stimuli such as heat and moisture from the human body.<sup>67,76,84–87</sup>

### 2.3.1 Phase Change Materials

PCMs incorporated into textiles can enable thermal regulation due to their ability to store and release large amounts of latent heat effectively as they go through the process of melting and freezing.<sup>21,88</sup> When PCMs undergo a latent heat absorption or release cycle, their temperature remains constant, and hence they are able to oscillate between solid and liquid/gas phases within a certain temperature range.<sup>89</sup> When the external environment temperature is higher than that of the PCM, heat transfers from the material to the surroundings and vice versa when the external temperature is lower than that from the PCM, as shown as shown in *Figure 2*. Thus they can create a heating or cooling effect when incorporated into textiles.<sup>90</sup>

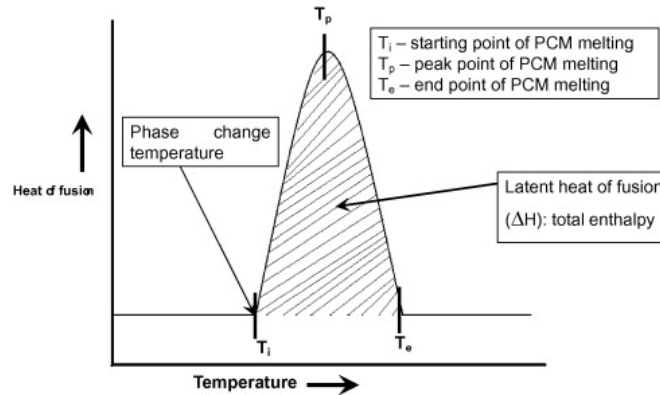


**Figure 2:** Typical differential scanning calorimetry (DSC) heating thermogram for PCM melting. During the phase change, the PCM material absorbs a large amount of latent heat from its surroundings. Reproduced with permissions.<sup>9</sup> Copyright 2007, Elsevier Ltd.

This form of heat storage is different from sensible heat storage (SHS) as it involves a phase change whereas SHS systems do not undergo a phase change but rather work by shifting the temperature of the storage medium.<sup>91</sup> PCMs can be classified based on various criteria such as their phase after transition into solid-gas, solid-liquid, and solid-solid PCMs,<sup>[1]</sup> the temperature ranges over which the phase transition occurs into low temperature (below 15 °C), mid temperature (15-90 °C) and high temperature PCMs (above 90 °C),<sup>92</sup> on the basis of their chemical structure into eutectic and inorganic PCMs,<sup>93</sup> and on the basis of their morphology into fibrous, porous and spherical structured PCMs.<sup>94</sup> While it is beyond the scope of this review to cover the vast literature in the field of PCMs, readers are referred to some excellent reviews on the various types of PCMs.<sup>9,21,89,92-96</sup>

For incorporation of PCMs into textiles for enabling thermal comfort, microencapsulation is an important technique since it allows the PCMs to undergo phase change from solid to liquid within a thin and resilient polymer shell (between 1 – 30 μm in diameter).<sup>9</sup> PCMs have been incorporated into textiles most commonly in three different ways: (i) addition of PCMs into the fiber matrix to

produce phase change fibers by various methods such as (a) wet spinning to create alginate fiber containing microencapsulated *n*-octadecane ( $\mu$ octadecane) PCM,<sup>10</sup> polyacrylonitrile vinylidene chloride fibers with  $\mu$ octadecane PCM,<sup>97</sup> and others,<sup>98,99</sup> (b) melt spinning to create core-sheath fibers with  $\mu$ octadecane-PE composite core/PP sheath,<sup>11</sup> poly(butylene terephthalate) (PBT) fibers containing  $\mu$ octadecane PCM,<sup>100</sup> PET/(polyethylene glycol) (PEG) copolymer that was melt spun into fibers,<sup>101</sup> and others,<sup>102,103</sup> and (c) electrospinning to create electrospun PCM containing fibers such as PET/fatty acids composite fibers,<sup>12</sup> core-sheath fibers with PCM octadecane core and a TiO<sub>2</sub>-polyvinylpyrrolidone (PVP) sheath,<sup>104</sup> and PEG/cellulose acetate composite fibers,<sup>105</sup> and others,<sup>106-109</sup> (ii) coating textiles with microencapsulated PCMs,<sup>13,77,110-112</sup> and (iii) incorporation of microencapsulated PCMs into foams which can subsequently be embedded into textile products.<sup>111,113,114</sup> Sanchez et al. synthesized polystyrene microcapsules containing paraffin wax PCM and coated them onto 100% cotton fabric.<sup>112</sup> Paraffin wax is one of the most commonly used PCMs for storing thermal energy due to its high heat storage capacity, chemical inertness, low toxicity and cost, and tunable phase change temperature; however it needs to be encapsulate for textile applications since it has a low melting point.<sup>115</sup> Sanchez et al. observed thermal insulation of the textiles when PCM microcapsules are incorporated into the fabric via coating by heating coated and uncoated cotton fabrics up to 45 °C and taking thermal images of the fabric surface.<sup>112</sup> The temperature 45 °C was chosen since it was higher than the phase change temperature of the paraffin wax, causing it to melt. They noted that fabrics with PCMs cooled down slower (or retain heat better) than the uncoated fabrics due to the high amount of heat released by the paraffin wax during the cooling process. Hence, the PCM incorporated fabrics were warmer by 8.8, 6.3, 5.6 and 2.5 °C after 6, 12, 44 and 75 s of cooling, respectively.

While PCMs can provide reversible passive heating and cooling, there are certain limitations that they suffer from when incorporated into textiles. Incorporating PCMs into textiles can result in adding excess weight to the fabric as well as reduce the durability of the textile.<sup>21</sup> Additionally, PCMs can also decrease the strength and flexibility of the fabric.<sup>9,21</sup>

### 2.3.2 Passive Heating in Textiles

Historically, pPTCS have been developed by modifying the structure of textiles to impart desirable thermal insulation, including multilayered structures incorporating interlinings,<sup>14,15</sup> specific fiber structures such as core-sheath fibers,<sup>116</sup> hollow fibers<sup>17</sup> and microfibers,<sup>117,118</sup> and various knitted<sup>119,120</sup> and woven fabric constructions.<sup>121,122</sup> Since one of the most fundamental reasons of textile usage is for warmth and protection from external elements, thermal insulation has been an important parameter in the assessment of the overall textile performance.<sup>123</sup> Factors such as the thermal insulation of the fiber, and the stationary air contained within the fabrics and yarns, often expressed as its bulk density or porosity have been considered primary determinants of its thermal properties.<sup>82,124</sup> For example, the scaled outer structure of wool combined with its natural crimp allows this fiber to hold a large amount of stationary air around it. Similarly, natural down fibers - derived from waterfowl such as duck, goose, mallard, and swan - are composed of a shaft of circular cross-section fibers known as barbs, wherein the barbs themselves consist of perpendicular protrusions known as barbules, as shown in *Figure 3*.<sup>125</sup> The barbules consist of periodically repeating hook-like structures which - together with the barbs - allow for greater air entrapment, resulting in more enhanced thermal insulation.<sup>75</sup> The thermal insulation properties of down are attributed to its thick and resilient construction that traps still air, and allows it to recover to its original shape after compressive deformations, thereby retaining the entrapped air.<sup>75</sup> Synthetic

fibers are processed in different ways to mimic this effect of holding a large amount of still air to create thermal insulation.<sup>17,126,127</sup> By having fiber cross-sections with a hollow core, manmade fibers can provide greater thermal insulation due to increasing trapped air within the fibers with higher bulk at lower weight – an imitation of the naturally occurring, hollow medulla in wool fibers and lumen in cotton fibers.<sup>17,126,127</sup> Varshney et al. studied the influence of fiber cross-sectional shape on the thermal comfort properties of fabrics thus created – incorporating four different cross-sections of polyester fibers (circular, trilobal, scalloped oval and tetrakelion) into their study.<sup>128</sup> They observed that fabrics composed of fibers with non-circular cross-sections such as tetrakelion and trilobal have higher thermal insulation due to greater bulk, thickness and trapped air, when compared to fabrics made of fibers with scalloped oval cross-sections. Development of microfibers or micro denier fibers (linear density between 0.3-1 decitex) has also led to enhanced thermal regulation due to their lower heat conductance.<sup>117,118</sup>

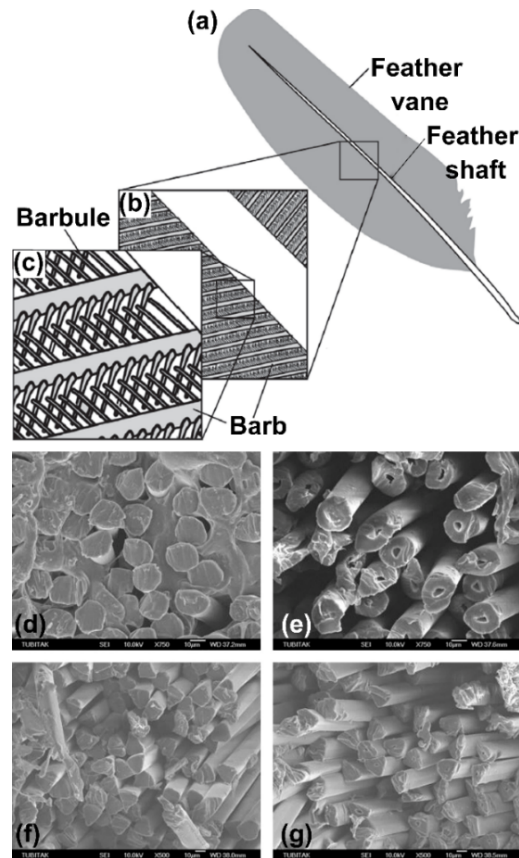


**Figure 3:** Feather structure of modern birds.<sup>129</sup> a) The feather shaft and feather vane. The vane contains barbs and barbules. b) Barbs branching from the feather shaft. c) Barbules are miniature beams branching from the barbs. Reproduced with permissions.<sup>129</sup> Copyright 2016, Acta Materialia Inc. Cross-sectional Scanning electron microscope (SEM) images melt spun polyester.<sup>130</sup> d) Round. e) Hollow-round. f) Trilobal. g) Hollow-trilobal. Reproduced with permissions.<sup>130</sup> Copyright 2006, Wiley Periodicals, Inc.

Another method of imparting higher thermal insulation to fibers and yarns is by enhancing its bulk via a texturization process. In this process, a bundle of flat and smooth fibers (yarn) is undergoes a significant change in its physical form by being crimped, looped, or curled using mechanical or thermal processes.<sup>131</sup> Texturization causes fibers to protrude from the surface of texturized yarns, enabling them to trap air and increase thermal insulation.<sup>132</sup> It also transforms flat, smooth, and slippery filaments into stronger, more cohesive and bulky yarns, enabling greater comfort and thermal properties.<sup>133</sup> Two of the most common methods of texturizing involve heating

thermoplastic fibers in distorted shapes followed by cooling, to retain the shape, or using a turbulent air-jet to entangle the fibers in a yarn to introduce volume.<sup>133</sup> Texturized yarns and resultant fabrics show enhanced elasticity and resiliency, along with an increase in the air spaces in their structure.<sup>15</sup> Texturizing contributes to a decrease in the thermal absorbance of the fabrics made from such yarns, resulting in a lower contact area between the fabric and skin, creating greater air insulation.<sup>133,134</sup>

In nature, thermal insulation plays an important role in the survival of animals in the cold Antarctic and Arctic regions, including penguins, polar bears, and harp seals.<sup>135-139</sup> Hence, these animals have innovatively adapted to their harsh environments by minimizing convection, conduction and radiation heat losses.<sup>139</sup> The long afterfeather and fine barbules in penguin feathers prevent radiative and convective heat losses and sufficiently trap air to increase insulation.<sup>138,140</sup> Additionally, by huddling together penguins also take advantage of social thermoregulation.<sup>141</sup> In the case of polar bears, their nearly transparent hair has a smooth outer surface and is hollow with a rough, lamellar foam-like core, enabling air to be trapped within the hollow structure of the hair, as well as between individual hairs; providing superior thermal insulation.<sup>137</sup> Moreover, polar bear hair traps radiation so well that polar bears appear invisible when viewed with an IR camera.<sup>136</sup> To mimic the structure of such thermally insulating fibers seen in animals, fibers with complex microstructures have been fabricated using various techniques such as microemulsion and microfluidic electrospinning,<sup>142-144</sup> biotemplating to make biomimetic fibers,<sup>145-147</sup> fiber printing,<sup>148,149</sup> microfluidic fiber formation,<sup>150-152</sup> and freeze-spinning.<sup>16,153-155</sup>

Electrospinning is a technique that uses electrostatic forces to drive a conductive fluid onto a collector plate to fabricate ultrathin fibers with diameters ranging from several micrometers to tens of nanometers. Hence, electrospinning has been used to fabricate fibers with both solid and hollow interiors with diverse compositions and mechanical properties.<sup>156</sup> It differs from commercial microscale fiber fabrication processes due to its use of electrostatic repulsion as a way to reduce the fiber diameter, rather than using mechanical or shear forces.<sup>157</sup> Chen et al. used emulsion electrospinning – a technique that can encapsulate materials into electrospun fibers to create functional core-shell structures without the use of elaborate spinneret designs – to create ultraporous TiO<sub>2</sub> nanofibers with diameters below 100 nm.<sup>142</sup> The pores within these fibers were aligned along the fiber length and were hierarchically structured due to demulsification of the oil phase within the fibers combined with the elongation of the liquid due to the electric forces applied during electrospinning. In this way, the pore size within the fibers could be controlled by varying the amount of oil in microemulsion used for fiber formation.<sup>142</sup> However, electrospinning still suffers from certain limitations such as the need for high voltage (in kV range), high sensitivity to fabrication conditions, low reproducibility of the fiber diameters, and toxic gas generation during the electrospinning process.<sup>83</sup>

Another method to fabricate complex biomimetic fibers is through biotemplating – a templating technique that uses natural systems as templates to impart novel functionalities into materials.<sup>158</sup> This technique has been used extensively to biomimick complex fiber morphologies of cotton fibers, wood, silk, and protein fibrils using inorganic materials such as SiC, TiO<sub>2</sub>, SiOC, MgO, Al<sub>2</sub>O<sub>3</sub> and AgNWs.<sup>145,159–164</sup> Reches and Gazit used peptide nanotubes observed in amyloid fibrils as biotemplates/molds for casting silver inside the fibrils to create silver nanowires ~ 20 nm in

diameter.<sup>164</sup> Similarly, Wang et al. used silk fibers as a template to create biomimetic Al<sub>2</sub>O<sub>3</sub> fibers which retained the morphological properties of silk.<sup>145</sup> Since silk has excellent heat insulating properties, it was selected as a natural template to enhance the same properties in Al<sub>2</sub>O<sub>3</sub> fibers, creating micro and meso pores within the fibers. However, fibers produced via bio-templating methods may not always be able to perfectly mimic the structure of their natural counterparts. In the case of Al<sub>2</sub>O<sub>3</sub> fibers, there were obvious non-uniformities on their surface and the biotemplating was not able to impart the smoothness of silk fibers, even though the biotemplated Al<sub>2</sub>O<sub>3</sub> fibers did have better thermal insulation than their traditionally-made counterparts.<sup>145</sup>

In recent years, using printing to create unique fiber cross-sections has been widely explored.<sup>83,148,149,165,166</sup> While some of these works in literature are for fabricating electronic textiles (e-textiles), and hence not directly related to the development of passive thermal comfort fibers, it is still interesting to note the approach used to create unique cross-sections. Note that this process is being referred to as “fiber printing” and not “3D printing” since many of the techniques used are not akin to 3D printing. Rather these fiber printing techniques are nozzle-based extrusion of unique cross-sections, unlike 3D printing where the stage or nozzle are controlled via a preselected computer generated pattern to create micro or macro structures in 3 dimensions using raw materials or inks.<sup>167</sup> Using four cylindrical nozzles aligned coaxially, Frutiger et al. printed capacitive soft strain sensor (CS3) fibers in a four layer configuration, with the cross section consisting of concentric ionically conductive fluid sandwich by layers of silicone elastomer as an insulator/dielectric medium.<sup>148</sup> Our research group also used extrusion of conductive silicone elastomers to create bicomponent dog-bone cross-sectional sensors for strain and touch sensing applications.<sup>165</sup> This extrusion printing method involved extruding photocurable silicone elastomer

and electrically conductive carbon-black containing heat-curing silicone elastomer onto an etched acrylic mold via a custom extrusion setup consisting of syringe pumps.<sup>165</sup> Gao et al. demonstrated a thermally conductive fibrous structure via a combination of wet spinning with 3DP of a suspension of polyvinyl alcohol (PVA) with boron nitride (BN) nanosheets (BNNSs) for use as a thermal regulation smart textile.<sup>83</sup> BN is traditionally used as an effective thermal management material due to its high thermal conductivity combined with electrical insulation.<sup>168,169</sup> Hence, BNNS show a high in-plane thermal conductivity of approximately 2000 W/mK.<sup>170</sup> Using a BN/PVA dispersion as ink for a 3D printer, the fibers were extruded into a cooled methanol bath, followed by drying and hot drawing to align the BNNSs. While the fibers were collected in a coagulation bath of methanol akin to wet spinning, the technique of extruding the fibers was still referred to as 3DP. This process can be considered a combination of wet spinning with material extrusion. Due to the flow-induced alignment of the BNNSs, further enhanced by a subsequent hot-drawing process, the resulting composite fiber had a high in-plane thermal conductivity. The hot-drawing process reduces the diameter of the BN/PVA fibers from 300 to 95  $\mu\text{m}$ , indicating that the structure of the fiber is denser, with high alignment of BNNS along the length of the fiber. These fibers showed good mechanical properties and were used to create knitted and woven fabrics, thereby demonstrating their scalability and application as a wearable thermal regulation fabric for enhanced personal comfort.

While the process of extrusion printing fibers is becoming more popular to create e-textiles, it is still difficult to obtain very long, continuous lengths at the length scale of typical textile fibers.<sup>165</sup> In Gao et al.'s work on thermally conductive BNNS fibers, while the method of making these fibers is referred to as "three-dimensional" printing, on further inspection it is a combination of

nozzle extrusion using a benchtop dispensing robot, followed by coagulation in a methanol bath, and subsequent hot drawing at 200°C.<sup>83</sup> It is important to note that the term “fiber” has been used loosely in research related to 3D printing of fibers. Traditionally, a textile fiber is characterized as having a length at least 100 times its diameter or width, and can be composed of either natural or manufactured materials.<sup>171</sup> Additionally, a fiber has a fibrillary microstructure with highly oriented molecular chains.<sup>172</sup> These fibers are then spun into yarns or made directly into fabrics using various techniques such as weaving, knitting, twisting, felting, braiding, and twisting. Moreover, for fibers to be able to form yarns, they need to be at least 5 mm in length, be flexible and cohesive, and be sufficiently strong so as to create durable yarns and fabrics.<sup>171</sup> Keeping these requirements in mind, printed fibers and filaments are inherently very different from conventional textile fibers and yarns. However, interest in rapid prototyping and 3D printing is consistently growing, and with new materials and techniques it may be possible to create textile-like structures in the future.

Microfluidic fiber formation involves using the microfluidic technique of precise manipulation of fluid within submillimeter scale channels to create fibers with unique cross-sections and morphologies, usually for biomedicine applications.<sup>173</sup> Using photopolymerization and ion crosslinking reactions, various fiber cross-sections have been composed in the submillimeter scale, including hydrodynamically shaped triaxial fibers composed of poly(ethylene glycol) dimethacrylate (PEGDMA) and gelatin,<sup>174,175</sup> coded fibers with varying spatiotemporal variation in material composition composed of alginate which is chelated with Ca<sup>2+</sup> ions to form solid alginate fibers,<sup>176</sup> and hollow hydrogel fibers.<sup>177</sup> While some complex microstructures can be thus obtained, microfluidics is limited by the types of materials that can be used, scalability of production, as well as uniformity of thus produced fibers.<sup>151,178</sup>

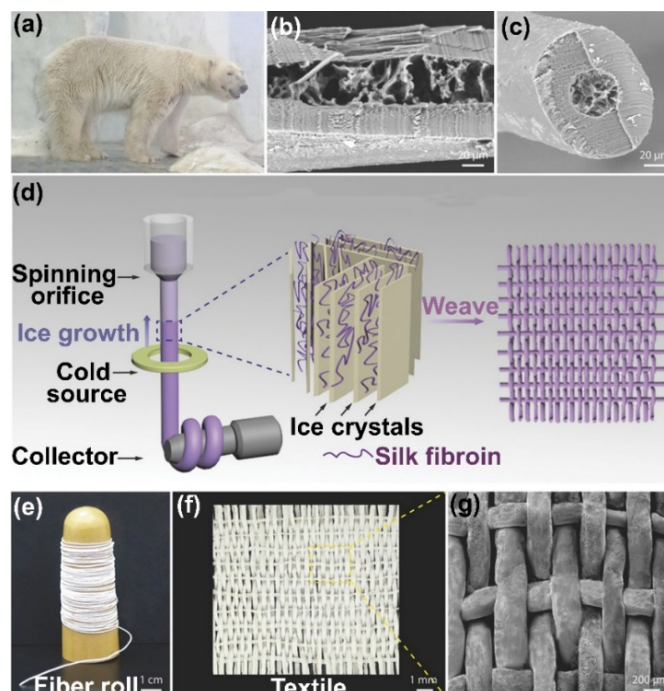


**Figure 4:** Biomimetic hollow core-shell fibers produced via freeze-spinning for thermal insulation.<sup>16</sup> a) A polar bear in its natural habitat. b) SEM image showing the hollow, foam-like structure of polar bear fur. c) SEM image of the core-shell structure of polar bear fur. d) Freeze-spinning method to produce biomimetic fibers, combines directional freezing with solution spinning. This process involves extrusion of silk fibroin solution from a syringe, followed by freezing as it passes through a cold copper ring. Thus formed porous structure is woven into a textile, as shown in figures e), f) and g). Reproduced with permissions.<sup>16</sup> Copyright 2018, WILEY-VCH Verlag GmbH & Co. KGaA, Weinheim.

Freeze spinning provides a simple method to produce large quantities of fibers with complex microstructures, as demonstrated by Cui et al. with hollow fibers consisting of an aligned microporous structure, mimicking the fiber structure of polar bear hair, as shown in **Figure 4**.<sup>16</sup> The fiber's aligned lamellar and axially aligned porous microstructure enabled enhanced mechanical properties, as shown in **Figure 5**. When a fabric made of these fibers was reportedly exposed to external cyclical temperature variation between  $-22$  and  $80^{\circ}\text{C}$ , its temperature only cycles between  $-10$  and  $64^{\circ}\text{C}$ . This superior thermal performance was attributed to the fiber's reduced heat losses through convection, conduction, and radiation. Convective heat losses were

minimized by air being trapped within the fiber microstructure. Additionally, due to high porosity, the thermal conductivity of the fiber is lower. Finally, radiative heat losses are reduced because the aligned microstructure results in higher reflectance and hence radiation can remain trapped within the fiber.<sup>16</sup>

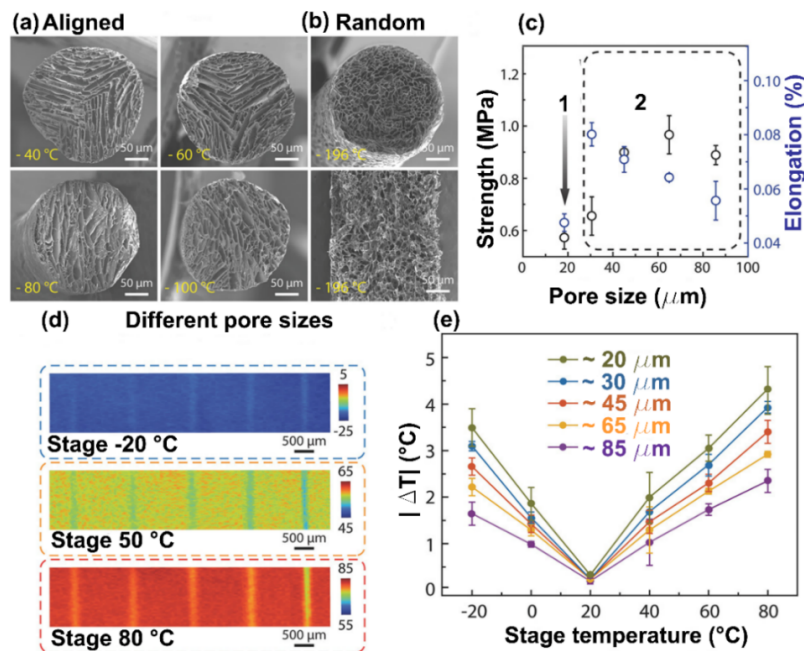


**Figure 5:** Mechanical and thermal insulation performance of biomimetic hollow core-shell fibers inspired by polar bear hair.<sup>16</sup> a) SEM images showing the aligned cross-sections of fibers prepared at - 40°C, - 60°C, - 80°C, and - 100°C. b) SEM images of randomly aligned fiber cross-sections prepared at - 196 °C. c) Comparison of tensile strength and elongation with pore size shows that the random pores (1) have worse mechanical properties than aligned pores (2). d) Infrared images of fibers placed vertically on a heated stage at various temperatures, showing the temperature difference between the fibers and the stage. From left to right, the pore sizes of the fibers (in μm) are: 85, 65, 45, 30 and 20, respectively. e) Absolute temperature difference ( $|\Delta T|$ ) between the stage and the fibers shows that smaller pore sizes have better thermal insulation. Reproduced with permissions.<sup>16</sup> Copyright 2018, WILEY-VCH Verlag GmbH & Co. KGaA, Weinheim.

With increasing global temperatures, cooling is also an important aspect of thermal comfort that can be provided to the human body using innovative textile-integrated technologies. Just as passive heating textiles work to minimize the heat loss from the body, passive cooling textiles explore the

possibility of moving heat away more efficiently. The subsequent section discusses the various implementations of passive cooling in textiles.

### **2.3.3 Passive Cooling in Textiles**

Along with insulation to provide warmth, cooling is also an important aspect of thermal comfort. With an estimated 15% of electricity consumption and 10% of greenhouse gas emissions attributed to global cooling systems, it is an important area of research in pPTCS.<sup>179</sup> Textiles with moisture wicking technology enable quick drying and evaporative cooling of the human body by facilitating the transport of sweat and water vapor from the body to the environment.<sup>18</sup> Traditional hydrophilic textiles such as cotton and wool are easily wetted by sweat due to their multiple bonding sites for water molecules resulting in higher sweat absorption, whereas synthetic hydrophobic textiles such as polyester have fewer water bonding sites which when combined with non-circular cross-sectional profiles allow for higher surface area and increased moisture wicking abilities.<sup>180–183</sup> Hence, to enable high moisture absorption and release, a combination of hydrophilic and hydrophobic textiles is needed.<sup>184</sup> Synthetic fibers are becoming increasingly popular in the textile industry due to their superior wash and wear, anti-wrinkle, and quick drying properties despite their low moisture regain (moisture regain of polyester is 0.42% while that of cotton is 8.5%).<sup>180,185,186</sup> For this reason, modifications to synthetic fabrics such as using profiled fibers i.e. fibers with non-circular cross-sections that allow for higher surface area and increased moisture wicking have been made.<sup>180–183</sup> For example, Coolmax® profiled polyester fibers have a unique “tetra-channel” cross-section with a flat trench that can form capillaries with adjacent fibers, allowing for sweat to wick through these capillaries and dissipate to the outer fabric.<sup>181</sup> Other modifications to enhance moisture wicking in synthetic fibers include hollow/microporous

fibers,<sup>187,188</sup> application of hydrophilic surface finishes on synthetic fabrics,<sup>189–191</sup> creating blended/layered hydrophilic and hydrophobic fabrics to enhance moisture wicking.<sup>18,190,192,193</sup>

A crucial limitation of the profiled moisture wicking fibers is that the transport of water is bi-directional, i.e. the inner side of the fabric that is towards the skin would also be wetted by sweat and cling to the body. On the other hand, application of surface finishes requires complex manufacturing processes and may suffer from slower moisture wicking rate. To combat this, directional or “one-way” water motion has been implemented into fabrics to enable more efficient moisture-wicking.[177,178,206,206–215]<sup>18,78–80,194–196</sup> This moisture transport and collection effect is observed in nature on the wings of the desert beetle<sup>197</sup> and butterfly,<sup>198</sup> on *Cactus* spine<sup>199</sup> and spider silk,<sup>81</sup> and on rice<sup>200</sup> and *Strelitzia reginae* leaves, as shown in **Figure 6**.<sup>201</sup> These mechanisms - observed in the desert beetle, cactus and spider silk - are referred to as Janus wettability which results in an asymmetric and abrupt change in wettability, and have been implemented in fabrics using hydrophobic and hydrophilic fibrous layers.<sup>18,184,202</sup>

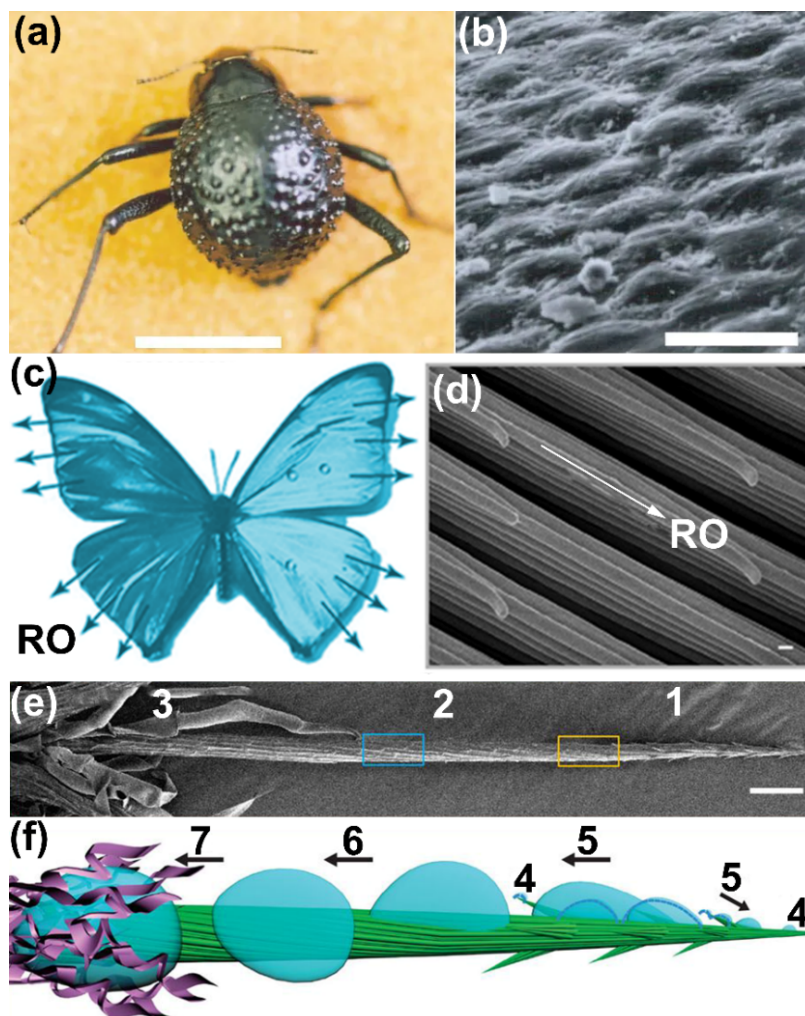


**Figure 6:** Moisture transport and collection in nature. a) Peaks and troughs on the overwings of the desert beetle.<sup>197</sup> Scale bar = 10 mm. b) SEM image of the overwings with flattened hemispheres in a hexagonal array, like the superhydrophobic surface of a lotus leaf. Scale bar = 10  $\mu\text{m}$ . Reproduced with permissions.<sup>197</sup> Copyright 2001, Springer Nature. Directional adhesion of water on the superhydrophobic wings of a butterfly.<sup>198</sup> c) Illustration showing arrows on the butterfly wings, indicating the radial-outward (RO) direction away from the body's central axis along which water droplets roll. d) SEM image shows lamellar stripes on the wings, stacked stepwise along the RO direction. Scale bar = 100 nm. Reproduced with permissions.<sup>198</sup> Copyright 2007, The Royal Society of Chemistry. Fog collection system on the spine of the cactus plant.<sup>199</sup> e) SEM image of a single cactus spine consisting of three regions: (1) tip with oriented barbs, (2) middle with gradient grooves, and (3) base with hair-like structures called trichomes. The blue and yellow boxes indicate regions with wider and narrower grooves, respectively. Scale bar = 20  $\mu\text{m}$ . f) Mechanism of fog collection on the cactus, water droplet deposition on the barbs and spine (4), followed by collection on its tip (5), transportation on grooves (6), and absorption onto trichomes (7). Adapted with permissions.<sup>199</sup> Copyright 2012, Springer Nature.

Miao et al. implemented the principle of Janus wettability by developing a trilayered fabric with electrospun polyacrylonitrile (PAN)-SiO<sub>2</sub> fibers on the outermost layer, hydrolyzed polyurethane (PU)-PAN as the middle transfer layer and hydrophobic PU membrane as the inner layer to create a fabric with progressive wettability, as shown in *Figure 7*.<sup>18</sup> In this manner, sweat would collect on the PU layer without spreading along the surface, creating an anisotropic movement of water. The sweat would then move through the hydrolyzed PU-PAN transfer layer that allows movement only in one direction, preventing penetration of sweat back towards the skin. Finally, at the PAN-SiO<sub>2</sub> layer the sweat would spread and dissipate over the entire membrane due to the capillary motion of the nanostructured fibers and their superhydrophilicity. Such fabrics have been explored by other researchers as well, wherein bilayered or trilayered fabrics with the moisture wicking layer composed of electrospun fibers such as PLA/cellulose acetate (CA),<sup>78</sup> PAN coated with polydopamine,<sup>195</sup> PVA,<sup>196</sup> and PAN-SiO<sub>2</sub>.<sup>80</sup> While such fabrics provide a method to create sudden transitions in wettability by creating multiple fabric layers, a challenge with this technique is to ensure that moisture transport retains its unidirectionality and does not travel backwards into the fabric. Another method of creating directional moisture wicking on a hydrophobic woven polyester fabric is by creating a hydrophobic to hydrophilic transition through the fabric thickness.<sup>194,203–205</sup> This was explored by Zeng et al. by electrospaying a thin layer of SU-8 (commercial photoresist) on one side of it, creating a hydrophilic finish which enabled one-way transport of moisture.<sup>194</sup> However, such finishes need further exploration in terms of washability and durability to the various stresses and strains textiles experience.

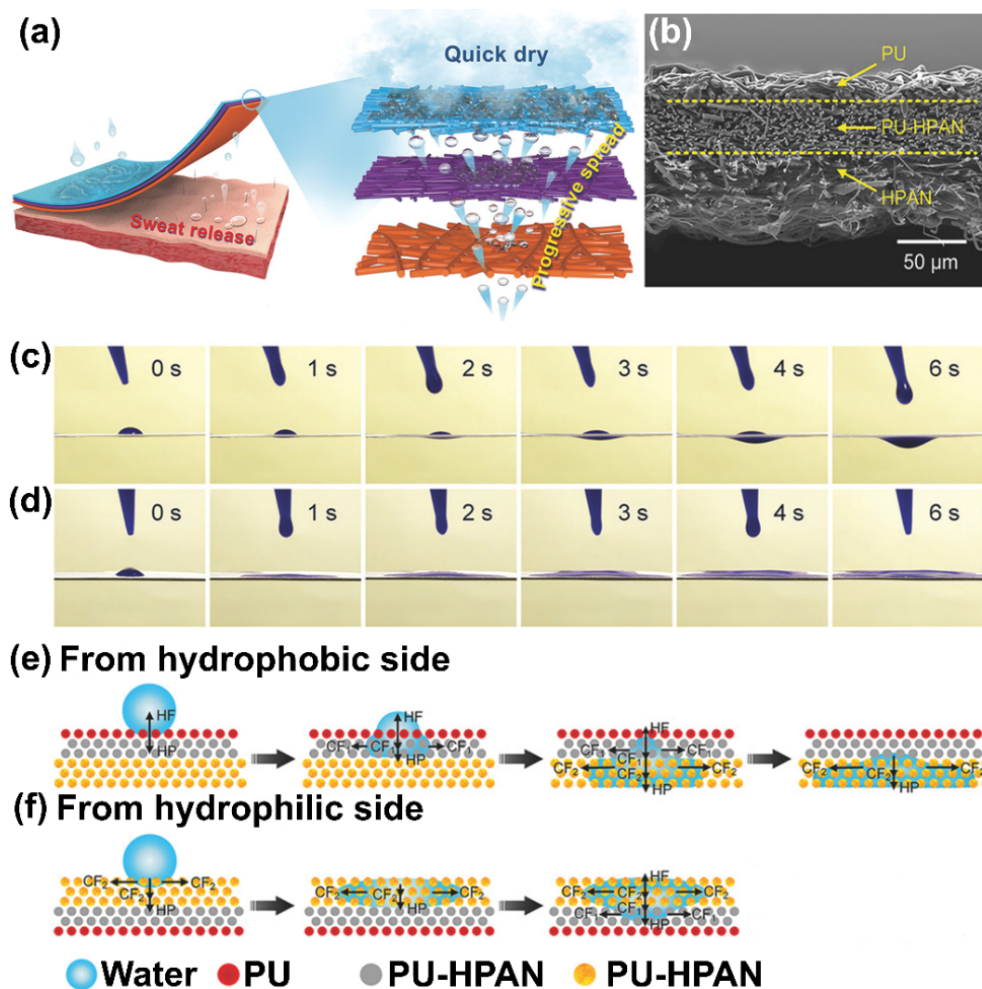


**Figure 7:** Trilayered moisture wicking membrane with directional water transport for thermal comfort.<sup>18</sup> a) Schematic showing the moisture wicking process in the trilayered fabric. The outermost layer (blue) is composed of electrospun hydrolyzed polyacrylonitrile-SiO<sub>2</sub> (HPAN) fibers and facilitates capillary motion to pull out sweat. The middle layer (purple) is composed of hydrolyzed PU-PAN (PU-HPAN) fibers and acts as a transfer layer with progressive wettability. It guides the water from the inner to the outer layer, without allowing transfer in the opposite direction. The layer closest to the skin (orange) is hydrophobic PU membrane which allows anisotropic wettability thorough the thickness, allowing sweat to penetrate through the inner layer without spreading on the surface. b) SEM image of the cross-section of the trilayered membrane. c) A drop of water placed on the hydrophobic PU side of the trilayered membrane penetrates it almost instantaneously. d) A drop of water placed on the hydrophilic HPAN side spreads across its surface. e) and f) illustrate the mechanism of water transport through the layers, depending on whether the water is dropped from the PU side or the HPAN side, where the transport depends on the balance of hydrostatic pressure (HP), hydrophobic force (HF), and capillary force (CF<sub>1</sub>, CF<sub>2</sub>) felt by the water droplet. Reproduced with permissions.<sup>18</sup> Copyright 2018, WILEY-VCH Verlag GmbH & Co. KGaA, Weinheim.

While moisture wicking or evaporative cooling is one of the most prevalent methods of cooling the body currently, it is limited by the fact that the fabric is only activated when there is considerable perspiration present on the wearer's skin.<sup>70</sup> Hence, this may not be the best method of providing cooling during sedentary conditions. Radiative cooling fabrics can be an efficient manner to deliver thermal comfort in such situations.<sup>19,20,68,69,206</sup> Mid-infrared (IR) radiation emitted from the human body accounts for over 50% of the total body heat loss.<sup>20</sup> Hence, being able to dissipate heat from the human body via radiation would enable efficient cooling. There are certain requirements that such textiles must fulfil in order to provide passive radiative cooling, including efficient reflection of incident sunlight and high emission in the 8 – 13  $\mu\text{m}$  wavelength with reflection in all other wavelengths.<sup>207</sup> Tong et al. developed a theoretical design for an infrared (IR)-transparent visible-opaque fabric (ITVOF) with polyethylene (PE) as the material taken into consideration for calculations.<sup>70</sup> They predicted that for a textile to be able to have sufficiently high transmittance and low reflectance in the IR wavelengths while still maintaining opacity in the visible wavelengths it would need to be made of a synthetic material and have a low material volume with small yarn (30  $\mu\text{m}$ ) and fiber (1  $\mu\text{m}$ ) diameters.<sup>70</sup> However, as Tong et al. point out in their research, PE is not compatible in terms of wearability, dyeability, and launderability of textiles. Additionally, the transmission of water vapor is an important aspect of comfort that is not possible in PE fabrics. To further this research on IR transparent fabrics, Hsu et al. created a nanoPE cooling fabric with dual-mode, bilayer passive heating and cooling, consisting of a low-emissivity layer combined with a high-emissivity layer, as shown in **Figure 8**.<sup>68</sup> The bilayers composed of a high-emissivity material (nanoPE coated with carbon) and low-emissivity material (copper coated nanoPE) layered together and sandwiched by uncoated nanoPE on both sides. Since nanoPE is IR transparent, it can allow radiation to travel through it, with the bilayer fabric acting

as a filter to regulate the amount of radiation that passes into the ambiance from the skin. Hence, in the cooling mode the high-emissivity layer is facing towards the ambient side, with a thin layer of nanoPE between the emitter and the skin. Radiation passes from the skin, through this thin layer, and is emitted into the ambient temperature more readily than a conventional textile fabric. Similarly, by flipping the bilayer in the heating mode such that the low emissivity layer is facing the ambient side, less radiative heat is lost from the body to the environment. Peng et al. developed a cooling fabric composed of nanoporous PE (nanoPE) microfibers made via large-scale fiber extrusion process, as shown in *Figure 8*.<sup>20</sup> This work expanded their previous work on the development of nanoPE in a nonwoven film form, which is not implementable into a wearable textile.<sup>69</sup> Due to the presence of nanoscale porosities within these fibers, they can scatter visible light of larger wavelengths while transmitting mid-IR radiation from the human body. Visible light scattering enables the fabric composed of these fibers to remain opaque, whereas mid-IR transmission enables radiative heat transfer away from the body. Compared to skin covered with a cotton fabric, nanoPE fabric raises the skin temperature by 1.3°C, whereas cotton raises it by 3.6°C.

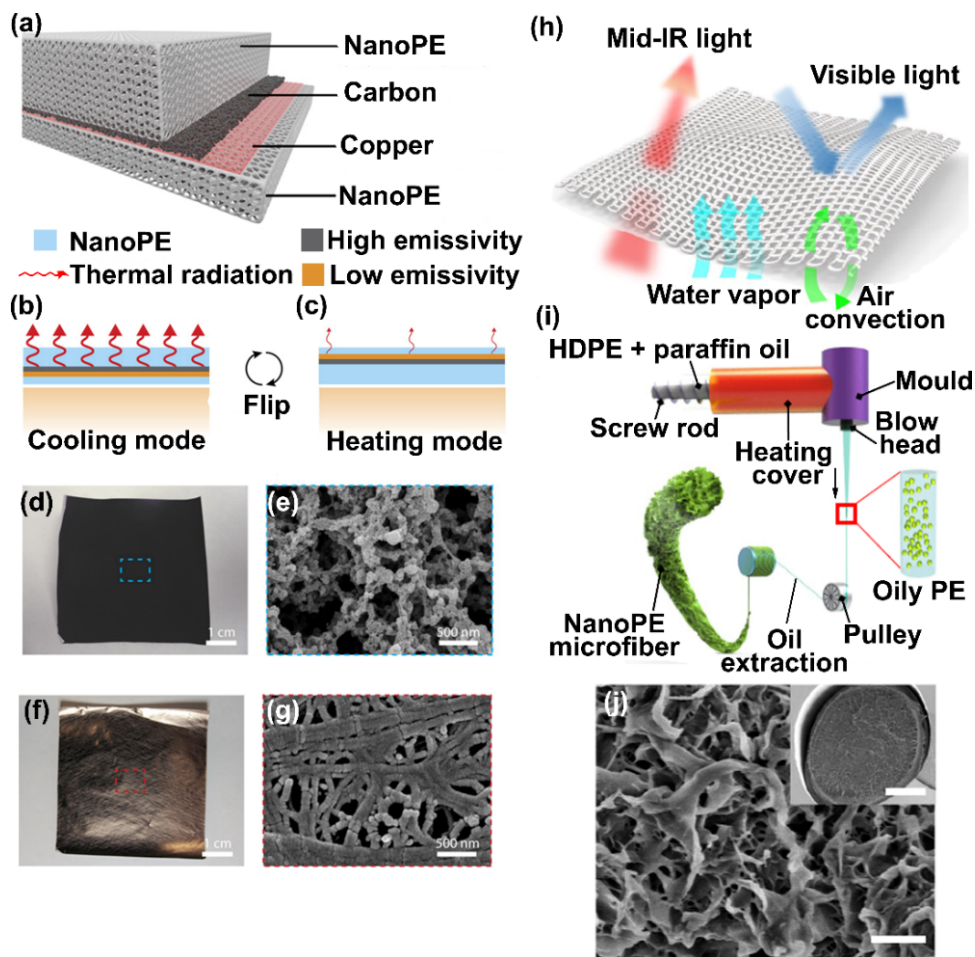


**Figure 8:** Dual mode coated textile composed of nanoPE for radiative heating and cooling.<sup>68</sup> a) Dual mode textile composed of multiple layers of nanoPE, carbon and copper with each layer consisting of a porous structure to enable comfort. b) and c) Illustrate the mechanism of dual mode textile. In cooling mode (b) with the high emissivity layer facing outside and the thinner nanoPE layer facing towards the skin, there is larger heat transfer resulting in cooling. In the heating mode (c) when the low emissivity layer is facing outside with the thicker nanoPE towards the skin, heat transfer coefficient decreases, enabling heating. d) High emissivity layer with carbon coating, with e) showing the SEM image of this side. The rough surface and pores enable higher emissivity. f) Low emissivity layer with copper coating, with g) showing the SEM image of this layer with its optically smooth surface and nanopores for moisture and vapor permeability. Reproduced with permissions.<sup>68</sup> Copyright 2017, Creative Commons Attribution NonCommercial License (CC BY-NC). Woven and knitted nanoPE fabric for large-scale radiative cooling.<sup>20</sup> h) Schematic illustrating the various modes of cooling integrated into the fabric. With its high mid-IR transparency, it allows for radiative cooling from the human body, while remaining opaque to visible light. i) nanoPE microfibers were manufactured using a modified wet spinning process wherein a solution of paraffin oil and PE is extruded, and solidified, thereby phase separating to create nanopores. The paraffin oil is subsequently removed using methylene chloride, creating nanoPE fibers. j) SEM image of the cross-section and pores of the nanoPE fiber, with the inset showing a lower magnification SEM image of the fiber's cross-section. Reproduced with permissions.<sup>20</sup> Copyright 2018, Springer Nature.

During the day time, textiles made for radiative cooling face the challenge of resolving the internal heat generated both by the body and external heating from solar irradiance (approximately  $1000 \text{ W m}^{-2}$ ).<sup>19,208</sup> Hence, such materials need to be responsive to mid-IR and solar wavelengths (0.3 – 4  $\mu\text{m}$ ) without sacrificing visual opaqueness. Such a material was first demonstrated by Cai et al. who made a nonwoven fabric by impregnating nanoPE with zinc oxide (ZnO) nanoparticles (NPs) – termed as a ZnO-PE.<sup>19</sup> The low refractive index of nanoPE was offset by the high refractive index and low absorption in the visible and mid-IR wavelengths of ZnO. In this way, ZnO-PE was able to cool the skin outdoors better than cotton and bare skin.

The pPTCS based on radiative cooling are able to provide much better performance than conventional textile materials such as cotton, and even bare skin itself. However, there are a few caveats in their design that need to be addressed: most of these implementations are in film or nonwoven form. While these are suitable for demonstrating efficiency of cooling, when it comes to actual wearability, dyeability, launderability, and moisture wicking, further research is needed. Modifications such as making a woven or knitted structure,<sup>20</sup> needlepunching and embedding cotton meshes into such fabrics to improve breathability,<sup>69</sup> applying coatings such as polydopamine to increase hydrophilicity,<sup>19,69</sup> and improving dyeability by incorporating pigments<sup>69</sup> or making blends rather than pure nanoPE fabrics<sup>70</sup> can enable radiative cooling textiles to be more applicable for practical use. Hence, the future of radiative cooling fabrics lies in developing them into dual mode heating and cooling fabrics to provide more extensive applications during both summer and winter seasons,<sup>68,206</sup> and incorporating aspects of moisture wicking fabrics into their design to allow wearability.

## 2.4 Active Systems for Thermal Comfort

An ideal self-correcting and adaptive PTCS system should use the active components that can either enhance the range of pPTCS or be used by themselves to provide thermal comfort in extreme temperature conditions. Active PTCS can be implemented using a variety of technologies such as liquid cooling integrated into textiles,<sup>22–25</sup> electrocaloric cooling,<sup>26–28</sup> magnetocaloric cooling,<sup>29–32</sup> TE temperature regulation,<sup>33–37,61</sup> and Joule heating devices.<sup>38–45</sup> Technologies such as Joule heating devices and TEs are easier to implement into textile structures, whereas others such as liquid cooling can be cumbersome and bulky, and in case of magnetocaloric and electrocaloric cooling, are emerging technologies existing mainly in flexible film form. Additionally, TE cooling is well-studied and has the highest exergetic efficiency amongst the various methods of solid state cooling.<sup>46</sup> Hence, this review will narrow its focus of aPTCS to Joule heating fabrics and TE temperature regulation systems. These systems have the capability to provide lightweight thermal comfort solutions that can be integrated into existing fabrics by coating or carbonizing,<sup>39,58</sup> or by integrating thermoregulatory patches into fabrics.<sup>34</sup>

### 2.4.1 Joule Heating

Resistive or ohmic or Joule heating is a fundamental principle by which electrical heaters operate. The basic principle of this phenomenon is the generation of heat due to collisions of electrons with atoms and other free electrons in an electrical conductor when current is passed through it. The amount of heating power ( $P$ ) produced by the electrical conductor is a product of the square of the current ( $I$ ) and the resistance ( $R$ ) the conductor,  $P = I^2R$ , known as the *Joule-Lenz law*.<sup>209</sup>

Integration of Joule heating technologies into wearable form factors has the potential for use in thermotherapy for alleviating joint pains,<sup>210,211</sup> promoting wound healing,<sup>212</sup> and PTC fabrics.<sup>38,213</sup> There are certain important aspects that have to be taken into account while integrating such elements into wearable applications: comfort, weight, haptic feedback where the heaters are located, sewability/weavability of the fabric, and the ability to withstand multiple cycles of use.<sup>(217)</sup> Due to the changes in resistance that occurs during mechanical deformation, it is important to ensure that when Joule heating elements are integrated into textiles they maintain their heating capability. Commonly used materials for creating such heating elements within textiles include carbon materials such as carbon nanotubes (CNTs)<sup>40-42</sup> and graphene,<sup>39,214</sup> metallic NWs,<sup>38,210,213</sup> and conducting polymers,<sup>43,44,215,216</sup> as well as composites of these materials.<sup>217-221</sup>

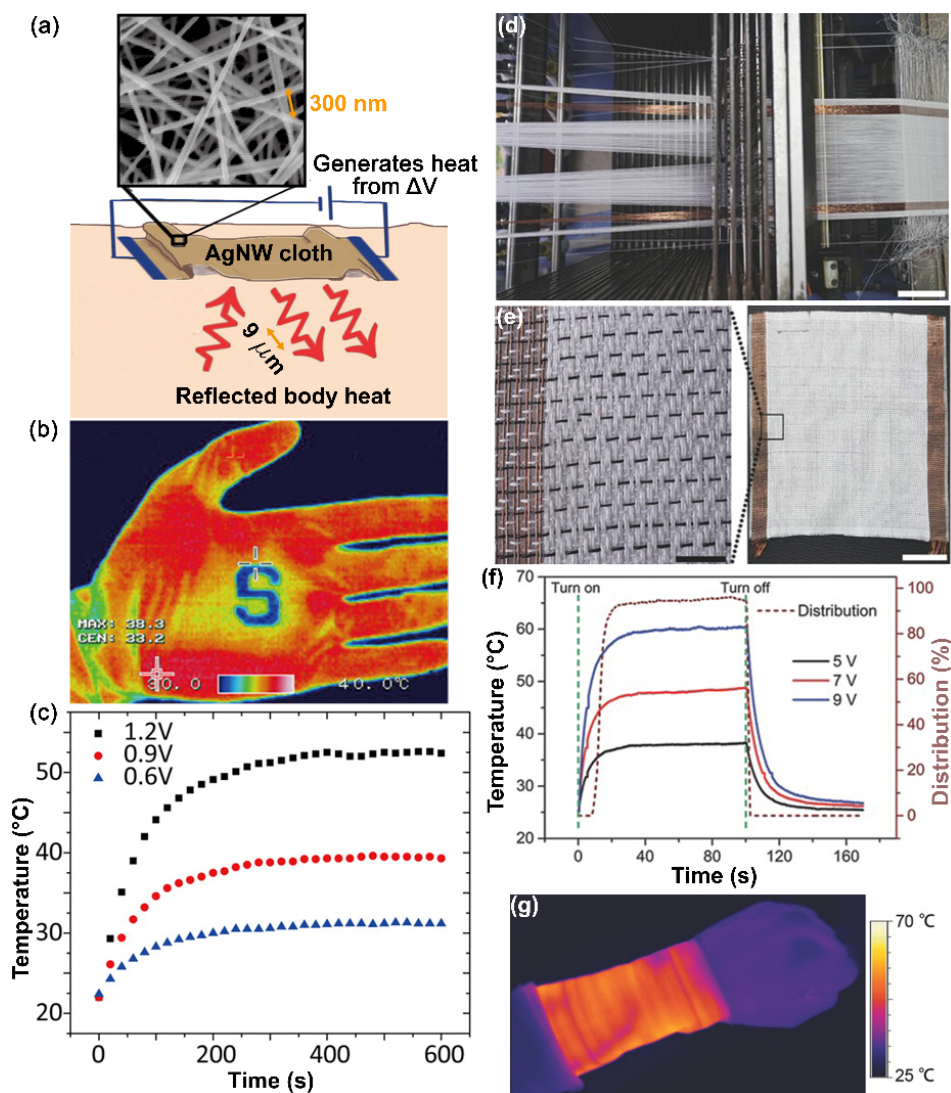


**Figure 9:** Cotton fabric dip coated with AgNW dispersion to create a resistive heating fabric for personal thermal comfort.<sup>38</sup> a) Concept of the AgNW coated fabric that enables passive thermal radiation insulation coupled with active Joule heating. b) The cloth was cut into an S shape and placed on the palm, with the thermal image showing that the AgNW cloth can effectively block IR radiation from the human body, thereby showing a lower temperature. c) Different voltages are applied to a 1 inch X 1 inch AgNW-cotton fabric and the temperature change is measured. A 0.9 V applied voltage can induce a temperature change up to 38 °C. Reproduced with permissions.<sup>38</sup> Copyright 2015, American Chemical Society. CNT fibers integrated into woven fabric for Joule heating textiles.<sup>222</sup> d) CNTs are woven with cotton threads and copper wires to create Joule heating fabrics. The copper wires were used as conductors so that no other conductive paste or tape was needed. Scale bar, 6 cm. e) Heating textile at high and low magnifications. Scale bars are 3 mm and 25 mm for the left and right images. f) The fabric had a large heating area of 13 cm X 10 cm and showed an increase in saturation temperatures of 38 °C, 48 °C and 60 °C when the voltage is increased from 5 V, 7 V to 9 V. g) Thermal image of the heating textile at 9 V wrapped around the wrist. Reproduced with permissions.<sup>222</sup> Copyright 2017, WILEY-VCH Verlag GmbH & Co. KGaA, Weinheim.

Metallic NWs are popular materials for creating PTCS fabrics due to the dual benefit of having low sheet resistivity, along with high optical transmittance – making them good candidates for transparent PTCS.<sup>38,213,219</sup> Hsu et al. demonstrated a combination of aPTCS and pPTCS using silver nanowires (AgNWs) dispersion to coat cotton cloth, creating a thermal heating textile which blocked radiative heat loss from the body (aPTCS) and provided Joule heating when connected to an external electrical source, as shown in **Figure 9**.<sup>38</sup> This was possible due to the AgNWs forming a continuous network on the cotton fabric, with a spacing of 200-300 nm that reflected IR radiation from the body (9  $\mu\text{m}$ ), retained water permeability and flexibility of the fabric, and kept sheet resistance low enough that a low driving voltage of 0.9 V could increase body core temperature up to 38°C higher. Additionally, this fabric was shown to have stable electrical behavior even after multiple wash cycles, and provided the added advantage of making fabrics anti-microbial.<sup>38</sup> Hong et al. also created AgNW-based flexible, stretchable, and transparent heater, partially embedded in a PDMS matrix.<sup>213</sup> This heater could operate even when strained, reaching 50°C at 40% strain at 6.2 V. This was possible due to the AgNWs being partially embedded within the PDMS matrix, combined with their high aspect ratios and the stretchability of the matrix. Hence, the composite would not lose its electrical connection (and conversely its Joule heating ability) even when elongated to 60% strain. Moreover, using laser ablation, Hong et al. were able to create location specific Joule heating effects that could be easily controlled without destroying the PDMS matrix.<sup>213</sup> The advantage of integrating metallic heating components into textiles is that these are easily available at a commercial scale and hence can be produced in larger quantities.<sup>45</sup> Additionally, they have robust electrical performance with high conductivity, thereby ensuring more efficient heating.

Nevertheless, creating efficient interfaces with organic materials, such as textiles, can be challenging with metallic NWs due to the differences in mechanical properties between the two.<sup>210</sup> Additionally, there can sometimes be a mismatch between the textures of metallic heaters and the fabrics they are combined with, creating a sensation of discomfort to the wearer.<sup>43</sup> Hence, using carbonaceous materials such as CNTs and graphene to create resistive heating fabrics has proven to be advantageous in this regard.<sup>222,223</sup> These materials also provide a good combination of electrical and mechanical properties, making them viable candidates for aPTCS applications. Li et al. developed a thermochromic resistive heater (TRH) composed of aligned CNT sheets applied to a prestretched thermochromic silicone strip, which is released to form a rippled strip.<sup>211</sup> These TRH strips were then woven to form a fabric structure which could indicate the temperature during resistive heating with the aid of thermochromic inks, when a voltage of up to 10 V is applied to the fabric. In this way, it was possible to create a resistive heater with a visual feedback that could make it safer for wearers. The electrical resistance and Joule heating effect was maintained for strains up to 100%. Ilanchezhiyan et al. also fabricated wearable and flexible resistive heaters by dip-coating cotton fabrics into SWNT solution, taking advantage of the strong van der Waals forces between CNTs and cotton fabrics.<sup>40</sup> Inspired by the helical and hierarchical structure of wool fibers, Liu et al. created stretchable and responsive hierarchical helical CNT fibers (HHF) from CNT ribbons for application as woven heating textiles, as shown in **Figure 9**.<sup>222</sup> Due to this structure, the helical voids within the HHF, they were able to provide passive thermal insulation along with active Joule heating, going up to 135°C at 5V applied voltage. The HHF could then be woven into a fabric with copper wire and cotton thread as warp yarns and CNT fiber with cotton thread as weft yarns. Thus, by combining traditional textile design with Joule heating principle,

Liu et al. were able to create a PTCS that was capable of both passive and active temperature control.

While carbonaceous materials are integrated readily into textiles, they still suffer from problems of having a percolation dependent conductivity, being incompatible with human skin, showing cracks and buckling within the textile structure, being compatible with only certain types of textile substrates, and in some cases needing complex processing methods.<sup>223–225</sup> In contrast, conductive polymers can provide lightweight and conformal coating of pre-existing textile materials to transform already manufactured garments into Joule heating devices.<sup>225–228</sup> Additionally, conductive polymers such as polypyrrole, polyaniline, and poly(3,4-ethylenedioxythiophene): poly(styrene sulfonate) (PEDOT:PSS) are compatible with various techniques such as dip-coating,<sup>229,230</sup> *in-situ* polymerization,<sup>231,232</sup> and vapor deposition techniques such as CVD,<sup>233,234</sup> with the ability to apply them on both synthetic and natural textile materials.<sup>216,235–237</sup> One of the most well-studied materials for coating textiles to create electrically conductive structures is PEDOT due to the fact that it forms a stable suspension in water when combined with PSS – making it solution processable, its lack of cytotoxicity, and the ease with which its conductivity and electrical behavior can be modulated using dopants.<sup>225,232</sup> Zhang et al. vapor coated PEDOT onto fourteen different fabrics: five cotton fabrics with varying weave densities, two silk fabrics, three linen fabrics, one wool gauze, one bamboo rayon fabric, and two bast fiber fabrics demonstrating the effectiveness of vapor coating methods to create a variety of textile electrodes.<sup>236</sup> Opwis et al. deposited PEDOT: *p*-toluenesulfonic acid (PEDOT:PTSA) on polyester fleece fabric using a one-step *in-situ* polymerization technique.<sup>227</sup> By optimizing their coating technique for the time, amount of material used, and temperature of polymerization they were able

to obtain a high add-on of PEDOT:PTSA in a single step onto polyester fleece. Correspondingly, they were able to obtain uniform temperatures as high as 170 °C at 24 V applied voltage, with a surface resistance of 11.6  $\Omega/\square$ . While they observed relatively stable electrical performance when the coated fabric was rubbed, exposed to light, and stored over 10 days of storage in varying relative humidity levels, there was an increase in surface resistance when the fabric was stretched by 20%.<sup>227</sup> Yeon et al. coated PEDOT:PSS onto cotton and polyurethane fabrics using a combination of blending and dip-coating, resulting in sheet resistances of 24 and 48  $\Omega/\square$  for cotton and polyurethane fabrics, respectively.<sup>43</sup> The resistance depended on the amount of material coated onto the fabrics, as well as the hydrophilicity, style of weave and porosity of the fabrics. These factors influence the amount of material that the fabric can absorb during coating. With the cotton fabric they were able to obtain a heating performance of 99.6 °C at an applied voltage of 12 V. Additionally, these fabrics demonstrated heating performance of 46 °C even when strained higher than 100%. However, creating uniform and conformal coatings with this dip-coating and blending method can be difficult depending on the type of fabric structure, making it difficult to obtain consistent performance over a range of fabric types. Moraes et al. plasma treated nylon fabrics to make them conducive to glycerol doped PEDOT:PSS deposition, which demonstrated a lower resistivity than dip-coated fabrics.<sup>225</sup> However, these fabrics had non-uniform coatings and corresponding heating performances, reaching a temperature of 64 °C at 12 V applied voltage, with certain sections of the fabric going up to 80 °C. Hence, while conductive polymers are promising materials for Joule heating fabrics, it is important that the coating is uniform, not so thick that it hampers the flexibility of the fabric itself, and the process is controllable such that consistent heating performance can be obtained without hotspots.

While Joule heating fabrics have the potential to be used in a variety of applications where either the performance of pPTCS has to be enhanced, or in harsh, cold environments where insulation can be cumbersome and inadequate, they are still limited by the fact that they only provide a single mode of temperature control – heating. Being able to combine heating and cooling into one fabric is very attractive for wearers and can reduce the number of garments required for humans, thereby lowering textile waste and combating the ill-effects of fast fashion. The next section explores how TE cooling could be a potential solution to this problem.

#### **2.4.2 Thermoelectric Temperature Regulation**

Since the discovery of the Seebeck effect (conversion of heat into electrical energy) in 1822 by Thomas Seebeck and Peltier effect (conversion of electrical energy into cooling/temperature gradient) by Jean Peltier in 1834, TE devices have been sought as solutions to make refrigerators and power generators obsolete.<sup>238,239</sup> The appeal to TE devices has persisted due to their potential to deliver solid state cooling or power generation without any moving parts, toxic emissions, or loud sound during operation.<sup>240,241</sup> Additionally, more than 90% of the energy we use is generated by thermal processes, and conversely, heat energy is the primary form in which we waste energy.<sup>242</sup> Hence, implementing TE devices for thermal comfort and power generation can be an eco-friendly solution to meet global energy demands.<sup>243,244</sup> To realize effective TE performance, researchers focus on two key areas: (i) improving the performance of TE materials,<sup>24,241,245–248</sup> and (ii) rational TE device design for performance optimization.<sup>249–252</sup> The dimensionless figure of merit ( $ZT$ ) is used to express the performance of TE materials, and is expressed as  $ZT = S^2\sigma T/\kappa$  where  $S$ ,  $\sigma$ ,  $T$ , and  $\kappa$  are the Seebeck coefficient, electrical conductivity, total thermal conductivity, and the absolute temperature, respectively.<sup>243,253,254</sup> To improve the performance of TE materials either the

power factor ( $PF = S^2\sigma$ ) of the material has to be increased or the thermal conductivity has to be decreased using various methods such as doping, nanostructural engineering, or by developing new materials.<sup>241,255–257</sup> A number of excellent reviews exploring the recent developments in TE materials and devices have also been published.<sup>241,242,253,258–263</sup>

#### **2.4.2.1 Principles of TE Materials and Devices**

The energy and entropy transportation in TE devices is caused by the motion of charges in TE materials. Consider the case of the Peltier effect, where current flowing through a pair of n-type and p-type materials connected in series causes a cooling at the junction, as shown in *Figure 10*. In this case, the electrons in the n-type material and holes in the p-type material carry heat away from the metal-semiconductor junction. A material is referred to as a hole (or electron) transporter when its ionization energy (or electron affinity) closely matches the Fermi level of the electrode material that is used to inject charges into the material.<sup>264</sup> Conversely, if a temperature gradient is maintained between the two ends of the n-p junction, electrons and holes diffuse to the cold side due to their higher thermal energy, thereby creating a potential difference – known as the Seebeck effect.<sup>265</sup>

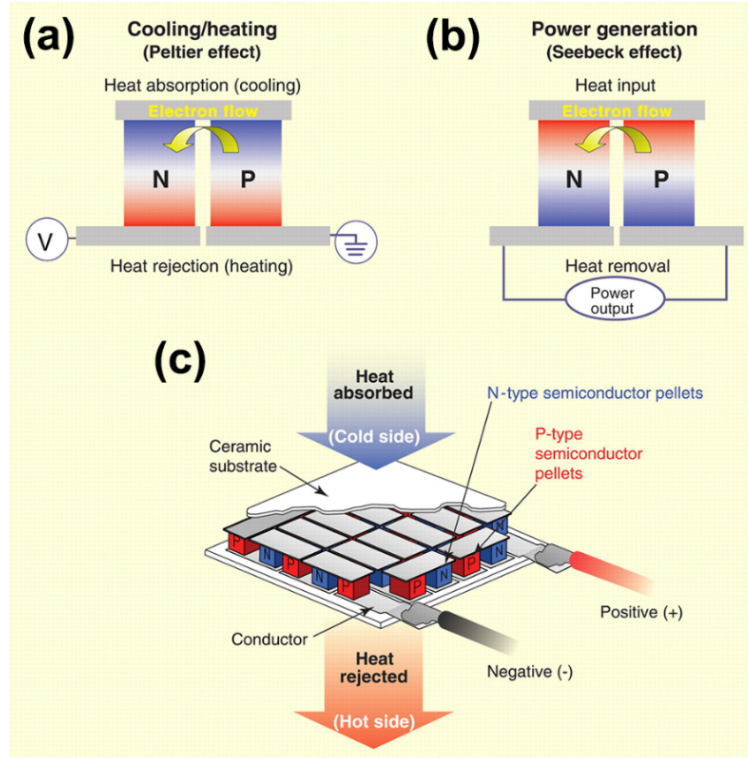


**Figure 10:** Principles of TE devices.<sup>266</sup> (a) When flows through a TE junction, it can either heat or cool the junction depending on the direction of the current, known as the Peltier effect. (b) When an external thermal gradient is applied to the junction, electrical current is generated through the Seebeck effect. (c) Commercial TE generators consist of many n and p TE legs connected to form TE junctions electrically in series and thermally in parallel to enable higher power output and spread heat flow over a larger area. Reproduced with permissions.<sup>266</sup> Copyright The Author and 2008, American Association for the Advancement of Science.

As stated previously,  $ZT$  governs the performance of TE materials, and in order to achieve high  $ZT$ , TE materials should have high  $\sigma$ , high  $S$ , and low  $\kappa$ . The thermal conductivity,  $\kappa = \kappa_l + \kappa_e$ , takes into account contributions from both lattice vibrations (lattice thermal conductivity,  $\kappa_l$  which characterizes the transport of thermal energy carried by phonons in the form of lattice vibrations) and electronic thermal conductivity ( $\kappa_e = L\sigma T$ , where  $L$  is the Lorenz number in the Wiedemann-Franz law).<sup>241</sup> In highly doped semiconductors,  $S$  can be expressed using the Pisarenko relation:<sup>258</sup>

$$S = \frac{8\pi^2 k_B^2}{3eh^2} m^* T \left( \frac{\pi}{3n} \right)^{2/3} \quad (1)$$

where  $k_B$ ,  $h$ ,  $n$ , and  $m^*$  are the Boltzmann constant, the Planck constant, charge carrier concentration, and the density of states (DOS) effective mass, respectively.<sup>263</sup>

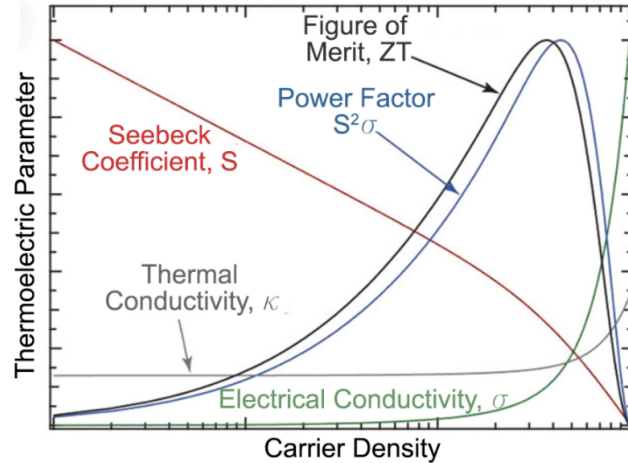


**Figure 11:** Interdependence of various TE parameters that influence  $ZT$  of the material, illustrating the challenge of optimizing  $ZT$ .<sup>261</sup> Data of actual semiconducting single walled carbon nanotube (SWCNT) networks, from Ref [259]. Reproduced with permissions.<sup>261</sup> Copyright 2018 WILEY-VCH Verlag GmbH & Co. KGaA, Weinheim.

Hence, while the task to optimize the performance of TE materials can simplistically be expressed as an optimization of  $ZT$ , it is important to note that the three factors,  $S$ ,  $\sigma$ , and  $\kappa$  are intricately interlinked and are “mutually counterindicated”, as indicated in **Figure 11**.<sup>258,267</sup> This mutual counterindication can be seen in the  $ZT$  equation when it is rewritten with  $\sigma = ne\mu$ , where  $n$  is the charge carrier concentration,  $e$  is its charge and  $\mu$  is its mobility. Then,  $ZT$  can be expressed as:

$$ZT = \frac{S^2\sigma}{\kappa}T = (S^2n) \left(\frac{\mu}{\kappa}\right) eT \quad (2)$$

where the ratio  $(\mu/\kappa)$  is counterindicated since defects and impurities that effect charge mobility also effect thermal conductivity and the product  $(S^2n)$  is counterindicated because higher charge carrier concentration can lead to lower thermopower, as indicated by the Pisarenko relation in Equation 1.<sup>258</sup> Hence, to enhance the performance of TE materials, strategies involve reducing,

specifically,  $\kappa_l$  by using strategies such as strengthening the phonon scattering of materials through various nano-microstructural methods, or using for TE materials that have specific lattice vibrational modes that result in intrinsically low  $\kappa_l$  values.<sup>241</sup> The other strategy is to enhance PF by developing new classes of materials,<sup>268–271</sup> optimizing existing materials via doping and band engineering,<sup>272–275</sup> and developing nanostructured materials with favorable TE properties.<sup>276–279</sup> In the case of semiconductors, generally TE power and electrically conductivity change in opposite directions with doping – attributed to the charge-transport theory, and hence a compromise has to be achieved between the two.<sup>253</sup>

#### **2.4.2.2 Flexible Thermoelectric Materials**

For integration into textiles, one of the most obvious requirements is for flexible TE (FTE) materials and devices. Being able to create conformal FTE devices enables better contact with the human body both for body heat harvesting to generate power and to impart TE temperature regulation via cooling or heating.<sup>263</sup> Additionally, bulk semiconductors pose certain limitations in terms of TE performance: the only way to reduce  $\kappa$  without affecting  $S$  or  $\sigma$  in bulk materials is by using semiconductors of high atomic weight such as  $\text{Bi}_2\text{Te}_3$  and its alloys with Pb, Sn, and Sb.<sup>280</sup> This in turn makes these materials very expensive and their processing quite complex. Hence, thin film TE materials can be more easily processed and be tailored for higher  $ZT$  than bulk materials. A variety of materials have been explored for creating FTEs, and these can be classified into three types: (1) inorganic thin film TEs,<sup>281–284</sup> (2) organic-inorganic hybrid FTEs,<sup>285–287</sup> and (3) organic FTEs – which themselves can be classified into two categories: (i) small molecules or oligomers which are processed using vacuum techniques, and (ii) polymers which are processed using wet

chemistry.<sup>248,264,288,289</sup> Subsequent sections will explore the application of these materials in textile form factors as wearable TE devices.

#### 2.4.2.2.1 Inorganic Thin Film Thermoelectric Materials

A film is considered thin as long as its surface properties are different from its bulk behavior, extending from a few micrometers to nanometer.<sup>290</sup> Thin films devices are usually prepared via deposition techniques that can be classified into either physical vapor deposition (PVD) or chemical vapor deposition (CVD). Compared to bulk alloyed materials used in state-of-the-art devices such as p-type  $\text{Bi}_x\text{Sb}_{2-x}\text{Te}_{3-y}\text{Se}_y$  ( $x \approx 0.5$ ,  $y \approx 0.12$ ) and n-type  $\text{Bi}_2(\text{Se}_y\text{Te}_{1-y})$ , thin film TE materials (thickness less than 10 nm)<sup>291</sup> offer the advantage of being able to achieve higher ZT values using techniques such as quantum-confinement effects to obtain enhanced density of states near the Fermi energy,<sup>291,292</sup> creating superlattice (SL) structures with low  $\kappa_1$  values,<sup>284,293</sup> and creating heterostructures.<sup>294,295</sup> To understand the advantage that thin film TEs provide over their bulk alloyed counterparts more clearly, take the example of thin films of  $\text{Bi}_2\text{Te}_3$ : its crystal structure's unit cell consists of five covalently bonded monoatomic sheets along the c-axis arranged in the sequences  $\text{—Te}^{(1)}\text{—Bi—Te}^{(2)}\text{—Bi—Te}^{(1)}$ , where <sup>(1)</sup> and <sup>(2)</sup> indicate the different bonding states of the anions, as shown in **Figure 12**.<sup>296</sup>  $\text{Te}^{(1)}$  and Bi are bonded via covalent and ionic bonds, whereas  $\text{Te}^{(2)}$  and Bi are bonded purely by covalent bonds. Between neighboring  $\text{Te}^{(1)}$  layers there exists a very weak van der Waals attraction. The anisotropic TE properties of thin films such as  $\text{Bi}_2\text{Te}_3$  are attributed to the fact that their lattice constant along the c axis is approximately 7 times larger than that along the a and b axes.<sup>296</sup> Hence,  $\text{Bi}_2\text{Te}_3$  thin films have electrical conductivity  $\sim 3$  times higher in the ab plane compared to the c axis, and  $\kappa_1$  value  $\sim 2$  times higher in the ab plane (1.5 W/mK) compared to the c axis (0.7 W/mK).<sup>296</sup>

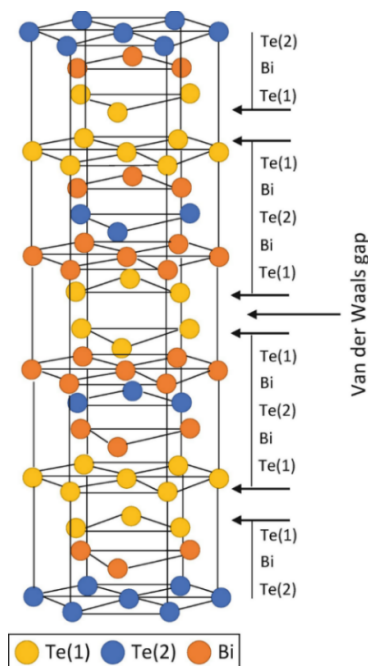


**Figure 12:** Crystal structure of  $\text{Bi}_2\text{Te}_3$ .<sup>296</sup> Reproduced with permissions.<sup>296</sup> Copyright 2019, Springer Nature Switzerland AG.

Various materials have been explored for use as thin film TE materials, including those based on  $\text{Bi-Te}$ ,<sup>281,282,297–299</sup>  $\text{Zn}$ ,<sup>283,300–302</sup>  $\text{Cu}$ ,<sup>303–306</sup> and cobalt oxide<sup>307–310</sup> based thin films. Inorganic thin films are usually applied onto various flexible substrates using either physical vapor deposition methods such as reactive sputtering,<sup>305,311–313</sup> thermal coevaporation<sup>297,314,315</sup> and magnetron sputtering,<sup>316–318</sup> atomic layer deposition (ALD),<sup>319</sup> printing,<sup>35,301</sup> spin coating,<sup>320</sup> and chemical bath deposition methods.<sup>321–324</sup> For integration into textiles, such inorganic materials are usually deposited onto flexible, organic substrates to allow flexibility and wearability. Such wearable TE devices are usually for energy harvesting applications in the form of the Seebeck effect.<sup>319</sup> However, some of these substrates are unable to withstand high temperatures required for processing the inorganic TE materials, and hence free-standing thin films have also been explored. Free-standing inorganic TE thin films can be fabricated via nanostructure tailoring that involves using randomly oriented nanolaminated grains and void spaces as a substrate for the thin film,

creating flexible inorganic TE thin films that can be removed from the substrate to form free-standing films.<sup>325</sup> Another method of creating free-standing thin films is by using CNTs as scaffolds to guide the deposition and growth of layered  $\text{Bi}_2\text{Te}_3$  thin films that can form a hybrid free-standing structure.<sup>326</sup>

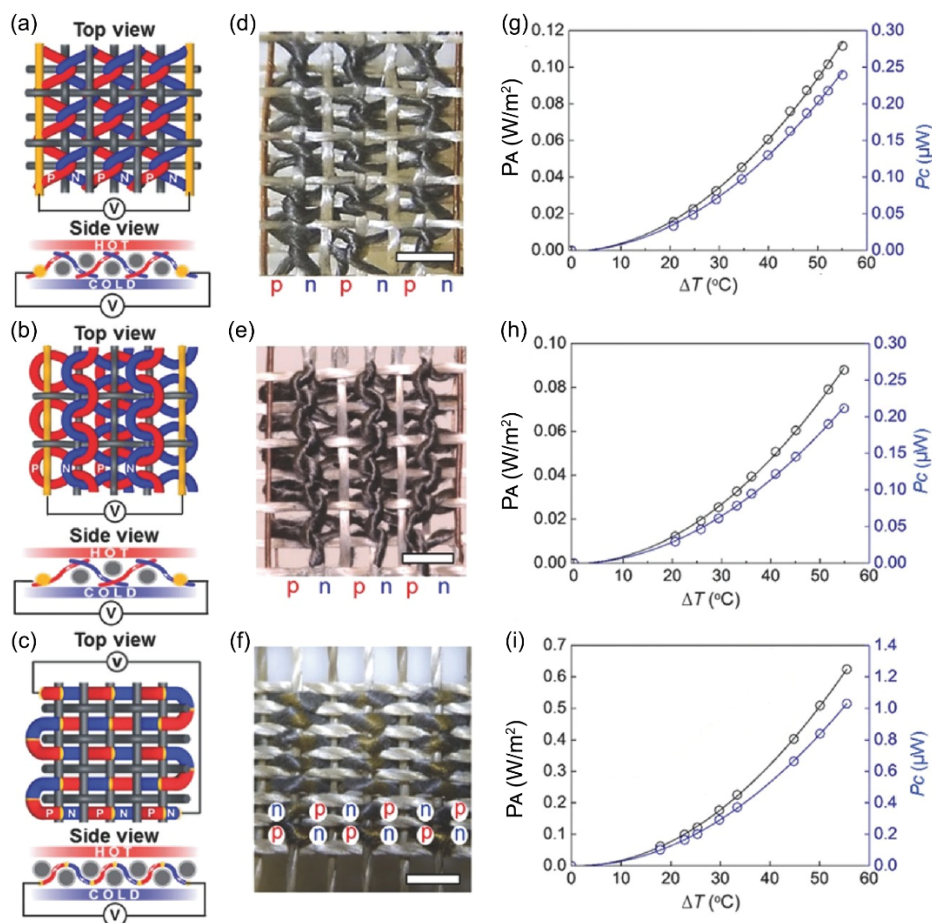


**Figure 13:** Woven-yarn TE fabrics.<sup>327</sup> a–f) Illustration (a–c) and photographs (d–f) of zigzag, garter, and plain-weave TE textiles, respectively. Scale bar = 2 mm. g–i) The output power per textile area and per TE couple as a function of applied thermal gradient ( $\Delta T$ ) for zigzag, garter, and plain-weave TE textiles, respectively. Reproduced with permissions.<sup>327</sup> Copyright 2016, 2016 WILEY-VCH Verlag GmbH & Co. KGaA, Weinheim.

Integration of thin film TE into textiles has been primarily focused on creating small-scale energy harvesting devices that can power other on-body wearable devices by harvesting the body heat via

the Seebeck effect.<sup>319,327</sup> Lee et al. fabricated thermoelectric yarns with n and p-type  $\text{Bi}_2\text{Te}_3$  and  $\text{Sb}_2\text{Te}_3$  coated onto aligned electrospun polyacrylonitrile (PAN) yarns using magnetron sputtering to produce a sheath-core structure with the semiconductor materials as sheath and PAN as core.<sup>327</sup> Three different fabric designs – plain woven, zigzag stitched and garter stitched – were used to convert an applied thermal gradient to electrical power, harvesting heat through the thickness of the fabric rather than in the plane of the fabric, as shown in **Figure 13**. Additionally, fiberglass yarn coated with polytetrafluoroethylene (PTFE) was used as an insulating spacer yarn within these structures. Lee et al. observed that the plain woven yarn with alternating n and p-type TE segments within the same yarn provided a much higher output power ( $0.62 \text{ W/m}^2$ ) than those made by knitting individual n and p-type yarns together ( $0.11$  and  $0.24 \text{ W/m}^2$  for zigzag and garter stitched fabrics).<sup>327</sup> While this is a good use of the inherent structure of textiles to create a TE generator that can harvest power through its thickness, it is important to note that the high amount of power can only be harvested at thermal gradients ( $\Delta T$ ) greater than  $50 \text{ }^\circ\text{C}$ .<sup>327</sup> Such high thermal gradients between the skin and the surroundings are seldom encountered, since average temperature of the skin ranges from range is between  $33.5 - 37.5 \text{ }^\circ\text{C}$ , and the normal habitable environment temperature ranges from  $5-40 \text{ }^\circ\text{C}$ , thereby providing a maximum  $\Delta T$  of  $\sim 30 \text{ K}$ ,<sup>328</sup> beyond which humans can experience significant thermal discomfort.<sup>329–331</sup> Other implementations of coating inorganic TE materials onto textiles for TE energy harvesting have also been explored by Kim et al. who screen printed  $\text{Sb}_2\text{Te}_3$  and  $\text{Bi}_2\text{Te}_3$  pellets on a bendable glass textile and subsequently integrated this structure into flexible rubber sheets,<sup>332</sup> Yadav et al. who deposited Ni-Ag thin films onto silica fiber by thermal evaporation,<sup>333</sup> Shin et al. who screen printed  $\text{Bi}_{0.5}\text{Sb}_{1.5}\text{Te}_3$  and  $\text{Bi}_2\text{Te}_{2.7}\text{Se}_{0.3}$  inks onto glass fabrics,<sup>334</sup> and Liang et al. who dip coated nanocrystalline PbTe onto glass fibers.<sup>335</sup> In all these cases, it is apparent that the substrates used

(glass, rubber and silica) may be flexible or in a “fiber/fabric” form factor but aren’t truly suitable for use as wearable devices due to the inherent discomfort caused by such materials. Lu et al. deposited nanostructured n-type  $\text{Bi}_2\text{Te}_3$  (Seebeck coefficient  $36.8 \mu\text{V/K}$ ) and p-type  $\text{Sb}_2\text{Te}_3$  (Seebeck coefficient  $110.8 \mu\text{V/K}$ ) onto commercially available silk fabric to form  $\sim 300 \mu\text{m}$  thick TE columns for use as human body heat harvesters.<sup>328</sup> They measured the performance of their device in the  $\Delta T$  range of 5 to 35 K, reporting an output power ranging from  $\sim 2$ -18 nW. While this technique did use a textile substrate, the overall TE performance of the device was quite low due to the use of liquid adhesive binder, as well as the contact resistance between the two sides of the fabric where the n and p-type materials are deposited.<sup>328</sup>

While research in TECs is scant compared to TEGs, the interest in achieving TE heating and cooling for human thermal comfort has been growing in recent years. Moreover, there is only a limited amount of temperature gradient that the human body can provide for TEGs, and coupled with their low ZT in many cases, TEGs are only capable of producing a few microwatts or nanowatts of power.<sup>339</sup> Lee et al. and Park et al. have demonstrated FTECs using inorganic, rigid Bi-Te p and n-type modules arranged in a mat-like fashion connected with wires and containing a flexible heat sink composed of solid-state silica gel mixed with hydrogel.<sup>337-339</sup> These devices were able to cool the skin by a temperature drop of 3.8 K with a cooling power of  $30 \text{ mW cm}^{-2}$ ,<sup>339</sup> with an improvement to 4.4 K and cooling power of  $33.5 \text{ mW cm}^{-2}$  and cooling power of 5.4 K and  $48.3 \text{ mW cm}^{-2}$  when the contact resistances in the devices were reduced by using flexible printed circuit boards (FPCB)<sup>338</sup> and liquid metal electrodes,<sup>338</sup> respectively. Kishore et al. also developed high performance wearable coolers which were able to cool the skin by a temperature drop of 8.2 °C below room temperature, as shown in *Figure 14* a-f.<sup>336</sup> They achieved this by using

commercially available n and p-type Bi-Te materials to fabricate a rigid TEC module with an aluminium heat sink. In all these instances, it is apparent that current research on TECs involves the use of rigid semiconductor materials. This can cause an obvious mismatch between the softness of the skin and the rigidity of the TEC, creating discomfort for the wearer. Hong et al. demonstrated a flexible TEC without the use of rigid or bulky heat sinks by sandwiching inorganic TE pillars between two layers of stretchable elastomers embedded with AlN microparticles that enhanced the sheets' lateral thermal conductivity, as shown in *Figure 14 g-l*.<sup>34</sup> This design creates a large air gap between the elastomer sheets, resulting in small thermal conductance between the hot and cold side of the TEC. In this way, they were able to ensure that the heat pumped from the cold side of the device and the expectant Joule heating in the device would dissipate into the air rather than back towards the skin. Additionally, the AlN embedded elastomer sheets ensured that the heat would spread uniformly throughout the sheets, enabling better heat dissipation. In this way, Hoang et al. were able to create a TEC with a long-lasting cooling effect of >8 hours and a large active cooling effect > 10 °C.<sup>34</sup>

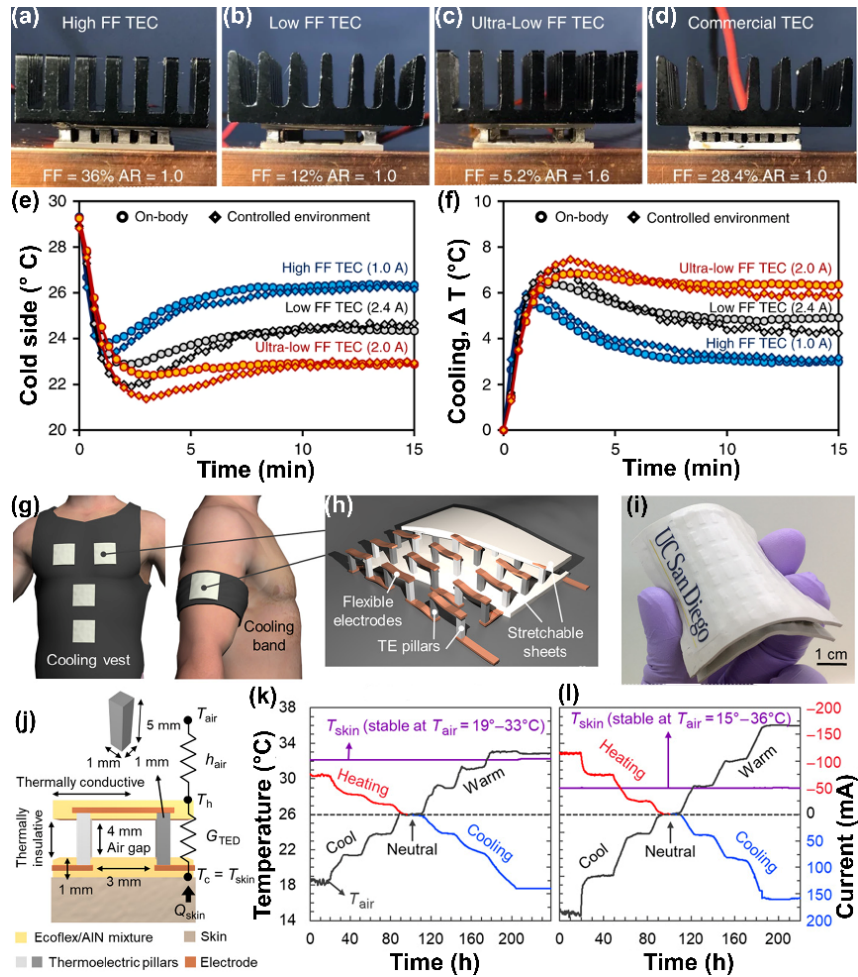


**Figure 14:** Wearable TEC for localized cooling.<sup>336</sup> a-d) TEC modules fabricated with commercial p- and n-type Bi-Te with a) high fill factor (FF = 36%, aspect ratio, AR = 1.0), b) low FF (FF = 12%, AR = 1.0), c) ultra-low FF (FF = 5.2%, AR = 1.6), and d) commercial TEC module (FF = 28.4%, AR = 1.0). The black heat sink is anodized aluminum. e), f) Show transient temperature data from cooling the human body and in controlled environments, for the various TECs. The optimal currents are 1 A for high FF TEC (blue), 2.4 A for low FF TEC (black), and 2 A for ultra-low FF TEC (red). Ultra-low FF TEC generates the lowest cold side temperature and has the highest cooling. Reproduced with permissions.<sup>336</sup> Copyright 2019, Creative Commons Attribution 4.0 International License (CC-BY-4.0). Flexible TED for on-body cooling.<sup>34</sup> g) Wearable TE device (TED) integrated into a vest and arm band. h) TED consists of alloy pillars connected with flexible copper electrodes and silicone sheets. i) A 5 cm X 5 cm fabricated TED. j) TED design with low thermal conduction inside and high thermal conduction within the silicone sheets enables cooling without the use of a heat sink.  $T_{air}$  = ambient temperature,  $h_{air}$  = heat transfer coefficient between TED and air,  $T_h$  = temperature at the top of TED,  $G_{TED}$  = thermal conductance of TED,  $T_c = T_{skin}$  = temperature at the bottom of TED,  $Q_{skin}$  = human metabolic heat. k) Thermal regulation by TED under natural convection shows that the surface temperature of the silicone layer remained 26 °C in temperature range of 19 °C – 33 °C. l) With forced convection of 5 km h<sup>-1</sup> the ambient temperature range broadens to 15 °C – 36°C. Reproduced with permissions.<sup>34</sup> Copyright 2019, Creative Commons Attribution NonCommercial License 4.0 (CC-BY-NC).

However, in all these instances, it is apparent that efficient TECs could only be fabricated using inorganic TE materials. It is not necessary that a material suitable for TEGs can be easily translated into a Peltier cooler. In the latter case, the TEC must be able to efficiently dissipate the waste heat generated from the cold side pumping heat away from the skin. Additionally, it must overcome both parasitic heating due to heat conduction from the hot side, as well as resistive heating within the device. Hence, the device and material requirements for a TEC are much different from a TEG. While currently TECs are using rigid materials, there is great potential in development of new materials for both TECs and heat sinks that can create more efficient cooling.

While inorganic thin film TE materials are capable of producing high ZT with low  $\kappa_l$ , their applications are limited mainly due to the low abundance of tellurium, which is one of the rarest elements in the Earth's crust.<sup>319</sup> Additionally, the interface formed between inflexible inorganic TE films and flexible fabrics are likely to be weak and cause for discomfort in next-to-skin applications. The addition of higher amount of TE material for better heating/cooling performance would also result in added bulk to the fabric, and hence other materials more conducive for wearable applications have also been explored.

#### **2.4.2.2.2 Organic Thermoelectric Materials**

Organic TEs (OTEs) provide considerable advantages over inorganic TE materials due to their inexpensive and scalable processing methods unlike inorganic materials which need complex vacuum processing methods, have the potential for heavy metal pollution, and have low abundances.<sup>262</sup> The lightweight and flexible nature of OTEs enables better integration into textiles; inorganic thin film semiconductors usually end up being brittle and bulky.<sup>289,340</sup> OTEs also

generally have thermal conductivity below 1 W/mK and have tunable molecular chemistry through doping that can enhance their TE performance, however they are sometimes limited by their low power factors ( $PF = S^2\sigma$ ), with their PF being 2-3 orders of magnitude lower than those of inorganic TE materials.<sup>340–342</sup> Enhancement of OTE performance is focused more on optimizing their PFs rather than optimizing their thermal conductivity, unlike inorganic TEs where the focus is on reducing the thermal conductivity.

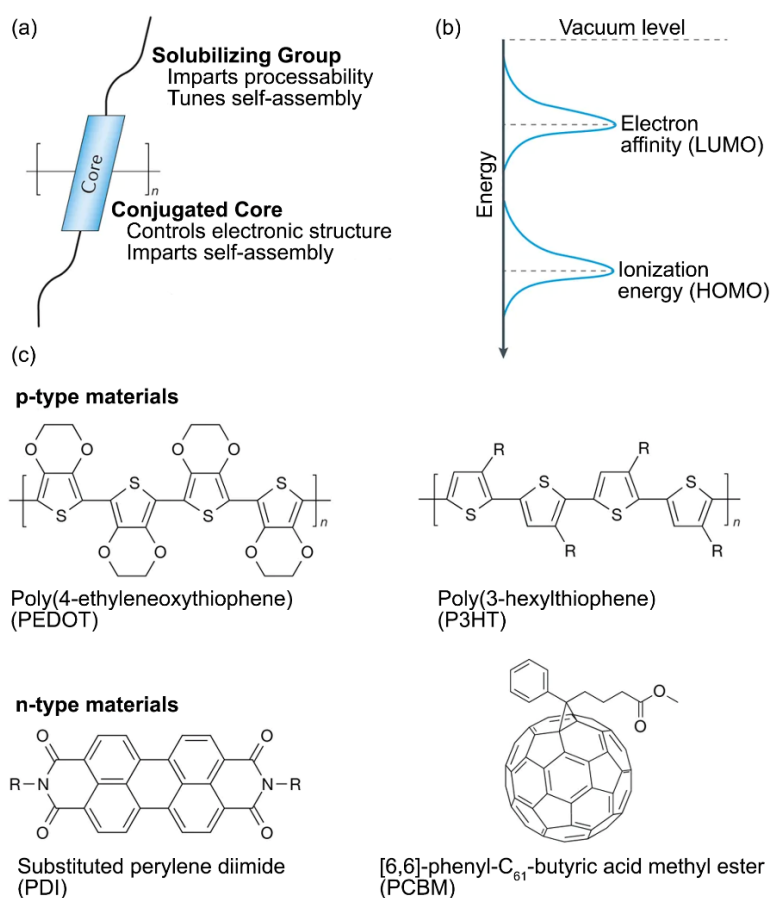


**Figure 15:** (a) Polymeric semiconductors have  $\pi$ -conjugated cores that enable charge transport and side chains that can impart solution processability, charge carrier creation, and molecular assembly. (b) Ionization energy (HOMO) and electron affinity (LUMO) of polymeric semiconductors can be tuned via their molecular design. (c) Molecular structures of high-performance p and n-type OTEs. Adapted from Russ et al.<sup>262</sup> copyright 2016, The Authors.

OTEs can be further classified broadly into two categories: (i) small molecules or oligomers which are usually processed in vacuum, and (ii) polymers which are usually processed by wet chemical techniques.<sup>264</sup> In OTE polymers, the interaction between the polymer unit cells leads to the formation of electron bands; the highest occupied electronic level consists of the valence band (VB) (also approximated as highest occupied molecular orbital or HOMO or oxidation potential) and the lowest unoccupied level consists of the conduction band (CB) (also approximated as lowest unoccupied molecular orbital or LUMO or reduction potential), as shown in **Figure 15**.<sup>343</sup> The width between the VB and CB is known as the forbidden band or energy bandgap ( $E_g$ ) whose value ranges between 1-3 eV for OTE materials.<sup>262,344</sup> Due to this relatively wide bandgap, many organic semiconductors need to be doped to increase their electrical conductivity. Doping is used in OTEs to either generate mobile carriers by donating electrons to the LUMO state (n-type doping) or remove electrons from the HOMO state (p-type doping). However, n-type doping is more difficult to achieve in OTEs because the HOMO level of the dopant has to be energetically above the LUMO level of the polymer being doped, making such materials unstable when exposed to oxygen.<sup>345</sup> Moreover, the electrical conductivity of these materials is affected both by introduction of carriers and their structural order ranging from the molecular scale to the macroscale.<sup>344</sup>

The majority of OTE materials are based on conductive polymers which include conjugated and some coordination polymers. The electronic structure of the  $\pi$  conjugated polymers originates from the  $sp^2p_z$  hybridized wavefunctions of the carbon atoms in the repeat units of the polymer, leading to one unpaired electron per carbon atom; this creates an electron delocalization that enables charge mobility along the polymer backbone chain, as shown in **Figure 15**.<sup>341,346</sup> Conjugated polymer repeat units in the backbone consist of both covalent  $\sigma$  bonds and delocalized alternating  $\pi$ -bonds,

with the conjugated repeat units strongly electronically coupled along the backbone of the polymer, but weakly coupled between stacked chains of the polymer.<sup>347,348</sup> Since the discovery of doped polyacetylene in the late 1970s,<sup>349</sup> conjugated polymers such as polyacetylenes,<sup>350,351</sup> polypyrroles,<sup>352,353</sup> polyanilines (PANI),<sup>354,355</sup> polthiophenes,<sup>356,357</sup> polycarbazoles,<sup>358,359</sup> and their derivatives have been widely used for various TE applications.<sup>360</sup> In terms of textile applications, the state of the art OTE is poly(3,4-ethylenedioxythiophene) (PEDOT) and its derivative poly(styrenesulfonic) (PSS) acid-doped PEDOT (PEDOT:PSS) with a ZT of 0.42,<sup>216,342,361–365</sup> with composites of polyaniline (PANI)<sup>366–368</sup> also being explored. While PEDOT:PSS has better TE properties compared to PANI due to the former's bipolaron network compared to PANI's polaron network,<sup>340</sup> it is still limited by the fact that it forms brittle films on textile substrates which cannot withstand the various stresses and strains textiles experience.

Most reported OTEs are intrinsically p-type because the electron affinity of organic polymers is usually low, and hence n-type behavior is difficult to obtain without doping.<sup>340</sup> Reported n-type OTEs include fullerenes,<sup>369,370</sup> organometallic derivatives,<sup>288,371</sup> and other small molecules.<sup>372,373</sup> However, fullerenes and organometallic derivatives are not solution processable which severely limits their usability in textile applications; small molecules such as poly{N,N'-bis(2-octyldodecyl)-1,4,5,8-naphthalenedicarboximide-2,6-diyl]-alt-5,5'-(2,2'-bithiophene)} (P(NDIOD-T2))<sup>373</sup> have complex fabrication processes, low TE performance and cannot be used at a large scale.<sup>322</sup> To combat some of these issues, Shi et al. developed three solution-processible n-type polymers: benzodifurandione-based poly(p-phenylene vinylene) (BDPPV), chlorine-BDPPV (CIBDPPV) and fluorine-BDPPV (FBDPPV) which showed high electrical conductivities of up to 14 S/cm and power factors up to 28  $\mu\text{W}/\text{mK}^2$  when mixed with the n-type dopant ((4-(1,3-

dimethyl-2,3-dihydro-1H-benzoimidazol-2-yl)phenyl)dimethylamine) (N-DMBI).<sup>374</sup> N-DMBI is often used as a dopant for n-type organic semiconductors such as [6,6]-phenyl C<sub>61</sub> butyric acid methyl ester (PCBM)<sup>375</sup> and P(NDIOD-T2)<sup>373</sup> due to its good chemical and air stability and efficient doping properties. More recently, Serrano-Claumarchirant et al. demonstrated n-type behavior for the first time in PEDOT thin films by treating it with cationic surfactant dodecyltrimethylammonium bromide (DTAB), reaching a maximum value of  $\sim -21 \mu\text{V/K}$ , with a 3 order of magnitude decrease in electrical conductivity compared to p-type PEDOT films.<sup>376</sup> This decrease in electrical conductivity is clearly undesirable for TE performance.

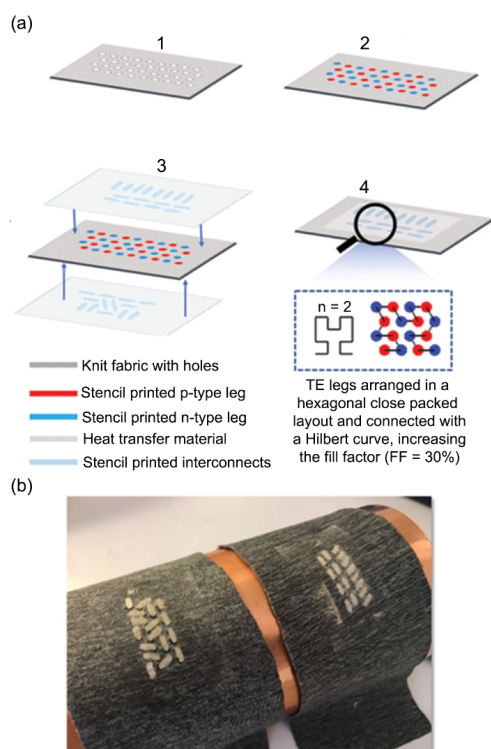


**Figure 16:** Polymer TEG for human body heat harvesting.<sup>342</sup> a) Fabrication process for textile integrated TEG: 1. Burning holes through the knitted fabric, 2. Filling the holes by stencil printing p- (red) and n-type (blue) materials on both sides of the fabric, 3. Silver interconnects (light blue) are printed onto a heat transfer membrane (light gray) on both sides of the device, 4. Heat pressing interconnects onto both sides of the device using the heat transfer membrane. b) Wearable TEG integrated into knitted fabric consisting of 32 p- and n-type legs. Reproduced with permissions.<sup>342</sup> Copyright 2019 WILEY-VCH Verlag GmbH & Co. KGaA, Weinheim.

Other developments in solution processible n-type OTEs include metal-coordination compounds, specifically metal-dithiolene coordination polymers, consisting of bridging ethenetetrathiolate ligands and nickel metal centers (nickel ethenetetrathiolate, NiETT) (poly[Na(NiETT)]) have resulted in higher performing n-type OTEs with electrical conductivity of 44 S/cm and power factor of  $20 \mu\text{W}/\text{mK}^2$ .<sup>377,378</sup> Elmoughni et al. demonstrated a textile-integrated TE generator consisting of both p and n-type organic semiconductors: PEDOT:PSS and poly[Na(NiETT)] respectively, stencil printed onto a knitted polyester fabric, as shown in **Figure 16**.<sup>342</sup> The unique deposition of the n and p-type legs in a hexagonal closed-packed layout helped achieve higher fill factor ( $\sim 91\%$ ), allowing for higher power density due to lower interconnect resistances.<sup>379</sup> At  $\Delta T = 3\text{K}$ , such a device consisting of 32-legs and 864-legs was able to provide a maximum open circuit voltage of 3mV and 47 mV. While this is an innovative application of fractal design to enhance the density of the TE legs, the device performance was still limited by the fact that OTEs have low power factors compared to their inorganic and hybrid counterparts and provide imperfect contacts between the organic p and n-type legs and the inorganic interconnects used to connect them in a TE device.<sup>342</sup> For this reason, organic composites consisting of polymeric semiconductors combined with nanomaterials such as CNTs,<sup>380–383</sup> graphene,<sup>384–387</sup> and reduced graphene oxide (rGO)<sup>388,389</sup> have also been explored to create OTEs with enhanced n and p-type performance.

Graphene consists of a two dimensional (2D) sheet of covalently bonded carbon atoms, forming the basis for both 3D graphite and 1D CNTs.<sup>390</sup> Due to its unique electrical,<sup>391,392</sup> mechanical,<sup>390</sup> thermal<sup>393</sup> and optical properties,<sup>394</sup> graphene is has been studied extensively for various flexible electronics applications.<sup>395–398</sup> Although its high thermal conductivity makes it more applicable for passive cooling rather than TE applications,<sup>399,400</sup> researchers have predicted that the TE

performance of graphene can be improved by patterning it into quasi 1D graphene nanoribbons (GNRs) which have lower thermal conductivity than graphene.<sup>401–403</sup> GNRs can be viewed as unrolled CNTs, with widths as low as a few nanometers.<sup>404</sup> Zheng et al. found that at such small scales, the quantum confinement effect enables an increase in ZT with decreasing ribbon width, and by optimizing the doping level a room temperature ZT of 0.6 could theoretically be obtained,<sup>405</sup> Ouyang and Guo found through theoretical modeling that the thermopower of GNRs (in the order of mV/K) is much larger than that of graphene ( $< 100 \mu\text{V/K}$ ) due to the existence of a band gap in semiconducting GNR compared to gapless 2D graphene.<sup>403</sup> Other theoretical methods proposed to reduce thermal conductivity of GNR without compromising its electrical performance include edge disorders,<sup>406</sup> edge passivation,<sup>407</sup> doping with carbon isotopes,<sup>408</sup> mechanical straining,<sup>409</sup> superlattice structures,<sup>410</sup> nanoporous GNRs and defect engineering,<sup>411,412</sup> and Antidot lattices.<sup>413</sup> However, GNRs are microscopic applications of TE graphene materials, and hence composites of conducting polymers and graphene are better suited for macroscopic applications, like those in textiles.

In terms of film-based applications of graphene and rGO for TE devices, researchers report a significant enhancement in the TE performance of intrinsically conducting polymers when combined with graphene or rGO.<sup>385,386,414,414–423</sup> Park et al. prepared a hybrid PEDOT:PSS/graphene film using rapid thermal chemical vapor deposition (RTCVD) of graphene followed by spin coating of PEDOT:PSS to create TE films with conductivity of 1090 S/cm and power factor of  $57.9 \mu\text{W/mK}^2$  attributing the enhancement of TE properties to the  $\pi$ - $\pi$  stacking interaction between graphene and PEDOT:PSS,<sup>424</sup> Xiong et al. made films of PEDOT:PSS and graphene nanocomposites, reaching a maximum electrical conductivity of 1250 S/cm (1 wt.%

graphene) and optimized power factor of  $38.6 \mu\text{W}/\text{mK}^2$  (3 wt.% graphene),<sup>425</sup> Xu et al. proposed three different methods – spin-coating and liquid layer polymerization, spin coating and vapor phase polymerization, and in-situ polymerization and then ethylene glycol post-treatment - to make PEDOT/rGO nanocomposites, all of which showed enhanced the TE performance of neat PEDOT with a maximum power factor of  $14.2 \mu\text{W}/\text{mK}^2$ ,<sup>423</sup> Han et al. grew polypyrrole coatings on both sides of rGO nanosheets via template-directed in situ polymerization to create rGO/PPy composites with power factor up to  $3.01 \mu\text{W}/\text{mK}^2$ .<sup>422</sup> However, these nanocomposites were only used to demonstrate film-type applications which are flexible but not necessarily in any textile form factor, thereby limiting their wearability.<sup>385,415,417</sup> For example, Zhang et al. used to roll-to-roll printing of PEDOT:PSS and nitrogen-doped graphene inks to continuously create large-area TE devices for energy harvesting on a plasma-treated plastic film,<sup>415</sup> whereas Xiang and Drzal folded the PANI-graphene nanocomposite film (termed as graphene/PANI paper) into an accordion design to create a flexible TE device,<sup>385</sup> however they do not demonstrate any practical wearability akin to a woven, knitted or nonwoven fabric design. Nevertheless, this is still important research in being able to understand which materials should be further investigated for textile based TE applications due to their enhanced PF and electrical conductivity.

Ma et al. studied the TE properties of macroscopic graphene fibers and the dependence of their thermal conductivity, electrical conductivity and Seebeck coefficient on temperature.<sup>426</sup> They noted that the thermal conductivity increases and then decreases, electrical conductivity increases, and Seebeck coefficient changes from positive (hole dominant) to negative (electron dominant) as temperature goes from 80 to 290 K.<sup>426</sup> They were further able to enhance the power factor and figure of merit to of the graphene fibers to  $624 \mu\text{W}/\text{mK}^2$  and  $2.76 \times 10^{-3}$  respectively, using

bromine doping which improves phonon scattering by introducing defects, thereby decreasing the thermal conductivity.<sup>427</sup> Electrical conductivity and Seebeck coefficient both increased due to the lowering of Fermi levels; electrons drained towards the highly electronegative Br sites, increasing the density of holes at the top of the valence band resulting in a positive Seebeck coefficient and increased electrical conductivity.<sup>427</sup> This research is promising since the graphene fibers have good TE properties at low temperatures, enabling their applicability in room-temperature applications and their fiber form enables more seamless integration into textiles. However, the fiber fabrication method requires high temperature annealing (2800 °C) with the need for vacuum processing and materials such liquid bromine and liquid nitrogen<sup>427</sup> which can prove to be time-consuming and expensive.

CNTs are attractive TE materials due to their remarkable electronic and atomic properties, enabling the nanotube to be either semiconducting or metallic, depending on the chirality indices (n, m) of the nanotubes and their diameter.<sup>428,429</sup> Chirality indices for SWCNTs can be understood as the roll-up vector of the graphene sheet from which it is made, as shown in *Figure 17*.<sup>261</sup> Of all possible (n, m) combinations of nanotubes, about two thirds are predicted to be semiconducting.<sup>430</sup>

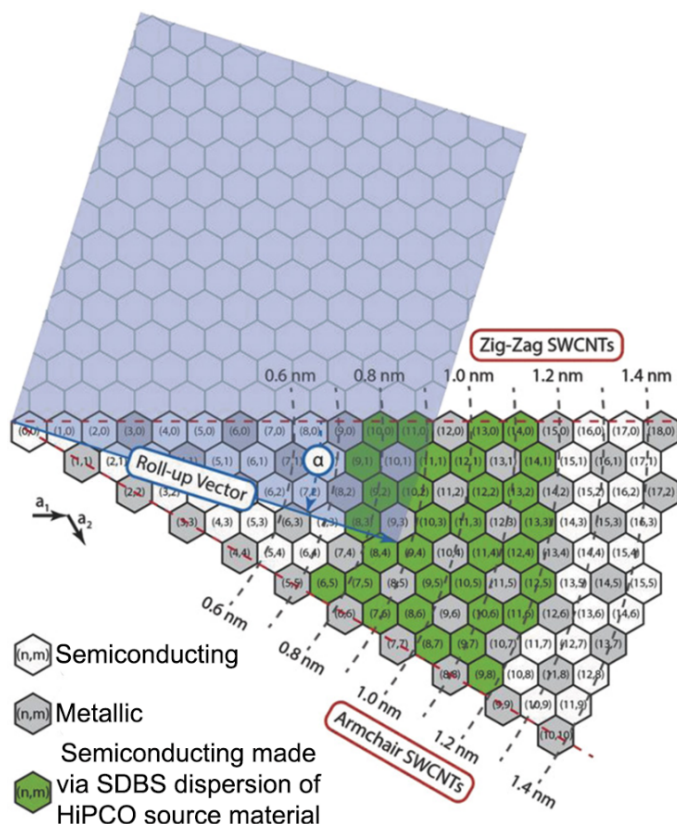


**Figure 17:** Part of a graphene sheet with chiral indices  $(n,m)$  corresponding to the SWCNT formed by rolling the sheet from  $(0,0)$  to  $(n,m)$  along the highlighted roll-up vector to form a cylinder.<sup>261</sup> Rolling up along the shaded blue area (indicated as roll-up vector) forms a  $(9,4)$  SWCNT cylinder. White hexagons correspond to chiral indices that form semiconducting SWCNTs, gray hexagons to chiral indices that form metallic SWCNTs, and green hexagons to chiral indices that form semiconducting SWCNTs present in a typical batch of commercial sodium dodecylbenzenesulfonate (SDBS) dispersed SWCNTs produced by the high-pressure carbon monoxide (HiPCO) process. Reproduced with permission.<sup>261</sup> Copyright 2018, WILEY-VCH Verlag GmbH & Co. KGaA, Weinheim.

Undoped semiconducting CNTs can be thought of as being adventitiously doped by atmospheric oxygen, and hence behave as p-type semiconductors, with Seebeck coefficients measured in the range of  $24 - 100 \mu\text{V/K}$ <sup>431,432</sup> and electrical conductivities ranging from  $35 - 3200 \text{ S/cm}$ <sup>432,433</sup> for such  $\text{O}_2$  doped SWCNTs. CNTs also present certain advantages when it comes to doping them to form n-type TE materials when compared to conducting polymers: they are porous and have high surface areas (in case of SWCNTs) which can result in more accessible sites for redox molecules

to adsorb to, the CNT network can be immersed in various dopant-containing solutions without causing a change in the morphology of the CNTs themselves, and finally the surface of CNTs is sensitive enough to redox moieties that no covalent bonds are needed to be formed to create large changes in carrier density – just the phenomenon of physisorption is able to achieve efficient doping.<sup>261</sup> Hence, CNTs provide a facile manner of creating TE materials without complex processing steps as observed in other organic TE materials. However, even with these advantages, it has proved to be difficult to achieve air-stable n-type doping in CNTs, since the electron density decreases rapidly due to O<sub>2</sub> and H<sub>2</sub>O adsorption.<sup>433</sup> Nevertheless, different amine and phosphine-based dopants have been studied for n-type doping of CNTs, as demonstrated by Nooguchi et al. who demonstrated eighteen different dopants that enabled air stable n-type doping of SWCNT films.<sup>434</sup> Commonly used polymers for easily creating solution processable and air-stable n-type CNTs include PEI,<sup>435–437</sup> PVP,<sup>438,439</sup> PVA,<sup>440</sup> poly(vinylidene fluoride) (PVDF),<sup>441</sup> PEG,<sup>442</sup> and poly(3-hexylthiophene) (P3HT).<sup>443</sup> It is important to note that the use of large band-gap insulating polymers such as PEI to create n-type doped CNTs should not be seen as charge injection but rather as surface modification that creates an intrinsic molecular dipole moment and a charge transfer interaction with the CNT surface, thereby leading to a decrease in work function and hence n-type behavior.<sup>444</sup>

For integration into textiles, CNT based materials have been used for energy harvesting combined with other polymers to form composites,<sup>435,436,438,441,445,446</sup> including intrinsically conductive polymers such as PANI<sup>366</sup> and PEDOT:PSS<sup>248,437</sup> for enhanced TE performance. At the fiber/yarn level, Ryan et al. developed a TE generator composed of commercial PET sewing yarns coated with multiwalled carbon nanotubes (MWCNTs)/PVP (n-type) and PEDOT:PSS dyed silk yarns

(p-type).<sup>438</sup> Their n-type yarns had a conductivity of 1 S/cm and Seebeck coefficient of  $-14 \mu\text{V/K}$ . Using 38 n/p yarns, they were able to produce an open-circuit voltage of 143 mV when exposed to a temperature gradient of  $116 \text{ }^\circ\text{C}$ .<sup>438</sup> Zheng et al. developed MWCNT yarns coated with PEDOT:PSS (p-type) and PEI (n-type) to form three-dimensional TE textiles (TETs) for out-of-plane TE power generation.<sup>437</sup> The PEDOT:PSS/CNT composite yarn had an average Seebeck coefficient of  $70.1 \mu\text{V/K}$ , electrical conductivity of 1043.5 S/cm and power factor of  $512.8 \mu\text{W/mK}^2$ , whereas the PEI/CNT yarn had an average Seebeck coefficient of  $-68.7 \mu\text{V/K}$ , electrical conductivity of 1408.3 S/cm and power factor of  $667.8 \mu\text{W/mK}^2$ .<sup>437</sup> Zheng et al. reported that the work function of the PEI/CNTs ( $\sim 4.15 \text{ eV}$ ) is smaller than that of the pristine CNTs ( $\sim 4.36 \text{ eV}$ ) even though they have similar band gaps. This was attributed to the dipole moments arising from both the ethylamine molecule from PEI as well as the ethylamine/CNT interface dipole as the PEI is physisorbed onto the outer layers of the MWCNTs.<sup>444</sup> These yarns were then knitted into a 3D fabric with a spacer in between, creating the TET with a maximum power output of  $51.5 \text{ mW/m}^2$  at an applied temperature gradient of  $47.5 \text{ K}$ .<sup>437</sup> At the fabric level, Yu et al used vacuum filtration to deposit SWCNTs of p-type and n-type (doped with PEI,  $\text{NaBH}_4$  and a combination of the two) onto a PTFE membrane to obtain maximum PFs of  $12.1 \mu\text{W/mK}^2$  ( $S = 22 \mu\text{V/K}$ ,  $\sigma \sim 2.5 \times 10^4 \text{ S/m}$ ) and  $32.49 \mu\text{W/mK}^2$  ( $S = -57 \mu\text{V/K}$ ,  $\sigma \sim 1 \times 10^4 \text{ S/m}$ ) for the pristine p-type SWCNT and PEI-doped n-type SWCNT membranes, respectively.<sup>435</sup> Kim et al. also used a similar materials system consisting of SWCNTs deposited onto PTFE and doped with PEI and/or  $\text{NaBH}_4$  for n-type performance and reported PFs of  $103.5 \mu\text{W/mK}^2$  ( $S = -97 \mu\text{V/K}$ ,  $\sigma = 1.1 \times 10^4 \text{ S/m}$ ) for p-type pristine SWCNT membranes and  $38 \mu\text{W/mK}^2$  ( $S = -86 \mu\text{V/K}$ ,  $\sigma = 5200 \text{ S/m}$ ) for n-type PEI +  $\text{NaBH}_4$  doped membranes.<sup>436</sup> While these works refer to PTFE membranes as fabrics, such membrane-type materials are not suitable for use as fabrics in their traditional applications for

wearable systems.<sup>441,447</sup> A crucial limitation of some of these works are that they measure the transport properties of such films in two different directions i.e. the Seebeck coefficient and electrical conductivities are measured in the plane of the film, whereas the thermal conductivities are measured out of plane or in some cases thermal conductivities are not reported at all.<sup>436,438,441,445</sup> This does not provide a true representation of the ZT of the TE materials, crucial for determining overall performance. While Zhou et al.<sup>255</sup> and Zheng et al.<sup>437</sup> have used the self-heating  $3\omega$  method to estimate the thermal conductivity of their n and p-type CNT legs, they large values (18 for n-type SWCNT/PEI film and 24 W/mK for p-type SWCNT film,<sup>255</sup> and 35 W/mK for p and n-type MWCNT and MWCNT/PEI yarns,<sup>437</sup> respectively) which depresses their ZT further. Accurately measuring the transport properties of CNTs can be challenging, and their high thermal conductivities can be a problem when it comes to TE applications despite their large PFs.

While CNTs are promising, they still possess high thermal conductivities, and hence this can reduce their ZT performance. A new approach to realizing TE materials is by integrating organic and inorganic materials together to create composites where the synergistic effects of their constituents can create materials with much higher ZTs. The next section will explore these materials.

#### **2.4.2.2.3 Organic-Inorganic Hybrid Thermoelectric Materials**

Organic-inorganic hybrid TE materials (OInTEs) present the opportunity to take advantage of both the low thermal conductivities of TE polymers and the high ZTs of inorganic TE materials to obtain OInTEs with maximized ZTs.<sup>448</sup> Additionally, TE materials like  $\text{Bi}_2\text{Te}_3$  suffer from the lack of flexibility and hence combining them with TE polymers can enable flexible TE devices.<sup>449</sup>

Moreover, by combining organic and inorganic materials, interesting interfacial transport properties arise in the resultant hybrid TE material, resulting in energy filtering and phonon scattering at the nanoscale, thereby providing an enhanced ZT.<sup>450</sup> The most commonly used ICPs include PANI, PEDOT (and PEDOT:PSS) and polythiophene (PTH),<sup>451</sup> which are used to create OInTEs such as PANI mixed with various metals and their oxides including Bi,<sup>452</sup> NaFe<sub>4</sub>P<sub>12</sub>,<sup>453</sup> V<sub>2</sub>O<sub>5</sub>,<sup>454</sup> Bi<sub>2</sub>Te<sub>3</sub> and its alloys<sup>455–457</sup> and PbTe,<sup>458</sup> PEDOT with Te nanorods,<sup>459</sup> Ca<sub>3</sub>Co<sub>4</sub>O<sub>9</sub>,<sup>460</sup> Au nanoparticles<sup>461</sup> and Bi<sub>2</sub>Te<sub>3</sub>,<sup>462,463</sup> and PTH with Bi<sub>2</sub>Te<sub>3</sub>.<sup>464,465</sup> Since PANI is stable and has a high electrical conductivity, it can be combined easily with inorganic TE materials mainly via physical mixing of dry powders of PANI and inorganic materials such as Bi<sub>0.5</sub>Sb<sub>1.5</sub>Te<sub>3</sub>,<sup>457</sup> solution mixing,<sup>466</sup> *in situ* oxidative polymerization to insert PANI in V<sub>2</sub>O<sub>5</sub>.*n*H<sub>2</sub>O to form a xerogel,<sup>454</sup> and *in situ* interfacial polymerization to form PbTe-PANI composite nanostructures.<sup>458</sup> While PEDOT itself is not particularly soluble and hence limited in terms of solution processability, when emulsified with PSS to form PEDOT:PSS it has been combined with inorganic materials using *in situ* synthesis combined with drop casting,<sup>467</sup> solution mixing of PEDOT:PSS with Bi<sub>2</sub>Te<sub>3</sub> particles,<sup>462</sup> and direct hybridization with Au nanoparticles.<sup>468</sup> Although PTH has low solubility and electrical conductivity, Du et al. used a two-step process of preparing Bi<sub>2</sub>Te<sub>3</sub> and PTH using hydrothermal synthesis and oxidative polymerization respectively and then pressing them together to form a TE film.<sup>465</sup> While most of these studies report on composite films, Karttunen et al. demonstrated TE fabrics made via atomic and molecular layer deposition (ALD and MLD) of ZnO and ZnO-C<sub>6</sub>H<sub>4</sub>-OZn (ZnO-organic) superlattice materials onto cotton fabric.<sup>319</sup> These were advantageous since they could be fabricated directly onto the textile substrate, and showed power factors ranging from 7.4 to 137 W/cmK<sup>2</sup>.

While integration of inorganic and organic TE materials to produce hybrid materials with high ZTs is a promising avenue, it still faces many challenges. Many of the fabrication methods require high temperatures, long processing times and high cost of processing. Moreover, the challenge of combining rigid inorganic small molecules efficiently with polymers is a challenge.<sup>340</sup> Nevertheless, with the fabrication of nanowire-based OInTEs, there may be some applicability in the future for such materials into textile fiber-like form factors.<sup>469</sup>

## 2.5 Conclusions

This review provides a broad overview of the passive and active systems that have been deployed onto textiles to provide next-to-skin thermal comfort. While thermal comfort is a complex phenomenon with a variety of interpretations,<sup>8</sup> it is safe to say that textiles have been used since prehistoric times to provide protection from the elements,<sup>470</sup> and hence are an excellent platform to deploy the next generation of smart and comfortable textile-based PTCS. The future of PTCS also lies in the field of integration of actuators into textile fabrics.<sup>76,471</sup> Such responsive materials that can allow a change in porosity/breathability of the fabric will enable faster evaporative and radiative cooling of the body and can be seen as either active or passive systems, depending on the type of actuator used.<sup>8</sup> This review also provides an overview of the various materials and devices that have been used to integrate TE elements into textiles – whether in the form of TEGs or TECs. While there is a lot of research in the integration of TEGs into textiles, the field of fabric based TECs is still emerging. This translated into a good opportunity for the integration of TECs at the fiber or yarn level to create a more seamless thermal comfort experience. However, TECs also suffer from the limitation of needing heat sinks or some method of waste heat management which may not always be the easiest to deploy, as well as low efficiency of organic TE materials that

limits how much cooling can be achieved. Developing a PTCS seamlessly integrated into textiles that does not need wearer intervention and can provide on-demand heating and cooling is the holy grail of research scientists working on textiles and comfort. From the review, TECs are one avenue of achieving this and there is a tremendous opportunity in the development of flexible, conformable and high ZT TE materials, as well as integration of these into fabric geometries such that they do not sacrifice the inherent strength, flexibility and comfort associated with textile fabrics. More broadly, there is also an opportunity to create PTCS integrated with moisture/temperature sensors that can result in a holistic monitoring and response system. This would result in a truly “smart” textile that can provide on-demand next-to-skin thermal comfort using data from sensors, without the need for human intervention.<sup>8</sup>

**3. PART 2 DISSERTATION RESEARCH: ON-BODY COOLING USING YARN-BASED THERMOELECTRICS FOR SEAMLESS INTEGRATION INTO TEXTILES**

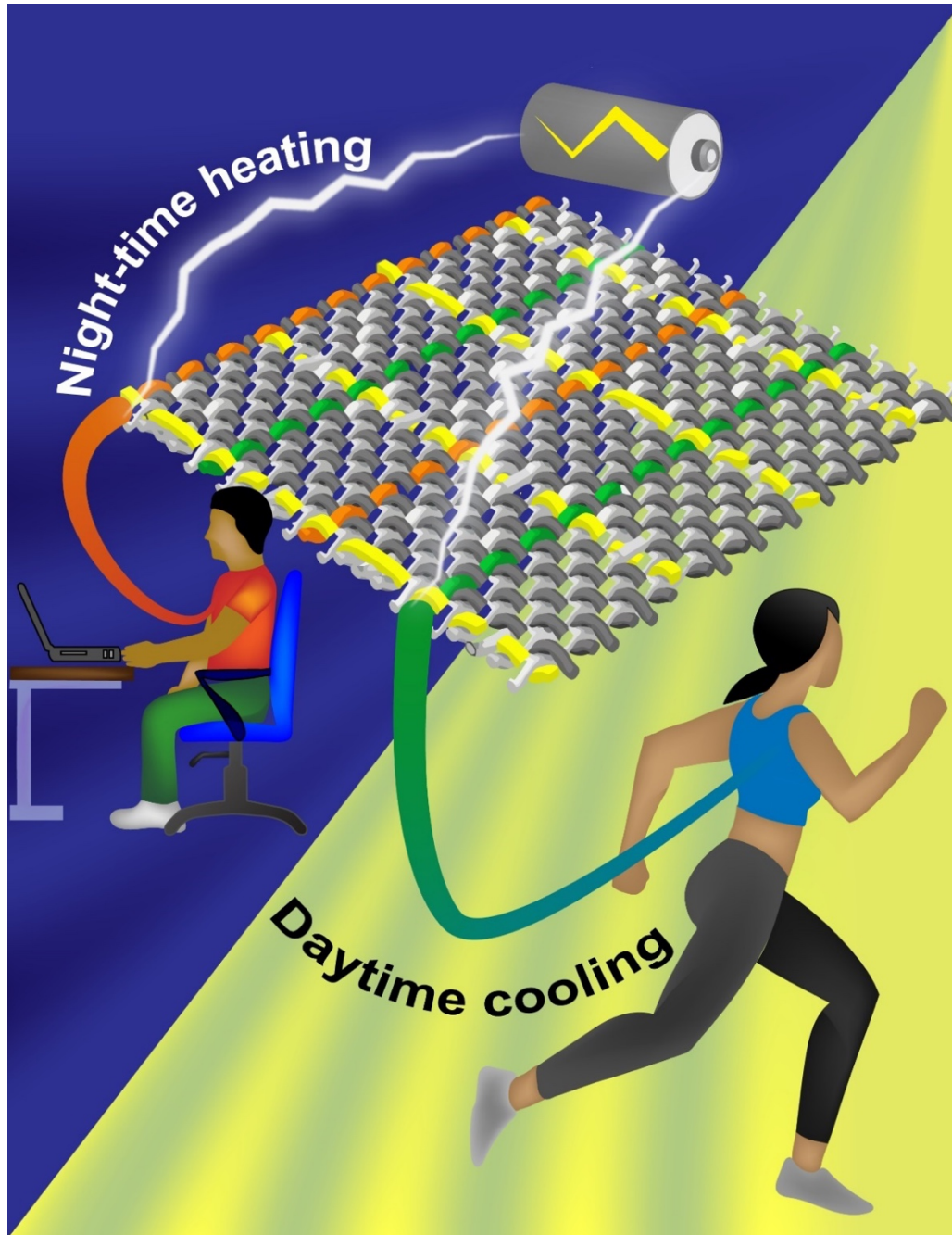


**Figure 18:** The concept of fabric integrated thermoelectric cooling (FabTEC) that enables next to skin heating and cooling in both indoor/outdoor and warm/cold conditions,

### 3.1 Introduction

Cooling devices account for nearly 20% of the total electricity consumed in buildings around the world, projected to increase from 2020 terawatt hours in 2016 to 6200 terawatt hours in 2050.<sup>2</sup> One way to combat this is by expanding the setpoint of air conditioners and heaters using personal cooling devices such as a TE cooler (TEC).<sup>55</sup> A TEC is a semiconducting, solid-state heat pump operating on the Peltier effect that transfers heat from one side of the device to the other.<sup>472</sup> TE coolers/heaters provide the advantage of highly reliable cooling/heating with no mechanical moving parts, compact in size and light in weight, and no working fluid.<sup>473</sup> Additionally, they have the advantage of being powered by DC electric sources. Localized thermoregulation by wearable TE cooling devices have the capability to decrease the usage of traditional systems, thereby reducing global reliance on space heating and cooling and providing savings on energy costs.<sup>336</sup> Integration of TECs for on-body cooling using textiles can provide customizable thermoregulation. Textiles provide an accessible platform for the deployment of TEC devices due to the conformal and intimate contact they make with the body. Additionally, the hierarchical nature of fabrics as they progress from fiber to yarn to fabric allows the integration of TEC modules directly into the woven structure, thereby creating a more seamless fabric based TEC device.<sup>437,438</sup>

When it comes to integration of TE elements into textiles, research has focused more heavily on power generation from human body heat (via TE generators or TEGs), rather than TE cooling (TEC). TEGs have been implemented into textiles using various materials and substrates such as PEDOT:PSS/MWCNT/PU composite dip coated onto polyester and cotton yarns,<sup>474,475</sup> PEDOT:PSS dip coated onto commercially available polyester fabric,<sup>476</sup> PANI/SWCNT composite ultrasonically inducted onto a polyester fabric,<sup>366</sup> electrospun polyacrylonitrile fibers

coated with n-type and p-type  $\text{Bi}_2\text{Te}_3$  and  $\text{Sb}_2\text{Te}_3$  and spun into yarns,<sup>327</sup> spun CNT yarn alternatively doped with polyethyleneimine (PEI) and  $\text{FeCl}_3$  solutions for n and p-type performance respectively,<sup>446</sup> graphite-PEDOT:PSS composite dip coated onto polyester fabric,<sup>477</sup> MWCNT/PVDF composite films deposited onto felt fabrics,<sup>441</sup> SWCNT inks doped with poly (acrylic acid) (PAA) and PEI for p and n-type performance, respectively and coated onto a flexible bracelet,<sup>478</sup> electrospun TE fibers composed MWCNT/CuO/PVP composite,<sup>479</sup> and glass fabric printed with n-type  $\text{Bi}_2\text{Te}_3$  and p-type  $\text{Sb}_2\text{Te}_3$  printing pastes.<sup>332</sup>

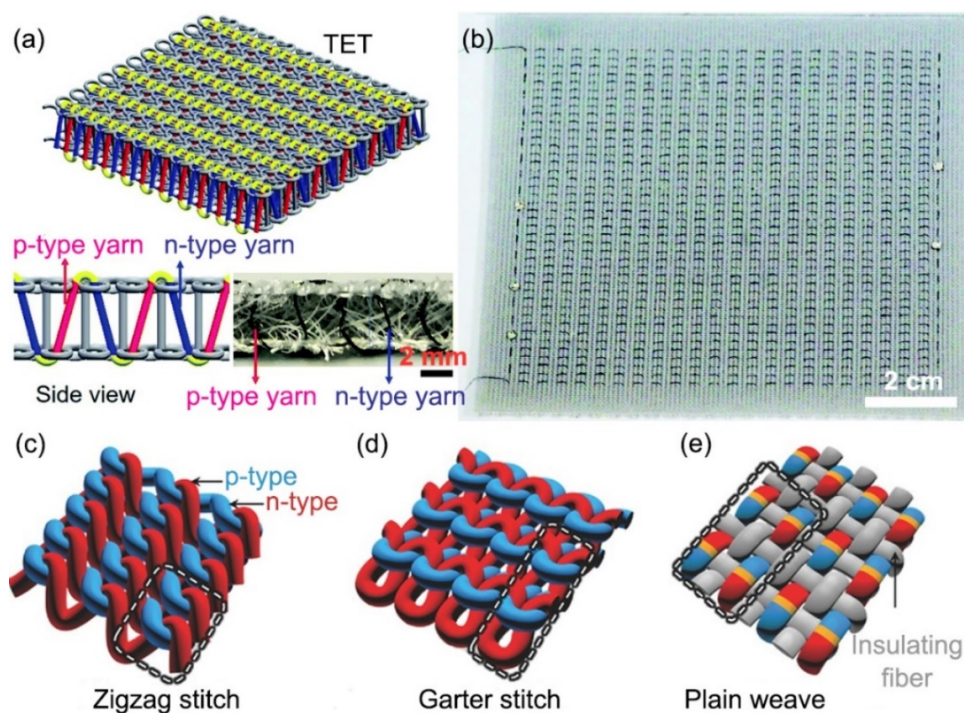


**Figure 19:** Three-dimensional thermoelectric textiles (TET) for power generation.<sup>437</sup> (a) Schematic diagram of the TET with PEDOT:PSS/MWCNT yarns as p-type and PEI/MWCNT yarns as n-type legs and optical image showing the vertical arrangement of legs. (b) A TET sample measuring 8 cm X 9.3 cm. Reproduced with permissions.<sup>437</sup> Copyright 2020, The Royal Society of Chemistry. Woven yarn TE fabric with n- and p-type semiconductor sheaths ( $\text{Bi}_2\text{Te}_3$  and  $\text{Sb}_2\text{Te}_3$ , respectively) coated onto nanofibers and then twisted into flexible yarns.<sup>327</sup> (c)-(e) Illustrations of TE textiles made via zigzag, garter and plain weave structures, respectively. Reproduced with permissions.<sup>327</sup> Copyright 2016 WILEY-VCH Verlag GmbH & Co. KGaA, Weinheim.

These fiber-based research works in some cases do not translate the coated fibers into conventional 2D fabrics,<sup>474</sup> while others coat commercial fabrics directly which does not provide a seamless integration.<sup>366</sup> While Zheng et al. demonstrated MWCNT-based TE yarns used to make a 3D warp-knitted spacer fabric shaped TEG,<sup>437</sup> and Lee et al. demonstrated  $\text{Sb}_2\text{Te}_3$  and  $\text{Bi}_2\text{Te}_3$  coated electrospun PAN yarns used to make woven TEGs,<sup>327</sup> these are still examples of energy harvesting and not TEC, although they do provide inspiration for integration of TE elements into woven textile structures, as shown in **Figure 19**. Additionally, these works do not explore how specific fabric parameters such as weave angle, aspect ratio of the TE yarn/fibers, spacing between the fabric TEC modules, and density of modules over the fabric area affect the performance of TE fabric. Finally, all these works focus not on TEC but rather on energy harvesting from the thermal difference between the human body and the environment (a gradient which maxes out at approximately 30 K).<sup>328</sup>

Lee et al. and Park et al. have demonstrated fabric TECs using inorganic, rigid Bi-Te p and n-type modules arranged in a mat-like fashion connected with wires and containing a flexible heat sink composed of solid-state silica gel mixed with hydrogel.<sup>337–339</sup> These devices were able to cool the skin by a temperature drop of 3.8 K,<sup>339</sup> with an improvement to 5.4 K.<sup>338</sup> Kishore et al. also developed high performance wearable coolers which were able to cool the skin by a temperature drop of 8.2 °C below room temperature by using commercially available n and p-type Bi-Te materials to fabricate a rigid TEC module with an aluminium heat sink.<sup>336</sup> In all these instances, it is apparent that current research on TECs involves the use of rigid semiconductor materials. This can cause an obvious mismatch between the softness of the skin and the rigidity of the TEC, creating discomfort for the wearer. Hong et al. demonstrated a flexible TEC without the use of

rigid or bulky heat sinks by sandwiching inorganic TE pillars between two layers of stretchable elastomers embedded with AlN microparticles that enhanced the sheets' lateral thermal conductivity.<sup>34</sup> This design creates a large air gap between the elastomer sheets, resulting in small thermal conductance between the hot and cold side of the TEC, but does not resemble a textile fabric in any manner, rather like an assembly of rigid materials within a flexible substrate.

There remains a tremendous opportunity to develop a fabric-integrated, soft and flexible, on-body, seamless Peltier heating/cooling device, termed as FabTEC (Fabric TEC) comprised of TE yarns of n and p-type semiconducting behavior. Such a practical system, with a detailed analysis of the fabric structure combined with well-characterized soft TE elements, has not yet been reported. A systematic understanding of exactly which fabric architecture should be used to obtain the maximum cooling without sacrificing the inherent nature of textiles i.e., comfort, flexibility and strength is needed. Even a 1 °C expansion of the thermostat set point of air conditioners used in the buildings in the US can result in a 7 – 15% increase in energy savings,<sup>3</sup> and hence TECs do not have to provide excessive amounts of heating/cooling at this stage. Additionally, humans can perceive temperature changes of 0.02 – 0.07 °C of cooling, and 0.03 – 0.09 °C of warming pulses.<sup>480</sup> The rate of temperature change is also important, with humans capable of detecting temperature changes if they happen more rapidly such as at 0.1 °C/s compared to 0.5 °C/minute.<sup>480,481</sup> Hence, lower efficiency TE materials can still be used for this purpose. It is important to note that the ZT of a TE material, alone, is not enough to describe some of the qualitative requirements from materials that are to be used for fabric-based cooling – other characteristics of importance are room temperature and solution processability, stability of

performance over time, flexibility and conformability, scalability and low cost. These qualities are not captured in ZT but are crucial to the creation of the next generation of TECs.

With the growing need for thermal comfort and added global temperature rise due to climate change,<sup>2,482</sup> it is important to intervene at a disruptive level to be able to bring about real change to the imminent global energy crisis that growing populations, rising incomes and greater built environments will have in the coming years. On-body thermal comfort systems can be that change, and thermoelectric elements integrated at the constituent level of textile fabrics are a novel approach of achieving this.

The objective of this research is to demonstrate a soft textile-based wearable thermoelectric (TE) fabric (FabTEC) that provides transformative levels of on-body heating and cooling, thermal comfort and aesthetics, as illustrated in *Figure 18*. This is achieved by developing nearly unobtrusive TE devices based on a carbon nanotube (CNT) ribbon yarn network with complimentary thermal management (TM) yarns integrated into a woven structure, combined with strategically programmed disconnects to ensure a congruous current path.

There are several key advances that are achieved in this research, with alternating positive and negative Seebeck coefficient TE yarns produced from air stable, solution and room temperature processable, cost effective and scalable multiwalled CNTs (MWCNT) that do not need a substrate, integration of these yarns into a woven fabric configuration, and optimization of the design by integrating woven yarn geometry with TE theory. This allows for a high density, flexible and conformable TEC module, which has not yet been reported elsewhere. The fabric module also

involves the study of thermal management through the weave design of the TM yarns, proposing a design that allows for better separation of hot and cold sides of the FabTEC device. The in-plane TE transport characteristics including thermal conductivity, electrical conductivity and Seebeck coefficient of the materials are thoroughly characterized to report a more accurate material power factor and figure of merit (ZT) and are detailed in Section 3.2. Geometric and theoretical modeling are combined to optimize the FabTEC structure and gain a clear understanding of the performance capabilities of such a device and are detailed in Section 3.3. While current textile-based TE devices focuses almost exclusively on TE generators (TEGs) to harvest body heat,<sup>327,361,366,437,446,474–477</sup> this device takes advantage of the Peltier effect to deliver both heating and cooling, enabling next-to-skin thermal comfort.

This research work is divided into the style of two research papers that explore the three goals of this project: (i) material selection and characterization in Section 3.2, (ii) integration of materials into a thermoelectric junction in Section 3.3, and (iii) theoretical modeling to optimize the performance of the FabTEC in Section 3.3.

Section 3.2 has been published in ACS Applied Energy Materials under the title “In-plane Thermoelectric Properties of Flexible and Room Temperature Processable Doped Carbon Nanotube Films”.<sup>47</sup>

Section 5 is in the process of submission to Materials Today, under the title “Design and Evaluation of a Woven Thermoelectric Heating/Cooling Fabric for On-Body Thermal Comfort”.

## 3.2 In-Plane Thermoelectric Properties of Flexible and Room Temperature Doped Carbon Nanotube Films

### 3.2.1 Introduction

Thermoelectric (TE) energy conversion is a highly reliable method of solid state energy harvesting and thermoregulation, without the use of moving parts or bulky fluids.<sup>238,240,243</sup> Flexible TE generators (FTEGs) are especially attractive for powering the next generation of wearable devices by harvesting the thermal gradient between the human body and the environment, via the Seebeck effect.<sup>328,332,333,483,484</sup> This has prompted a substantial amount of research both in the design of FTEG devices<sup>255,437,485–489</sup> as well as the materials used to make them.<sup>248,288,490–493,421,423,371</sup> The performance of thermoelectric materials can be quantified by their figure of merit ( $ZT$ ) =  $S^2\sigma/\kappa T$  where  $S$  is the Seebeck coefficient,  $\sigma$  is the electrical conductivity,  $\kappa$  is the thermal conductivity and  $T$  is the absolute temperature, and by their power factor ( $PF$ ) =  $S^2\sigma$ .<sup>494</sup> Since there is a strong correlation between  $S$ ,  $\sigma$  and  $\kappa$  it is a challenging task to enhance the  $PF$  of TE materials without sacrificing their  $ZT$ .<sup>258</sup> State of the art bulk TE materials include alloys based on Bi-Te-Sb-Pb which have high  $ZT$  ( $>1$ )<sup>495–498</sup> but are heavy, brittle, expensive, and contain toxic elements such as tellurium and lead.<sup>261,262</sup> Moreover, to create efficient TE devices for energy harvesting or thermoregulation,  $ZT$  is not the only important criterion – room temperature and solution processable doping, air stability, scalable synthesis, low cost, and efficient near-ambient temperature performance are all crucial parameters to create truly wearable and flexible TE devices.<sup>246</sup>

In terms of use as FabTECs, a number of different materials were explored in this study, and their viability in terms of their PFs, mechanical flexibility, and ease of processing were evaluated. Specifically, we explored the materials shown in **Table 1**.

**Table 1:** Seebeck coefficients, electrical conductivities and resultant power factors of flexible thermoelectric materials explored for FabTEC

Material	Type	Seebeck Coefficient ( $\mu\text{V/K}$ )	Electrical Conductivity (S/m)	Power Factor ( $\mu\text{W/mK}^2$ )
SWCNT on PTFE membrane	p-type	$98.4 \pm 0.011$	$140.4 \pm 0.04$	1.36
SWCNT/PEI on PTFE membrane	n-type	$92.5 \pm 0.025$	$78.1 \pm 0.07$	0.67
PEDOT:PSS + 5% DMSO	p-type	$19.2 \pm 0.030$	$35000 \pm 0.05$	12.5
MWCNT film	p-type	$56 \pm 0.002$	$107977.61 \pm 0.01$	340.94
MWCNT film + 5% PEI	n-type	$54.29 \pm 0.004$	$134238.78 \pm 30036.18$	395.59

From **Table 1** it is apparent that MWCNT films performed much better than the other candidate materials in terms of TE PFs, thereby justifying their selection as materials to incorporate into the FabTEC design.

CNTs are a promising class of TE materials due to their flexibility and strength,<sup>499</sup> high electrical conductivities,<sup>500</sup> low density ( $\sim 1 \text{ g/cm}^3$  compared to  $7.86 \text{ g/cm}^3$  for popular TE material

$\text{Bi}_2\text{Te}_3$ ),<sup>248</sup> and their oxygen sensitivity which makes them behave as p-type semiconductors in ambient conditions.<sup>431</sup> Moreover, their high surface area provides for facile physisorption of electron rich polymers to create n-type CNT materials.<sup>261,435,493,501–505</sup> Previous studies have reported TE properties of CNT films, such as for single walled CNTs (SWCNTs), Yu et al. reported p-type single walled CNTs (SWCNTs) doped with an intrinsically conducting polymer poly (3,4-ethylenedioxythiophene):poly(styrenesulfonate) (PEDOT:PSS) to achieve PF of  $\sim 160 \mu\text{W}/\text{mK}^2$  ( $\sigma = 1.35 \times 10^5 \text{ S}/\text{cm}$ ,  $S = 40 \mu\text{V}/\text{K}$ ) and reported the cross-plane (through the thickness)  $\kappa$  as  $0.2 - 0.4 \text{ W}/\text{mK}$ ,<sup>248</sup> and Zhou et al. reported p-type pristine SWCNT and n-type SWCNT doped with polyethyleneimine (PEI) with PFs of  $1840 \mu\text{W}/\text{mK}^2$  ( $\sigma = 3.02 \times 10^5 \text{ S}/\text{m}$ ,  $S = 87 \mu\text{V}/\text{K}$ ) and  $1500 \mu\text{W}/\text{mK}^2$  ( $\sigma = 1.78 \times 10^5 \text{ S}/\text{m}$ ,  $S = -82 \mu\text{V}/\text{K}$ ) and in-plane  $\kappa$  of the p-type and n-type films as 24 and 18  $\text{W}/\text{mK}$ , respectively.<sup>255</sup> Similarly for MWCNTs, Meng et al. reported p-type MWCNTs combined with the ICP polyaniline (PANI) with a maximum PF of  $5.04 \mu\text{W}/\text{mK}^2$  ( $\sigma = 4441 \text{ S}/\text{m}$ ,  $S = 33 \mu\text{V}/\text{K}$ ) and cross-plane  $\kappa = 0.45 \text{ W}/\text{mK}$ ,<sup>494</sup> Wang et al. reported p-type MWCNT combined with the ICP polythiophene (PTh) with a PF of  $2.29 \mu\text{W}/\text{mK}^2$  ( $\sigma = 2982 \text{ S}/\text{m}$ ,  $S = 27.7 \mu\text{V}/\text{K}$ ) and cross-plane  $\kappa = 0.6 \text{ W}/\text{mK}$ ,<sup>506</sup> and Zheng et al. reported p-type MWCNT/PEDOT:PSS yarns and n-type MWCNT/PEI yarns with PF of  $512.8 \mu\text{W}/\text{mK}^2$  ( $\sigma = 1.04 \times 10^5 \text{ S}/\text{m}$ ,  $S = 70.1 \mu\text{V}/\text{K}$ ) and  $667.8 \mu\text{W}/\text{mK}^2$  ( $\sigma = 1.41 \times 10^5 \text{ S}/\text{m}$ ,  $S = -68.7 \mu\text{V}/\text{K}$ ), respectively with in-plane  $\kappa$  of 35  $\text{W}/\text{mK}$  for both p-type and n-type yarns.<sup>437</sup> It is important to note that in many of these works,  $S$  and  $\sigma$  are measured in-plane whereas  $\kappa$  is measured in the cross-plane direction. While certain works have demonstrated in-plane measurement of  $\kappa$ ,<sup>507,508</sup> it is not commonly reported due to the complex methods required for measuring in-plane  $\kappa$  accurately with a reasonably low uncertainty ( $<15\%$ ). This discrepancy in measurement of ZT can result in inaccuracies and is disadvantageous in FTEG applications where in-plane thermal and electrical transport are observed. While Zheng

et al. have measured the in-plane  $\kappa$ , it is quite high and negatively impacts their ZT.<sup>437</sup> Zhou et al. have reported comparatively lower values of  $\kappa$ <sup>255</sup> but SWCNTs are comparatively more expensive, can suffer problems of purity, and are obtained in small scales, putting them at a disadvantage when compared to MWCNTs. In comparison to the purity of 77% for the SWCNT films used by Zhou et al.,<sup>255,500</sup> the MWCNT films in this work have a purity of 87.7%.<sup>509</sup> Additionally, both Zheng and Zhou have utilized the self-heating methods for measuring thermal conductivity which require complex photolithography techniques and materials processing,<sup>255,437</sup> whereas pump-probe optical spectroscopy techniques such as time-domain thermoreflectance (TDTR) can provide a fast and non-contact method for the estimation of in-plane  $\kappa$ .<sup>510</sup>

In this work, we characterize the TE properties of pristine p-type MWCNT and n-type MWCNT/PEI composite films with high PFs ( $\sim 340$  and  $\sim 520 \mu\text{W}/\text{mK}^2$ , respectively) and comparatively low values of in-plane  $\kappa$  ( $\sim 5.5$  and  $\sim 8.1 \text{ W}/\text{mK}$ , respectively). We report ZT values of 0.019 and 0.015 for the p-type and n-type MWCNT films, respectively, considering the in-plane TE properties for  $S$ ,  $\sigma$  and  $\kappa$  of these materials, that are crucial for truly accurate characterization of their TE performance. These are almost equivalent to the ZT values for n- and p-type SWCNTs reported by Zhou et al.,<sup>255</sup> but here we have utilized a simple fabrication technique with relatively lower cost and easily scalable MWCNTs. Using a two-step, room temperature and solution-based doping process, we were able to synthesize air-stable flexible n-type MWCNT/PEI films with high PFs. Their TE properties are optimized with regards to the amount of PEI doping, and these properties are retained even after weeks of air exposure. Additionally, since the MWCNTs used in this work are scalable and low-cost, we can easily make large quantities of these p- and n-type

materials. While our PFs are lower than those reported by Zheng et al. for yarns made of similar materials, our overall ZT is much higher due to our lower in-plane  $\kappa$  values.

### 3.2.2 Sample Preparation

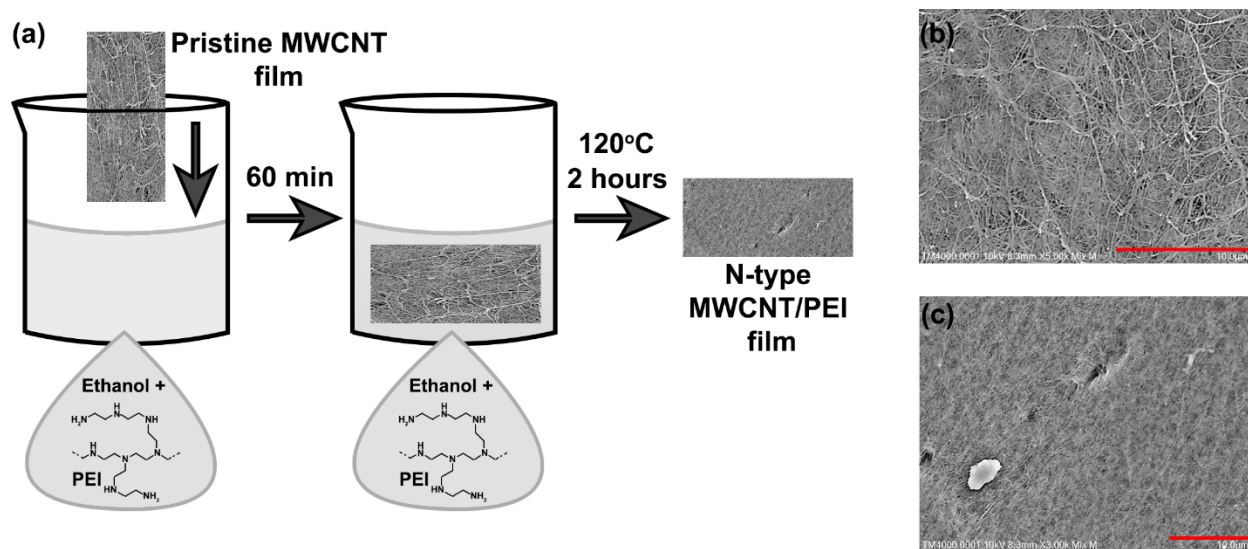


**Figure 20:** (a) Simple fabrication of doped PEI-MWCNT film using a PEI-Ethanol solution of varying concentrations. SEM images of (b) pristine MWCNT film and (c) 5 wt.% PEI-Ethanol treated film shows a deposition of PEI on the surface of the MWCNTs. Scale bars for (b) and (c) are 10  $\mu\text{m}$ .

The pristine MWCNT films were generously donated by Prof. Fujun Xu at College of Textiles, Donghua University, China obtained from Suzhou Xinyin nanotechnology company and were used as received for p-type MWCNT materials. Their preparation and properties are detailed in previous publications.<sup>509,511</sup> Briefly, floating catalyst chemical vapor deposition (FCCVD) method was used to obtain large scale CNT films,<sup>509,511</sup> similar to the films used by Zheng et al.<sup>437,511</sup> For preparation of the n-type films, a measured amount of PEI (molecular weight 600, 99% from Alfa Aesar) by weight was added to a fixed amount of ethanol, such that the weight concentrations of PEI in ethanol increased from 5 weight% (wt.%), 10 wt.%, 15 wt.% to 20 wt.%, termed as 5-

MWCNT/PEI, 10-MWCNT/PEI, 15-MWCNT/PEI and 20-MWCNT/PEI, respectively as shown in **Figure 20(a)**. Values beyond 20 wt.% were not evaluated due to the excessive tackiness of the films when treated with high quantities of PEI, thereby hampering ease of handling and accuracy of measurement. The pristine MWCNT films were immersed into the PEI-Ethanol solution and left for 60 minutes at room temperature. This was followed by heat treatment of the doped films for 2 hours at 120 °C to get rid of the excess ethanol from the films. The thickness of the films was measured using a Mitutoyo Absolute Digimatic digital thickness gage (Mitutoyo Corp) and reported as  $8.4 \pm 0.5 \mu\text{m}$ ,  $10.2 \pm 1.5 \mu\text{m}$ ,  $10.7 \pm 1.3 \mu\text{m}$ ,  $9.9 \pm 0.7 \mu\text{m}$  and  $9.1 \pm 1.7 \mu\text{m}$  for the pristine MWCNT film, 5-MWCNT/PEI, 10-MWCNT/PEI, 15-MWCNT/PEI and 20-MWCNT/PEI, respectively, as shown in **Figure S32**. A Hitachi TM4000 scanning electron microscope (SEM) was used to take SE micrographs of sputter coated pristine MWCNT film and 5-MWCNT/PEI film after sputter coating them with gold and palladium, with the images shown in **Figure 20(b), (c)**.

### **3.2.3 Measurements**

#### **3.2.3.1 Electrical Conductivity**

Electrical conductivity of the films was measured using a custom-built 4-Probe measurement system with gold probes of 2 mm probe spacing, with the outer probes applying current and the inner probes measuring the voltage. The probes were attached to a Keithley 6221 alternating current (AC) and direct current (DC) current source and a Keithley 2182a Nanovoltmeter and recording 1000 readings for resistance of three different film of each type (pristine MWCNT film, 5-MWCNT/PEI, 10-MWCNT/PEI, 15-MWCNT/PEI and 20-MWCNT/PEI). A correction term

considering the dimensions and thicknesses of the films was applied and an average of 1000 readings was reported along with the standard error of mean.

### 3.2.3.2 Seebeck Coefficient

The Seebeck coefficient of the films was measured using a homemade benchtop evaluation setup, as shown in *Figure S30*. The setup consisted of a cold side Peltier TE cooler module and heatsink assembly and a hot side Peltier TE cooler module without the heat sink (both purchased from Adafruit Industries) which were connected to a Keithley 2231A-30-3 triple channel DC power supply to maintain a thermal gradient. The MWCNT film was cut in the dimension of 3 cm X 1 cm and one end was secured on the hot side while the other on the cold side, using MX-4 thermal compound (Arctic GmbH) to maintain thermal contact. Once a thermal gradient was applied, the temperatures of the hot and cold sides were measured using a Type-K thermocouple attached to a Keysight U1272A multimeter with temperature measurement capabilities. Electrically conductive tape (3M™ Copper Foil Tape 1181) with electrically conductive, pressure-sensitive acrylic adhesive (Digi-Key Electronics) was cut into 2 mm X 2 mm squares and attached to the MWCNT film on the hot and cold ends. A multimeter (Keysight U1272A) was used to measure the voltage generated at various applied thermal gradients, with the multimeter probes connecting with the copper foil tapes to ensure low contact resistance. The resulting voltage was recorded for the calculation of the Seebeck coefficient of the MWCNT films. Three different films of each p-type pristine MWCNT and n-type 5-MWCNT/PEI, 10-MWCNT/PEI, 15-MWCNT/PEI and 20-MWCNT/PEI films were characterized three times for each applied temperature gradient and an average value with standard error of mean was reported for Seebeck coefficient. The measurement of Seebeck coefficient was repeated after 14 days for all samples in the same manner to determine

the air stability of doping. PF and ZT were calculated from the measured values of  $S$ ,  $\sigma$  and in-plane  $\kappa$  at 300 K.

The TE device which comprised of a single p-n junction was fabricated by laying the p-type MWCNT leg on the 5- MWCNT/PEI leg and securing them together using electrically conductive tape (3M™ Copper Foil Tape 1181) with electrically conductive, pressure-sensitive acrylic adhesive. This formed a triangular shape with the junction at the apex and the ends of the p and n-legs at the base. Both legs measured 3 cm length X 1 cm width X 8.4  $\mu\text{m}$  thickness. This TE device was then secured to the TE measurement setup using thermal compound such that the junction rested on the hot side and the ends of the legs were resting on the cold side. A thermal gradient was thus created between the junction and the legs, and the resulting open circuit Seebeck voltage was measured. For each thermal gradient, three measurements were taken, and this was repeated for three different samples.

### 3.2.3.3 In-plane Thermal Conductivity

The in-plane thermal conductivity values of the p- and n-type films were measured using TDTR, an optical pump probe method commonly used for characterizing thin films.<sup>512,513</sup> A mode-locked Ti:Sapphire laser emits a train of pulses that are bifurcated into pump and probe beams. The former is advanced through a delay stage to change the optical lengths between the two beams which are then focused on the sample through a common objective lens. The pump beam acts as a periodic heat source (modulated by a square wave), creating a temperature rise that triggers reflectivity change which is captured by the probe beam at the modulation frequency. The temporal decay of the measured signals is used to deduce  $\kappa$  with a heat diffusion model.<sup>514,515</sup> In principle, the thermal

model used for analyzing the TDTR experiment consists of seven parameters: thickness, volumetric heat capacity and  $\kappa$  of the transducer (in this case aluminum (Al)) film, diameter of the laser spot, thermal conductance of the Al/MWCNT interface, and  $\kappa$  and volumetric heat capacity of the MWCNT sample. Of these,  $\kappa$  of the MWCNT film and interfacial thermal conductance are varied to fit the data.<sup>516,517</sup> Other experimental and modelling details are similar to the one described in previous works.<sup>515,518</sup> This method has been used to measure various porous thin films and network structures.<sup>519–524</sup>

In-plane thermal conductivity measurement of MWCNT films using TDTR requires additional sample preparation steps. The films are first embedded into an epoxy matrix to form a composite which is then cut to expose the cross-sectional surface of the film using diamond blade ultramicrotome. Typically, a root mean square (RMS) roughness of <15 nm in areas larger than the laser spot size is sufficient to avoid artifacts created by thermoelastic effects that modulate the intensity of diffuse light scattering in the measurement. This was achieved by ultramicrotome in these samples. Similar procedure is applied in our previous works for PEDOT:PSS<sup>525</sup> and CPE/SWNT<sup>520</sup> films. The cutting is followed by sputtering about 80 nm of Al transducer over the film surface, the same as in a conventional TDTR sample preparation. The samples were then oriented so that the direction of the incident laser beam is parallel to the original plane of the film. When embedding the composite film in epoxy, most of the sample preparation steps were at room temperature, therefore it is safe to assume that any reaction between the epoxy and film would be limited around the interface between the composite film and epoxy, but as measurement is done close to center of the sample, this possible effect can then be neglected.

Charge-coupled device (CCD) image of the epoxy-film surface with pump beam focused on the sample film are taken. The laser beams are modulated at 7.2 MHz and focused using a 20x objective on a smooth region over the film, as confirmed by laser reflectance ( $> 99\%$ ). The objective lens is selected such that laser beam spot size ( $2.95 \mu\text{m}$ ) is smaller than the film thickness. The laser power is adjusted to keep the steady state temperature rise below 20 K. Finally, the experimental temperature decay is fitted to the heat conduction model with  $\kappa$  of the MWCNT film and interfacial conductance being the fitting parameters.<sup>514,515</sup>

### 3.2.4 Results and Discussion

With  $S \approx 56.19 \mu\text{V/K}$  and  $\sigma \approx 1.08 \times 10^5 \text{ S/m}$ , the PF of the pristine MWCNT film was calculated as approximately  $340 \mu\text{W/mK}^2$  (**Figure 21**), with an in-plane thermal conductivity of  $5.5 \pm 0.8 \text{ W/mK}$ , resulting in a ZT of approximately 0.019 at 300 K. Hence, this film was used as is, without any treatment for the p-type leg. The SEM image of the pristine MWCNT film shows that the CNT aggregates into bundles, as seen in Figure 1 (b) and Figure S2 (a), thereby forming multiple contact points with each other in Y-shaped junctions. This enhances the electrical conductivity of the pristine films. Due to exposure to the electron-withdrawing group  $\text{O}_2$  which gets physisorbed on the MWCNT surface, the pristine film behaves as a p-type semiconductor with holes as the predominant charge carriers.<sup>431</sup>

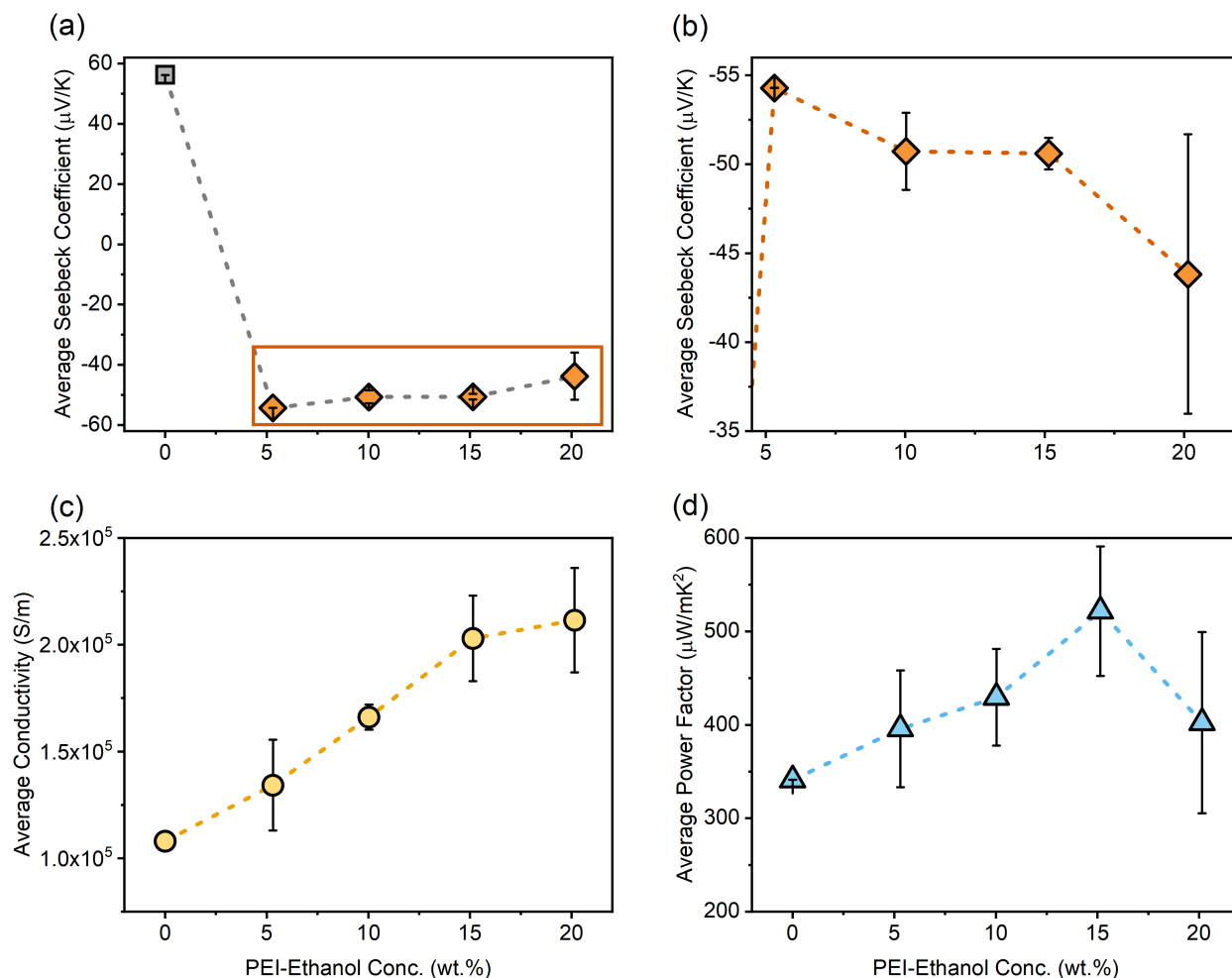


**Figure 21:** Electrical and thermoelectric properties of undoped MWCNT and n-type doped MWCNT/PEI films as PEI-Ethanol concentration increases from 0 wt.% to 20 wt.%. (a) Seebeck coefficient of pristine MWCNT film (p-type indicated by  $\square$ ) and doped MWCNT films (n-type indicated by  $\diamond$ ). (b) Seebeck coefficients of just n-type doped MWCNT/PEI films ( $\diamond$ ), representing the area highlighted in the box in (a). (c) Electrical conductivity ( $\circ$ ) increases as the amount of PEI increases. (d) Overall power factors ( $\triangle$ ) of the pristine MWCNT and doped MWCNT films, with a maximum power factor at 15 wt.% PEI calculated as  $521.67 \pm 69.33 \mu\text{W/mK}^2$ .

The facile method for creating n-type MWCNT films with the commonly used, amine-abundant polymer PEI enabled room temperature and solution processable doping of the pristine MWCNT films. The MWCNT surface is coated with the PEI such that the Y-junctions of the pristine film are no longer visible, as shown in the SEM image of 5-MWCNT/PEI film in **Figure 20(c)** and

*Figure S30* (b), indicating a physical deposition of PEI onto the surface of the MWCNT bundles. PEI is known to be a physical modifier rather than a chemical attachment, with physisorption of the ethylamine group creating a molecular dipole moment between the PEI and the MWCNT surface, thereby reducing its work function.<sup>444</sup> Even with a 5 wt.% PEI-ethanol solution we see a change in Seebeck coefficient of the MWCNT film, going from positive to negative (+56  $\mu\text{V/K}$  to -54  $\mu\text{V/K}$ ), indicating that the majority charge carriers have changed from holes to electrons, as shown in *Figure 21*(a). Due to the high electron-donating ability of the amine groups in the branched PEI, the MWCNT undergo a hole depletion and hence there is a significant n-type doping of the pristine MWCNT film.<sup>503</sup>

As the concentration of PEI increases, the Seebeck coefficient decreases slightly, as shown in *Figure 21*(b) while the electrical conductivity keeps increasing as the concentration of the PEI-ethanol solution increases from 5 wt.% to 20 wt.%, see *Figure 21*(c). This increase in electrical conductivity can be attributed to the fact that the number of charge carriers (holes and electrons) keep increasing as the amount of PEI increases in the 5 wt.% to 20 wt.% range. Additionally, the treatment of the films with ethanol can result in further consolidation of the CNT bundles within the film, creating better contacts between the CNTs and enabling enhanced electrical conductivity. However, for Seebeck coefficient, there is only an optimized level of PEI that causes the largest absolute value of the n-type Seebeck coefficient i.e. 5 wt.% PEI. Beyond that, no increase in Seebeck coefficient is observed. This could be attributed to the fact there is a saturation to the amount of PEI that can be attached to the MWCNT leading to a stagnation in the n-type Seebeck coefficient value, a phenomenon consistently observed in other studies of PEI/CNT systems as well.<sup>255,493,505,526</sup> Nevertheless, this is advantageous since it indicates that only an intermediate

level of doping is required to produce the n-type MWCNT films, with all the doped films showing a PF values in the same order of magnitude, as shown in **Figure 21(d)**. Due to the increased tackiness of the films as the amount of PEI is increased, we proceeded to use the 5-MWCNT/PEI film for thermal conductivity characterization and junction Seebeck coefficient measurement, since it uses the least amount of dopant and still has a comparable PF of  $\sim 396 \mu\text{W}/\text{mK}^2$ , while maintaining ease of handling.

An important aspect of ZT for TE materials is the thermal conductivity. While the thermal conductivity of individual tubes can be very high, CNT films themselves are expected to have lower thermal conductivity due to contact resistance between tubes and their bundles. It is important to understand the in-plane thermal conductivity of these films, since a more accurate picture of ZT can only be presented when all three transport properties ( $\sigma$ , S and  $\kappa$ ) are measured in the same direction.

The in-plane thermal conductivity values for both n-type 5-MWCNT/PEI and p-type MWCNT samples are calculated from **Figure 22(b)**. The Al thickness is determined from acoustic echoes observed during early delay time ( $< 100$  ps). Thermal conductivity of Al thin film was calculated from the Wiedemann–Franz law based on the measured in-plane electrical conductivity.<sup>525</sup> The experimental data is fitted between 600-3500 ps to avoid strong thermoelastic effects.<sup>520</sup> The densities of p-type and n-type MWCNT films were calculated as  $0.877 \pm 0.013$  and  $0.937 \pm 0.019$  g/cm<sup>3</sup>, respectively by averaging fifteen mass and thickness readings of pre-cut samples measuring 7 cm X 7 cm. The specific heat capacity was estimated as 0.287 J/gK for the p-type MWCNT film and 0.501 J/gK for the n-type 5-MWCNT/PEI films based on the porosity of the MWCNT film

(reported as 80%)<sup>511</sup> using a linear mixing rule applied to PEI, air, and MWCNT with reported values of specific heat capacities for each of the constituents as 1.25, 1.005 and 0.75, respectively.<sup>527,528</sup> The thermal conductivity of MWCNT film and interfacial conductance between Al and MWCNT film are the fitting parameters in the thermal model, as previously mentioned in Section 3.2.3.3.

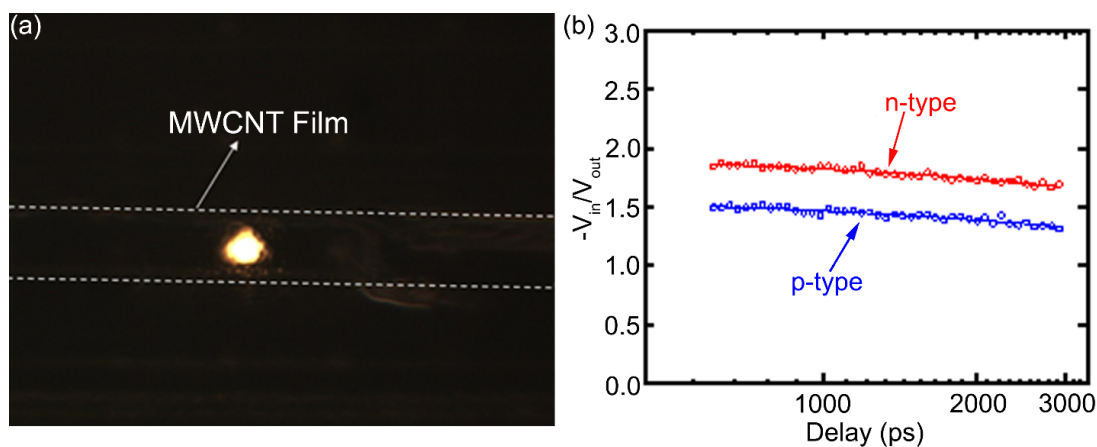


**Figure 22:** (a) CCD image of pump beam focused (20x, Gaussian beam spot radius = 2.95  $\mu\text{m}$ ) on microtomed MWCNT sample surface covered with 80 nm Al. (b) Data fitting for in-plane thermal conductivity of n-type 5-MWCNT/PEI (red) and p-type MWCNT (blue) calculated from the ratio of in-phase signal ( $V_{\text{in}}$ ) to the out-of-phase signal ( $V_{\text{out}}$ ).

The in-plane thermal conductivities are determined to be  $5.5 \pm 0.8$  W/m/K for the pristine MWCNT film and  $8.1 \pm 1.2$  W/m/K for the 5-MWCNT/PEI film. We repeated our measurements at different locations (many locations are sufficiently smooth for measurements as shown in the CCD image in **Figure 22(a)**) and found that the thermal conductivity variations at different locations are within 10%. The experimental uncertainties and systematic uncertainties were combined to provide the total error. The systematic uncertainties of the thermal conductivity measurements are calculated by considering the individual uncertainties and sensitivities of the parameters in the thermal model.<sup>514</sup> These values of  $\kappa$  are lower than that reported in other work

potentially due to higher phonon boundary scattering.<sup>437</sup> The n-type sample shows a higher  $\kappa$  value due to its higher density as conductive polymer matrix replaces relatively more insulating air. These values were used to calculate the ZT of the pristine film as 0.019 and that for the 5-MWCNT/PEI film as 0.015.

We also measured the junction performance of the TE device, when a junction of the pristine MWCNT film and n-type 5-MWCNT/PEI film was created, using the same setup as described in Section 3.2. The junction Seebeck coefficient was measured to be  $\sim 139 \mu\text{V/K}$ , with an applied thermal gradient ranging from 0 to 12 K, as shown in **Figure 23(a)**. Additionally, the air stability of the n-type doped films was studied over 28 days, with the 5-MWCNT/PEI film only showing a slight decrease (from  $\sim -54$  to  $\sim -51 \mu\text{V/K}$ ) whereas the 10-MWCNT/PEI, 15-MWCNT/PEI and 20 MWCNT/PEI showed a greater decrease in their Seebeck coefficients, although still retaining their negative Seebeck coefficients, as shown in **Figure 23(b)**.

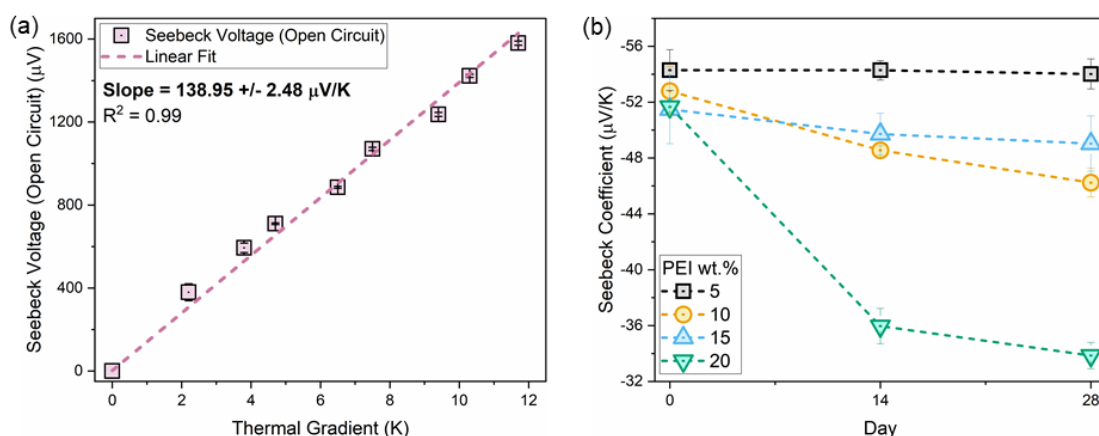


**Figure 23:** (a) Open circuit Seebeck voltage of a single junction composed of a pristine MWCNT film (3 cm length X 1 cm width X  $8.4 \mu\text{m}$ ) as p-type leg and 5-MWCNT/PEI (3 cm length X 1 cm width X  $10 \mu\text{m}$ ) as n-type leg ( $\square$ ), as a function of applied thermal gradient. The measured Seebeck coefficient of a single junction is  $138.95 \pm 2.48 \mu\text{V/K}$ . (b) Air stability of n-type doped MWCNT/PEI films over 28 days with 5-MWCNT/PEI ( $\square$ ), 10-MWCNT/PEI ( $\circ$ ), 15-MWCNT/PEI ( $\triangle$ ), and 20-MWCNT/PEI ( $\nabla$ ).

The decrease in Seebeck coefficient could be attributed to the air oxidation of the MWCNT films, although the overall over 28 days decrease is only approximately 12 and 4.7 % in the 10-MWCNT/PEI and 15-MWCNT/PEI films, respectively. The decrease in Seebeck coefficient is the largest over 14 days in the 20-MWCNT/PEI film at approximately 34.5 %. Although it is unclear exactly why the 20-MWCNT/PEI shows the most air degradation, one of the reasons could be poor attachment of residual PEI once all the attachment sites on MWCNTs have been occupied, leading to easier air oxidation and degradation of the n-type behavior, since it is unlikely that PEI has permeated through the entire MWCNT film bundle.<sup>493</sup> The stability behavior also reinforces our preference of the 5-MWCNT/PEI film for forming the p-n junction in *Figure 23(a)*, since it shows the least amount of air degradation, attributed to the more effective attachment of PEI due to many available surface sites.

### 3.2.5 Conclusions

We were able to fabricate n-type MWCNT films with high power factors and low in-plane thermal conductivity, using a facile two-step method. The increase in electrical conductivity of the MWCNTs as the amount of PEI increased was attributed to the increase in total number of charge carriers, whereas the stagnation of Seebeck coefficient beyond a certain amount of PEI indicated a saturation in the number of electrons that could be donated for n-type semiconducting performance. This is advantageous since even at low levels of PEI doping, the MWCNT film has high power factor. The p-type MWCNT film was used as is and hence tedious preparation methods could be avoided, resulting in p and n-type flexible, low-cost materials that are solution and room temperature doped, and have air stable TE properties. Measurement of in-plane thermal conductivity ensured an accurate measurement of the ZT of these materials – reported as 0.019 and 0.015 for p- and n-type MWCNT films, respectively. This characterization of in-plane TE

transport properties are crucial for many FTEG and TE heating/cooling devices. The TE properties of the materials explored in this work are summarized in **Table S2** and are compared to other reported CNT-based TE materials in **Figure S33**. Such MWCNT materials are promising for their application in wearable TE devices where not just high ZTs but flexible form factors with air stable processing and properties are crucial.

#### ASSOCIATED CONTENT

##### **Supporting Information – Appendix A**

Seebeck coefficient evaluation setup; SEM images at 10000X magnification of p and n-type MWCNT films; thickness of MWCNT films as a function of PEI; summary table of TE properties of p and n-type MWCNT films; and comparison of this work with other reported works (PDF).

### **3.3 Design and Evaluation of a Woven Thermoelectric Heating/Cooling Fabric for On-Body Thermal Comfort**

#### **3.3.1 Introduction**

Cooling devices account for nearly 20% of the total electricity consumed in buildings around the world, projected to increase from 2020 terawatt hours in 2016 to 6200 terawatt hours in 2050.<sup>2</sup> One way to combat this is by expanding the setpoint of air conditioners and heaters using personal cooling devices such as a TE cooler (TEC).<sup>55</sup> A TEC is a semiconducting, solid-state heat pump operating on the Peltier effect that transfers heat from one side of the device to the other.<sup>472</sup> TE coolers/heaters provide the advantage of highly reliable cooling/heating with no mechanical moving parts, compact in size and light in weight, and no working fluid.<sup>473</sup> Localized thermoregulation by wearable TE cooling devices have the capability to decrease the usage of traditional systems, thereby reducing global reliance on space heating and cooling and providing savings on energy costs.<sup>336</sup> Integration of TECs for on-body cooling using textiles can provide customizable thermoregulation. Textiles provide an accessible platform for the deployment of TEC devices due to the conformal and intimate contact they make with the body. Additionally, the hierarchical nature of fabrics as they progress from fiber to yarn to fabric allows the integration of TEC modules directly into the woven structure, thereby creating a more seamless fabric based TEC device.<sup>437,438</sup>

When it comes to integration of TE elements into textiles, research has focused more heavily on power generation from human body heat (via TE generators or TEGs), rather than TE cooling (TEC). TEGs have been implemented into textiles using various materials and substrates such as

PEDOT:PSS/MWCNT/PU coated polyester and cotton yarns,<sup>474,475</sup> PEDOT:PSS coated polyester fabric,<sup>476</sup> PANI/SWCNT composite inducted onto a polyester fabric,<sup>366</sup> electrospun polyacrylonitrile fibers coated with Bi<sub>2</sub>Te<sub>3</sub> and Sb<sub>2</sub>Te<sub>3</sub> and spun into yarns,<sup>327</sup> spun CNT yarn doped with polyethyleneimine (PEI) and FeCl<sub>3</sub> solutions,<sup>446</sup> graphite-PEDOT:PSS composite coated onto polyester fabric,<sup>477</sup> MWCNT/PVDF composite films deposited onto felt fabrics,<sup>441</sup> SWCNT inks doped with poly (acrylic acid) (PAA) and PEI coated onto a flexible bracelet,<sup>478</sup> electrospun MWCNT/CuO/PVP TE fibers,<sup>479</sup> and glass fabric printed with Bi<sub>2</sub>Te<sub>3</sub> and Sb<sub>2</sub>Te<sub>3</sub>.<sup>332</sup> These fiber-based research works in some cases do not translate the coated fibers into conventional 2D fabrics,<sup>474</sup> while others coat commercial fabrics directly which does not provide a seamless integration.<sup>366</sup> While Zheng et al. used MWCNT-based TE yarns used to make a 3D knitted TEG,<sup>437</sup> and Lee et al. coated Sb<sub>2</sub>Te<sub>3</sub> and Bi<sub>2</sub>Te<sub>3</sub> on PAN yarns to make woven TEGs,<sup>327</sup> these are still examples of energy harvesting and not TEC. Lee et al. and Park et al. have demonstrated fabric TECs using inorganic, rigid Bi-Te p and n-type modules arranged in a mat-like fashion with a flexible heat sink composed of solid-state silica gel mixed with hydrogel.<sup>337-339</sup> These devices were able to cool the skin by a temperature drop of 3.8 K,<sup>339</sup> with an improvement to 5.4 K.<sup>338</sup> Kishore et al. also developed high performance, rigid TEC modules composed of commercially available Bi-Te materials which were able to cool the skin by a temperature drop of 8.2 °C below room temperature.<sup>336</sup> In all these instances, the use of rigid semiconducting materials creates an obvious mismatch between the softness of the skin and the rigidity of the TE cooling device, resulting in discomfort for the wearer. Hong et al. demonstrated a flexible TEC without the use of heat sinks by sandwiching inorganic TE pillars between two layers of stretchable elastomers that enhanced the sheets' lateral thermal conductivity, achieving a cooling of > 10 °C.<sup>34</sup> This does not resemble

a textile fabric in any manner, and is rather an assembly of rigid materials within a flexible substrate.

In this work, we explore the integration of p- and n-type TE MWCNT films cut into ribbon yarns that we have previously reported on,<sup>47</sup> into a simple woven fabric configuration with the aim to create a TEC fabric (termed as FabTEC) with distinct heating and cooling zones. We measure the heating and cooling performance of the FabTEC on a 4 cm X 4 cm wrist-worn device and achieve a cooling of 13.3 °C and heating of 3 °C using p-type and n-type thermoelectric MWCNTs as the TE legs, and the p-type MWCNT as the interconnect as well. These materials were selected for their flexibility, relatively high power factors and low thermal conductivities. The p-type and n-type MWCNT films have a thermoelectric figure of merit (ZT) of 0.019 at 300 K. While our heating and cooling performances aren't as high as those previously reported,<sup>34,336</sup> the design of the FabTEC provides an innovative manner of integrating TE elements into a planar woven fabric configuration, without sacrificing the flexibility and conformability of textiles. We also performed geometric and thermoelectric analysis of the FabTEC design to predict the ideal ZT required for various cooling levels, as well as the possible cooling that could be theoretically achieved with the addition of more junctions.

### **3.3.2 Materials and Methods**

#### **3.3.2.1 TE Materials Characterization**

The fabrication and characterization of the n-type and p-type MWCNT films have been extensively detailed in our previous work,<sup>47</sup> and are summarized in **Table S2**. Briefly, a custom-built setup consisting of Peltier cooling and heating devices and a DC power supply were used to provide a

thermal gradient to the n- and p-type films, and this gradient was measured using a Type-K thermal probe. The n-type film was prepared by doping with polyethyleneimine (PEI) and the doping level was optimized to 15 wt.% of PEI, ensuring a high ZT of 0.019. The in-plane thermal conductivities were measured using time-domain thermoreflectance (TDTR), and in-plane electrical conductivities were measured using a 4-probe electrical conductivity measurement setup, ensuring that all three quantities: Seebeck coefficient, electrical conductivity, and thermal conductivity are measured in-plane.<sup>47</sup>

### 3.3.2.2 Junction Fabrication

The single and two junction devices were fabricated in a similar manner; the p-type leg and the n-type leg, both measuring 10 mm X 2 mm with a thickness of 8.4  $\mu\text{m}$  and 9.9  $\mu\text{m}$ , respectively, were connected together electrically using a 6 mm X 2 mm p-type leg as interconnect, as shown in *Figure 24(a)*. This was done to ensure that there would not be a material mismatch between the legs and the interconnect, allowing for better flexibility. Additionally, z-axis tape (3M™ Electrically Conductive Adhesive Transfer Tape 9703) measuring 1 mm X 1 mm with electrical conductivity in the z-direction was used to connect the p-type interconnect with the p-type and n-type legs to ensure low contact resistance and good electrical connection. Copper wire was used to connect the two ends of the junction to a DC power supply (Keithley 2231A-30-3 triple channel DC power supply) and the temperature was measured using a Type-K probe attached to a temperature sensor (Keysight U1272A). Thermal paste was used to ensure that the Type-K probe accurately measured the temperature of the junction. The heating and cooling performance of the junction were achieved by switching the polarity of the device i.e. connecting the p-type leg to the positive terminal and n-type leg to the negative terminal of the power supply in heating mode, and

vice versa in cooling mode. For the dual junction setup, the p-type leg was connected to the positive terminal and n-type leg to the negative terminal, creating a PN and an NP junction, showing heating and cooling performances, respectively. Each reading was repeated three times and the average and standard deviation are reported in the data.

### 3.3.2.3 FabTEC Device Fabrication

The FabTEC woven fabric device (4 cm X 4 cm) was fabricated by cutting transparent polyethylene terephthalate (PET) film of 0.13 mm thickness into 2 mm X 60 mm strips that were used as support yarns, along with 2 mm X 60 mm strips of p-type MWCNT and n-type MWCNT film as the TE yarns, and 2 mm X 60 mm strips of p-type MWCNT film as the interconnect yarn. The PET yarns were first woven in a 1-up 1-down plain weave structure, and subsequently the TE yarns and interconnect yarns were incorporated into the fabric according to the weave of the FabTEC, as shown in **Figure 25(a)**. Six support PET yarns were added in both the warp and the weft directions of the fabric to ensure a more stable fabric structure with the TE and interconnect yarns terminated in a “W” structure as shown in **Figure S34(c)** and (d). Appropriate disconnects were made by cutting the p-type and n-type yarns as well as the interconnects at the desired locations using an X-ACTO® knife, and copper wires were attached to either ends of the FabTEC as well as the DC power supply for applying current. The time-current-temperature measurement was done by holding each current value for 60 seconds and continuously measuring the temperature with the Type-K thermal probe. All measurements were repeated three times and an average value along with standard deviation was reported. In all cases of Peltier effect measurements, the current applied was kept to a minimal for the FabTEC to ensure that there isn't excessive resistive heating, and that the applied current does not exceed unsafe levels.

### 3.3.3 Theory and Calculation

To calculate the geometric effects of the woven FabTEC on its thermoelectric performance, we study the influence of aspect ratio of the TE yarns and junction density on the cooling density of the FabTEC, at various current levels. While many factors can be modeled, we believe these are the most important in order to quantify the fabric design. Peirce's flexible thread model was used to calculate the projected area ( $A_p$ ) of the fabric, as shown in **Figure S34** and **Section I** of supplementary information.<sup>529,530</sup> This derivation was then combined with the thermoelectric equations,<sup>336</sup> as discussed in **Section II** of the supplementary information, to obtain the cooling density formula as **Equation 1**.

*Equation 1:*

$$\text{Cooling Density} = \frac{\{n\alpha T_c I - \frac{I^2 R_{elec-TEC}}{2} - \frac{(T_h - T_c)}{R_{therm-TEC}}\}}{[12[(d_1 + d_2) \sin \theta + \{l_2 - (d_1 + d_2)\theta\} \cos \theta] + 6[l_2 \cos \theta + d_2(\sin \theta - \theta \cos \theta) + 0.5(d_1 + d_3)(\sin \theta - \theta \cos \theta)]] X [12[(d_1 + d_3) \sin \theta + \{l_1 - (d_1 + d_3)\theta\} \cos \theta] + 6[l_1 \cos \theta + d_3(\sin \theta - \theta \cos \theta) + 0.5(d_1 + d_2)(\sin \theta - \theta \cos \theta)]]}$$

Additionally, we consider three cases for junction density (defined as the number of junctions per square meter of FabTEC): (i) 1666 junctions/m<sup>2</sup>, (ii) 6666 junctions/m<sup>2</sup>, and (iii) 18518 junctions/m<sup>2</sup>, as shown in **Section IV** of supplementary information.

### 3.3.4 Results and Discussion

#### 3.3.4.1 Single and Two Junction Characterization

As previously stated, we have reported the TE characterization of our materials has been previously reported,<sup>47</sup> as well as summarized in Table S2. Following the materials characterization, we conducted the temperature characterization of a single and double junction composed of p-type

MWCNT, n-type MWCNT and another p-type MWCNT used as the interconnect. We used the p-type MWCNT as the interconnect itself since it has a high electrical conductivity ( $\sim 10^5$  S/m) and can be easily attached to the p-type and n-type MWCNT legs of the junction using the Z-axis electrically conductive tape. It also ensures that there isn't a materials mismatch between the TE legs and the interconnect material being used. Figure 24 illustrates the fabrication of the single, as shown in Figure 24(a) and Figure 24(b), and two junction planar TE device, as shown in Figure 24(c). We selected the single and two junction planar devices as a means to characterize the initial performance of the TE materials for heating and cooling before we incorporate them into a fabric structure.

We used the p-type MWCNT as the interconnect itself since it has high electrical conductivity ( $\sim 10^5$  S/m) and prevents a mismatch in materials, allowing for a more seamless TE device, especially when integrating into fabric. Additionally, we also used Z-axis tape, as shown in Figure 24(a), to enable a more conductive and robust connection between the p-type and n-type legs and the interconnect. Once connected to the DC power supply, we observe that the single junction device achieves a cooling of  $20.6$  °C at  $9$  mA current, with room temperature at  $21.0$  °C, as shown in Figure 24(d) resulting in a  $0.4$  °C cooling thermal gradient, as shown in Figure 24(e). This is not a very high cooling gradient, but it does achieve this without the need for any heat sinks. After the device achieves its maximum cooling, the temperature starts rising again and continues to rise till it goes above room temperature. This is attributed to the effect of resistive heating that exceeds the thermoelectric cooling. Since this is just a single junction, the resistive heating rapidly exceeds the thermoelectric cooling, and hence the cooling is limited to  $0.4$  °C. From the voltage-current graph

of the single junction, we observed an overall resistance of  $80.24 \pm 3.75 \Omega$ , which contributes to the resistive heating of the device above 12 mA current.

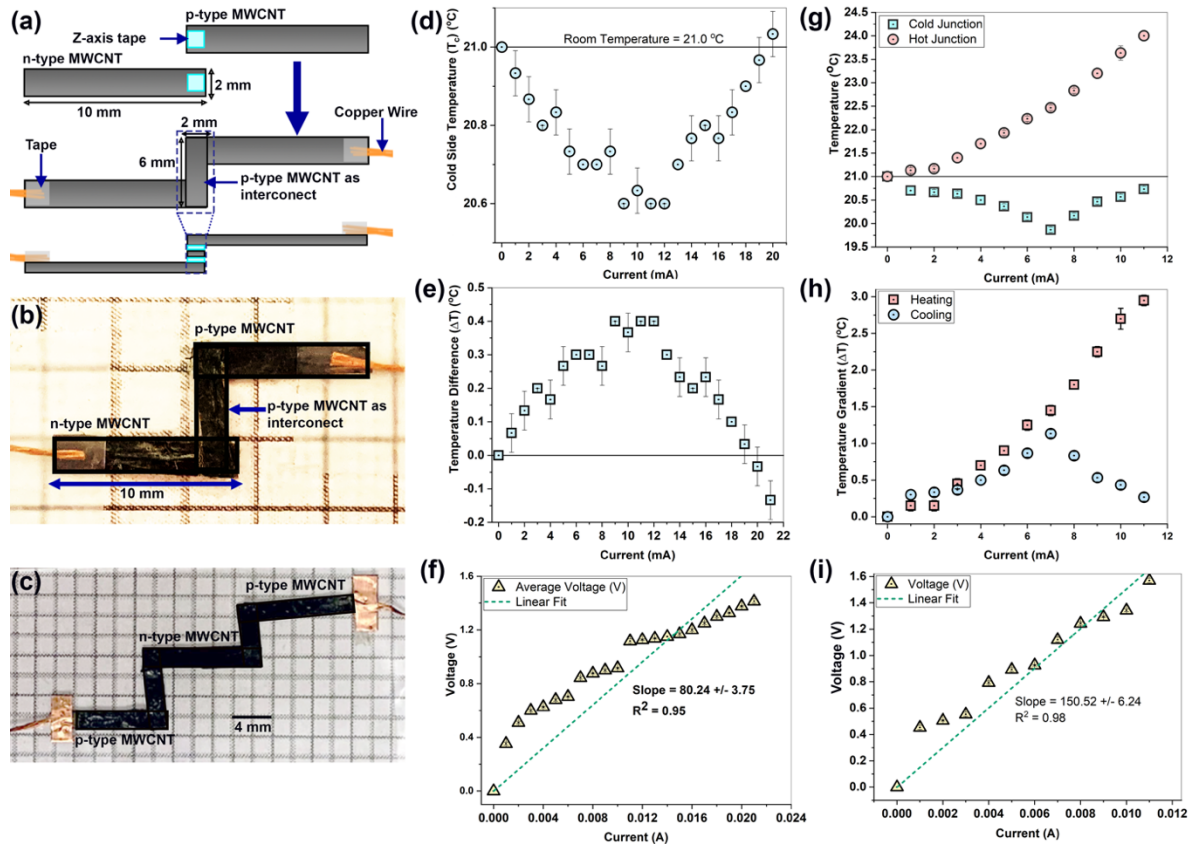


**Figure 24:** Fabrication and characterization of single and double junction MWCNT devices. (a) The p-type and n-type MWCNT TE legs are cut into 10 mm X 2 mm strips with 1 mm X 1 mm Z-axis tape (shown in blue) attached to the ends. The p-type MWCNT interconnect is placed on the tape and attached firmly, with the copper wire being used as connectors to the power supply. (b) Single junction configuration. (c) Two junction configuration with the legs connected as p-type MWCNT, n-type MWCNT and p-type MWCNT, forming a PN and an NP junction. Copper tape was used to secure the copper wire to form a more robust connection. (d) Cooling by the single junction shown in (b). (e) The average cooling gradient achieved by the single junction in (b) is further highlighted to show a cooling of 0.4 °C. (f) Voltage-current graph obtained from the DC power supply connected to the single junction shows that the device has an overall resistance of  $80.24 \pm 3.75 \Omega$ . (g) Heating and cooling above and below room temperature, respectively for the two junction setup shown in (c). (h) Thermal gradient achieved by the two junction setup shows a cooling of 1.1 °C and heating of 3 °C below and above room temperature, respectively. (i) Voltage-current graph obtained from DC power supply connected to the two junction system in (c) shows an overall resistance of  $150.52 \pm 6.24 \Omega$  of the system.

To reduce the contact resistance of the device, we use ethanol treatment at the interconnection points along with Z-axis tape, enabling a higher degree of cooling in the two junction system. The setup of the two junction device is such that there is a PN junction and an NP junction, which when connected in series to the DC power supply, create a heating and a cooling junction depending on the polarity of the two ends. It achieves a cooling of 19.9 °C, going 1.1 °C below room temperature at 7 mA current, as shown in **Figure 24(g)** and **Figure 24(h)**. In terms of heating performance, due to the additive effect of resistive heating the two junction setup goes up to 24 °C, 3°C above room temperature. Since the resistive heating keeps increasing with the current, we stop the experiment once no more cooling is observed. Due to the ZT of our materials, we are also limited in terms of the total cooling that we can achieve, but we expect materials with higher ZT to have a better performance. Nevertheless, the 1.1 °C of cooling is significant for a device that does not have any bulky heat sinks and does not sacrifice flexibility or require special packaging or processing steps.

#### **3.3.4.2 Fabric TEC Characterization**

Since the materials perform well in terms of cooling and heating, we integrated them into a woven fabric configuration, termed as FabTEC (fabric TEC), shown in **Figure 25**. It is important to understand the structure of the FabTEC as shown in **Figure 25(a)**: the plain woven fabric consists of warp (up and down) and weft (left to right) direction yarns. The p-type (indicated by orange in **Figure 25(a)**) and n-type (indicated by green in **Figure 25(b)**) yarns are in the weft direction whereas the interconnect p-type (indicated by yellow in **Figure 25(a)**) is in the warp direction. The grey and black yarns in the weft and warp direction, respectively, are treated as support yarns to hold the fabric and TE yarns in place. The symmetric placement of physical disconnects (indicated by the red crosses in **Figure 25(a)**) ensures that the path of the electric current is in a ladder-like manner

(indicated by blue arrows in **Figure 25(a)**), going from the p-type yarn, through the interconnect, to the next n-type yarn. The placement of the interconnect is such that one junction is laying on the top surface of the fabric (away from the skin) and the next junction is laying on the bottom surface of the fabric (towards the skin). In this manner, the heating junction will be facing outwards, whereas the cooling junction is in contact with the skin, to ensure that the waste heat is released to the environment and not towards the skin.

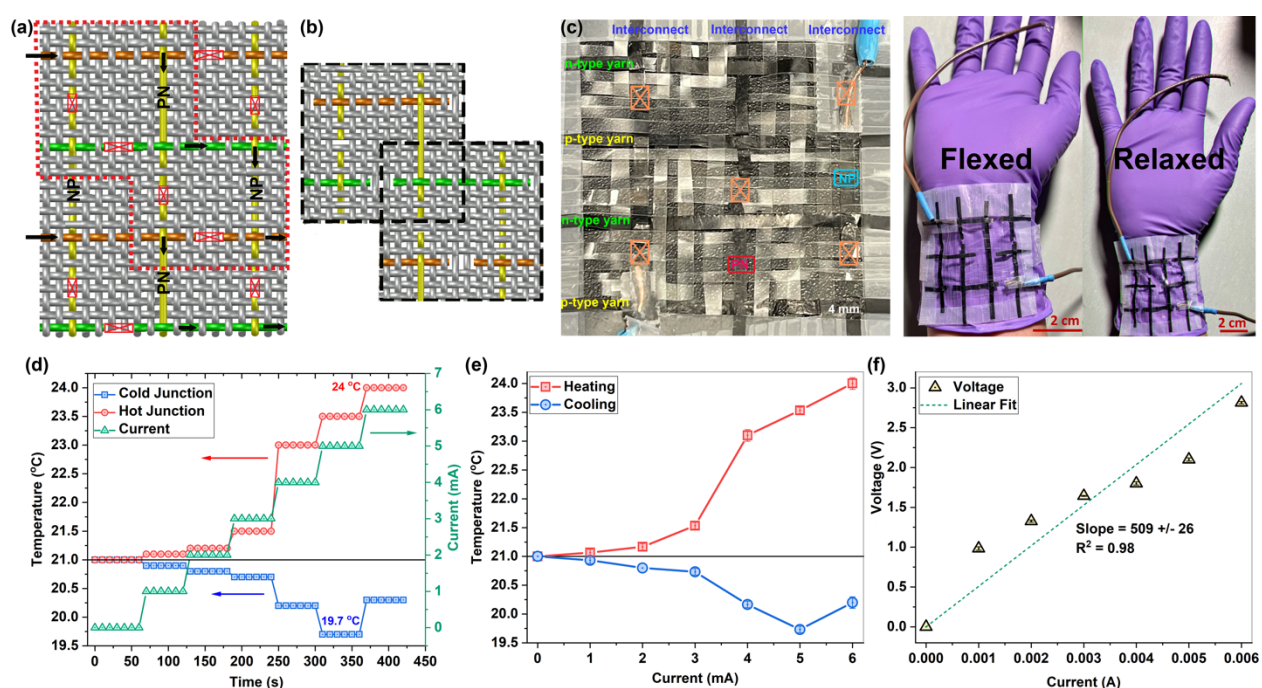


**Figure 25:** (a) Overall proposed FabTEC design with the grey and black yarns as the support yarns, yellow yarns as the interconnect, and the green and orange yarns as n-type and p-type yarns, respectively. The yarns are physically disconnected as indicated by the red crosses. The path of current is illustrated by the blue arrows. The repeat unit of the fabric is illustrated in the red box and (b). (c) The representative unit highlighted in (b) is fabricated into a woven configuration with transparent PET as support yarns and n- and p-type MWCNT films as flat yarns and interconnects. Disconnects are illustrated with red crosses. The 4 cm X 4 cm FabTEC demonstration fabric can be mounted on the wrist as shown on the right, with the ability to flex with the body. (d) Heating and cooling performance of the FabTEC as a function of time. Each current value is held for 60 seconds, and the experiment is stopped when the cold junction starts heating. The maximum cooling is 1.3 °C below room temperature (21 °C) and heating is 3 °C above room temperature. (e) Heating and cooling performances as a function of the applied current. (d) The voltage-current graph of the FabTEC shows an overall resistance of  $509 \pm 26 \Omega$ .

It is also important to understand that there are two different repeat units within this fabric design: (i) the repeat unit of having two TE yarns with one interconnect, which we term as the TE repeat, and (ii) the repeat unit with one junction towards the skin and one away from the skin, which we term as the design repeat. These, shown in **Figure 25(b)**, help define the unique symmetry of the fabric, with six support yarns in the warp and weft directions each and three TE yarns per two interconnects. This design repeat is replicated experimentally, see **Figure 25(c)** with transparent PET yarns and for demonstration purposes is placed on the wrist to show its flexibility as the wrist moves from a flexed to a relaxed state.

The cooling and heating performance of this FabTEC design repeat is shown in **Figure 25(d)**, (e). In **Figure 25(d)**, each current value is held for 60 seconds, and the resultant hot and cold junction temperatures are recorded, providing a maximum cooling of 1.3 °C below room temperature. The heating achieved was 3 °C, but the experiment was stopped once the temperature of the cooling junction started increasing. The Peltier cooling power of the device was calculated to be 0.162 mW, with a cooling density of 0.101 W/m<sup>2</sup> for the single cooling junction at 5 mA current. The variation of heating and cooling with current is shown in **Figure 25(e)**, demonstrating that measurable thermal gradients are achievable at safe current levels for this fabric. The overall resistance of the FabTEC demonstration device was measured to be  $509 \pm 26 \Omega$ , attributed to the contact resistance between the connecting wires and the fabric, as well as contact resistances between the interconnects and the p-type and n-type yarns. Nevertheless, we were able to achieve a cooling performance of > 1 °C, which is significant for indoor thermal comfort and adjustment of setpoint for HVAC systems.<sup>55,480,481</sup>

### 3.3.4.3 FabTEC Modeling

An important aspect of modeling is to understand the correlation between the ZT of TE materials, and their cooling performance. While the materials we use have a ZT of 0.019, materials with higher ZT would result in more enhanced cooling. Nevertheless, it is important to consider not just the ZT of TE materials but also their room temperature stability, processability, strength, conformability and ease of handling. Considering all of these factors, MWCNT films perform relatively well for creating cooling and heating zones in the fabric without the need for bulky heat sinks. We modeled the impact of increasing  $\sigma$  and S (resulting in an increased overall ZT of the TE materials) on the cooling density provided by the FabTEC design, as shown in **Figure 26**.

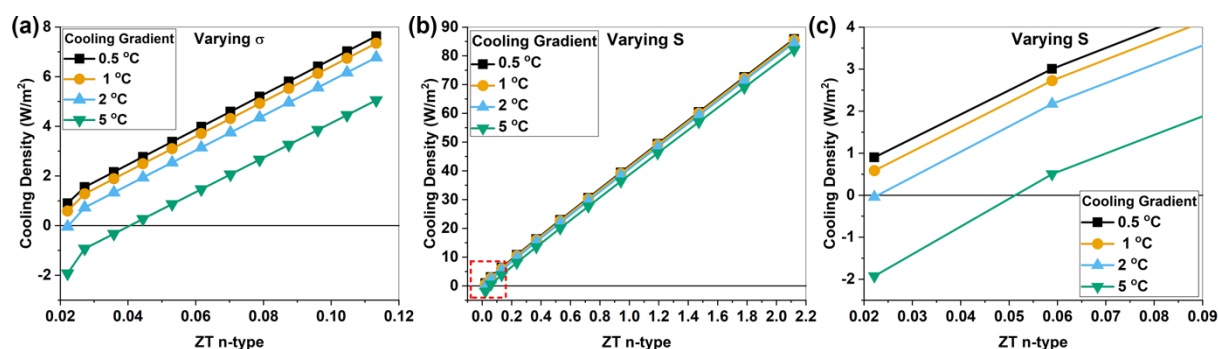


**Figure 26:** Variation in ZT of TE materials and resultant cooling density at different cooling gradients. (a) The electrical conductivity is increased and resultant ZT and its effect on cooling density is reported. (b) The Seebeck coefficient is increased to result in increasing ZT and resultant cooling density is reported. (c) Graph illustrates the region highlighted by the red, dashed box in (b), showing the region where cooling density is positive (i.e. there is cooling) and where it is negative (i.e. no cooling) at lower values of ZT.

The increase in  $\sigma$  causes a lower increase in ZT than S, which is apparent when considering the ZT equation which is proportional to electrical  $\sigma$  and  $S^2$ . From **Figure 26(a)** we observe that at close to the ZT of our MWCNT materials, the cooling is limited to a maximum of 1 °C, which is approximately the same as what we observe experimentally, as shown in **Figure 25**. For higher

cooling, materials with a higher  $ZT$  are required. Additionally, we see that as the cooling gradient increases, the cooling density decreases, attributed to the fact that at higher cooling gradients the heat transfer within the TEC increases as well. From **Figure 26(b)** we see the larger effect of increasing  $S$  on the resultant cooling density (higher than when increasing only  $\sigma$ ), as well as the reduced cooling density as the cooling gradient is increased, although not as pronounced as in **Figure 26(a)**. Additionally, **Figure 26(c)** shows the area highlighted by the dotted rectangle in **Figure 26(b)** which once again highlights that our MWCNT materials are limited in their cooling due to lower  $ZT$ . From these graphs we can conclude that designing higher  $ZT$  materials would result in greater cooling gradient, however even at lower  $ZT$ s we can still achieve  $0.5\text{ }^{\circ}\text{C} - 2\text{ }^{\circ}\text{C}$  of cooling. This is promising because it can help guide material scientists to predict the  $ZT$  of their materials required for maximizing cooling density in this FabTEC design.

While our materials show limited cooling, they are flexible and easily processable, and hence they merit use in the FabTEC design. Further, we also explore how the design considerations of the FabTEC can influence the heating and cooling performance, including the aspect ratio (AR) of the TE leg in a single junction, i.e. in the single PN or NP junction shown in **Figure 25(b)** and discussed in **Section III** of supplementary information. **Table S3** shows the various values of AR we have considered in the model by varying the total length of the TE yarn in a single junction, while keeping the diameter of the yarns constant as 0.2 mm. The current is fixed at 10 mA so as to isolate the effect of AR on the overall cooling density and cooling of the FabTEC without influence from changing current. The cooling gradient (i.e. the temperature difference between the hot and cold sides) is varied to observe the effect of AR on higher cooling densities as well.

From **Figure 27(a)** we see the expected result that as the AR increases, the  $A_p$  of the FabTEC also increases, since the length of the TE yarns is increasing, thereby affecting the overall projected lengths of the FabTEC. This increasing  $A_p$  influences cooling density as well, as seen in **Figure 27(b)**. With increasing AR the cooling density decreases, attributed to the increasing  $A_p$ . Additionally, with higher cooling gradient the overall cooling density also reduces, attributed to the increase in heat exchange within the TEC as well as increased resistive heating due to longer TE yarns. **Figure 27(c)** shows a zoomed-in version wherein we can more clearly observe the reduction in cooling density with increasing AR, as well as increased cooling gradient. It is also important to understand the influence of AR on the total cooling itself, as shown in **Figure 27(d)**.

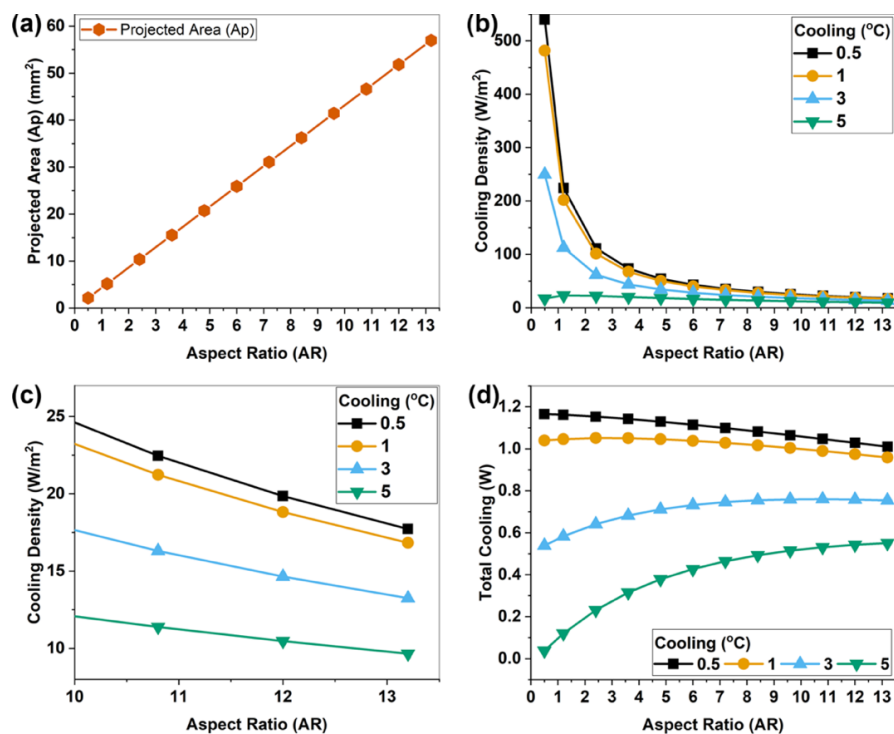


**Figure 27:** Influence of aspect ratio (AR) of the TE leg in each junction on the total cooling and cooling density of the FabTEC. (a) Increase in projected area of FabTEC as AR increases. (b) Decrease in cooling density with increasing AR for various cooling gradients. (c) Zoomed-in version of the graph in (b) which shows in greater detail the reduction in cooling density with increased AR at higher values of AR. (d) Total cooling (not considering the change in  $A_p$ ) as a function of AR.

At lower cooling gradients of 0.5 °C and 1 °C, the resistive heating is higher than the heat transfer within the FabTEC due to the longer TE legs having a greater influence on resistive heating, and the lower cooling gradient keeping the heat transfer term in Equation 1 low. However, as the cooling gradient increases, the heat transfer effect overtakes the resistive heating effect due to greater temperature difference between the hot and cold junctions. Hence, at higher gradients of 3 °C and 5 °C we see that the heat transfer within the TEC is higher than the resistive heating, as shown in **Figure S35**. Additionally, at higher cooling gradients we also observe that the heat transfer decreases with increasing AR, since the thermal resistance of the device is directly proportional to the length of the TE leg. At lower leg lengths the overall thermal resistance of the FabTEC is lower, and hence the overall heat transfer is higher, since it is inversely proportional to the thermal resistance of the device. As the leg length (and AR) increases, the overall device thermal resistance also increases, and hence the heat transfer within the TEC decreases (due to higher resistance faced by the heat to move from the hot to the cold side). This results in lower heat transfer within the TEC at higher ARs. Hence, we see the trend of increased cooling with higher ARs for higher cooling gradient, and decreased cooling with higher ARs for lower cooling gradient. This competing resistive heating and heat transfer effect is hence important, and when designing such a fabric a target cooling gradient has to be identified to determine whether resistive heating has to be minimized or thermal resistance of the device has to be increased. These effects are highlighted in Figure S35 of the supplementary information as well.

Finally, we also took into account the influence of junction density and the theoretical cooling possible with a large FabTEC array with conventional ends per inch and picks per inch values ranging from 30-120 ends and picks per inch, usually encountered in textile fabrics. **Section IV** of

supplementary information shows that the three cases we can consider: 1200 ends and picks per meter, 2400 ends and picks per meter and 4000 ends and picks per meter of FabTEC result in 1666 junctions/m<sup>2</sup>, 6666 junctions/m<sup>2</sup> and 18518 junctions/m<sup>2</sup> of FabTEC. Using these junctions, we modeled the maximum possible cooling, as shown in **Figure 28**.

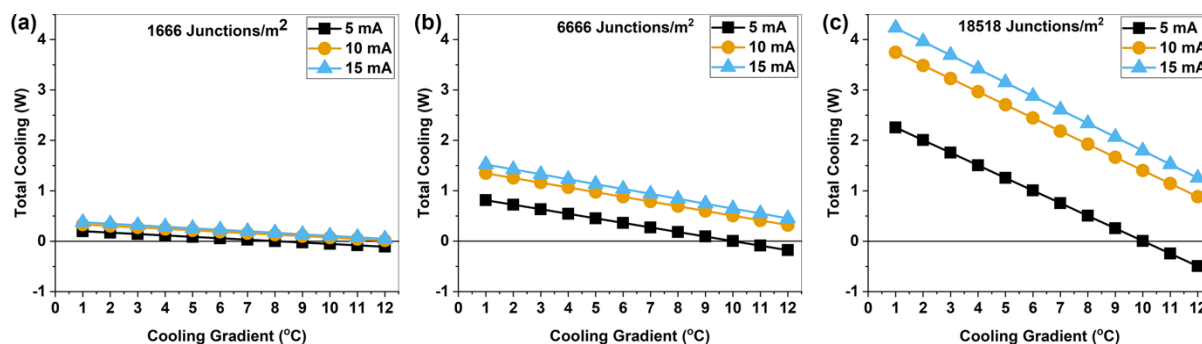


**Figure 28:** Junction density and its influence on the overall cooling achieved by FabTEC at various current levels. Total cooling for (a) 1666 junctions/m<sup>2</sup> (30 ends/picks per inch), (b) 6666 junctions/m<sup>2</sup> (60 ends/picks per inch) and (c) 18518 junctions/m<sup>2</sup> (100 ends/picks per inch) of FabTEC.

Expectedly, at higher junction densities, the total cooling of the FabTEC is higher due to increased Peltier cooling. Additionally, as the current is increased the total cooling also increases due to Peltier cooling being directly proportional to the amount of current applied to the device. With increasing cooling gradient, the amount of cooling decreases due to the increased thermal heat exchange between the hot and cold junctions. This model does show that higher cooling gradients are possible at the ZT of our materials with a larger fabric array and denser junction distribution. It is important to note that these junction densities are modeled for fabrics in the 30 – 120 ends per inch and picks per inch range, which is typically encountered in textile fabrics, and with modern fabric weaving capabilities, such a fabric would be possible to manufacture on current weaving machines. At lower current value of 5 mA, we see that the cooling is limited to 8 °C for 1666 junctions/m<sup>2</sup> of FabTEC, see **Figure 28** (a), whereas it increases to 10 °C for 6666 junctions/m<sup>2</sup>

and 18518 junctions/m<sup>2</sup>, as shown in **Figure 28** (b) and (c), respectively. This is attributed to lower Peltier cooling at lower current values, increased resistive heating at higher levels of current, as well as increased thermal transfer at higher cooling gradients. From **Figure S36**, **Figure S37**, **Figure S38** we can see the dominant effect of heat transfer at lower currents and resistive heating at higher currents on the overall cooling of the FabTEC at different junction densities. Nevertheless, higher current does allow for enough of a Peltier cooling effect to overcome the resistive heating and parasitic heat transfer, which isn't possible at lower current and lower junction density.

#### **3.3.4.4 Separation of Junctions via Fabric Weave Design**

In order to manage the waste heat generated in the FabTEC device, we propose a design that would allow taking advantage of the weave geometry of the fabric to further push the interconnects towards and away from the central plane of the fabric, to allow for better dissipation of waste heat to the atmosphere when the cooling side of the FabTEC is towards the skin. This could be achieved in a number of methods, including:

- (i) Using higher stiffness yarns such as auxetic yarns,<sup>531</sup> that push the interconnect junctions out of the plane of the fabric, creating a separation between the junctions.
- (ii) Increasing the yarn diameters to increase the weave angle, resulting in greater separation between the hot and cold sides. This would, however, also influence the overall electrical conductivity of the yarns, which may result in lower TE effect.
- (iii) Changing the crimp in specific yarns that support the junction such that it is almost eliminated, resulting in an increase in the separation between hot and cold sides. This is further explained in **Figure 29**.<sup>532</sup>

To achieve a change in crimp, we consider the two junctions in Boxes A and B that are on the top face of the fabric in case of Box A, and on the bottom face of the fabric in case of Box B, as shown in **Figure 29** (a). With the intention to separate these two junctions, we can consider the method of decreasing the crimp in the weft direction yarns that the junctions go over and under, respectively as shown in **Figure 29** (b). By increasing the crimp, there would be an increase in the amount that the junction yarn is pushed down (Box B) closer to the skin and pushed up (Box A) away from the skin, thereby increasing the separation between the hot and cold sides of the junction. Hence, when looking at the fabric cross-section, one can see the separation between the two junctions over and under the plane of the fabric, as shown in **Figure 29** (c).

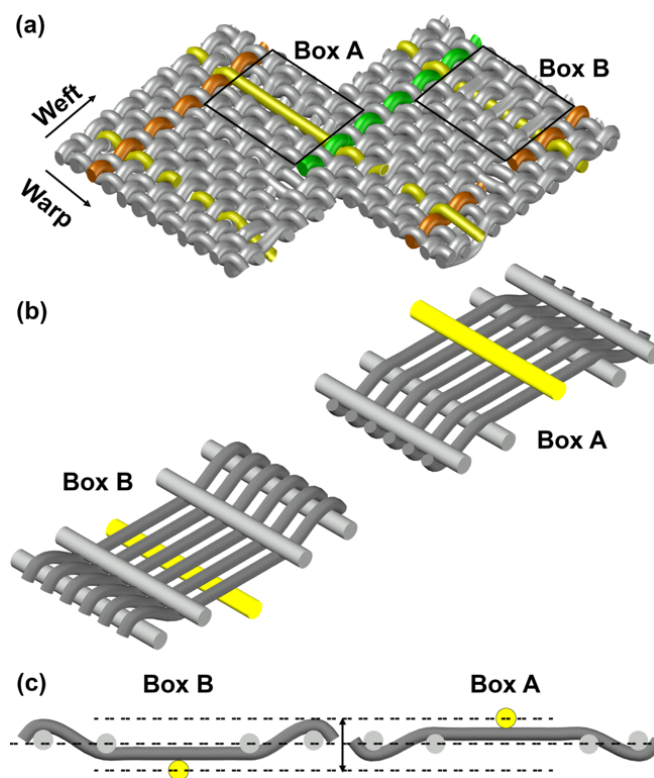


**Figure 29:** Thermal management weave design for separation hot and cold junctions. (a) Repeat unit with two junctions on the face and back of FabTEC. (b) Proposed design that reduces crimp and imparts greater separation to the two junctions. (c) Junction separation as seen from the front view of the modified FabTEC.

While we have not shown an implementation of this design, it is important to consider such aspects when designing a woven fabric FabTEC, as the fabric design itself will be able to provide solutions to separation of the heating and cooling junctions, without adding additional thermal conductivity or electrical resistance to the design.

### 3.3.5 Conclusions

In this work, characterized the cooling performance of a single and two-junction TEC composed of MWCNTs, achieving a resultant cooling of 0.4 °C and 1.1 °C, respectively. These were then integrated into a flexible, woven configuration to form the FabTEC design akin to a woven textile fabric, with programmed disconnects to ensure that the heating and cooling junctions are separated. In such a configuration, we were able to achieve a cooling of 1.3 °C without the need for bulky heat sinks or sacrificing the flexibility of the materials. While this was not a high amount of cooling, it is still significant because of the form factor of the FabTEC. It is also important to note that humans can perceive temperature changes of 0.02 – 0.07 °C of cooling, and 0.03 – 0.09 °C of warming pulses.<sup>480</sup> The rate of temperature change is also important, with humans capable of detecting temperature changes if they happen more rapidly such as at 0.1 °C/s compared to 0.5 °C/minute.<sup>480,481</sup> Hence, even a small change in temperature can result in perceived thermal comfort, especially when the wearer is sedentary and indoors. Additionally, while the cooling was limited by the ZT of our materials, in the future more promising TE materials with flexibility and conformability would ensure that this design would enable greater cooling.

Additionally, we also modeled the behavior of the FabTEC design when the AR, ZT and junction density are varied. We found that AR and junction density have a significant impact on the overall

cooling density of the FabTEC, and that by taking into consideration the AR of the TE legs, we can minimize parasitic heat loss in large area TECs. Additionally, higher ZT would also result in higher cooling gradients. These modeling results are promising because they provide a tool to integrate textile geometry with TE performance to optimize cooling density without the need for bulky heat sinks or rigid materials.

Additionally, the inclusion of a design criterion to reduce crimp in the fabric and thereby separate the heating and cooling junctions more efficiently provides an outlook for how these fabrics can be more efficiently designed. These results also suggest that FabTEC modules would be advantageous for next-to-skin heating and cooling where a low cooling density is required over a larger, conformable and flexible area where heat sinks might be incompatible. The facile fabrication method of our MWCNT materials suggests that such a FabTEC design could lead to future applications where next-to-skin heating/cooling devices can enable energy savings by leading to an increase in air conditioning setpoint.

## ASSOCIATED CONTENT

### **Supporting Information – Appendix B**

Projected area calculation; Thermoelectric Equations; FabTEC Modeling Assumptions and Data; Peltier Cooling, Resistive Heating, and Heat Transfer Within the TEC as a Function of the AR for Various Cooling Gradients; Junction Density Calculation; Peltier cooling, resistive heating and heat transfer within the FabTEC for 1666 junctions/m<sup>2</sup> density; Peltier cooling, resistive heating and heat transfer within the FabTEC for 6666 junctions/m<sup>2</sup> density; Peltier cooling, resistive heating and heat transfer within the FabTEC for 18518 junctions/m<sup>2</sup> density.

#### 4. CONCLUSIONS AND FUTURE OUTLOOK

The aim of this work was to develop an understanding of the exiting research in the field of smart, wearable and textile-based personal thermal comfort systems to move heating and cooling away from the built environment to the space next-to-skin. We started with a broad look at the research and development of active and passive thermal comfort systems, including phase change materials that can provide both heating and cooling, passive heating textiles that can provide warmth to the body due to their unique geometry and/or material properties, passive cooling textiles that can directionally move heat away from the body, allow better wicking of sweat, or allow better transfer of radiative heat away from the body. Additionally, active thermal comfort systems such as Joule heating fabrics that rely on resistive heating to provide warmth, and thermoelectric fabrics that can reversibly heat or cool due to the Peltier effect were also discussed. Amongst all of these, thermoelectric fabrics seem to be a promising avenue for the deployment of next-to-skin thermal comfort systems due to their ability to provide reversible heating/cooling, and the myriad different materials available to develop flexible TE devices.

We began with efforts to identify materials that would be appropriate for fabric-based TE cooling/heating systems and identified p-type MWCNTs and n-type PEI doped MWCNTs as the best candidate materials that satisfy our specific requirements of having relatively high TE performance, room temperature and solution processability, flexibility, strength, and non-reactivity. We reported some of the highest ZTs of these MWCNT materials, both p-type and n-type, as 0.019 by evaluating all three transport properties – Seebeck coefficient, electrical conductivity, and thermal conductivity – in the same direction using in-plane thermal conductivity measurements, which are not often reported for TE materials. Then, we integrated these materials

into a FabTEC design, resulting in a prototype fabric that could provide up to 1.3 °C of cooling, 3 °C of heating, and a resultant 0.101 W/m<sup>2</sup> cooling density, all within a small current of 6 mA. We further analyzed the woven fabric geometry to optimize the theoretical design of FabTEC and arrived on the conclusion that higher ZT, combined with lower aspect ratio (length/diameter) of the TE yarns, as well as higher junction density would be important factors in maximizing the cooling density of the fabric. Additionally, we also proposed a design route that would allow for greater separation of the hot and cold sides of the fabric by reducing the crimp the thermal management yarns that support the interconnecting junctions, thereby pushing them further away from the plane of the fabric.

This work presented here provides an important toolbox for the evaluation of TE fabrics, combining TE concepts with woven fabric geometry to enable researchers to develop high efficiency TE designs that do not compromise on the strength, flexibility, conformability, and inherent comfort of the woven textile fabric. It is also important to note that by preserving the textile geometry, we can further optimize it to aid the TE performance, without the need for extremely efficient materials, since all of our modeling has used the TE properties of our MWCNT materials.

The outlook of this research provides for many areas of that could be explored for future work including:

- i. Development of higher efficiency TE materials that are room temperature processable, flexible, strong, and air-stable to achieve greater levels of heating and cooling

- ii. Using the various woven fabric designs to integrate TE modules into. While this work only explores the plain-woven design as the proof-of-concept, other promising specialty woven structures with combinations of interlacement patterns, yarn sizes, and yarn crimp should be also investigated.
- iii. Transport and release of the waste heat such that it could be reused back in the system, which would require a method of storing the waste heat and then releasing it at a different time. Such a system could be made by incorporating PCMs, however currently such a method would result in additionally bulk in the fabric. Hence, with the development of lighter heat storage materials, more efficient waste heat management would be possible.

Finally, as it has previously been stated, there is a dire need to move heating and cooling away from built environments due to the undue energy requirements of HVAC systems. Textiles such as FabTEC provide a way to achieve indoor personal thermal comfort, especially in sedentary environments such as offices and homes. This would also bridge the gender, age, and metabolism gap that causes humans to experience thermal comfort at different temperatures, by providing a personalized mechanism to experience thermal satisfaction without relying on a common HVAC setpoint.

## 5. REFERENCES

- (1) Profile, M. I. *Global Energy Consumption*; 2018; Vol. 2019.
- (2) Agency, I. E. *The Future of Cooling: Opportunities for Energy-Efficient Air Conditioning*; OECD/International Energy Agency, 2018; pp 11–88.
- (3) Hoyt, T.; Lee, K. H.; Zhang, H.; Arens, E.; Webster, T. Energy Savings from Extended Air Temperature Setpoints and Reductions in Room Air Mixing. In *THE 13th INTERNATIONAL CONFERENCE ON ENVIRONMENTAL ERGONOMICS*; Indoor Environmental Quality; Center for the Built Environment, UC Berkeley: Boston, USA, 2009.
- (4) Karjalainen, S. Gender Differences in Thermal Comfort and Use of Thermostats in Everyday Thermal Environments. *Build. Environ.* **2007**, *42* (4), 1594–1603. <https://doi.org/10.1016/j.buildenv.2006.01.009>.
- (5) Indraganti, M.; Rao, K. D. Effect of Age, Gender, Economic Group and Tenure on Thermal Comfort: A Field Study in Residential Buildings in Hot and Dry Climate with Seasonal Variations. *Energy Build.* **2010**, *42* (3), 273–281. <https://doi.org/10.1016/j.enbuild.2009.09.003>.
- (6) Höpfe, P. Different Aspects of Assessing Indoor and Outdoor Thermal Comfort. *Energy Build.* **2002**, *34* (6), 661–665. [https://doi.org/10.1016/S0378-7788\(02\)00017-8](https://doi.org/10.1016/S0378-7788(02)00017-8).
- (7) Chatterjee, K.; Ghosh, T. K. 3D Printing of Textiles: Potential Roadmap to Printing with Fibers. *Adv. Mater.* **2019**, *32* (4), 1902086. <https://doi.org/10.1002/adma.201902086>.
- (8) Tabor, J.; Chatterjee, K.; Ghosh, T. K. Smart Textile-Based Personal Thermal Comfort Systems: Current Status and Potential Solutions. *Adv. Mater. Technol.* **2020**, *5* (5), 1901155. <https://doi.org/10.1002/admt.201901155>.
- (9) Mondal, S. Phase Change Materials for Smart Textiles: An Overview. *Appl. Therm. Eng.* **2008**, *28* (11), 1536–1550. <https://doi.org/10.1016/j.applthermaleng.2007.08.009>.
- (10) Li, W.; Ma, Y.; Tang, X.; Jiang, N.; Zhang, R.; Han, N.; Zhang, X. Composition and Characterization of Thermoregulated Fiber Containing Acrylic-Based Copolymer Microencapsulated Phase-Change Materials (MicroPCMs). *Ind. Eng. Chem. Res.* **2014**, *53* (13), 5413–5420. <https://doi.org/10.1021/ie404174a>.
- (11) Zhang, X.; Wang, X.; Tao, X.; Yick, K. Energy Storage Polymer/MicroPCMs Blended Chips and Thermo-Regulated Fibers. *J. Mater. Sci.* **2005**, *40* (14), 3729–3734. <https://doi.org/10.1007/s10853-005-3314-8>.
- (12) Chen, C.; Wang, L.; Huang, Y. Morphology and Thermal Properties of Electrospun Fatty Acids/Polyethylene Terephthalate Composite Fibers as Novel Form-Stable Phase Change Materials. *Sol. Energy Mater. Sol. Cells* **2008**, *92* (11), 1382–1387. <https://doi.org/10.1016/j.solmat.2008.05.013>.
- (13) Gao, C.; Kuklane, K.; Holmér, I. Cooling Vests with Phase Change Materials: The Effects of Melting Temperature on Heat Strain Alleviation in an Extremely Hot Environment. *Eur. J. Appl. Physiol.* **2011**, *111* (6), 1207–1216. <https://doi.org/10.1007/s00421-010-1748-4>.
- (14) Morris, M. A. Thermal Insulation of Single and Multiple Layers of Fabrics. *Text. Res. J.* **1955**, *25* (9), 766–773. <https://doi.org/10.1177/004051755502500904>.
- (15) Watkins, S. M. *Clothing: The Portable Environment*; Ames : Iowa State University Press, c1995: Ames, Iowa, 1995.

- (16) Cui, Y.; Gong, H.; Wang, Y.; Li, D.; Bai, H. A Thermally Insulating Textile Inspired by Polar Bear Hair. *Adv. Mater.* **2018**, *30* (14), 1706807. <https://doi.org/10.1002/adma.201706807>.
- (17) Das, A.; Ishtiaque, S. M. Comfort Characteristics of Fabrics Containing Twist-Less and Hollow Fibrous Assemblies in Weft. *J. Text. Appar. Technol. Manag.* **2004**, *3* (4), 1–7.
- (18) Miao, D.; Huang, Z.; Wang, X.; Yu, J.; Ding, B. Continuous, Spontaneous, and Directional Water Transport in the Trilayered Fibrous Membranes for Functional Moisture Wicking Textiles. *Small* **2018**, *14* (32), e1801527. <https://doi.org/10.1002/smll.201801527>.
- (19) Cai, L.; Song, A. Y.; Li, W.; Hsu, P.-C.; Lin, D.; Catrysse, P. B.; Liu, Y.; Peng, Y.; Chen, J.; Wang, H.; Xu, J.; Yang, A.; Fan, S.; Cui, Y. Spectrally Selective Nanocomposite Textile for Outdoor Personal Cooling. *Adv. Mater.* **2018**, *30* (35), 1802152. <https://doi.org/10.1002/adma.201802152>.
- (20) Peng, Y.; Chen, J.; Song, A. Y.; Catrysse, P. B.; Hsu, P.-C.; Cai, L.; Liu, B.; Zhu, Y.; Zhou, G.; Wu, D. S.; Lee, H. R.; Fan, S.; Cui, Y. Nanoporous Polyethylene Microfibres for Large-Scale Radiative Cooling Fabric. *Nat. Sustain.* **2018**, *1* (2), 105–112. <https://doi.org/10.1038/s41893-018-0023-2>.
- (21) Sarier, N.; Onder, E. Organic Phase Change Materials and Their Textile Applications: An Overview. *Thermochim. Acta* **2012**, *540*, 7–60. <https://doi.org/10.1016/j.tca.2012.04.013>.
- (22) Cao, H.; Branson, D. H.; Peksoz, S.; Nam, J.; Farr, C. A. Fabric Selection for a Liquid Cooling Garment. *Text. Res. J.* **2006**, *76* (7), 587–595. <https://doi.org/10.1177/0040517506067375>.
- (23) Kayacan, Ö.; Kurbak, A. Effect of Garment Design on Liquid Cooling Garments. *Text. Res. J.* **2010**, *80* (14), 1442–1455. <https://doi.org/10.1177/0040517509358800>.
- (24) Kotagama, P.; Phadnis, A.; Manning, K. C.; Rykaczewski, K. Rational Design of Soft, Thermally Conductive Composite Liquid-Cooled Tubes for Enhanced Personal, Robotics, and Wearable Electronics Cooling. *Adv. Mater. Technol.* **2019**, *4* (7), 1800690. <https://doi.org/10.1002/admt.201800690>.
- (25) Flouris, A.; Cheung, S. Design and Control Optimization of Microclimate Liquid Cooling Systems Underneath Protective Clothing. *Ann. Biomed. Eng.* **2006**, *34* (3), 359–372. <https://doi.org/10.1007/s10439-005-9061-9>.
- (26) Ma, R.; Zhang, Z.; Tong, K.; Huber, D.; Kornbluh, R.; Ju, Y. S.; Pei, Q. Highly Efficient Electrocaloric Cooling with Electrostatic Actuation. *Science* **2017**, *357* (6356), 1130–1134. <https://doi.org/10.1126/science.aan5980>.
- (27) Zhang, G.; Zhang, X.; Huang, H.; Wang, J.; Li, Q.; Chen, L.-Q.; Wang, Q. Toward Wearable Cooling Devices: Highly Flexible Electrocaloric Ba<sub>0.67</sub>Sr<sub>0.33</sub>TiO<sub>3</sub> Nanowire Arrays. *Adv. Mater.* **2016**, *28* (24), 4811–4816. <https://doi.org/10.1002/adma.201506118>.
- (28) Zhang, G.; Li, Q.; Gu, H.; Jiang, S.; Han, K.; Gadinski, M. R.; Haque, M. A.; Zhang, Q.; Wang, Q. Ferroelectric Polymer Nanocomposites for Room-Temperature Electrocaloric Refrigeration. *Adv. Mater.* **2015**, *27* (8), 1450–1454. <https://doi.org/10.1002/adma.201404591>.
- (29) Tishin, A. M.; Spichkin, Y. I.; Zverev, V. I.; Egolf, P. W. A Review and New Perspectives for the Magnetocaloric Effect: New Materials and Local Heating and Cooling inside the Human Body. *Int. J. Refrig.* **2016**, *68*, 177–186. <https://doi.org/10.1016/j.ijrefrig.2016.04.020>.
- (30) Fähler, S.; Rößler, U. K.; Kastner, O.; Eckert, J.; Eggeler, G.; Emmerich, H.; Entel, P.; Müller, S.; Quandt, E.; Albe, K. Caloric Effects in Ferriic Materials: New Concepts for

- Cooling. *Adv. Eng. Mater.* **2012**, *14* (1–2), 10–19.  
<https://doi.org/10.1002/adem.201100178>.
- (31) Moya, X.; Hueso, L. E.; Maccherozzi, F.; Tovstolytkin, A. I.; Podyalovskii, D. I.; Ducati, C.; Phillips, L. C.; Ghidini, M.; Hovorka, O.; Berger, A.; Vickers, M. E.; Defay, E.; Dhessi, S. S.; Mathur, N. D. Giant and Reversible Extrinsic Magnetocaloric Effects in La<sub>0.7</sub>Ca<sub>0.3</sub>MnO<sub>3</sub> Films Due to Strain. *Nat. Mater.* **2013**, *12* (1), 52–58.  
<https://doi.org/10.1038/nmat3463>.
- (32) Zhu, H.; Xiao, C.; Cheng, H.; Grote, F.; Zhang, X.; Yao, T.; Li, Z.; Wang, C.; Wei, S.; Lei, Y.; Xie, Y. Magnetocaloric Effects in a Freestanding and Flexible Graphene-Based Superlattice Synthesized with a Spatially Confined Reaction. *Nat. Commun.* **2014**, *5* (1), 3960. <https://doi.org/10.1038/ncomms4960>.
- (33) He, W.; Zhang, X.; Zhang, G.; Ji, J.; Li, G.; Zhao, X. Recent Development and Application of Thermoelectric Generator and Cooler. *Appl. Energy* **2015**, *143*, 1–25.  
<https://doi.org/10.1016/j.apenergy.2014.12.075>.
- (34) Hong, S.; Gu, Y.; Seo, J. K.; Wang, J.; Liu, P.; Meng, Y. S.; Xu, S.; Chen, R. Wearable Thermoelectrics for Personalized Thermoregulation. *Sci. Adv.* **2019**, *5* (5), eaaw0536.  
<https://doi.org/10.1126/sciadv.aaw0536>.
- (35) Lu, Z.; Layani, M.; Zhao, X.; Tan, L. P.; Sun, T.; Fan, S.; Yan, Q.; Magdassi, S.; Hng, H. H. Fabrication of Flexible Thermoelectric Thin Film Devices by Inkjet Printing. *Small* **2014**, *10* (17), 3551–3554. <https://doi.org/10.1002/sml.201303126>.
- (36) Li, X.; Mahmoud, S.; Al-Dadah, R. K.; Elsayed, A. Thermoelectric Cooling Device Integrated with PCM Heat Storage for MS Patients. *Energy Procedia* **2014**, *61*, 2399–2402. <https://doi.org/10.1016/j.egypro.2014.12.014>.
- (37) Kim, S. H.; Min, T.; Choi, J. W.; Choi, J.-P.; Baek, S. H.; Aranas, C. Ternary Bi<sub>2</sub>Te<sub>3</sub>In<sub>2</sub>Te<sub>3</sub>Ga<sub>2</sub>Te<sub>3</sub> (n-Type) Thermoelectric Film on a Flexible PET Substrate for Use in Wearables. *Energy* **2018**, *144*, 607–618. <https://doi.org/10.1016/j.energy.2017.12.063>.
- (38) Hsu, P.-C.; Liu, X.; Liu, C.; Xie, X.; Lee, H. R.; Welch, A. J.; Zhao, T.; Cui, Y. Personal Thermal Management by Metallic Nanowire-Coated Textile. *Nano Lett.* **2015**, *15* (1), 365–371. <https://doi.org/10.1021/nl5036572>.
- (39) Guo, Y.; Dun, C.; Xu, J.; Mu, J.; Li, P.; Gu, L.; Hou, C.; Hewitt, C. A.; Zhang, Q.; Li, Y.; Carroll, D. L.; Wang, H. Ultrathin, Washable, and Large-Area Graphene Papers for Personal Thermal Management. *Small* **2017**, *13* (44), 1702645.  
<https://doi.org/10.1002/sml.201702645>.
- (40) Ilanchezhyan, P.; Zakirov, A. S.; Kumar, G. M.; Yuldashev, S. U.; Cho, H. D.; Kang, T. W.; Mamadalimov, A. T. Highly Efficient CNT Functionalized Cotton Fabrics for Flexible/Wearable Heating Applications. *RSC Adv.* **2015**, *5* (14), 10697–10702.  
<https://doi.org/10.1039/C4RA10667A>.
- (41) Jung, D.; Kim, D.; Lee, G. S.; Lee, K. H.; Overzet, L. J. Transparent Film Heaters Using Multi-Walled Carbon Nanotube Sheets. *Sens. Actuators Phys.* **2013**, *199*, 176–180.  
<https://doi.org/10.1016/j.sna.2013.05.024>.
- (42) Fischer, T.; Rühling, J.; Wetzold, N.; Zillger, T.; Weissbach, T.; Göschel, T.; Würfel, M.; Hübner, A.; Kroll, L. Roll-to-roll Printed Carbon Nanotubes on Textile Substrates as a Heating Layer in Fiber-reinforced Epoxy Composites. *J. Appl. Polym. Sci.* **2018**, *135* (10), 4595-n/a. <https://doi.org/10.1002/app.45950>.

- (43) Yeon, C.; Kim, G.; Lim, J. W.; Yun, S. J. Highly Conductive PEDOT:PSS Treated by Sodium Dodecyl Sulfate for Stretchable Fabric Heaters. *RSC Adv.* **2017**, *7* (10), 5888–5897. <https://doi.org/10.1039/C6RA24749K>.
- (44) Bhat, N. V.; Seshadri, D. T.; Nate, M. M.; Gore, A. V. Development of Conductive Cotton Fabrics for Heating Devices. *J. Appl. Polym. Sci.* **2006**, *102* (5), 4690–4695. <https://doi.org/10.1002/app.24708>.
- (45) Shahariar, H.; Kim, I.; Soewardiman, H.; Jur, J. S. Inkjet Printing of Reactive Silver Ink on Textiles. *ACS Appl. Mater. Interfaces* **2019**, *11* (6), 6208–6216. <https://doi.org/10.1021/acsami.8b18231>.
- (46) Qian, S.; Nasuta, D.; Rhoads, A.; Wang, Y.; Geng, Y.; Hwang, Y.; Radermacher, R.; Takeuchi, I. Not-in-Kind Cooling Technologies: A Quantitative Comparison of Refrigerants and System Performance. *Int. J. Refrig.* **2016**, *62* (C), 177–192. <https://doi.org/10.1016/j.ijrefrig.2015.10.019>.
- (47) Chatterjee, K.; Negi, A.; Kim, K. H.; Liu, J.; Ghosh, T. K. In-Plane Thermoelectric Properties of Flexible and Room Temperature Processable Doped Carbon Nanotube Films. *ACS Appl. Energy Mater.* **2020**, *3* (7), 6929–6936. <https://doi.org/10.1021/acsam.0c00995>.
- (48) Agency, I. E. *Technology Roadmap: Energy Efficient Building Envelopes*; 2013; Vol. 2019.
- (49) Amasyali, K.; El-Gohary, N. M. A Review of Data-Driven Building Energy Consumption Prediction Studies. *Renew. Sustain. Energy Rev.* **2018**, *81* (1), 1192–1205. <https://doi.org/10.1016/j.rser.2017.04.095>.
- (50) Lam, J. C.; Wan, K. K. W.; Tsang, C. L.; Yang, L. Building Energy Efficiency in Different Climates. *Energy Convers. Manag.* **2008**, *49* (8), 2354–2366. <https://doi.org/10.1016/j.enconman.2008.01.013>.
- (51) Huo, T.; Ren, H.; Zhang, X.; Cai, W.; Feng, W.; Zhou, N.; Wang, X. China's Energy Consumption in the Building Sector: A Statistical Yearbook-Energy Balance Sheet Based Splitting Method. *J. Clean. Prod.* **2018**, *185*, 665–679. <https://doi.org/10.1016/j.jclepro.2018.02.283>.
- (52) Berardi, U. A Cross-Country Comparison of the Building Energy Consumptions and Their Trends. *Resour. Conserv. Recycl.* **2017**, *123*, 230–241. <https://doi.org/10.1016/j.resconrec.2016.03.014>.
- (53) Ürge-Vorsatz, D.; Cabeza, L. F.; Serrano, S.; Barreneche, C.; Petrichenko, K. Heating and Cooling Energy Trends and Drivers in Buildings. *Renew. Sustain. Energy Rev.* **2015**, *41*, 85–98. <https://doi.org/10.1016/j.rser.2014.08.039>.
- (54) Urge-Vorsatz, D.; Petrichenko, K.; Staniec, M.; Eom, J. Energy Use in Buildings in a Long-Term Perspective. *Curr. Opin. Environ. Sustain.* **2013**, *5* (2), 141–151. <https://doi.org/10.1016/j.cosust.2013.05.004>.
- (55) Hoyt, T.; Arens, E.; Zhang, H. Extending Air Temperature Setpoints: Simulated Energy Savings and Design Considerations for New and Retrofit Buildings. *Build. Environ.* **2015**, *88*, 89–96. <https://doi.org/10.1016/j.buildenv.2014.09.010>.
- (56) Gao, C.; Kuklane, K.; Wang, F.; Holmér, I. Personal Cooling with Phase Change Materials to Improve Thermal Comfort from a Heat Wave Perspective. *Indoor Air* **2012**, *22* (6), 523–530. <https://doi.org/10.1111/j.1600-0668.2012.00778.x>.
- (57) Lan, L.; Wargocki, P.; Lian, Z. Quantitative Measurement of Productivity Loss Due to Thermal Discomfort. *Energy Build.* **2011**, *43* (5), 1057–1062. <https://doi.org/10.1016/j.enbuild.2010.09.001>.

- (58) Zhang, M.; Wang, C.; Liang, X.; Yin, Z.; Xia, K.; Wang, H.; Jian, M.; Zhang, Y. Weft-Knitted Fabric for a Highly Stretchable and Low-Voltage Wearable Heater. *Adv. Electron. Mater.* **2017**, *3* (9), 170019-n/a. <https://doi.org/10.1002/aelm.201700193>.
- (59) Kang, J.; Jang, Y.; Kim, Y.; Cho, S.-H.; Suhr, J.; Hong, B. H.; Choi, J.-B.; Byun, D. An Ag-Grid/Graphene Hybrid Structure for Large-Scale, Transparent, Flexible Heaters. *Nanoscale* **2015**, *7* (15), 6567–6573. <https://doi.org/10.1039/C4NR06984F>.
- (60) Guo, Y.; Li, K.; Hou, C.; Li, Y.; Zhang, Q.; Wang, H. Fluoroalkylsilane-Modified Textile-Based Personal Energy Management Device for Multifunctional Wearable Applications. *ACS Appl. Mater. Interfaces* **2016**, *8* (7), 4676–4683. <https://doi.org/10.1021/acsami.5b11622>.
- (61) Zhang, T.; Zhang, J.; Zhang, N.; Li, K.; Chen, M.; Wang, Z.; Ma, S.; Wei, L. High-Performance, Flexible, and Ultralong Crystalline Thermoelectric Fibers. *Nano Energy* **2017**, *41*, 35–42. <https://doi.org/10.1016/j.nanoen.2017.09.019>.
- (62) Zhao, D.; Lu, X.; Fan, J.; Fan, T.; Wu, Y. S.; Lou, L.; Wang, Q.; Yang, R. Personal Thermal Management Using Portable Thermoelectrics for Potential Building Energy Saving. *Appl. Energy* **2018**, *218* (C), 282–291. <https://doi.org/10.1016/j.apenergy.2018.02.158>.
- (63) Chen, P.; Xu, Y.; He, S.; Sun, X.; Pan, S.; Deng, J.; Chen, D.; Peng, H. Hierarchically Arranged Helical Fibre Actuators Driven by Solvents and Vapours. *Nat. Nanotechnol.* **2015**, *10* (12), 1077–1083. <https://doi.org/10.1038/nnano.2015.198>.
- (64) He, S.; Chen, P.; Qiu, L.; Wang, B.; Sun, X.; Xu, Y.; Peng, H. A Mechanically Actuating Carbon-Nanotube Fiber in Response to Water and Moisture. *Angew. Chem.* **2015**, *54* (49), 14880–14884. <https://doi.org/10.1002/anie.201507108>.
- (65) Gong, J.; Lin, H.; Dunlop, J. W. C.; Yuan, J. Hierarchically Arranged Helical Fiber Actuators Derived from Commercial Cloth. *Adv. Mater.* **2017**, *29* (16), 160510-n/a. <https://doi.org/10.1002/adma.201605103>.
- (66) Merati, A. A. Application of Stimuli-Sensitive Materials in Smart Textiles; ul-Islam, S., Butola, B. S., Eds.; Advanced Textile Engineering Materials; John Wiley & Sons, Inc: Hoboken, NJ, USA, 2018; pp 1–29. <https://doi.org/10.1002/9781119488101.ch1>.
- (67) Jia, T.; Wang, Y.; Dou, Y.; Li, Y.; Andrade, M. J. de; Wang, R.; Fang, S.; Li, J.; Yu, Z.; Qiao, R.; Liu, Z.; Cheng, Y.; Su, Y.; Minary-Jolandan, M.; Baughman, R. H.; Qian, D.; Liu, Z. Moisture Sensitive Smart Yarns and Textiles from Self-Balanced Silk Fiber Muscles. *Adv. Funct. Mater.* **2019**, 1808241. <https://doi.org/10.1002/adfm.201808241>.
- (68) Hsu, P.-C.; Liu, C.; Song, A. Y.; Zhang, Z.; Peng, Y.; Xie, J.; Liu, K.; Wu, C.-L.; Catrysse, P. B.; Cai, L.; Zhai, S.; Majumdar, A.; Fan, S.; Cui, Y. A Dual-Mode Textile for Human Body Radiative Heating and Cooling. *Sci. Adv.* **2017**, *3* (11), e1700895. <https://doi.org/10.1126/sciadv.1700895>.
- (69) Hsu, P.-C.; Song, A. Y.; Catrysse, P. B.; Liu, C.; Peng, Y.; Xie, J.; Fan, S.; Cui, Y. Radiative Human Body Cooling by Nanoporous Polyethylene Textile. *Science* **2016**, *353* (6303), 1019–1023. <https://doi.org/10.1126/science.aaf5471>.
- (70) Tong, J. K.; Huang, X.; Boriskina, S. V.; Loomis, J.; Xu, Y.; Chen, G. Infrared-Transparent Visible-Opaque Fabrics for Wearable Personal Thermal Management. *ACS Photonics* **2015**, *2* (6), 769–778. <https://doi.org/10.1021/acsp Photonics.5b00140>.
- (71) Xu, Y.; Kraemer, D.; Song, B.; Jiang, Z.; Zhou, J.; Loomis, J.; Wang, J.; Li, M.; Ghasemi, H.; Huang, X.; Li, X.; Chen, G. Nanostructured Polymer Films with Metal-like Thermal

- Conductivity. *Nat. Commun.* **2019**, *10* (1), 1–8. <https://doi.org/10.1038/s41467-019-09697-7>.
- (72) Henry, A.; Shen, S.; Zheng, R.; Chen, G.; Tong, J. Polyethylene Nanofibres with Very High Thermal Conductivities. *Nat. Nanotechnol.* **2010**, *5* (4), 251–255. <https://doi.org/10.1038/nnano.2010.27>.
- (73) Shim, H.; McCullough, E. A.; Jones, B. W. Using Phase Change Materials in Clothing. *Text. Res. J.* **2001**, *71* (6), 495–502. <https://doi.org/10.1177/004051750107100605>.
- (74) Matusiak, M. Investigation of the Thermal Insulation Properties of Multilayer Textiles. *FIBERS Text. East. Eur.* **2006**, *14* (5 (59)), 98–102. <https://doi.org/10.1155/2016/1726475>.
- (75) Gao, J.; Yu, W.; Pan, N. Structures and Properties of the Goose Down as a Material for Thermal Insulation. *Text. Res. J.* **2007**, *77* (8), 617–626. <https://doi.org/10.1177/0040517507079408>.
- (76) Zhong, Y.; Zhang, F.; Wang, M.; Gardner, C. J.; Kim, G.; Liu, Y.; Leng, J.; Jin, S.; Chen, R. Reversible Humidity Sensitive Clothing for Personal Thermoregulation. *Sci. Rep.* **2017**, *7* (1), 44208. <https://doi.org/10.1038/srep44208>.
- (77) Salaün, F.; Devaux, E.; Bourbigot, S.; Rumeau, P. Thermoregulating Response of Cotton Fabric Containing Microencapsulated Phase Change Materials. *Thermochim. Acta* **2010**, *506* (1), 82–93. <https://doi.org/10.1016/j.tca.2010.04.020>.
- (78) Wang, X.; Huang, Z.; Miao, D.; Zhao, J.; Yu, J.; Ding, B. Biomimetic Fibrous Murray Membranes with Ultrafast Water Transport and Evaporation for Smart Moisture Wicking Fabrics. *ACS Nano* **2018**, *13* (2), 1060–1070. <https://doi.org/10.1021/acsnano.8b08242>.
- (79) Zhou, H.; Wang, H.; Niu, H.; Zeng, C.; Zhao, Y.; Xu, Z.; Fu, S.; Lin, T. One-Way Water-Transport Cotton Fabrics with Enhanced Cooling Effect. *Adv. Mater. Interfaces* **2016**, *3* (17), 1600283. <https://doi.org/10.1002/admi.201600283>.
- (80) Babar, A. A.; Wang, X.; Iqbal, N.; Yu, J.; Ding, B. Tailoring Differential Moisture Transfer Performance of Nonwoven/Polyacrylonitrile-SiO<sub>2</sub> Nanofiber Composite Membranes. *Adv. Mater. Interfaces* **2017**, *4* (15), 1700062. <https://doi.org/10.1002/admi.201700062>.
- (81) Zhao, Y.; Zheng, Y.; Tian, X.; Jiang, L.; Nie, F.-Q.; Huang, Z.; Zhai, J.; Bai, H. Directional Water Collection on Wetted Spider Silk. *Nature* **2010**, *463* (7281), 640–643. <https://doi.org/10.1038/nature08729>.
- (82) Majumdar, A.; Mukhopadhyay, S.; Yadav, R. Thermal Properties of Knitted Fabrics Made from Cotton and Regenerated Bamboo Cellulosic Fibres. *Int. J. Therm. Sci.* **2010**, *49* (10), 2042–2048. <https://doi.org/10.1016/j.ijthermalsci.2010.05.017>.
- (83) Gao, T.; Yang, Z.; Chen, C.; Li, Y.; Fu, K.; Dai, J.; Hitz, E. M.; Xie, H.; Liu, B.; Song, J.; Yang, B.; Hu, L. Three-Dimensional Printed Thermal Regulation Textiles. *ACS Nano* **2017**, *11* (11), 11513–11520. <https://doi.org/10.1021/acsnano.7b06295>.
- (84) Cheng, H.; Liu, J.; Zhao, Y.; Hu, C.; Zhang, Z.; Chen, N.; Jiang, L.; Qu, L. Graphene Fibers with Predetermined Deformation as Moisture-Triggered Actuators and Robots. *Angew. Chem. Int. Ed.* **2013**, *52* (40), 10482–10486. <https://doi.org/10.1002/anie.201304358>.
- (85) Cho, J. W.; Jung, Y. C.; Chun, B. C.; Chung, Y.-C. Water Vapor Permeability and Mechanical Properties of Fabrics Coated with Shape-memory Polyurethane. *J. Appl. Polym. Sci.* **2004**, *92* (5), 2812–2816. <https://doi.org/10.1002/app.20322>.
- (86) Emile, O.; Floch, A. L.; Vollrath, F. Shape Memory in Spider Draglines. *Nature* **2006**, *440* (7084), 621. <https://doi.org/10.1038/440621a>.

- (87) Ji, F.; Zhu, Y.; Hu, J.; Liu, Y.; Yeung, L.-Y.; Ye, G. Smart Polymer Fibers with Shape Memory Effect. *Smart Mater. Struct.* **2006**, *15* (6), 1547–1554. <https://doi.org/10.1088/0964-1726/15/6/006>.
- (88) Pakdel, E.; Naebe, M.; Sun, L.; Wang, X. Advanced Functional Fibrous Materials for Enhanced Thermoregulating Performance. *ACS Appl. Mater. Interfaces* **2019**, *11* (14), 13039–13057. <https://doi.org/10.1021/acsami.8b19067>.
- (89) Mohamed, S. A.; Al-Sulaiman, F. A.; Ibrahim, N. I.; Zahir, M. H.; Al-Ahmed, A.; Saidur, R.; Yılbaş, B. S.; Sahin, A. Z. A Review on Current Status and Challenges of Inorganic Phase Change Materials for Thermal Energy Storage Systems. *Renew. Sustain. Energy Rev.* **2017**, *70*, 1072–1089. <https://doi.org/10.1016/j.rser.2016.12.012>.
- (90) Shaid, A.; Wang, L.; Islam, S.; Cai, J. Y.; Padhye, R. Preparation of Aerogel-Eicosane Microparticles for Thermoregulatory Coating on Textile. *Appl. Therm. Eng.* **2016**, *107*, 602–611. <https://doi.org/10.1016/j.applthermaleng.2016.06.187>.
- (91) Sarbu, I.; Sebarchievici, C. A Comprehensive Review of Thermal Energy Storage. *MDPI Sustain.* **2018**, *10* (191), 1–32. <https://doi.org/10.3390/su10010191>.
- (92) Pielichowska, K.; Pielichowski, K. *Phase Change Materials for Thermal Energy Storage*; 2014; Vol. 65. <https://doi.org/10.1016/j.pmatsci.2014.03.005>.
- (93) Rathod, M. K.; Banerjee, J. Thermal Stability of Phase Change Materials Used in Latent Heat Energy Storage Systems: A Review. *Renew. Sustain. Energy Rev.* **2013**, *18*, 246–258. <https://doi.org/10.1016/j.rser.2012.10.022>.
- (94) Huang, X.; Alva, G.; Jia, Y.; Fang, G. Morphological Characterization and Applications of Phase Change Materials in Thermal Energy Storage: A Review. *Renew. Sustain. Energy Rev.* **2017**, *72*, 128–145. <https://doi.org/10.1016/j.rser.2017.01.048>.
- (95) Fallahi, A.; Guldentops, G.; Tao, M.; Granados-Focil, S.; Dessel, S. V. Review on Solid-Solid Phase Change Materials for Thermal Energy Storage: Molecular Structure and Thermal Properties. *Appl. Therm. Eng.* **2017**, *127*, 1427–1441. <https://doi.org/10.1016/j.applthermaleng.2017.08.161>.
- (96) Faird, M. M.; Khudhair, A. M.; Razack, S. A. K.; Al-Hallaj, S. A Review on Phase Change Energy Storage: Materials and Applications. *Energy Convers. Manag.* **2004**, *45* (9), 1597–1615.
- (97) Zhang, X.-X.; Wang, X.-C.; Tao, X.-M.; Yick, K.-L. Structures and Properties of Wet Spun Thermo-Regulated Polyacrylonitrile-Vinylidene Chloride Fibers. *Text. Res. J.* **2006**, *76* (5), 351–359. <https://doi.org/10.1177/0040517506061959>.
- (98) Xu, W.; Lu, Y.; Wang, B.; Xu, J.; Ye, G.; Jiang, M. Preparation and Characterization of High Latent Heat Thermal Regulating Fiber Made of PVA and Paraffin. *J. Eng. Fibers Fabr.* **2013**, *8* (2), 155892501300800. <https://doi.org/10.1177/155892501300800205>.
- (99) Mengjin, J.; Xiaoqing, S.; Jianjun, X.; Guandong, Y. Preparation of a New Thermal Regulating Fiber Based on PVA and Paraffin. *Sol. Energy Mater. Sol. Cells* **2008**, *92* (12), 1657–1660. <https://doi.org/10.1016/j.solmat.2008.07.018>.
- (100) Gao, X.; Han, N.; Zhang, X.; Yu, W. Melt-Processable Acrylonitrile–Methyl Acrylate Copolymers and Melt-Spun Fibers Containing MicroPCMs. *J. Mater. Sci.* **2009**, *44* (21), 5877–5884. <https://doi.org/10.1007/s10853-009-3830-z>.
- (101) Hu, J.; Yu, H.; Chen, Y.; Zhu, M. Study on Phase-Change Characteristics of PET-PEG Copolymers. *J. Macromol. Sci. Part B* **2006**, *45* (4), 615–621. <https://doi.org/10.1080/00222340600770210>.

- (102) Iqbal, K.; Sun, D. Development of Thermal Stable Multifilament Yarn Containing Micro-Encapsulated Phase Change Materials. *Fibers Polym.* **2015**, *16* (5), 1156–1162. <https://doi.org/10.1007/s12221-015-1156-9>.
- (103) Iqbal, K.; Sun, D. Development of Thermo-Regulating Polypropylene Fibre Containing Microencapsulated Phase Change Materials. *Renew. Energy* **2014**, *71*, 473–479. <https://doi.org/10.1016/j.renene.2014.05.063>.
- (104) McCann, J. T.; Marquez, M.; Xia, Y. Melt Coaxial Electrospinning: A Versatile Method for the Encapsulation of Solid Materials and Fabrication of Phase Change Nanofibers. *Nano Lett.* **2006**, *6* (12), 2868–2872. <https://doi.org/10.1021/nl0620839>.
- (105) Chen, C.; Wang, L.; Huang, Y. Crosslinking of the Electrospun Polyethylene Glycol/Cellulose Acetate Composite Fibers as Shape-Stabilized Phase Change Materials. *Mater. Lett.* **2009**, *63* (5), 569–571. <https://doi.org/10.1016/j.matlet.2008.11.033>.
- (106) Chen, C.; Wang, L.; Huang, Y. Ultrafine Electrospun Fibers Based on Stearyl Stearate/Polyethylene Terephthalate Composite as Form Stable Phase Change Materials. *Chem. Eng. J.* **2009**, *150* (1), 269–274. <https://doi.org/10.1016/j.cej.2009.03.007>.
- (107) Lin, J.; Hu, Y.; Dong, J.; Fong, H.; Wei, Q.; Cai, Y.; Huang, F.; Ke, H.; Song, L.; Zhao, Y.; Gao, W. Effects of Nano-SiO<sub>2</sub> on Morphology, Thermal Energy Storage, Thermal Stability, and Combustion Properties of Electrospun Lauric Acid/PET Ultrafine Composite Fibers as Form-Stable Phase Change Materials. *Appl. Energy* **2011**, *88* (6), 2106–2112. <https://doi.org/10.1016/j.apenergy.2010.12.071>.
- (108) Chen, C.; Zhao, Y.; Liu, W. Electrospun Polyethylene Glycol/Cellulose Acetate Phase Change Fibers with Core–Sheath Structure for Thermal Energy Storage. *Renew. Energy* **2013**, *60*, 222–225. <https://doi.org/10.1016/j.renene.2013.05.020>.
- (109) Lu, Y.; Xiao, X.; Fu, J.; Huan, C.; Qi, S.; Zhan, Y.; Zhu, Y.; Xu, G. Novel Smart Textile with Phase Change Materials Encapsulated Core-Sheath Structure Fabricated by Coaxial Electrospinning. *Chem. Eng. J.* **2019**, *355*, 532–539. <https://doi.org/10.1016/j.cej.2018.08.189>.
- (110) Shin, Y.; Yoo, D.-I.; Son, K. Development of Thermoregulating Textile Materials with Microencapsulated Phase Change Materials (PCM). IV. Performance Properties and Hand of Fabrics Treated with PCM Microcapsules. *J. Appl. Polym. Sci.* **2005**, *97* (3), 910–915. <https://doi.org/10.1002/app.21846>.
- (111) Onder, E.; Sarier, N.; Cimen, E. Encapsulation of Phase Change Materials by Complex Coacervation to Improve Thermal Performances of Woven Fabrics. *Thermochim. Acta* **2008**, *467* (1), 63–72. <https://doi.org/10.1016/j.tca.2007.11.007>.
- (112) Sánchez, P.; Sánchez-Fernandez, M. V.; Romero, A.; Rodríguez, J. F.; Sánchez-Silva, L. Development of Thermo-Regulating Textiles Using Paraffin Wax Microcapsules. *Thermochim. Acta* **2010**, *498* (1), 16–21. <https://doi.org/10.1016/j.tca.2009.09.005>.
- (113) Pause, B. Nonwoven Protective Garments with Thermo-Regulating Properties. *J. Ind. Text.* **2003**, *33* (2), 93–99. <https://doi.org/10.1177/152808303038859>.
- (114) You, M.; Zhang, X.; Wang, J.; Wang, X. Polyurethane Foam Containing Microencapsulated Phase-Change Materials with Styrene–Divinylbenzene Co-Polymer Shells. *J. Mater. Sci.* **2009**, *44* (12), 3141–3147. <https://doi.org/10.1007/s10853-009-3418-7>.
- (115) Jin, Z.; Wang, Y.; Liu, J.; Yang, Z. Synthesis and Properties of Paraffin Capsules as Phase Change Materials. *Polymer* **2008**, *49* (12), 2903–2910. <https://doi.org/10.1016/j.polymer.2008.04.030>.

- (116) Rameshkumar, C.; Rengasamy, R. S.; Anbumani, N. Studies on Polyester/Waste Silk Core-Spun Yarns and Fabrics. *J. Ind. Text.* **2009**, *38* (3), 191–203. <https://doi.org/10.1177/1528083708091065>.
- (117) Ramakrishnan, G.; Dhurai, B.; Mukhopadhyay, S. An Investigation into the Properties of Knitted Fabrics Made from Viscose Microfibers. *J. Text. Appar. Technol. Manag.* **2009**, *6* (1), 1–9.
- (118) Gun, A. *Dimensional, Physical and Thermal Comfort Properties of Plain Knitted Fabrics Made from Modal Viscose Yarns Having Microfibers and Conventional Fibers*; 2011; Vol. 12. <https://doi.org/10.1007/s12221-011-0258-2>.
- (119) Erdumlu, N.; Saricam, C. Investigating the Effect of Some Fabric Parameters on the Thermal Comfort Properties of Flat Knitted Acrylic Fabrics for Winter Wear. *Text. Res. J.* **2017**, *87* (11), 1349–1359. <https://doi.org/10.1177/0040517516652347>.
- (120) Oglakcioglu, N.; Marmarali, A. Thermal Comfort Properties of Some Knitted Structures. *FIBERS Text. East. Eur.* **2007**, *15* (5–6), 94–96.
- (121) Asayesh, A.; Talaei, M.; Maroufi, M. The Effect of Weave Pattern on the Thermal Properties of Woven Fabrics. *Int. J. Cloth. Sci. Technol.* **2018**, *30* (4), 525–535. <https://doi.org/10.1108/IJCST-10-2017-0163>.
- (122) Behera, B. K.; Ishtiaque, S. M.; Chand, S. Comfort Properties of Fabrics Woven from Ring-, Rotor-, and Friction-Spun Yarns. *J. Text. Inst.* **1997**, *88* (3), 255–264. <https://doi.org/10.1080/00405009708658549>.
- (123) Slater, K. Comfort Properties of Textiles. *Text. Prog.* **1977**, *9* (4), 1–70.
- (124) Morris, G. J. Thermal Properties of Textile Materials. *J. Text. Inst. Trans.* **1953**, *44* (10), T44–T476.
- (125) Bonser, R.; Dawson, C. The Structural Mechanical Properties of down Feathers and Biomimicking Natural Insulation Materials. *J. Mater. Sci. Lett.* **1999**, *18* (21), 1769–1770. <https://doi.org/1006631328233>.
- (126) Karaca, E.; Kahraman, N.; Meroglu, S.; Becerir, B. Effects of Fiber Cross Sectional Shape and Weave Pattern on Thermal Comfort Properties of Polyester Woven Fabrics. *Fibers Text. East. Eur.* **2012**, *3* (92), 67–72. <https://doi.org/10.1080/00405000.2016.1247616>.
- (127) Rwei, S.-P. Formation of Hollow Fibers in the Melt-spinning Process. *J. Appl. Polym. Sci.* **2001**, *82* (12), 2896–2902. <https://doi.org/10.1002/app.2145>.
- (128) Varshney, R. K.; Kothari, V. K.; Dhamija, S. A Study on Thermophysiological Comfort Properties of Fabrics in Relation to Constituent Fibre Fineness and Cross-Sectional Shapes. *J. Text. Inst.* **2010**, *101* (6), 495–505. <https://doi.org/10.1080/00405000802542184>.
- (129) Sullivan, T. N.; Pissarenko, A.; Herrera, S. A.; Kisailus, D.; Lubarda, V. A.; Meyers, M. A. A Lightweight, Biological Structure with Tailored Stiffness: The Feather Vane. *Acta Biomater.* **2016**, *41* (Journal Article), 27–39. <https://doi.org/10.1016/j.actbio.2016.05.022>.
- (130) Karaca, E.; Ozelik, F. Influence of the Cross-sectional Shape on the Structure and Properties of Polyester Fibers. *J. Appl. Polym. Sci.* **2007**, *103* (4), 2615–2621. <https://doi.org/10.1002/app.25350>.
- (131) Hearle, J. W. S.; Hollick, L.; Wilson, D. K. The Origins of Texturing. In *Yarn texturing technology*; Hearle, J. W. S., Hollick, L., Wilson, D. K., Eds.; Woodhead Publishing Ltd.: Cambridge, England, 2001; pp 1–15.
- (132) Ramachandran, T.; Manonmani, G.; Vigneswaran, C. Thermal Behaviour of Ring- and Compact-Spun Yarn Single Jersey, Rib and Interlock Knitted Fabrics. *Indian J. Fibre Text. Res.* **2010**, *35* (3), 250–257.

- (133) Shaikh, T. N.; Bhattacharya, S. S. Mechanical Crimp Texturizing: A Novel Concept. *Text. Res. J.* **2010**, *80* (6), 483–486. <https://doi.org/10.1177/0040517509339223>.
- (134) Hosseini, S. A. R.; Valizadeh, M. Properties of Fibers and Fabrics That Contribute to Human Comfort; Song, G., Ed.; *Improving Comfort in Clothing*; Woodhead Publishing Series in Textiles, Woodhead Publishing: Oxford, 2011; pp 61–78.
- (135) Zhao, N.; Wang, Z.; Cai, C.; Shen, H.; Liang, F.; Wang, D.; Wang, C.; Zhu, T.; Guo, J.; Wang, Y.; Liu, X.; Duan, C.; Wang, H.; Mao, Y.; Jia, X.; Dong, H.; Zhang, X.; Xu, J. Bioinspired Materials: From Low to High Dimensional Structure. *Adv. Mater.* **2014**, *26* (41), 6994–7017. <https://doi.org/10.1002/adma.201401718>.
- (136) Koon, D. W. Is Polar Bear Hair Fiber Optic? *Appl. Opt.* **1998**, *37* (15), 3198. <https://doi.org/10.1364/AO.37.003198>.
- (137) Stegmaier, T.; Linke, M.; Planck, H. Bionics in Textiles: Flexible and Translucent Thermal Insulations for Solar Thermal Applications. *Philos. Trans. R. Soc. Math. Phys. Eng. Sci.* **2009**, *367* (1894), 1749–1758. <https://doi.org/10.1098/rsta.2009.0019>.
- (138) Dawson, C.; Vincent, J. F. V.; Jeronimidis, G.; Rice, G.; Forshaw, P. Heat Transfer through Penguin Feathers. *J. Theor. Biol.* **1999**, *199* (3), 291–295. <https://doi.org/10.1006/jtbi.1999.0959>.
- (139) Tao, P.; Shang, W.; Song, C.; Shen, Q.; Zhang, F.; Luo, Z.; Yi, N.; Zhang, D.; Deng, T. Bioinspired Engineering of Thermal Materials. *Adv. Mater.* **2015**, *27* (3), 428–463. <https://doi.org/10.1002/adma.201401449>.
- (140) Du, N.; Fan, J.; Wu, H.; Chen, S.; Liu, Y. An Improved Model of Heat Transfer through Penguin Feathers and Down. *J. Theor. Biol.* **2007**, *248* (4), 727–735. <https://doi.org/10.1016/j.jtbi.2007.06.020>.
- (141) Ancel, A.; Gilbert, C.; Poulin, N.; Beaulieu, M.; Thierry, B. New Insights into the Huddling Dynamics of Emperor Penguins. *Anim. Behav.* **2015**, *110*, 91–98. <https://doi.org/10.1016/j.anbehav.2015.09.019>.
- (142) Chen, H.; Di, J.; Wang, N.; Dong, H.; Wu, J.; Zhao, Y.; Yu, J.; Jiang, L. Fabrication of Hierarchically Porous Inorganic Nanofibers by a General Microemulsion Electrospinning Approach. *Small* **2011**, *7* (13), 1779–1783. <https://doi.org/10.1002/smll.201002376>.
- (143) Zhao, Y.; Cao, X.; Jiang, L. Bio-Mimic Multichannel Microtubes by a Facile Method. *J. Am. Chem. Soc.* **2007**, *129* (4), 764–765. <https://doi.org/10.1021/ja068165g>.
- (144) Chen, H.; Wang, N.; Di, J.; Zhao, Y.; Song, Y.; Jiang, L. Nanowire-in-Microtube Structured Core/Shell Fibers via Multifluidic Coaxial Electrospinning. *Langmuir* **2010**, *26* (13), 11291–11296. <https://doi.org/10.1021/la100611f>.
- (145) Wang, T.; Kong, S.; Jia, Y.; Chang, L.; Wong, C.; Xiong, D. Synthesis and Thermal Conductivities of the Biomorphic Al<sub>2</sub>O<sub>3</sub> Fibers Derived from Silk Template. *Int. J. Appl. Ceram. Technol.* **2013**, *10* (2), 285–292. <https://doi.org/10.1111/j.1744-7402.2012.02841.x>.
- (146) Dong, Q.; Su, H.; Zhang, D. In Situ Depositing Silver Nanoclusters on Silk Fibroin Fibers Supports by a Novel Biotemplate Redox Technique at Room Temperature. *J Phys Chem B* **2005**, *109* (37), 17429–17434. <https://doi.org/10.1021/jp052826z>.
- (147) Xiao, G.; Huang, X.; Liao, X.; Shi, B. One-Pot Facile Synthesis of Cerium-Doped TiO<sub>2</sub> Mesoporous Nanofibers Using Collagen Fiber As the Biotemplate and Its Application in Visible Light Photocatalysis. *J. Phys. Chem. C* **2013**, *117* (19), 9739–9746. <https://doi.org/10.1021/jp312013m>.

- (148) Frutiger, A.; Muth, J. T.; Vogt, D. M.; Mengüç, Y.; Campo, A.; Valentine, A. D.; Walsh, C. J.; Lewis, J. A. Capacitive Soft Strain Sensors via Multicore–Shell Fiber Printing. *Adv. Mater.* **2015**, *27* (15), 2440–2446. <https://doi.org/10.1002/adma.201500072>.
- (149) Yeo, M.; Lee, J.-S.; Chun, W.; Kim, G. H. An Innovative Collagen-Based Cell-Printing Method for Obtaining Human Adipose Stem Cell-Laden Structures Consisting of Core–Sheath Structures for Tissue Engineering. *Biomacromolecules* **2016**, *17* (4), 1365–1375. <https://doi.org/10.1021/acs.biomac.5b01764>.
- (150) Shin, S.-J.; Park, J.-Y.; Lee, J.-Y.; Park, H.; Park, Y.-D.; Lee, K.-B.; Whang, C.-M.; Lee, S.-H. “On the Fly” Continuous Generation of Alginate Fibers Using a Microfluidic Device. *Langmuir* **2007**, *23* (17), 9104–9108.
- (151) Jun, Y.; Kang, E.; Chae, S.; Lee, S.-H. Microfluidic Spinning of Micro- and Nano-Scale Fibers for Tissue Engineering. *Lab Chip* **2014**, *14* (13), 2145–2160. <https://doi.org/10.1039/C3LC51414E>.
- (152) Boyd, D. A.; Shields, A. R.; Naciri, J.; Ligler, F. S. Hydrodynamic Shaping, Polymerization, and Subsequent Modification of Thiol Click Fibers. *ACS Appl. Mater. Interfaces* **2013**, *5* (1), 114–119. <https://doi.org/10.1021/am3022834>.
- (153) Deville, S.; Saiz, E.; Nalla, R. K.; Tomsia, A. P. Freezing as a Path to Build Complex Composites. *Science* **2006**, *311* (5760), 515–518. <https://doi.org/10.1126/science.1120937>.
- (154) Bai, H.; Chen, Y.; Delattre, B.; Tomsia, A. P.; Ritchie, R. O. Bioinspired Large-Scale Aligned Porous Materials Assembled with Dual Temperature Gradients. *Sci. Adv.* **2015**, *1* (11), e1500849. <https://doi.org/10.1126/sciadv.1500849>.
- (155) Bai, H.; Walsh, F.; Gludovatz, B.; Delattre, B.; Huang, C.; Chen, Y.; Tomsia, A. P.; Ritchie, R. O. Bioinspired Hydroxyapatite/Poly(Methyl Methacrylate) Composite with a Nacre-Mimetic Architecture by a Bidirectional Freezing Method. *Adv. Mater.* **2016**, *28* (1), 50–56. <https://doi.org/10.1002/adma.201504313>.
- (156) Cheng, J.; Jun, Y.; Qin, J.; Lee, S.-H. Electrospinning versus Microfluidic Spinning of Functional Fibers for Biomedical Applications. *Biomaterials* **2016**, *114* (Journal Article), 121–143. <https://doi.org/10.1016/j.biomaterials.2016.10.040>.
- (157) Li, D.; Xia, Y. Electrospinning of Nanofibers: Reinventing the Wheel? *Adv. Mater.* **2004**, *16* (14), 1151–1170. <https://doi.org/10.1002/adma.200400719>.
- (158) Paris, O.; Burgert, I.; Fratzl, P. Biomimetics and Biotemplating of Natural Materials. *MRS Bull.* **2010**, *35* (3), 219–225. <https://doi.org/10.1557/mrs2010.655>.
- (159) Sun, R.-Q.; Sun, L.-B.; Chun, Y.; Xu, Q.-H.; Wu, H. Synthesizing Nanocrystal-Assembled Mesoporous Magnesium Oxide Using Cotton Fibres as Exotemplate. *Microporous Mesoporous Mater.* **2008**, *111* (1), 314–322. <https://doi.org/10.1016/j.micromeso.2007.08.006>.
- (160) Zollfrank, C.; Kladny, R.; Sieber, H.; Greil, P. Biomorphous SiOC/C-Ceramic Composites from Chemically Modified Wood Templates. *J. Eur. Ceram. Soc.* **2004**, *24* (2), 479–487. [https://doi.org/10.1016/S0955-2219\(03\)00202-4](https://doi.org/10.1016/S0955-2219(03)00202-4).
- (161) Qiao, G.; Ma, R.; Cai, N.; Zhang, C.; Jin, Z. Mechanical Properties and Microstructure of Si/SiC Materials Derived from Native Wood. *Mater. Sci. Eng. A* **2002**, *323* (1), 301–305. [https://doi.org/10.1016/S0921-5093\(01\)01387-9](https://doi.org/10.1016/S0921-5093(01)01387-9).
- (162) Kim, J.-W.; Kim, H.-C.; Myoung, S.-W.; Lee, J.-H.; Jung, Y.-G.; Jo, C.-Y. Synthesis of SiC Microtubes with Radial Morphology Using Biomorphic Carbon Template. *Mater. Sci. Eng. A* **2006**, *434* (1), 171–177. <https://doi.org/10.1016/j.msea.2006.06.135>.

- (163) Cao, J.; Rusina, O.; Sieber, H. Processing of Porous TiO<sub>2</sub>-Ceramics from Biological Preforms. *Ceram. Int.* **2004**, *30* (7), 1971–1974. <https://doi.org/10.1016/j.ceramint.2003.12.180>.
- (164) Reches, M.; Gazit, E. Casting Metal Nanowires Within Discrete Self-Assembled Peptide Nanotubes. *Science* **2003**, *300* (5619), 625–627. <https://doi.org/10.1126/science.1082387>.
- (165) Kapoor, A.; McKnight, M.; Chatterjee, K.; Agcayazi, T.; Kausche, H.; Bozkurt, A.; Ghosh, T. K. Toward Fully Manufacturable, Fiber Assembly–Based Concurrent Multimodal and Multifunctional Sensors for E-Textiles. *Adv. Mater. Technol.* **2019**, *4* (1800281), 1800281.
- (166) Guo, S.-Z.; Qiu, K.; Meng, F.; Park, S. H.; McAlpine, M. C. 3D Printed Stretchable Tactile Sensors. *Adv. Mater.* **2017**, *29* (27), n/a. <https://doi.org/10.1002/adma.201701218>.
- (167) Truby, R. L.; Lewis, J. A. Printing Soft Matter in Three Dimensions. *Nature* **2016**, *540* (7633), 371–378. <https://doi.org/10.1038/nature21003>.
- (168) Chen, J.; Huang, X.; Zhu, Y.; Jiang, P. Cellulose Nanofiber Supported 3D Interconnected BN Nanosheets for Epoxy Nanocomposites with Ultrahigh Thermal Management Capability. *Adv. Funct. Mater.* **2017**, *27* (5), 1604754. <https://doi.org/10.1002/adfm.201604754>.
- (169) Golberg, D.; Bando, Y.; Huang, Y.; Terao, T.; Mitome, M.; Tang, C.; Zhi, C. Boron Nitride Nanotubes and Nanosheets. *ACS Nano* **2010**, *4* (6), 2979–2993. <https://doi.org/10.1021/nn1006495>.
- (170) Wang, Y.; Xu, N.; Li, D.; Zhu, J. Thermal Properties of Two Dimensional Layered Materials. *Adv. Funct. Mater.* **2017**, *27* (19), 1604134. <https://doi.org/10.1002/adfm.201604134>.
- (171) Qin, Y. A Brief Description of Textile Fibers. In *Medical Textile Materials*; Qin, Y., Ed.; Woodhead Publishing: Cambridge, UK, 2016; pp 23–42.
- (172) Agcayazi, T.; Chatterjee, K.; Bozkurt, A.; Ghosh, T. K. Flexible Interconnects for Electronic Textiles. *Adv. Mater. Technol.* **2018**, 1700277. <https://doi.org/10.1002/admt.201700277>.
- (173) Sackmann, E. K.; Fulton, A. L.; Beebe, D. J. The Present and Future Role of Microfluidics in Biomedical Research. *Nature* **2014**, *507* (7491), 181–189. <https://doi.org/10.1038/nature13118>.
- (174) Daniele, M. A.; Radom, K.; Ligler, F. S.; Adams, A. A. Microfluidic Fabrication of Multiaxial Microvessels via Hydrodynamic Shaping. *RSC Adv.* **2014**, *4* (45), 23440–23446. <https://doi.org/10.1039/C4RA03667K>.
- (175) Thangawng, A. L.; Peter B. Howell, J.; Spillmann, C. M.; Naciri, J.; Ligler, F. S. UV Polymerization of Hydrodynamically Shaped Fibers. *Lab. Chip* **2011**, *11* (6), 1157–1160. <https://doi.org/10.1039/C0LC00392A>.
- (176) Kang, E.; Jeong, G. S.; Choi, Y. Y.; Lee, K. H.; Khademhosseini, A.; Lee, S.-H. Digitally Tunable Physicochemical Coding of Material Composition and Topography in Continuous Microfibres. *Nat Mater* **2011**, *10* (11), 877–883.
- (177) Hu, M.; Deng, R.; Schumacher, K. M.; Kurisawa, M.; Ye, H.; Purnamawati, K.; Ying, J. Y. Hydrodynamic Spinning of Hydrogel Fibers. *Biomaterials* **2010**, *31* (5), 863–869. <https://doi.org/10.1016/j.biomaterials.2009.10.002>.
- (178) Choi, C.-H.; Yi, H.; Hwang, S.; Weitz, D. A.; Lee, C.-S. Microfluidic Fabrication of Complex-Shaped Microfibers by Liquid Template-Aided Multiphase Microflow. *Lab. Chip* **2011**, *11* (8), 1477–1483. <https://doi.org/10.1039/C0LC00711K>.

- (179) Goldstein, E. A.; Raman, A. P.; Fan, S. Sub-Ambient Non-Evaporative Fluid Cooling with the Sky. *Nat. Energy* **2017**, *2* (9), 17143. <https://doi.org/10.1038/nenergy.2017.143>.
- (180) Su, C.-I.; Fang, J.-X.; Chen, X.-H.; Wu, W.-Y. Moisture Absorption and Release of Profiled Polyester and Cotton Composite Knitted Fabrics. *Text. Res. J.* **2007**, *77* (10), 764–769. <https://doi.org/10.1177/0040517507080696>.
- (181) Li, D.; Ni, M. Moisture Properties of Coolmax Fiber Blended with Regenerated Cellulose Fibers. In *2009 Second International Conference on Information and Computing Science*; IEEE: Manchester, UK, 2009; Vol. 2, pp 129–131. <https://doi.org/10.1109/ICIC.2009.141>.
- (182) Fanguero, R.; Filgueiras, A.; Soutinho, F.; Meidi, X. Wicking Behavior and Drying Capability of Functional Knitted Fabrics. *Text. Res. J.* **2010**, *80* (15), 1522–1530. <https://doi.org/10.1177/0040517510361796>.
- (183) Bagherzadeh, R.; Gorji, M.; Latifi, M.; Payvandy, P.; Kong, L. *Evolution of Moisture Management Behavior of High-Wicking 3D Warp Knitted Spacer Fabrics*; 2012; Vol. 13. <https://doi.org/10.1007/s12221-012-0529-6>.
- (184) Dai, B.; Li, K.; Shi, L.; Wan, X.; Liu, X.; Zhang, F.; Jiang, L.; Wang, S. Bioinspired Janus Textile with Conical Micropores for Human Body Moisture and Thermal Management. *Adv. Mater.* **2019**, *31* (41), e1904113. <https://doi.org/10.1002/adma.201904113>.
- (185) Zaman, M.; Liu, H.; Xiao, H.; Chibante, F.; Ni, Y. Hydrophilic Modification of Polyester Fabric by Applying Nanocrystalline Cellulose Containing Surface Finish. *Carbohydr. Polym.* **2013**, *91* (2), 560–567. <https://doi.org/10.1016/j.carbpol.2012.08.070>.
- (186) Alakara, Ş.; Karakişla, M.; Saçak, M. Preparation of Poly(Ethylene Terephthalate)-g-Methacrylamide Copolymers Initiated by Azobisisobutyronitrile: Characterization and Investigation of Some Properties. *J. Macromol. Sci. Part A* **2008**, *45* (4), 276–280. <https://doi.org/10.1080/10601320701863700>.
- (187) Mukhopadhyay, A.; Ishtiaque, S. M.; Uttam, D. Impact of Structural Variations in Hollow Yarn on Heat and Moisture Transport Properties of Fabrics. *J. Text. Inst.* **2011**, *102* (8), 700–712. <https://doi.org/10.1080/00405000.2010.515104>.
- (188) Kim, H.; Kim, S. *Moisture and Thermal Permeability of the Hollow Textured PET Imbedded Woven Fabrics for High Emotional Garments*; 2016; Vol. 17. <https://doi.org/10.1007/s12221-016-5942-9>.
- (189) Sampath, M. B.; Senthilkumar, M. Effect of Moisture Management Finish on Comfort Characteristics of Microdenier Polyester Knitted Fabrics. *J. Ind. Text.* **2009**, *39* (2), 163–173. <https://doi.org/10.1177/1528083709102922>.
- (190) Yoo, S.; Barker, R. L. Moisture Management Properties of Heat-Resistant Workwear Fabrics—Effects of Hydrophilic Finishes and Hygroscopic Fiber Blends. *Text. Res. J.* **2004**, *74* (11), 995–1000. <https://doi.org/10.1177/004051750407401110>.
- (191) Zeronian, S. H.; Collins, M. J. SURFACE MODIFICATION OF POLYESTER BY ALKALINE TREATMENTS. *Text. Prog.* **1989**, *20* (2), 1–26. <https://doi.org/10.1080/00405168908688948>.
- (192) Das, B.; Das, A.; Kothari, V.; Fanguero, R.; Araujo, M. D. Moisture Flow through Blended Fabrics – Effect of Hydrophilicity. *J. Eng. Fibers Fabr.* **2009**, *4* (4), 155892500900400. <https://doi.org/10.1177/155892500900400405>.
- (193) Harper, R. J.; Bruno, J. S.; Blanchard, E. J.; Gautreaux, G. A. Moisture-Related Properties of Cotton-Polyester Blend Fabrics. *Text. Res. J.* **1976**, *46* (2), 82–90. <https://doi.org/10.1177/004051757604600202>.

- (194) Zeng, C.; Wang, H.; Zhou, H.; Lin, T. Directional Water Transport Fabrics with Durable Ultra-High One-Way Transport Capacity. *Adv. Mater. Interfaces* **2016**, *3* (14), 1600036. <https://doi.org/10.1002/admi.201600036>.
- (195) Dong, Y.; Kong, J.; Phua, S. L.; Zhao, C.; Thomas, N. L.; Lu, X. Tailoring Surface Hydrophilicity of Porous Electrospun Nanofibers to Enhance Capillary and Push–Pull Effects for Moisture Wicking. *ACS Appl. Mater. Interfaces* **2014**, *6* (16), 14087–14095. <https://doi.org/10.1021/am503417w>.
- (196) Wu, J.; Wang, N.; Wang, L.; Dong, H.; Zhao, Y.; Jiang, L. Unidirectional Water-Penetration Composite Fibrous Film via Electrospinning. *Soft Matter* **2012**, *8* (22), 5996. <https://doi.org/10.1039/c2sm25514f>.
- (197) Parker, A. R.; Lawrence, C. R. Water Capture by a Desert Beetle. *Nature* **2001**, *414* (6859), 33–34. <https://doi.org/10.1038/35102108>.
- (198) Zheng, Y.; Gao, X.; Jiang, L. Directional Adhesion of Superhydrophobic Butterfly Wings. *Soft Matter* **2007**, *3* (2), 178–182. <https://doi.org/10.1039/B612667G>.
- (199) Ju, J.; Bai, H.; Zheng, Y.; Zhao, T.; Fang, R.; Jiang, L. A Multi-Structural and Multi-Functional Integrated Fog Collection System in Cactus. *Nat. Commun.* **2012**, *3* (1), 1247. <https://doi.org/10.1038/ncomms2253>.
- (200) Feng, L.; Li, S.; Li, Y.; Li, H.; Zhang, L.; Zhai, J.; Song, Y.; Liu, B.; Jiang, L.; Zhu, D. Super-Hydrophobic Surfaces: From Natural to Artificial. *Adv. Mater.* **2002**, *14* (24), 1857–1860. <https://doi.org/10.1002/adma.200290020>.
- (201) Mele, E.; Girardo, S.; Pisignano, D. *Strelitzia Reginae* Leaf as a Natural Template for Anisotropic Wetting and Superhydrophobicity. *Langmuir* **2012**, *28* (11), 5312–5317. <https://doi.org/10.1021/la300243x>.
- (202) Wang, Z.; Yang, X.; Cheng, Z.; Liu, Y.; Shao, L.; Jiang, L. Simply Realizing “Water Diode” Janus Membranes for Multifunctional Smart Applications. *Mater. Horiz.* **2017**, *4* (4), 701–708. <https://doi.org/10.1039/C7MH00216E>.
- (203) Zhou, H.; Wang, H.; Niu, H.; Lin, T. Superphobicity/Philicity Janus Fabrics with Switchable, Spontaneous, Directional Transport Ability to Water and Oil Fluids. *Sci. Rep.* **2013**, *3* (1), 2964. <https://doi.org/10.1038/srep02964>.
- (204) Wang, H.; Ding, J.; Dai, L.; Wang, X.; Lin, T. Directional Water-Transfer through Fabrics Induced by Asymmetric Wettability. *J. Mater. Chem.* **2010**, *20* (37), 7938. <https://doi.org/10.1039/c0jm02364g>.
- (205) Kong, Y.; Liu, Y.; Xin, J. H. Fabrics with Self-Adaptive Wettability Controlled by “Light-and-Dark.” *J. Mater. Chem.* **2011**, *21* (44), 17978. <https://doi.org/10.1039/c1jm12516h>.
- (206) Yang, A.; Cai, L.; Zhang, R.; Wang, J.; Hsu, P.-C.; Wang, H.; Zhou, G.; Xu, J.; Cui, Y. Thermal Management in Nanofiber-Based Face Mask. *Nano Lett.* **2017**, *17* (6), 3506–3510. <https://doi.org/10.1021/acs.nanolett.7b00579>.
- (207) Raman, A. P.; Anoma, M. A.; Zhu, L.; Rephaeli, E.; Fan, S. Passive Radiative Cooling below Ambient Air Temperature under Direct Sunlight. *Nature* **2014**, *515* (7528), 540–544. <https://doi.org/10.1038/nature13883>.
- (208) Zhou, L.; Song, H.; Liang, J.-W.; Singer, M.; Zhou, M.; Stegenburgs, E.; Zhang, N.; Xu, C.; Ng, T. K.; Yu, Z.; Ooi, B. S.; Gan, Q. A Polydimethylsiloxane-Coated Metal Structure for All-Day Radiative Cooling. *Nat. Sustain.* **2019**, *2*, 718–724. <https://doi.org/10.1038/s41893-019-0348-5>.
- (209) Shah, Y. T. Electrical Heating - Part 1. In *Thermal Energy: Sources, Recovery, and Applications*; Shah, Y. T., Ed.; CRC Press: Boca Raton, FL, 2018; pp 419–443.

- (210) Choi, S.; Park, J.; Hyun, W.; Kim, J.; Kim, J.; Lee, Y. B.; Song, C.; Hwang, H. J.; Kim, J. H.; Hyeon, T.; Kim, D.-H. Stretchable Heater Using Ligand-Exchanged Silver Nanowire Nanocomposite for Wearable Articular Thermotherapy. *ACS Nano* **2015**, *9* (6), 6626–6633. <https://doi.org/10.1021/acsnano.5b02790>.
- (211) Li, Y.; Zhang, Z.; Li, X.; Zhang, J.; Lou, H.; Shi, X.; Cheng, X.; Peng, H. A Smart, Stretchable Resistive Heater Textile. *J. Mater. Chem. C* **2017**, *5* (1), 41–46. <https://doi.org/10.1039/C6TC04399B>.
- (212) Ikeda, T.; Tayefeh, F.; Sessler, D. I.; Kurz, A.; Plattner, O.; Petschnigg, B.; Hopf, H. W.; West, J. Local Radiant Heating Increases Subcutaneous Oxygen Tension. *Am. J. Surg.* **1998**, *175* (1), 33–37. [https://doi.org/10.1016/S0002-9610\(97\)00237-7](https://doi.org/10.1016/S0002-9610(97)00237-7).
- (213) Hong, S.; Lee, H.; Lee, J.; Kwon, J.; Han, S.; Suh, Y. D.; Cho, H.; Shin, J.; Yeo, J.; Ko, S. H. Highly Stretchable and Transparent Metal Nanowire Heater for Wearable Electronics Applications. *Adv. Mater.* **2015**, *27* (32), 4744–4751. <https://doi.org/10.1002/adma.201500917>.
- (214) Jeong, Y. G.; An, J.-E. UV-Cured Epoxy/Graphene Nanocomposite Films: Preparation, Structure and Electric Heating Performance. *Polym. Int.* **2014**, *63* (11), 1895–1901. <https://doi.org/10.1002/pi.4713>.
- (215) Laforgue, A. Electrically Controlled Colour-Changing Textiles Using the Resistive Heating Properties of PEDOT Nanofibers. *J. Mater. Chem.* **2010**, *20* (38), 8233. <https://doi.org/10.1039/c0jm02307h>.
- (216) Ryan, J. D.; Mengistie, D. A.; Gabrielsson, R.; Lund, A.; Müller, C. Machine-Washable PEDOT:PSS Dyed Silk Yarns for Electronic Textiles. *ACS Appl. Mater. Interfaces* **2017**, *9* (10), 9045–9050. <https://doi.org/10.1021/acsaami.7b00530>.
- (217) Deka, B. K.; Hazarika, A.; Kong, K.; Kim, D.; Park, H. W.; Park, Y.-B. Interfacial Resistive Heating and Mechanical Properties of Graphene Oxide Assisted CuO Nanoparticles in Woven Carbon Fiber/Polyester Composite. *Compos. Part A* **2016**, *80*, 159–170. <https://doi.org/10.1016/j.compositesa.2015.10.023>.
- (218) Roh, J.-S.; Kim, S. All-Fabric Intelligent Temperature Regulation System for Smart Clothing Applications. *J. Intell. Mater. Syst. Struct.* **2016**, *27* (9), 1165–1175. <https://doi.org/10.1177/1045389X15585901>.
- (219) Li, J.; Liang, J.; Jian, X.; Hu, W.; Li, J.; Pei, Q. A Flexible and Transparent Thin Film Heater Based on a Silver Nanowire/Heat-resistant Polymer Composite. *Macromol. Mater. Eng.* **2014**, *299* (11), 1403–1409. <https://doi.org/10.1002/mame.201400097>.
- (220) Wang, Q.-W.; Zhang, H.-B.; Liu, J.; Zhao, S.; Xie, X.; Liu, L.; Yang, R.; Koratkar, N.; Yu, Z.-Z. Multifunctional and Water-Resistant MXene-Decorated Polyester Textiles with Outstanding Electromagnetic Interference Shielding and Joule Heating Performances. *Adv. Funct. Mater.* **2019**, *29* (7), 180681-n/a. <https://doi.org/10.1002/adfm.201806819>.
- (221) Chien, A.-T.; Cho, S.; Joshi, Y.; Kumar, S. Electrical Conductivity and Joule Heating of Polyacrylonitrile/Carbon Nanotube Composite Fibers. *Polymer* **2014**, *55* (26), 6896–6905. <https://doi.org/10.1016/j.polymer.2014.10.064>.
- (222) Liu, P.; Li, Y.; Xu, Y.; Bao, L.; Wang, L.; Pan, J.; Zhang, Z.; Sun, X.; Peng, H. Stretchable and Energy-Efficient Heating Carbon Nanotube Fiber by Designing a Hierarchically Helical Structure. *Small* **2018**, *14* (4), 1702926. <https://doi.org/10.1002/sml.201702926>.
- (223) Yang, M.; Pan, J.; Luo, L.; Xu, A.; Huang, J.; Xia, Z.; Cheng, D.; Cai, G.; Wang, X. CNT/Cotton Composite Yarn for Electro-Thermochromic Textiles. *Smart Mater. Struct.* **2019**, *28* (8), 85003. <https://doi.org/10.1088/1361-665X/ab21ef>.

- (224) Wang, Y.; Zhu, C.; Pfattner, R.; Yan, H.; Jin, L.; Chen, S.; Molina-Lopez, F.; Lissel, F.; Liu, J.; Rabiah, N. I.; Chen, Z.; Chung, J. W.; Linder, C.; Toney, M. F.; Murmann, B.; Bao, Z. A Highly Stretchable, Transparent, and Conductive Polymer. *Sci. Adv.* **2017**, *3* (3), e1602076. <https://doi.org/10.1126/sciadv.1602076>.
- (225) Moraes, M. R.; Alves, A. C.; Toptan, F.; Martins, M. S.; Vieira, E. M. F.; Paleo, A. J.; Souto, A. P.; Santos, W. L. F.; Esteves, M. F.; Zille, A. Glycerol/PEDOT:PSS Coated Woven Fabric as a Flexible Heating Element on Textiles. *J. Mater. Chem. C* **2017**, *5* (15), 3807–3822. <https://doi.org/10.1039/C7TC00486A>.
- (226) Alf, M. E.; Asatekin, A.; Barr, M. C.; Baxamusa, S. H.; Chelawat, H.; Ozaydin-Ince, G.; Petruczok, C. D.; Sreenivasan, R.; Tenhaeff, W. E.; Trujillo, N. J.; Vaddiraju, S.; Xu, J.; Gleason, K. K. Chemical Vapor Deposition of Conformal, Functional, and Responsive Polymer Films. *Adv. Mater.* **2010**, *22* (18), 1993–2027. <https://doi.org/10.1002/adma.200902765>.
- (227) Opwis, K.; Knittel, D.; Gutmann, J. S. Oxidative in Situ Deposition of Conductive PEDOT:PTSA on Textile Substrates and Their Application as Textile Heating Element. *Synth. Met.* **2012**, *162* (21–22), 1912–1918. <https://doi.org/10.1016/j.synthmet.2012.08.007>.
- (228) Zhou, J.; Mulle, M.; Zhang, Y.; Xu, X.; Li, E. Q.; Han, F.; Thoroddsen, S. T.; Lubineau, G. High-Ampacity Conductive Polymer Microfibers as Fast Response Wearable Heaters and Electromechanical Actuators. *J. Mater. Chem. C* **2016**, *4* (6), 1238–1249. <https://doi.org/10.1039/C5TC03380B>.
- (229) Hou, S.; Lv, Z.; Wu, H.; Cai, X.; Chu, Z.; Yiliguma; Zou, D. Flexible Conductive Threads for Wearable Dye-Sensitized Solar Cells. *J. Mater. Chem.* **2012**, *22* (14), 6549. <https://doi.org/10.1039/c2jm16773e>.
- (230) Irwin, M. D.; Roberson, D. A.; Olivas, R. I.; Wicker, R. B.; MacDonald, E. Conductive Polymer-Coated Threads as Electrical Interconnects in e-Textiles. *Fibers Polym.* **2011**, *12* (7), 904–910. <https://doi.org/10.1007/s12221-011-0904-8>.
- (231) Knittel, D.; Schollmeyer, E. Electrically High-Conductive Textiles. *Synth. Met.* **2009**, *159* (14), 1433–1437. <https://doi.org/10.1016/j.synthmet.2009.03.021>.
- (232) Åkerfeldt, M.; Strååt, M.; Walkenström, P. Electrically Conductive Textile Coating with a PEDOT-PSS Dispersion and a Polyurethane Binder. *Text. Res. J.* **2013**, *83* (6), 618–627. <https://doi.org/10.1177/0040517512444330>.
- (233) Bashir, T.; Ali, M.; Cho, S.-W.; Persson, N.-K.; Skrifvars, M. OCVD Polymerization of PEDOT: Effect of Pre-treatment Steps on PEDOT-coated Conductive Fibers and a Morphological Study of PEDOT Distribution on Textile Yarns. *Polym. Adv. Technol.* **2013**, *24* (2), 210–219. <https://doi.org/10.1002/pat.3073>.
- (234) Cheng, N.; Zhang, L.; Kim, J. J.; Andrew, T. L. Vapor Phase Organic Chemistry to Deposit Conjugated Polymer Films on Arbitrary Substrates. *J. Mater. Chem. C* **2017**, *5* (23), 5787–5796. <https://doi.org/10.1039/C7TC00293A>.
- (235) Zhang, L.; Baima, M.; Andrew, T. L. Transforming Commercial Textiles and Threads into Sewable and Weavable Electric Heaters. *ACS Appl. Mater. Interfaces* **2017**, *9* (37), 32299–32307. <https://doi.org/10.1021/acsami.7b10514>.
- (236) Zhang, L.; Fairbanks, M.; Andrew, T. L. Rugged Textile Electrodes for Wearable Devices Obtained by Vapor Coating Off-the-Shelf, Plain-Woven Fabrics. *Adv. Funct. Mater.* **2017**, *27* (24), 1700415. <https://doi.org/10.1002/adfm.201700415>.

- (237) Bashir, T.; Skrifvars, M.; Persson, N.-K. Synthesis of High Performance, Conductive PEDOT-Coated Polyester Yarns by OCVD Technique. *Polym. Adv. Technol.* **2012**, *23* (3), 611–617. <https://doi.org/10.1002/pat.1932>.
- (238) DiSalvo, F. J. Thermoelectric Cooling and Power Generation. *Science* **1999**, *285* (5428), 703–706. <https://doi.org/10.1126/science.285.5428.703>.
- (239) Vining, C. B. Semiconductors Are Cool. *Nature* **2001**, *413* (6856), 577–578. <https://doi.org/10.1038/35098159>.
- (240) He, R.; Schierning, G.; Nielsch, K. Thermoelectric Devices: A Review of Devices, Architectures, and Contact Optimization. *Adv. Mater. Technol.* **2018**, *3* (4), 1700256. <https://doi.org/10.1002/admt.201700256>.
- (241) Zhou, X.; Yan, Y.; Lu, X.; Zhu, H.; Han, X.; Chen, G.; Ren, Z. Routes for High-Performance Thermoelectric Materials. *Mater. Today* **2018**, *21* (9), 974–988. <https://doi.org/10.1016/j.mattod.2018.03.039>.
- (242) He, J.; Tritt, T. M. Advances in Thermoelectric Materials Research: Looking Back and Moving Forward. *Science* **2017**, *357* (6358), eaak9997. <https://doi.org/10.1126/science.aak9997>.
- (243) Snyder, G. J.; Toberer, E. S. Complex Thermoelectric Materials. *Nat. Mater.* **2008**, *7* (2), 105–114. <https://doi.org/10.1038/nmat2090>.
- (244) Moshwan, R.; Yang, L.; Zou, J.; Chen, Z. Eco-Friendly SnTe Thermoelectric Materials: Progress and Future Challenges. *Adv. Funct. Mater.* **2017**, *27* (43), 1703278. <https://doi.org/10.1002/adfm.201703278>.
- (245) Kim, G.-H.; Shao, L.; Zhang, K.; Pipe, K. P. Engineered Doping of Organic Semiconductors for Enhanced Thermoelectric Efficiency. *Nat. Mater.* **2013**, *12*, 719–723.
- (246) Bubnova, O.; Khan, Z. U.; Malti, A.; Braun, S.; Fahlman, M.; Berggren, M.; Crispin, X. Optimization of the Thermoelectric Figure of Merit in the Conducting Polymer Poly(3,4-Ethylenedioxythiophene). *Nat. Mater.* **2011**, *10* (6), 429–433. <https://doi.org/10.1038/nmat3012>.
- (247) Piao, M.; Na, J.; Choi, J.; Kim, J.; Kennedy, G. P.; Kim, G.; Roth, S.; Dettlaff-Weglikowska, U. Increasing the Thermoelectric Power Generated by Composite Films Using Chemically Functionalized Single-Walled Carbon Nanotubes. *Carbon* **2013**, *62*, 430–437. <https://doi.org/10.1016/j.carbon.2013.06.028>.
- (248) Yu, C.; Choi, K.; Yin, L.; Grunlan, J. C. Light-Weight Flexible Carbon Nanotube Based Organic Composites with Large Thermoelectric Power Factors. *ACS Nano* **2011**, *5* (10), 7885.
- (249) Bahk, J.-H.; Fang, H.; Yazawa, K.; Shakouri, A. Flexible Thermoelectric Materials and Device Optimization for Wearable Energy Harvesting. *J. Mater. Chem. C* **2015**, *3* (40), 10362–10374. <https://doi.org/10.1039/C5TC01644D>.
- (250) Snyder, G. J.; Ursell, T. S. Thermoelectric Efficiency and Compatibility. *Phys. Rev. Lett.* **2003**, *91* (14), 148301. <https://doi.org/10.1103/PhysRevLett.91.148301>.
- (251) Xuan, X. C. Optimum Design of a Thermoelectric Device. *Semicond. Sci. Technol.* **2002**, *17* (2), 114–119. <https://doi.org/10.1088/0268-1242/17/2/304>.
- (252) Antonik, M.; O'Connor, B. T.; Ferguson, S. Performance and Design Comparison of a Bulk Thermoelectric Cooler With a Hybrid Architecture. *J. Therm. Sci. Eng. Appl.* **2016**, *8* (2), 02102–02113. <https://doi.org/10.1115/1.4032637>.

- (253) Sootsman, J. R.; Chung, D. Y.; Kanatzidis, M. G. New and Old Concepts in Thermoelectric Materials. *Angew. Chem. Int. Ed Engl.* **2009**, *48* (46), 8616–8639. <https://doi.org/10.1002/anie.200900598>.
- (254) Zhao, L.-D.; Lo, S.-H.; Zhang, Y.; Sun, H.; Tan, G.; Uher, C.; Wolverton, C.; Dravid, V. P.; Kanatzidis, M. G. Ultralow Thermal Conductivity and High Thermoelectric Figure of Merit in SnSe Crystals. *Nature* **2014**, *508* (7496), 373–377. <https://doi.org/10.1038/nature13184>.
- (255) Zhou, W.; Fan, Q.; Zhang, Q.; Cai, L.; Li, K.; Gu, X.; Yang, F.; Zhang, N.; Wang, Y.; Liu, H.; Zhou, W.; Xie, S. High-Performance and Compact-Designed Flexible Thermoelectric Modules Enabled by a Reticulate Carbon Nanotube Architecture. *Nat. Commun.* **2017**, *8* (1), 14886. <https://doi.org/10.1038/ncomms14886>.
- (256) Gnanaseelan, M.; Chen, Y.; Luo, J.; Krause, B.; Pionteck, J.; Pötschke, P.; Qi, H. Cellulose-Carbon Nanotube Composite Aerogels as Novel Thermoelectric Materials. *Compos. Sci. Technol.* **2018**, *163* (Journal Article), 133–140. <https://doi.org/10.1016/j.compscitech.2018.04.026>.
- (257) Zaia, E. W.; Gordon, M. P.; Niemann, V.; Choi, J.; Chatterjee, R.; Hsu, C.; Yano, J.; Russ, B.; Sahu, A.; Urban, J. J. Molecular Level Insight into Enhanced N-Type Transport in Solution-Printed Hybrid Thermoelectrics. *Adv. Energy Mater.* **2019**, *9* (13), 1803469. <https://doi.org/10.1002/aenm.201803469>.
- (258) Heremans, J. P.; Dresselhaus, M. S.; Bell, L. E.; Morelli, D. T. When Thermoelectrics Reached the Nanoscale. *Nat. Nanotechnol.* **2013**, *8* (7), 471–473. <https://doi.org/10.1038/nnano.2013.129>.
- (259) Du, Y.; Xu, J.; Paul, B.; Eklund, P. Flexible Thermoelectric Materials and Devices. *Appl. Mater. Today* **2018**, *12* (Journal Article), 366–388. <https://doi.org/10.1016/j.apmt.2018.07.004>.
- (260) Zhang, Q.; Sun, Y.; Xu, W.; Zhu, D. Organic Thermoelectric Materials: Emerging Green Energy Materials Converting Heat to Electricity Directly and Efficiently. *Adv. Mater.* **2014**, *26* (40), 6829–6851. <https://doi.org/10.1002/adma.201305371>.
- (261) Blackburn, J. L.; Ferguson, A. J.; Cho, C.; Grunlan, J. C. Carbon-Nanotube-Based Thermoelectric Materials and Devices. *Adv. Mater.* **2018**, *30* (11), 1870072. <https://doi.org/10.1002/adma.201704386>.
- (262) Russ, B.; Glauddell, A.; Urban, J. J.; Chabinye, M. L.; Segalman, R. A. Organic Thermoelectric Materials for Energy Harvesting and Temperature Control. *Nat. Rev. Mater.* **2016**, *1*, 16050.
- (263) Wang, Y.; Yang, L.; Shi, X.; Shi, X.; Chen, L.; Dargusch, M. S.; Zou, J.; Chen, Z. Flexible Thermoelectric Materials and Generators: Challenges and Innovations. *Adv. Mater.* **2019**, *31* (29), e1807916. <https://doi.org/10.1002/adma.201807916>.
- (264) Coropceanu, V.; Cornil, J.; da Silva Filho, D. A.; Olivier, Y.; Silbey, R.; Brédas, J.-L. Charge Transport in Organic Semiconductors. *Chem. Rev.* **2007**, *107* (4), 926–952. <https://doi.org/10.1021/cr050140x>.
- (265) Shakouri, A. Recent Developments in Semiconductor Thermoelectric Physics and Materials. *Annu. Rev. Mater. Res.* **2011**, *41* (1), 399–431. <https://doi.org/10.1146/annurev-matsci-062910-100445>.
- (266) Bell, L. E. Cooling, Heating, Generating Power, and Recovering Waste Heat with Thermoelectric Systems. *Science* **2008**, *321* (5895), 1457–1461. <https://doi.org/10.1126/science.1158899>.

- (267) Heremans, J. P.; Wiendlocha, B.; Chamoire, A. M. Resonant Levels in Bulk Thermoelectric Semiconductors. *Energy Environ. Sci.* **2012**, *5* (2), 5510–5530. <https://doi.org/10.1039/C1EE02612G>.
- (268) Saeed, Y.; Singh, N.; Schwingenschlögl, U. Colossal Thermoelectric Power Factor in K7/8RhO2. *Adv. Funct. Mater.* **2012**, *22* (13), 2792–2796. <https://doi.org/10.1002/adfm.201103106>.
- (269) Zhao, H.; Sui, J.; Tang, Z.; Lan, Y.; Jie, Q.; Kraemer, D.; McEnaney, K.; Guloy, A.; Chen, G.; Ren, Z. High Thermoelectric Performance of MgAgSb-Based Materials. *Nano Energy* **2014**, *7*, 97–103. <https://doi.org/10.1016/j.nanoen.2014.04.012>.
- (270) Gonçalves, A. P.; Lopes, E. B.; Delaizir, G.; Vaney, J. B.; Lenoir, B.; Piarristeguy, A.; Pradel, A.; Monnier, J.; Ochin, P.; Godart, C. Semiconducting Glasses: A New Class of Thermoelectric Materials? *J. Solid State Chem.* **2012**, *193*, 26–30. <https://doi.org/10.1016/j.jssc.2012.03.031>.
- (271) Mehta, R. J.; Zhang, Y.; Karthik, C.; Singh, B.; Siegel, R. W.; Borca-Tasciuc, T.; Ramanath, G. A New Class of Doped Nanobulk High-Figure-of-Merit Thermoelectrics by Scalable Bottom-up Assembly. *Nat. Mater.* **2012**, *11* (3), 233–240. <https://doi.org/10.1038/nmat3213>.
- (272) Tsujii, N.; Mori, T. High Thermoelectric Power Factor in a Carrier-Doped Magnetic Semiconductor CuFeS2. *Appl. Phys. Express* **2013**, *6* (4), 043001. <https://doi.org/10.7567/APEX.6.043001>.
- (273) Tsubota, T.; Ohtaki, M.; Eguchi, K.; Arai, H. Thermoelectric Properties of Al-Doped ZnO as a Promising Oxide Material for High-Temperature Thermoelectric Conversion. *J. Mater. Chem.* **1997**, *7* (1), 85–90. <https://doi.org/10.1039/A602506D>.
- (274) Zhao, L.-D.; Tan, G.; Hao, S.; He, J.; Pei, Y.; Chi, H.; Wang, H.; Gong, S.; Xu, H.; Dravid, V. P.; Uher, C.; Snyder, G. J.; Wolverton, C.; Kanatzidis, M. G. Ultrahigh Power Factor and Thermoelectric Performance in Hole-Doped Single-Crystal SnSe. *Science* **2016**, *351* (6269), 141–144. <https://doi.org/10.1126/science.aad3749>.
- (275) Pei, Y.; Shi, X.; LaLonde, A.; Wang, H.; Chen, L.; Snyder, G. J. Convergence of Electronic Bands for High Performance Bulk Thermoelectrics. *Nature* **2011**, *473* (7345), 66–69. <https://doi.org/10.1038/nature09996>.
- (276) Harman, T. C.; Walsh, M. P.; laforge, B. E.; Turner, G. W. Nanostructured Thermoelectric Materials. *J. Electron. Mater.* **2005**, *34* (5), L19–L22. <https://doi.org/10.1007/s11664-005-0083-8>.
- (277) Li, J.-F.; Liu, W.-S.; Zhao, L.-D.; Zhou, M. High-Performance Nanostructured Thermoelectric Materials. *NPG Asia Mater.* **2010**, *2* (4), 152–158. <https://doi.org/10.1038/asiamat.2010.138>.
- (278) Zhang, Q.; Liao, B.; Lan, Y.; Lukas, K.; Liu, W.; Esfarjani, K.; Opeil, C.; Broido, D.; Chen, G.; Ren, Z. High Thermoelectric Performance by Resonant Dopant Indium in Nanostructured SnTe. *Proc. Natl. Acad. Sci.* **2013**, *110* (33), 13261–13266. <https://doi.org/10.1073/pnas.1305735110>.
- (279) Vargiamidis, V.; Neophytou, N. Hierarchical Nanostructuring Approaches for Thermoelectric Materials with High Power Factors. *Phys. Rev. B* **2019**, *99* (4), 045405. <https://doi.org/10.1103/PhysRevB.99.045405>.
- (280) Majumdar, A. Thermoelectricity in Semiconductor Nanostructures. *Science* **2004**, *303* (5659), 777–778. <https://doi.org/10.1126/science.1093164>.

- (281) Takashiri, M.; Shirakawa, T.; Miyazaki, K.; Tsukamoto, H. Fabrication and Characterization of Bismuth–Telluride-Based Alloy Thin Film Thermoelectric Generators by Flash Evaporation Method. *Sens. Actuators Phys.* **2007**, *138* (2), 329–334. <https://doi.org/10.1016/j.sna.2007.05.030>.
- (282) Venkatasubramanian, R.; Siivola, E.; Colpitts, T.; O’Quinn, B. Thin-Film Thermoelectric Devices with High Room-Temperature Figures of Merit. *Nature* **2001**, *413* (6856), 597–602. <https://doi.org/10.1038/35098012>.
- (283) Fan, P.; Zheng, Z.; Li, Y.; Lin, Q.; Luo, J.; Liang, G.; Cai, X.; Zhang, D.; Ye, F. Low-Cost Flexible Thin Film Thermoelectric Generator on Zinc Based Thermoelectric Materials. *Appl. Phys. Lett.* **2015**, *106* (7), 73901. <https://doi.org/10.1063/1.4909531>.
- (284) Bulman, G.; Barletta, P.; Lewis, J.; Baldasaro, N.; Manno, M.; Bar-Cohen, A.; Yang, B. Superlattice-Based Thin-Film Thermoelectric Modules with High Cooling Fluxes. *Nat. Commun.* **2016**, *7* (1), 10302. <https://doi.org/10.1038/ncomms10302>.
- (285) Wan, C.; Tian, R.; Kondou, M.; Yang, R.; Zong, P.; Koumoto, K. Ultrahigh Thermoelectric Power Factor in Flexible Hybrid Inorganic–Organic Superlattice. *Nat. Commun.* **2017**, *8* (1), 1024–1029. <https://doi.org/10.1038/s41467-017-01149-4>.
- (286) Wan, C.; Gu, X.; Dang, F.; Itoh, T.; Wang, Y.; Sasaki, H.; Kondo, M.; Koga, K.; Yabuki, K.; Snyder, G. J.; Yang, R.; Koumoto, K. Flexible N-Type Thermoelectric Materials by Organic Intercalation of Layered Transition Metal Dichalcogenide TiS<sub>2</sub>. *Nat. Mater.* **2015**, *14* (6), 622–627. <https://doi.org/10.1038/nmat4251>.
- (287) We, J. H.; Kim, S. J.; Cho, B. J. Hybrid Composite of Screen-Printed Inorganic Thermoelectric Film and Organic Conducting Polymer for Flexible Thermoelectric Power Generator. *Energy* **2014**, *73* (Journal Article), 506–512. <https://doi.org/10.1016/j.energy.2014.06.047>.
- (288) Sun, Y.; Sheng, P.; Di, C.; Jiao, F.; Xu, W.; Qiu, D.; Zhu, D. Organic Thermoelectric Materials and Devices Based on P- and n-Type Poly(Metal 1,1,2,2-Ethenetetrathiolate)s. *Adv. Mater.* **2012**, *24* (7), 932–937. <https://doi.org/10.1002/adma.201104305>.
- (289) Cho, C.; Stevens, B.; Hsu, J.; Bureau, R.; Hagen, D. A.; Regev, O.; Yu, C.; Grunlan, J. C. Completely Organic Multilayer Thin Film with Thermoelectric Power Factor Rivaling Inorganic Tellurides. *Adv. Mater.* **2015**, *27* (19), 2996–3001. <https://doi.org/10.1002/adma.201405738>.
- (290) Arunkumar, P.; Kuanr, S. K.; Babu, K. S. Thin Film: Deposition, Growth Aspects, and Characterization. In *Thin Film Structures in Energy Applications*; Babu Krishna Moorthy, S., Ed.; Springer International Publishing: Cham, 2015; pp 1–49. [https://doi.org/10.1007/978-3-319-14774-1\\_1](https://doi.org/10.1007/978-3-319-14774-1_1).
- (291) Osterhage, H.; Gooth, J.; Hamdou, B.; Gwozdz, P.; Zierold, R.; Nielsch, K. Thermoelectric Properties of Topological Insulator Bi<sub>2</sub>Te<sub>3</sub>, Sb<sub>2</sub>Te<sub>3</sub>, and Bi<sub>2</sub>Se<sub>3</sub> Thin Film Quantum Wells. *Appl. Phys. Lett.* **2014**, *105* (12), 123117. <https://doi.org/10.1063/1.4896680>.
- (292) Zahid, F.; Lake, R. Thermoelectric Properties of Bi<sub>2</sub>Te<sub>3</sub> Atomic Quintuple Thin Films. *Appl. Phys. Lett.* **2010**, *97* (21), 212102. <https://doi.org/10.1063/1.3518078>.
- (293) Venkatasubramanian, R.; Colpitts, T. Enhancement in Figure-Of-Merit with Superlattice Structures for Thin-Film Thermoelectric Devices. *MRS Online Proc. Libr. Arch.* **1997**, *478*. <https://doi.org/10.1557/PROC-478-73>.
- (294) Rogacheva, E. I.; Grigorov, S. N.; Nashchekina, O. N.; Tavrina, T. V.; Lyubchenko, S. G.; Sipatov, A. Yu.; Volobuev, V. V.; Fedorov, A. G.; Dresselhaus, M. S. Growth Mechanism

- and Thermoelectric Properties of PbTe/SnTe/PbTe Heterostructures. *Thin Solid Films* **2005**, *493* (1), 41–48. <https://doi.org/10.1016/j.tsf.2005.06.039>.
- (295) Ramos, R.; Anadón, A.; Lucas, I.; Uchida, K.; Algarabel, P. A.; Morellón, L.; Aguirre, M. H.; Saitoh, E.; Ibarra, M. R. Thermoelectric Performance of Spin Seebeck Effect in Fe<sub>3</sub>O<sub>4</sub>/Pt-Based Thin Film Heterostructures. *APL Mater.* **2016**, *4* (10), 104802. <https://doi.org/10.1063/1.4950994>.
- (296) Takashiri, M. Thin Films of Bismuth-Telluride-Based Alloys. In *Thermoelectric Thin Films: Materials and Devices*; Mele, P., Narducci, D., Ohta, M., Biswas, K., Morante, J., Saini, S., Endo, T., Eds.; Springer International Publishing: Cham, 2019; pp 1–29. [https://doi.org/10.1007/978-3-030-20043-5\\_1](https://doi.org/10.1007/978-3-030-20043-5_1).
- (297) Goncalves, L. M.; Couto, C.; Alpuim, P.; Rolo, A. G.; Völklein, F.; Correia, J. H. Optimization of Thermoelectric Properties on Bi<sub>2</sub>Te<sub>3</sub> Thin Films Deposited by Thermal Co-Evaporation. *Thin Solid Films* **2010**, *518* (10), 2816–2821. <https://doi.org/10.1016/j.tsf.2009.08.038>.
- (298) Francioso, L.; De Pascali, C.; Farella, I.; Martucci, C.; Cretì, P.; Siciliano, P.; Perrone, A. Flexible Thermoelectric Generator for Ambient Assisted Living Wearable Biometric Sensors. *J. Power Sources* **2011**, *196* (6), 3239–3243. <https://doi.org/10.1016/j.jpowsour.2010.11.081>.
- (299) Zou, H.; Rowe, D. M.; Williams, S. G. K. Peltier Effect in a Co-Evaporated Sb<sub>2</sub>Te<sub>3</sub>(P)-Bi<sub>2</sub>Te<sub>3</sub>(N) Thin Film Thermocouple. *Thin Solid Films* **2002**, *408* (1), 270–274. [https://doi.org/10.1016/S0040-6090\(02\)00077-9](https://doi.org/10.1016/S0040-6090(02)00077-9).
- (300) Sun, Y.; Christensen, M.; Johnsen, S.; Nong, N. V.; Ma, Y.; Sillassen, M.; Zhang, E.; Palmqvist, A. E. C.; Böttiger, J.; Iversen, B. B. Low-Cost High-Performance Zinc Antimonide Thin Films for Thermoelectric Applications. *Adv. Mater.* **2012**, *24* (13), 1693–1696. <https://doi.org/10.1002/adma.201104947>.
- (301) Lee, H. B.; We, J. H.; Yang, H. J.; Kim, K.; Choi, K. C.; Cho, B. J. Thermoelectric Properties of Screen-Printed ZnSb Film. *Thin Solid Films* **2011**, *519* (16), 5441–5443. <https://doi.org/10.1016/j.tsf.2011.03.031>.
- (302) Fan, P.; Fan, W.; Zheng, Z.; Zhang, Y.; Luo, J.; Liang, G.; Zhang, D. Thermoelectric Properties of Zinc Antimonide Thin Film Deposited on Flexible Polyimide Substrate by RF Magnetron Sputtering. *J. Mater. Sci. Mater. Electron.* **2014**, *25* (11), 5060–5065. <https://doi.org/10.1007/s10854-014-2271-x>.
- (303) Hankare, P. P.; Khomane, A. S.; Chate, P. A.; Rathod, K. C.; Garadkar, K. M. Preparation of Copper Selenide Thin Films by Simple Chemical Route at Low Temperature and Their Characterization. *J. Alloys Compd.* **2009**, *469* (1), 478–482. <https://doi.org/10.1016/j.jallcom.2008.02.062>.
- (304) Leonard, W. F.; Yu, H. Thermoelectric Power of Thin Copper Films. *J. Appl. Phys.* **1973**, *44* (12), 5320–5323. <https://doi.org/10.1063/1.1662150>.
- (305) Yang, C.; Souchay, D.; Kneiß, M.; Bogner, M.; Wei, H. M.; Lorenz, M.; Oeckler, O.; Benstetter, G.; Fu, Y. Q.; Grundmann, M. Transparent Flexible Thermoelectric Material Based on Non-Toxic Earth-Abundant p-Type Copper Iodide Thin Film. *Nat. Commun.* **2017**, *8* (1), 1–7. <https://doi.org/10.1038/ncomms16076>.
- (306) Lin, Z.; Hollar, C.; Kang, J. S.; Yin, A.; Wang, Y.; Shiu, H.-Y.; Huang, Y.; Hu, Y.; Zhang, Y.; Duan, X. A Solution Processable High-Performance Thermoelectric Copper Selenide Thin Film. *Adv. Mater.* **2017**, *29* (21), 1606662. <https://doi.org/10.1002/adma.201606662>.

- (307) An, H. P.; Zhu, C. H.; Ge, W. W.; Li, Z. Z.; Tang, G. D. Growth and Thermoelectric Properties of Ca<sub>3</sub>Co<sub>4</sub>O<sub>9</sub> Thin Films with C-Axis Parallel to Si Substrate Surface. *Thin Solid Films* **2013**, *545*, 229–233. <https://doi.org/10.1016/j.tsf.2013.08.045>.
- (308) Masset, A. C.; Michel, C.; Maignan, A.; Hervieu, M.; Toulemonde, O.; Studer, F.; Raveau, B.; Hejtmanek, J. Misfit-Layered Cobaltite with an Anisotropic Giant Magnetoresistance: Ca<sub>3</sub>Co<sub>4</sub>O<sub>9</sub>. *Phys. Rev. B* **2000**, *62* (1), 166–175. <https://doi.org/10.1103/PhysRevB.62.166>.
- (309) Paul, B.; Björk, E. M.; Kumar, A.; Lu, J.; Eklund, P. Nanoporous Ca<sub>3</sub>Co<sub>4</sub>O<sub>9</sub> Thin Films for Transferable Thermoelectrics. *ACS Appl. Energy Mater.* **2018**, *1* (5), 2261–2268. <https://doi.org/10.1021/acsaem.8b00333>.
- (310) Rivas-Murias, B.; Vila-Fungueiriño, J. M.; Rivadulla, F. High Quality Thin Films of Thermoelectric Misfit Cobalt Oxides Prepared by a Chemical Solution Method. *Sci. Rep.* **2015**, *5* (1), 1–8. <https://doi.org/10.1038/srep11889>.
- (311) Yang, C.; Kneiß, M.; Lorenz, M.; Grundmann, M. Room-Temperature Synthesized Copper Iodide Thin Film as Degenerate p-Type Transparent Conductor with a Boosted Figure of Merit. *Proc. Natl. Acad. Sci.* **2016**, *113* (46), 12929–12933. <https://doi.org/10.1073/pnas.1613643113>.
- (312) Burmistrova, P. V.; Maassen, J.; Favaloro, T.; Saha, B.; Salamat, S.; Rui Koh, Y.; Lundstrom, M. S.; Shakouri, A.; Sands, T. D. Thermoelectric Properties of Epitaxial ScN Films Deposited by Reactive Magnetron Sputtering onto MgO(001) Substrates. *J. Appl. Phys.* **2013**, *113* (15), 153704. <https://doi.org/10.1063/1.4801886>.
- (313) Perez-Taborda, J. A.; Vera, L.; Caballero-Calero, O.; Lopez, E. O.; Romero, J. J.; Stroppa, D. G.; Briones, F.; Martin-Gonzalez, M. Pulsed Hybrid Reactive Magnetron Sputtering for High ZT Cu<sub>2</sub>Se Thermoelectric Films. *Adv. Mater. Technol.* **2017**, *2* (7), 1700012. <https://doi.org/10.1002/admt.201700012>.
- (314) Goncalves, L. M.; Alpuim, P.; Rolo, A. G.; Correia, J. H. Thermal Co-Evaporation of Sb<sub>2</sub>Te<sub>3</sub> Thin-Films Optimized for Thermoelectric Applications. *Thin Solid Films* **2011**, *519* (13), 4152–4157. <https://doi.org/10.1016/j.tsf.2011.01.395>.
- (315) Goncalves, L. M.; Alpuim, P.; Min, G.; Rowe, D. M.; Couto, C.; Correia, J. H. Optimization of Bi<sub>2</sub>Te<sub>3</sub> and Sb<sub>2</sub>Te<sub>3</sub> Thin Films Deposited by Co-Evaporation on Polyimide for Thermoelectric Applications. *Vacuum* **2008**, *82* (12), 1499–1502. <https://doi.org/10.1016/j.vacuum.2008.03.076>.
- (316) Kusano, K.; Yamamoto, A.; Nakata, M.; Suemasu, T.; Toko, K. Thermoelectric Inorganic SiGe Film Synthesized on Flexible Plastic Substrate. *ACS Appl. Energy Mater.* **2018**, *1* (10), 5280–5285. <https://doi.org/10.1021/acsaem.8b00899>.
- (317) Kong, D.; Zhu, W.; Guo, Z.; Deng, Y. High-Performance Flexible Bi<sub>2</sub>Te<sub>3</sub> Films Based Wearable Thermoelectric Generator for Energy Harvesting. *Energy* **2019**, *175*, 292–299. <https://doi.org/10.1016/j.energy.2019.03.060>.
- (318) Shen, S.; Zhu, W.; Deng, Y.; Zhao, H.; Peng, Y.; Wang, C. Enhancing Thermoelectric Properties of Sb<sub>2</sub>Te<sub>3</sub> Flexible Thin Film through Microstructure Control and Crystal Preferential Orientation Engineering. *Appl. Surf. Sci.* **2017**, *414*, 197–204. <https://doi.org/10.1016/j.apsusc.2017.04.074>.
- (319) Karttunen, A. J.; Sarnes, L.; Townsend, R.; Mikkonen, J.; Karppinen, M. Flexible Thermoelectric ZnO–Organic Superlattices on Cotton Textile Substrates by ALD/MLD. *Adv. Electron. Mater.* **2017**, *3* (6), 1600459. <https://doi.org/10.1002/aelm.201600459>.

- (320) Yang, S.; Cho, K.; Yun, J.; Choi, J.; Kim, S. Thermoelectric Characteristics of  $\gamma$ -Ag<sub>2</sub>Te Nanoparticle Thin Films on Flexible Substrates. *Thin Solid Films* **2017**, *641*, 65–68. <https://doi.org/10.1016/j.tsf.2017.01.068>.
- (321) Shi, X.; Chen, H.; Hao, F.; Liu, R.; Wang, T.; Qiu, P.; Burkhardt, U.; Grin, Y.; Chen, L. Room-Temperature Ductile Inorganic Semiconductor. *Nat. Mater.* **2018**, *17* (5), 421–426. <https://doi.org/10.1038/s41563-018-0047-z>.
- (322) Zhao, Y.; S. Dyck, J.; Burda, C. Toward High-Performance Nanostructured Thermoelectric Materials: The Progress of Bottom-up Solution Chemistry Approaches. *J. Mater. Chem.* **2011**, *21* (43), 17049–17058. <https://doi.org/10.1039/C1JM11727K>.
- (323) Pejova, B.; Grozdanov, I. Chemical Deposition and Characterization of Glassy Bismuth(III) Selenide Thin Films. *Thin Solid Films* **2002**, *408* (1), 6–10. [https://doi.org/10.1016/S0040-6090\(02\)00085-8](https://doi.org/10.1016/S0040-6090(02)00085-8).
- (324) Xu, X.; Bullock, J.; Schelhas, L. T.; Stutz, E. Z.; Fonseca, J. J.; Hettick, M.; Pool, V. L.; Tai, K. F.; Toney, M. F.; Fang, X.; Javey, A.; Wong, L. H.; Ager, J. W. Chemical Bath Deposition of P-Type Transparent, Highly Conducting (CuS)<sub>x</sub>:(ZnS)<sub>1-x</sub> Nanocomposite Thin Films and Fabrication of Si Heterojunction Solar Cells. *Nano Lett.* **2016**, *16* (3), 1925–1932. <https://doi.org/10.1021/acs.nanolett.5b05124>.
- (325) Paul, B.; Lu, J.; Eklund, P. Nanostructural Tailoring to Induce Flexibility in Thermoelectric Ca<sub>3</sub>Co<sub>4</sub>O<sub>9</sub> Thin Films. *ACS Appl. Mater. Interfaces* **2017**, *9* (30), 25308–25316. <https://doi.org/10.1021/acsami.7b06301>.
- (326) Jin, Q.; Jiang, S.; Zhao, Y.; Wang, D.; Qiu, J.; Tang, D.-M.; Tan, J.; Sun, D.-M.; Hou, P.-X.; Chen, X.-Q.; Tai, K.; Gao, N.; Liu, C.; Cheng, H.-M.; Jiang, X. Flexible Layer-Structured Bi<sub>2</sub>Te<sub>3</sub> Thermoelectric on a Carbon Nanotube Scaffold. *Nat. Mater.* **2019**, *18* (1), 62–68. <https://doi.org/10.1038/s41563-018-0217-z>.
- (327) Lee, J. A.; Aliev, A. E.; Bykova, J. S.; de Andrade, M. J.; Kim, D.; Sim, H. J.; Lepró, X.; Zakhidov, A. A.; Lee, J.; Spinks, G. M.; Roth, S.; Kim, S. J.; Baughman, R. H. Woven-Yarn Thermoelectric Textiles. *Adv. Mater.* **2016**, *28* (25), 5038–5044. <https://doi.org/10.1002/adma.201600709>.
- (328) Lu, Z.; Zhang, H.; Mao, C.; Li, C. M. Silk Fabric-Based Wearable Thermoelectric Generator for Energy Harvesting from the Human Body. *Appl. Energy* **2016**, *164*, 57–63. <https://doi.org/10.1016/j.apenergy.2015.11.038>.
- (329) Wang, D.; Zhang, H.; Arens, E.; Huizenga, C. Observations of Upper-Extremity Skin Temperature and Corresponding Overall-Body Thermal Sensations and Comfort. *Build. Environ.* **2007**, *42* (12), 3933–3943. <https://doi.org/10.1016/j.buildenv.2006.06.035>.
- (330) Lan, L.; Wargocki, P.; Wyon, D. P.; Lian, Z. Effects of Thermal Discomfort in an Office on Perceived Air Quality, SBS Symptoms, Physiological Responses, and Human Performance. *Indoor Air* **2011**, *21* (5), 376–390. <https://doi.org/10.1111/j.1600-0668.2011.00714.x>.
- (331) Jay, O.; Reardon, F. D.; Webb, P.; DuCharme, M. B.; Ramsay, T.; Nettlefold, L.; Kenny, G. P. Estimating Changes in Mean Body Temperature for Humans during Exercise Using Core and Skin Temperatures Is Inaccurate Even with a Correction Factor. *J. Appl. Physiol.* **2007**, *103* (2), 443–451. <https://doi.org/10.1152/jappphysiol.00117.2007>.
- (332) Kim, S. J.; We, J. H.; Cho, B. J. A Wearable Thermoelectric Generator Fabricated on a Glass Fabric. *Energy Environ. Sci.* **2014**, *7* (6), 1959–1965. <https://doi.org/10.1039/c4ee00242c>.

- (333) Yadav, A.; Pipe, K. P.; Shtein, M. Fiber-Based Flexible Thermoelectric Power Generator. *J. Power Sources* **2008**, *175* (2), 909–913. <https://doi.org//dx.doi.org/10.1016/j.jpowsour.2007.09.096>.
- (334) Shin, S.; Kumar, R.; Roh, J. W.; Ko, D.-S.; Kim, H.-S.; Kim, S. I.; Yin, L.; Schlossberg, S. M.; Cui, S.; You, J.-M.; Kwon, S.; Zheng, J.; Wang, J.; Chen, R. High-Performance Screen-Printed Thermoelectric Films on Fabrics. *Sci. Rep.* **2017**, *7* (1), 1–9. <https://doi.org/10.1038/s41598-017-07654-2>.
- (335) Liang, D.; Yang, H.; Finefrock, S. W.; Wu, Y. Flexible Nanocrystal-Coated Glass Fibers for High-Performance Thermoelectric Energy Harvesting. *Nano Lett.* **2012**, *12* (4), 2140–2145. <https://doi.org/10.1021/nl300524j>.
- (336) Kishore, R. A.; Nozariasbmarz, A.; Poudel, B.; Sanghadasa, M.; Priya, S. Ultra-High Performance Wearable Thermoelectric Coolers with Less Materials. *Nat. Commun.* **2019**, *10* (1), 1765–13. <https://doi.org/10.1038/s41467-019-09707-8>.
- (337) Lee, D.; Park, H.; Park, G.; Kim, J.; Kim, H.; Cho, H.; Han, S.; Kim, W. Liquid-Metal-Electrode-Based Compact, Flexible, and High-Power Thermoelectric Device. *Energy* **2019**, *188* (Journal Article), 116019.
- (338) Park, H.; Lee, D.; Kim, D.; Cho, H.; Eom, Y.; Hwang, J.; Kim, H.; Kim, J.; Han, S.; Kim, W. High Power Output from Body Heat Harvesting Based on Flexible Thermoelectric System with Low Thermal Contact Resistance. *J. Phys. Appl. Phys.* **2018**, *51* (36), 365501. <https://doi.org/10.1088/1361-6463/aad270>.
- (339) Park, H.; Kim, D.; Eom, Y.; Wijethunge, D.; Hwang, J.; Kim, H.; Kim, W. Mat-like Flexible Thermoelectric System Based on Rigid Inorganic Bulk Materials. *J. Phys. Appl. Phys.* **2017**, *50* (49), 494006. <https://doi.org/10.1088/1361-6463/aa94f7>.
- (340) Zhang, L.; Lin, S.; Hua, T.; Huang, B.; Liu, S.; Tao, X. Fiber-Based Thermoelectric Generators: Materials, Device Structures, Fabrication, Characterization, and Applications. *Adv. Energy Mater.* **2018**, *8* (5), 1700524. <https://doi.org/10.1002/aenm.201700524>.
- (341) Heeger, A. J. Semiconducting and Metallic Polymers: The Fourth Generation of Polymeric Materials. *J. Phys. Chem. B* **2001**, *105* (36), 8475–8491. <https://doi.org/10.1021/jp011611w>.
- (342) Elmoughni, H. M.; Menon, A. K.; Wolfe, R. M. W.; Yee, S. K. A Textile-Integrated Polymer Thermoelectric Generator for Body Heat Harvesting. *Adv. Mater. Technol.* **2019**, *4* (7), 1800708. <https://doi.org/10.1002/admt.201800708>.
- (343) Anthony, J. E.; Facchetti, A.; Heeney, M.; Marder, S. R.; Zhan, X. N-Type Organic Semiconductors in Organic Electronics. *Adv. Mater.* **2010**, *22* (34), 3876–3892. <https://doi.org/10.1002/adma.200903628>.
- (344) Bredas, J. L.; Street, G. B. Polarons, Bipolarons, and Solitons in Conducting Polymers. *Acc. Chem. Res.* **1985**, *18* (10), 309–315. <https://doi.org/10.1021/ar00118a005>.
- (345) Walzer, K.; Maennig, B.; Pfeiffer, M.; Leo, K. Highly Efficient Organic Devices Based on Electrically Doped Transport Layers. *Chem. Rev.* **2007**, *107* (4), 1233–1271. <https://doi.org/10.1021/cr050156n>.
- (346) Heeger, A. J.; Kivelson, S.; Schrieffer, J. R.; Su, W.-P. Solitons in Conducting Polymers. *Rev. Mod. Phys.* **1988**, *60* (3), 781–850. <https://doi.org/10.1103/RevModPhys.60.781>.
- (347) Heeger, A. J. Semiconducting Polymers: The Third Generation. *Chem. Soc. Rev.* **2010**, *39* (7), 2354–2371. <https://doi.org/10.1039/B914956M>.
- (348) Noriega, R.; Rivnay, J.; Vandewal, K.; Koch, F. P. V.; Stingelin, N.; Smith, P.; Toney, M. F.; Salleo, A. A General Relationship between Disorder, Aggregation and Charge

- Transport in Conjugated Polymers. *Nat. Mater.* **2013**, *12* (11), 1038–1044.  
<https://doi.org/10.1038/nmat3722>.
- (349) Shirakawa, H.; Louis, E. J.; MacDiarmid, A. G.; Chiang, C. K.; Heeger, A. J. Synthesis of Electrically Conducting Organic Polymers: Halogen Derivatives of Polyacetylene, (CH). *J. Chem. Soc. Chem. Commun.* **1977**, No. 16, 578–580.  
<https://doi.org/10.1039/C39770000578>.
- (350) Pukacki, W.; Płocharski, J.; Roth, S. Anisotropy of Thermoelectric Power of Stretch-Oriented New Polyacetylene. *Synth. Met.* **1994**, *62* (3), 253–256.  
[https://doi.org/10.1016/0379-6779\(94\)90213-5](https://doi.org/10.1016/0379-6779(94)90213-5).
- (351) Kaiser, A. B.; Rogers, S. A.; Park, Y. W. Charge Transport in Conducting Polymers: Polyacetylene Nanofibres. *Mol. Cryst. Liq. Cryst.* **2004**, *415* (1), 115–124.  
<https://doi.org/10.1080/15421400490481421>.
- (352) Kemp, N. T.; Kaiser, A. B.; Liu, C.-J.; Chapman, B.; Mercier, O.; Carr, A. M.; Trodahl, H. J.; Buckley, R. G.; Partridge, A. C.; Lee, J. Y.; Kim, C. Y.; Bartl, A.; Dunsch, L.; Smith, W. T.; Shapiro, J. S. Thermoelectric Power and Conductivity of Different Types of Polypyrrole. *J. Polym. Sci. Part B Polym. Phys.* **1999**, *37* (9), 953–960.  
[https://doi.org/10.1002/\(SICI\)1099-0488\(19990501\)37:9<953::AID-POLB7>3.0.CO;2-L](https://doi.org/10.1002/(SICI)1099-0488(19990501)37:9<953::AID-POLB7>3.0.CO;2-L).
- (353) Wu, J.; Sun, Y.; Pei, W.-B.; Huang, L.; Xu, W.; Zhang, Q. Polypyrrole Nanotube Film for Flexible Thermoelectric Application. *Synth. Met.* **2014**, *196* (Journal Article), 173–177.  
<https://doi.org/10.1016/j.synthmet.2014.08.001>.
- (354) Yakuphanoglu, F.; Şenkal, B. Fi.; Saraç, A. Electrical Conductivity, Thermoelectric Power, and Optical Properties of Organo-Soluble Polyaniline Organic Semiconductor. *J. Electron. Mater.* **2008**, *37* (6), 930–934. <https://doi.org/10.1007/s11664-008-0404-9>.
- (355) Yan, H.; Sada, N.; Toshima, N. Thermal Transporting Properties of Electrically Conductive Polyaniline Films as Organic Thermoelectric Materials. *J. Therm. Anal. Calorim.* **2002**, *69* (3), 881–887. <https://doi.org/10.1023/A:1020612123826>.
- (356) Bao-Yang, L.; Cong-Cong, L.; Shan, L.; Jing-Kun, X.; Feng-Xing, J.; Yu-Zhen, L.; Zhuo, Z. Thermoelectric Performances of Free-Standing Polythiophene and Poly(3-Methylthiophene) Nanofilms. *Chin. Phys. Lett.* **2010**, *27* (5), 057201.  
<https://doi.org/10.1088/0256-307X/27/5/057201>.
- (357) Hiraishi, K.; Masuhara, A.; Nakanishi, H.; Oikawa, H.; Shinohara, Y. Evaluation of Thermoelectric Properties of Polythiophene Films Synthesized by Electrolytic Polymerization. *Jpn. J. Appl. Phys.* **2009**, *48* (7R), 071501.  
<https://doi.org/10.1143/JJAP.48.071501>.
- (358) Lévesque, I.; Bertrand, P.-O.; Blouin, N.; Leclerc, M.; Zecchin, S.; Zotti, G.; Ratcliffe, C. I.; Klug, D. D.; Gao, X.; Gao, F.; Tse, J. S. Synthesis and Thermoelectric Properties of Polycarbazole, Polyindolocarbazole, and Polydiindolocarbazole Derivatives. *Chem. Mater.* **2007**, *19* (8), 2128–2138. <https://doi.org/10.1021/cm070063h>.
- (359) Yao, C.-J.; Zhang, H.-L.; Zhang, Q. Recent Progress in Thermoelectric Materials Based on Conjugated Polymers. *Polymers* **2019**, *11* (1), 107.  
<https://doi.org/10.3390/polym11010107>.
- (360) Dubey, N.; Leclerc, M. Conducting Polymers: Efficient Thermoelectric Materials. *J. Polym. Sci. Part B Polym. Phys.* **2011**, *49* (7), 467–475.  
<https://doi.org/10.1002/polb.22206>.
- (361) Jia, Y.; Shen, L.; Liu, J.; Zhou, W.; Du, Y.; Xu, J.; Liu, C.; Zhang, G.; Zhang, Z.; Jiang, F. An Efficient PEDOT-Coated Textile for Wearable Thermoelectric Generators and Strain

- Sensors. *J. Mater. Chem. C* **2019**, *7* (12), 3496–3502.  
<https://doi.org/10.1039/C8TC05906C>.
- (362) Khoso, N. A.; Ahmed, A.; Deb, H.; Tian, S.; Jiao, X.; Gong, X. Y.; Wang, J. Controlled Template-Free in-Situ Polymerization of PEDOT for Enhanced Thermoelectric Performance on Textile Substrate. *Org. Electron.* **2019**, *75*, 105368.  
<https://doi.org/10.1016/j.orgel.2019.07.026>.
- (363) Kirihara, K.; Wei, Q.; Mukaida, M.; Ishida, T. Thermoelectric Power Generation Using Nonwoven Fabric Module Impregnated with Conducting Polymer PEDOT:PSS. *Synth. Met.* **2017**, *225*, 41–48. <https://doi.org/10.1016/j.synthmet.2017.01.001>.
- (364) Trindade, I. G.; Matos, J.; Lucas, J.; Miguel, R.; Pereira, M.; Silva, M. S. Synthesis of Poly(3, 4-Ethylenedioxythiophene) Coating on Textiles by the Vapor Phase Polymerization Method: *Text. Res. J.* **2014**. <https://doi.org/10.1177/0040517514545259>.
- (365) Torah, R.; Lawrie-Ashton, J.; Li, Y.; Arumugam, S.; Sodano, H. A.; Beeby, S. Energy-Harvesting Materials for Smart Fabrics and Textiles. *MRS Bull.* **2018**, *43* (3), 214–219.  
<https://doi.org/10.1557/mrs.2018.9>.
- (366) Li, P.; Guo, Y.; Mu, J.; Wang, H.; Zhang, Q.; Li, Y. Single-Walled Carbon Nanotubes/Polyaniline-Coated Polyester Thermoelectric Textile with Good Interface Stability Prepared by Ultrasonic Induction. *RSC Adv.* **2016**, *6* (93), 9347–9353.  
<https://doi.org/10.1039/c6ra16532j>.
- (367) Tissera, N. D.; Wijesena, R. N.; Rathnayake, S.; de Silva, R. M.; de Silva, K. M. N. Heterogeneous in Situ Polymerization of Polyaniline (PANI) Nanofibers on Cotton Textiles: Improved Electrical Conductivity, Electrical Switching, and Tuning Properties. *Carbohydr. Polym.* **2018**, *186*, 35–44. <https://doi.org/10.1016/j.carbpol.2018.01.027>.
- (368) Seeberg, T. M.; Røyset, A.; Jähren, S.; Strisland, F. Printed Organic Conductive Polymers Thermocouples in Textile and Smart Clothing Applications. In *2011 Annual International Conference of the IEEE Engineering in Medicine and Biology Society*; IEEE: Boston, MA, USA, 2011; pp 3278–3281. <https://doi.org/10.1109/IEMBS.2011.6090890>.
- (369) Sumino, M.; Harada, K.; Ikeda, M.; Tanaka, S.; Miyazaki, K.; Adachi, C. Thermoelectric Properties of N-Type C60 Thin Films and Their Application in Organic Thermovoltaic Devices. *Appl. Phys. Lett.* **2011**, *99* (9), 093308. <https://doi.org/10.1063/1.3631633>.
- (370) Inabe, T.; Ogata, H.; Maruyama, Y.; Achiba, Y.; Suzuki, S.; Kikuchi, K.; Ikemoto, I. Electronic Structure of Alkali Metal Doped C60 Derived from Thermoelectric Power Measurements. *Phys. Rev. Lett.* **1992**, *69* (26), 3797–3799.  
<https://doi.org/10.1103/PhysRevLett.69.3797>.
- (371) Sun, Y.; Qiu, L.; Tang, L.; Geng, H.; Wang, H.; Zhang, F.; Huang, D.; Xu, W.; Yue, P.; Guan, Y.; Jiao, F.; Sun, Y.; Tang, D.; Di, C.; Yi, Y.; Zhu, D. Flexible N-Type High-Performance Thermoelectric Thin Films of Poly(Nickel-Ethylenetetra-thiolate) Prepared by an Electrochemical Method. *Adv. Mater.* **2016**, *28* (17), 3351–3358.  
<https://doi.org/10.1002/adma.201505922>.
- (372) Huang, D.; Yao, H.; Cui, Y.; Zou, Y.; Zhang, F.; Wang, C.; Shen, H.; Jin, W.; Zhu, J.; Diao, Y.; Xu, W.; Di, C.; Zhu, D. Conjugated-Backbone Effect of Organic Small Molecules for n-Type Thermoelectric Materials with ZT over 0.2. *J. Am. Chem. Soc.* **2017**, *139* (37), 13013–13023. <https://doi.org/10.1021/jacs.7b05344>.
- (373) Schlitz, R. A.; Brunetti, F. G.; Glauddell, A. M.; Miller, P. L.; Brady, M. A.; Takacs, C. J.; Hawker, C. J.; Chabynyc, M. L. Solubility-Limited Extrinsic n-Type Doping of a High

- Electron Mobility Polymer for Thermoelectric Applications. *Adv. Mater.* **2014**, *26* (18), 2825–2830. <https://doi.org/10.1002/adma.201304866>.
- (374) Shi, K.; Zhang, F.; Di, C.-A.; Yan, T.-W.; Zou, Y.; Zhou, X.; Zhu, D.; Wang, J.-Y.; Pei, J. Toward High Performance N-Type Thermoelectric Materials by Rational Modification of BDPPV Backbones. *J. Am. Chem. Soc.* **2015**, *137* (22), 6979–6982. <https://doi.org/10.1021/jacs.5b00945>.
- (375) Wei, P.; Oh, J. H.; Dong, G.; Bao, Z. Use of a 1H-Benzoimidazole Derivative as an n-Type Dopant and To Enable Air-Stable Solution-Processed n-Channel Organic Thin-Film Transistors. *J. Am. Chem. Soc.* **2010**, *132* (26), 8852–8853. <https://doi.org/10.1021/ja103173m>.
- (376) Serrano-Claumarchirant, J. F.; Culebras, M.; Muñoz-Espí, R.; Cantarero, A.; Gómez, C. M.; Collins, M. N. PEDOT Thin Films with N-Type Thermopower. *ACS Appl. Energy Mater.* **2020**, *3* (1), 861–867. <https://doi.org/10.1021/acsaem.9b01985>.
- (377) Wolfe, R. M. W.; Menon, A. K.; Fletcher, T. R.; Marder, S. R.; Reynolds, J. R.; Yee, S. K. Simultaneous Enhancement in Electrical Conductivity and Thermopower of N-Type NiETT/PVDF Composite Films by Annealing. *Adv. Funct. Mater.* **2018**, *28* (37), 1803275. <https://doi.org/10.1002/adfm.201803275>.
- (378) Menon, A. K.; Wolfe, R. M. W.; Marder, S. R.; Reynolds, J. R.; Yee, S. K. Systematic Power Factor Enhancement in N-Type NiETT/PVDF Composite Films. *Adv. Funct. Mater.* **2018**, *28* (29), 1801620. <https://doi.org/10.1002/adfm.201801620>.
- (379) Gordiz, K.; Menon, A. K.; Yee, S. K. Interconnect Patterns for Printed Organic Thermoelectric Devices with Large Fill Factors. *J. Appl. Phys.* **2017**, *122* (12), 124507. <https://doi.org/10.1063/1.4989589>.
- (380) Yao, Q.; Chen, L.; Zhang, W.; Liufu, S.; Chen, X. Enhanced Thermoelectric Performance of Single-Walled Carbon Nanotubes/Polyaniline Hybrid Nanocomposites. *ACS Nano* **2010**, *4* (4), 2445–2451. <https://doi.org/10.1021/nn1002562>.
- (381) Bounioux, C.; Díaz-Chao, P.; Campoy-Quiles, M.; S. Martín-González, M.; R. Goñi, A.; Yerushalmi-Rozen, R.; Müller, C. Thermoelectric Composites of Poly(3-Hexylthiophene) and Carbon Nanotubes with a Large Power Factor. *Energy Environ. Sci.* **2013**, *6* (3), 918–925. <https://doi.org/10.1039/C2EE23406H>.
- (382) Liu, J.; Sun, J.; Gao, L. Flexible Single-Walled Carbon Nanotubes /Polyaniline Composite Films and Their Enhanced Thermoelectric Properties. *Nanoscale* **2011**, *3* (9), 3616–3619. <https://doi.org/10.1039/C1NR10386E>.
- (383) Wang, J.; Cai, K.; Shen, S.; Yin, J. Preparation and Thermoelectric Properties of Multi-Walled Carbon Nanotubes/Polypyrrole Composites. *Synth. Met.* **2014**, *195*, 132–136. <https://doi.org/10.1016/j.synthmet.2014.06.003>.
- (384) Du, Y.; Shen, S. Z.; Yang, W.; Donelson, R.; Cai, K.; Casey, P. S. Simultaneous Increase in Conductivity and Seebeck Coefficient in a Polyaniline/Graphene Nanosheets Thermoelectric Nanocomposite. *Synth. Met.* **2012**, *161* (23), 2688–2692. <https://doi.org/10.1016/j.synthmet.2011.09.044>.
- (385) Xiang, J.; Drzal, L. T. Improving Thermoelectric Properties of Graphene/Polyaniline Paper by Folding. *Chem. Phys. Lett.* **2014**, *593*, 109–114. <https://doi.org/10.1016/j.cplett.2013.12.079>.
- (386) Kim, G. H.; Hwang, D. H.; Woo, S. I. Thermoelectric Properties of Nanocomposite Thin Films Prepared with Poly(3,4-Ethylenedioxythiophene) Poly(Styrenesulfonate) and

- Graphene. *Phys. Chem. Chem. Phys.* **2012**, *14* (10), 3530–3536.  
<https://doi.org/10.1039/C2CP23517J>.
- (387) Du, Y.; Cai, K. F.; Shen, S. Z.; Casey, P. S. Preparation and Characterization of Graphene Nanosheets/Poly(3-Hexylthiophene) Thermoelectric Composite Materials. *Synth. Met.* **2012**, *162* (23), 2102–2106. <https://doi.org/10.1016/j.synthmet.2012.09.011>.
- (388) Mitra, M.; Kulsi, C.; Chatterjee, K.; Kargupta, K.; Ganguly, S.; Banerjee, D.; Goswami, S. Reduced Graphene Oxide-Polyaniline Composites—Synthesis, Characterization and Optimization for Thermoelectric Applications. *RSC Adv.* **2015**, *5* (39), 31039–31048.  
<https://doi.org/10.1039/C5RA01794G>.
- (389) Li, F.; Cai, K.; Shen, S.; Chen, S. Preparation and Thermoelectric Properties of Reduced Graphene Oxide/PEDOT:PSS Composite Films. *Synth. Met.* **2014**, *197*, 58–61.  
<https://doi.org/10.1016/j.synthmet.2014.08.014>.
- (390) Lee, C.; Wei, X.; Kysar, J. W.; Hone, J. Measurement of the Elastic Properties and Intrinsic Strength of Monolayer Graphene. *Science* **2008**, *321* (5887), 385–388.  
<https://doi.org/10.1126/science.1157996>.
- (391) Novoselov, K. S.; Geim, A. K.; Morozov, S. V.; Jiang, D.; Zhang, Y.; Dubonos, S. V.; Grigorieva, I. V.; Firsov, A. A. Electric Field Effect in Atomically Thin Carbon Films. *Science* **2004**, *306* (5696), 666–669. <https://doi.org/10.1126/science.1102896>.
- (392) Geim, A. K.; Novoselov, K. S. The Rise of Graphene. *Nat. Mater.* **2007**, *6* (3), 183–191.  
<https://doi.org/10.1038/nmat1849>.
- (393) Balandin, A. A. Thermal Properties of Graphene and Nanostructured Carbon Materials. *Nat. Mater.* **2011**, *10* (8), 569–581. <https://doi.org/10.1038/nmat3064>.
- (394) Falkovsky, L. A. Optical Properties of Graphene. *J. Phys. Conf. Ser.* **2008**, *129*, 012004.  
<https://doi.org/10.1088/1742-6596/129/1/012004>.
- (395) Ahn, J.-H.; Hong, B. H. Graphene for Displays That Bend. *Nat. Nanotechnol.* **2014**, *9* (10), 737–738. <https://doi.org/10.1038/nnano.2014.226>.
- (396) Cheng, Y.; Wang, R.; Sun, J.; Gao, L. A Stretchable and Highly Sensitive Graphene-Based Fiber for Sensing Tensile Strain, Bending, and Torsion. *Adv. Mater.* **2015**, *27* (45), 7365–7371. <https://doi.org/10.1002/adma.201503558>.
- (397) Capasso, A.; Del Rio Castillo, A. E.; Sun, H.; Ansaldo, A.; Pellegrini, V.; Bonaccorso, F. Ink-Jet Printing of Graphene for Flexible Electronics: An Environmentally-Friendly Approach. *Solid State Commun.* **2015**, *224*, 53–63.  
<https://doi.org/10.1016/j.ssc.2015.08.011>.
- (398) Du, P.; Hu, X.; Yi, C.; Liu, H. C.; Liu, P.; Zhang, H.-L.; Gong, X. Self-Powered Electronics by Integration of Flexible Solid-State Graphene-Based Supercapacitors with High Performance Perovskite Hybrid Solar Cells. *Adv. Funct. Mater.* **2015**, *25* (16), 2420–2427. <https://doi.org/10.1002/adfm.201500335>.
- (399) Pop, E.; Sinha, S.; Goodson, K. E. Heat Generation and Transport in Nanometer-Scale Transistors. *Proc. IEEE* **2006**, *94* (8), 1587–1601.  
<https://doi.org/10.1109/JPROC.2006.879794>.
- (400) Seol, J. H.; Jo, I.; Moore, A. L.; Lindsay, L.; Aitken, Z. H.; Pettes, M. T.; Li, X.; Yao, Z.; Huang, R.; Broido, D.; Mingo, N.; Ruoff, R. S.; Shi, L. Two-Dimensional Phonon Transport in Supported Graphene. *Science* **2010**, *328* (5975), 213–216.  
<https://doi.org/10.1126/science.1184014>.

- (401) Ni, X.; Liang, G.; Wang, J.-S.; Li, B. Disorder Enhances Thermoelectric Figure of Merit in Armchair Graphane Nanoribbons. *Appl. Phys. Lett.* **2009**, *95* (19), 192114. <https://doi.org/10.1063/1.3264087>.
- (402) Karamitaheri, H.; Neophytou, N.; Pourfath, M.; Faez, R.; Kosina, H. Engineering Enhanced Thermoelectric Properties in Zigzag Graphene Nanoribbons. *J. Appl. Phys.* **2012**, *111* (5), 054501. <https://doi.org/10.1063/1.3688034>.
- (403) Ouyang, Y.; Guo, J. A Theoretical Study on Thermoelectric Properties of Graphene Nanoribbons. *Appl. Phys. Lett.* **2009**, *94* (26), 263107. <https://doi.org/10.1063/1.3171933>.
- (404) Tapasztó, L.; Dobrik, G.; Lambin, P.; Biró, L. P. Tailoring the Atomic Structure of Graphene Nanoribbons by Scanning Tunnelling Microscope Lithography. *Nat. Nanotechnol.* **2008**, *3* (7), 397–401. <https://doi.org/10.1038/nnano.2008.149>.
- (405) Zheng, H.; Liu, H. J.; Tan, X. J.; Lv, H. Y.; Pan, L.; Shi, J.; Tang, X. F. Enhanced Thermoelectric Performance of Graphene Nanoribbons. *Appl. Phys. Lett.* **2012**, *100* (9), 093104. <https://doi.org/10.1063/1.3689780>.
- (406) Savin, A. V.; Kivshar, Y. S.; Hu, B. Suppression of Thermal Conductivity in Graphene Nanoribbons with Rough Edges. *Phys. Rev. B* **2010**, *82* (19), 195422. <https://doi.org/10.1103/PhysRevB.82.195422>.
- (407) Hu, J.; Schiffl, S.; Vallabhaneni, A.; Ruan, X.; Chen, Y. P. Tuning the Thermal Conductivity of Graphene Nanoribbons by Edge Passivation and Isotope Engineering: A Molecular Dynamics Study. *Appl. Phys. Lett.* **2010**, *97* (13), 133107. <https://doi.org/10.1063/1.3491267>.
- (408) Jiang, J.-W.; Lan, J.; Wang, J.-S.; Li, B. Isotopic Effects on the Thermal Conductivity of Graphene Nanoribbons: Localization Mechanism. *J. Appl. Phys.* **2010**, *107* (5), 054314. <https://doi.org/10.1063/1.3329541>.
- (409) Guo, Z.; Zhang, D.; Gong, X.-G. Thermal Conductivity of Graphene Nanoribbons. *Appl. Phys. Lett.* **2009**, *95* (16), 163103. <https://doi.org/10.1063/1.3246155>.
- (410) Yang, K.; Chen, Y.; D'Agosta, R.; Xie, Y.; Zhong, J.; Rubio, A. Enhanced Thermoelectric Properties in Hybrid Graphene/Boron Nitride Nanoribbons. *Phys. Rev. B* **2012**, *86* (4), 045425. <https://doi.org/10.1103/PhysRevB.86.045425>.
- (411) Haskins, J.; Kınacı, A.; Sevik, C.; Sevinçli, H.; Cuniberti, G.; Çağın, T. Control of Thermal and Electronic Transport in Defect-Engineered Graphene Nanoribbons. *ACS Nano* **2011**, *5* (5), 3779–3787. <https://doi.org/10.1021/nn200114p>.
- (412) Chang, P.-H.; Nikolić, B. K. Edge Currents and Nanopore Arrays in Zigzag and Chiral Graphene Nanoribbons as a Route toward High-ZT Thermoelectrics. *Phys. Rev. B* **2012**, *86* (4), 041406. <https://doi.org/10.1103/PhysRevB.86.041406>.
- (413) Karamitaheri, H.; Pourfath, M.; Faez, R.; Kosina, H. Geometrical Effects on the Thermoelectric Properties of Ballistic Graphene Antidot Lattices. *J. Appl. Phys.* **2011**, *110* (5), 054506. <https://doi.org/10.1063/1.3629990>.
- (414) Xiang, J.; Drzal, L. T. Templated Growth of Polyaniline on Exfoliated Graphene Nanoplatelets (GNP) and Its Thermoelectric Properties. *Polymer* **2012**, *53* (19), 4202–4210. <https://doi.org/10.1016/j.polymer.2012.07.029>.
- (415) Zhang, Z.; Qiu, J.; Wang, S. Roll-to-Roll Printing of Flexible Thin-Film Organic Thermoelectric Devices. *Manuf. Lett.* **2016**, *8*, 6–10. <https://doi.org/10.1016/j.mfglet.2016.04.002>.
- (416) Hsieh, Y.-Y.; Zhang, Y.; Zhang, L.; Fang, Y.; Narayan Kanakaraaj, S.; Bahk, J.-H.; Shanov, V. High Thermoelectric Power-Factor Composites Based on Flexible Three-

- Dimensional Graphene and Polyaniline. *Nanoscale* **2019**, *11* (14), 6552–6560. <https://doi.org/10.1039/C8NR10537E>.
- (417) Novak, T. G.; Kim, J.; Kim, J.; Shin, H.; Tiwari, A. P.; Song, J. Y.; Jeon, S. Flexible Thermoelectric Films with High Power Factor Made of Non-Oxidized Graphene Flakes. *2D Mater.* **2019**, *6* (4), 045019. <https://doi.org/10.1088/2053-1583/ab2c32>.
- (418) Zeng, W.; Tao, X.-M.; Lin, S.; Lee, C.; Shi, D.; Lam, K.; Huang, B.; Wang, Q.; Zhao, Y. Defect-Engineered Reduced Graphene Oxide Sheets with High Electric Conductivity and Controlled Thermal Conductivity for Soft and Flexible Wearable Thermoelectric Generators. *Nano Energy* **2018**, *54*, 163–174. <https://doi.org/10.1016/j.nanoen.2018.10.015>.
- (419) Guo, Y.; Mu, J.; Hou, C.; Wang, H.; Zhang, Q.; Li, Y. Flexible and Thermostable Thermoelectric Devices Based on Large-Area and Porous All-Graphene Films. *Carbon* **2016**, *107*, 146–153. <https://doi.org/10.1016/j.carbon.2016.05.063>.
- (420) Wang, L.; Yao, Q.; Bi, H.; Huang, F.; Wang, Q.; Chen, L. Large Thermoelectric Power Factor in Polyaniline/Graphene Nanocomposite Films Prepared by Solution-Assistant Dispersing Method. *J. Mater. Chem. A* **2014**, *2* (29), 11107–11113. <https://doi.org/10.1039/C4TA01541J>.
- (421) Li, T.; Pickel, A. D.; Yao, Y.; Chen, Y.; Zeng, Y.; Lacey, S. D.; Li, Y.; Wang, Y.; Dai, J.; Wang, Y.; Yang, B.; Fuhrer, M. S.; Marconnet, A.; Dames, C.; Drew, D. H.; Hu, L. Thermoelectric Properties and Performance of Flexible Reduced Graphene Oxide Films up to 3,000 K. *Nat. Energy* **2018**, *3* (2), 148–156. <https://doi.org/10.1038/s41560-018-0086-3>.
- (422) Han, S.; Zhai, W.; Chen, G.; Wang, X. Morphology and Thermoelectric Properties of Graphene Nanosheets Enwrapped with Polypyrrole. *RSC Adv.* **2014**, *4* (55), 29281–29285. <https://doi.org/10.1039/C4RA04003A>.
- (423) Xu, K.; Chen, G.; Qiu, D. In Situ Chemical Oxidative Polymerization Preparation of Poly(3,4-Ethylenedioxythiophene)/Graphene Nanocomposites with Enhanced Thermoelectric Performance. *Chem. – Asian J.* **2015**, *10* (5), 1225–1231. <https://doi.org/10.1002/asia.201500066>.
- (424) Park, C.; Yoo, D.; Im, S.; Kim, S.; Cho, W.; Ryu, J.; Hyun Kim, J. Large-Scalable RTCVD Graphene/PEDOT:PSS Hybrid Conductive Film for Application in Transparent and Flexible Thermoelectric Nanogenerators. *RSC Adv.* **2017**, *7* (41), 25237–25243. <https://doi.org/10.1039/C7RA02980B>.
- (425) Xiong, J.; Jiang, F.; Shi, H.; Xu, J.; Liu, C.; Zhou, W.; Jiang, Q.; Zhu, Z.; Hu, Y. Liquid Exfoliated Graphene as Dopant for Improving the Thermoelectric Power Factor of Conductive PEDOT:PSS Nanofilm with Hydrazine Treatment. *ACS Appl. Mater. Interfaces* **2015**, *7* (27), 14917–14925. <https://doi.org/10.1021/acsami.5b03692>.
- (426) Ma, W.; Liu, Y.; Shen, Y.; Miao, T.; Shi, S.; Yang, M.; Zhang, X.; Gao, C. Systematic Characterization of Transport and Thermoelectric Properties of a Macroscopic Graphene Fiber. *Nano Res. Beijing* **2016**, *9* (11), 3536–3546. <http://dx.doi.org/10.1007/s12274-016-1231-6>.
- (427) Ma, W.; Liu, Y.; Shen, Y.; Miao, T.; Shi, S.; Xu, Z.; Zhang, X.; Gao, C. Chemically Doped Macroscopic Graphene Fibers with Significantly Enhanced Thermoelectric Properties. *Nano Res. Beijing* **2018**, *11* (2), 741–750. <http://dx.doi.org/10.1007/s12274-017-1683-3>.

- (428) Hamada, N.; Sawada, S.; Oshiyama, A. New One-Dimensional Conductors: Graphitic Microtubules. *Phys. Rev. Lett.* **1992**, *68* (10), 1579–1581. <https://doi.org/10.1103/PhysRevLett.68.1579>.
- (429) Mintmire, J. W.; Dunlap, B. I.; White, C. T. Are Fullerene Tubules Metallic? *Phys. Rev. Lett.* **1992**, *68* (5), 631–634. <https://doi.org/10.1103/PhysRevLett.68.631>.
- (430) Venema, L. C.; Janssen, J. W.; Buitelaar, M. R.; Wildöer, J. W. G.; Lemay, S. G.; Kouwenhoven, L. P.; Dekker, C. Spatially Resolved Scanning Tunneling Spectroscopy on Single-Walled Carbon Nanotubes. *Phys. Rev. B* **2000**, *62* (8), 5238–5244. <https://doi.org/10.1103/PhysRevB.62.5238>.
- (431) Collins, P. G.; Bradley, K.; Ishigami, M.; Zettl, A. Extreme Oxygen Sensitivity of Electronic Properties of Carbon Nanotubes. *Science* **2000**, *287* (5459), 1801.
- (432) Zhou, W.; Fan, Q.; Zhang, Q.; Li, K.; Cai, L.; Gu, X.; Yang, F.; Zhang, N.; Xiao, Z.; Chen, H.; Xiao, S.; Wang, Y.; Liu, H.; Zhou, W.; Xie, S. Ultrahigh-Power-Factor Carbon Nanotubes and an Ingenious Strategy for Thermoelectric Performance Evaluation. *Small* **2016**, *12* (25), 3407–3414. <https://doi.org/10.1002/sml.201600501>.
- (433) Nonoguchi, Y.; Hata, K.; Kawai, T. Dispersion of Synthetic MoS<sub>2</sub> Flakes and Their Spontaneous Adsorption on Single-Walled Carbon Nanotubes. *ChemPlusChem* **2015**, *80* (7), 1158–1163. <https://doi.org/10.1002/cplu.201500084>.
- (434) Nonoguchi, Y.; Ohashi, K.; Kanazawa, R.; Ashiba, K.; Hata, K.; Nakagawa, T.; Adachi, C.; Tanase, T.; Kawai, T. Systematic Conversion of Single Walled Carbon Nanotubes into N-Type Thermoelectric Materials by Molecular Dopants. *Sci. Rep.* **2013**, *3* (1), 1–7. <https://doi.org/10.1038/srep03344>.
- (435) Yu, C.; Murali, A.; Choi, K.; Ryu, Y. Air-Stable Fabric Thermoelectric Modules Made of N- and P-Type Carbon Nanotubes. *Energy Environ. Sci.* **2012**, *5* (11), 9481–9486. <https://doi.org/10.1039/c2ee22838f>.
- (436) Kim, S. L.; Choi, K.; Tazebay, A.; Yu, C. Flexible Power Fabrics Made of Carbon Nanotubes for Harvesting Thermoelectricity. *ACS Nano* **2014**, *8* (3), 2377–2386. <https://doi.org/10.1021/nn405893t>.
- (437) Zheng, Y.; Zhang, Q.; Jin, W.; Jing, Y.; Chen, X.; Han, X.; Bao, Q.; Liu, Y.; Wang, X.; Wang, S.; Qiu, Y.; Di, C.; Zhang, K. Carbon Nanotube Yarn Based Thermoelectric Textiles for Harvesting Thermal Energy and Powering Electronics. *J. Mater. Chem. A* **2020**, *8* (6), 2984–2994. <https://doi.org/10.1039/C9TA12494B>.
- (438) Ryan, J. D.; Lund, A.; Hofmann, A. I.; Kroon, R.; Sarabia-Riquelme, R.; Weisenberger, M. C.; Müller, C. All-Organic Textile Thermoelectrics with Carbon-Nanotube-Coated n-Type Yarns. *ACS Appl. Energy Mater.* **2018**, *1* (6), 2934–2941. <https://doi.org/10.1021/acsaem.8b00617>.
- (439) Sarabia-Riquelme, R.; Craddock, J.; Morris, E. A.; Eaton, D.; Andrews, R.; Anthony, J.; Weisenberger, M. C. Simple, Low-Cost, Water-Processable n-Type Thermoelectric Composite Films from Multiwall Carbon Nanotubes in Polyvinylpyrrolidone. *Synth. Met.* **2017**, *225*, 86–92. <https://doi.org/10.1016/j.synthmet.2016.11.014>.
- (440) Aikawa, S.; Kim, S.; Thurakitserree, T.; Einarsson, E.; Inoue, T.; Chiashi, S.; Tsukagoshi, K.; Maruyama, S. Carrier Polarity Engineering in Carbon Nanotube Field-Effect Transistors by Induced Charges in Polymer Insulator. *Appl. Phys. Lett.* **2018**, *112* (1), 013501. <https://doi.org/10.1063/1.4994114>.

- (441) Hewitt, C. A.; Kaiser, A. B.; Roth, S.; Craps, M.; Czerw, R.; Carroll, D. L. Multilayered Carbon Nanotube/Polymer Composite Based Thermoelectric Fabrics. *Nano Lett.* **2012**, *12* (3), 1307–1310. <https://doi.org/10.1021/nl203806q>.
- (442) Luo, J.; Cerretti, G.; Krause, B.; Zhang, L.; Otto, T.; Jenschke, W.; Ullrich, M.; Tremel, W.; Voit, B.; Pötschke, P. Polypropylene-Based Melt Mixed Composites with Singlewalled Carbon Nanotubes for Thermoelectric Applications: Switching from p-Type to n-Type by the Addition of Polyethylene Glycol. *Polymer* **2017**, *108*, 513–520. <https://doi.org/10.1016/j.polymer.2016.12.019>.
- (443) Dörling, B.; Ryan, J. D.; Craddock, J. D.; Sorrentino, A.; Basaty, A. E.; Gomez, A.; Garriga, M.; Pereiro, E.; Anthony, J. E.; Weisenberger, M. C.; Goñi, A. R.; Müller, C.; Campoy-Quiles, M. Photoinduced P- to n-Type Switching in Thermoelectric Polymer-Carbon Nanotube Composites. *Adv. Mater.* **2016**, *28* (14), 2782–2789. <https://doi.org/10.1002/adma.201505521>.
- (444) Zhou, Y.; Fuentes-Hernandez, C.; Shim, J.; Meyer, J.; Giordano, A. J.; Li, H.; Winget, P.; Papadopoulos, T.; Cheun, H.; Kim, J.; Fenoll, M.; Dindar, A.; Haske, W.; Najafabadi, E.; Khan, T. M.; Sojoudi, H.; Barlow, S.; Graham, S.; Brédas, J.-L.; Marder, S. R.; Kahn, A.; Kippelen, B. A Universal Method to Produce Low-Work Function Electrodes for Organic Electronics. *Science* **2012**, *336* (6079), 327–332. <https://doi.org/10.1126/science.1218829>.
- (445) Ito, M.; Koizumi, T.; Kojima, H.; Saito, T.; Nakamura, M. From Materials to Device Design of a Thermoelectric Fabric for Wearable Energy Harvesters. *J. Mater. Chem. A* **2017**, *5* (24), 12068–12072. <https://doi.org/10.1039/C7TA00304H>.
- (446) Choi, J.; Jung, Y.; Yang, S. J.; Oh, J. Y.; Oh, J.; Jo, K.; Son, J. G.; Moon, S. E.; Park, C. R.; Kim, H. Flexible and Robust Thermoelectric Generators Based on All-Carbon Nanotube Yarn without Metal Electrodes. *ACS Nano* **2017**, *11* (8), 7608–7614. <https://doi.org/10.1021/acsnano.7b01771>.
- (447) Montgomery, D. S.; Hewitt, C. A.; Barbalace, R.; Jones, T.; Carroll, D. L. Spray Doping Method to Create a Low-Profile High-Density Carbon Nanotube Thermoelectric Generator. *Carbon* **2016**, *96*, 778–781. <https://doi.org/10.1016/j.carbon.2015.09.029>.
- (448) Jin, H.; Li, J.; Iocozzia, J.; Zeng, X.; Wei, P.-C.; Yang, C.; Li, N.; Liu, Z.; He, J. H.; Zhu, T.; Wang, J.; Lin, Z.; Wang, S. Hybrid Organic–Inorganic Thermoelectric Materials and Devices. *Angew. Chem. Int. Ed.* **2019**, *58* (43), 15206–15226. <https://doi.org/10.1002/anie.201901106>.
- (449) Wang, L.; Zhang, Z.; Geng, L.; Yuan, T.; Liu, Y.; Guo, J.; Fang, L.; Qiu, J.; Wang, S. Solution-Printable Fullerene/TiS<sub>2</sub> Organic/Inorganic Hybrids for High-Performance Flexible n-Type Thermoelectrics. *Energy Environ. Sci.* **2018**, *11* (5), 1307–1317. <https://doi.org/10.1039/C7EE03617E>.
- (450) Wang, L.; Zhang, Z.; Liu, Y.; Wang, B.; Fang, L.; Qiu, J.; Zhang, K.; Wang, S. Exceptional Thermoelectric Properties of Flexible Organic–inorganic Hybrids with Monodispersed and Periodic Nanophase. *Nat. Commun.* **2018**, *9* (1), 1–8. <https://doi.org/10.1038/s41467-018-06251-9>.
- (451) Du, Y.; Shen, S. Z.; Cai, K.; Casey, P. S. *Research Progress on Polymer–Inorganic Thermoelectric Nanocomposite Materials*; 2012; Vol. 37. <https://doi.org/10.1016/j.progpolymsci.2011.11.003>.
- (452) Anno, H.; Fukamoto, M.; Heta, Y.; Koga, K.; Itahara, H.; Asahi, R.; Satomura, R.; Sannomiya, M.; Toshima, N. Preparation of Conducting Polyaniline–Bismuth Nanoparticle

- Composites by Planetary Ball Milling. *J. Electron. Mater.* **2009**, *38* (7), 1443–1449. <https://doi.org/10.1007/s11664-009-0786-3>.
- (453) Liu, H.; Wang, J.; Hu, X.; Boughton, R. I.; Zhao, S.; Li, Q.; Jiang, M. Structure and Electronic Transport Properties of Polyaniline/NaFe<sub>4</sub>P<sub>12</sub> Composite. *Chem. Phys. Lett.* **2002**, *352* (3), 185–190. [https://doi.org/10.1016/S0009-2614\(01\)01389-6](https://doi.org/10.1016/S0009-2614(01)01389-6).
- (454) Wu, C.-G.; DeGroot, D. C.; Marcy, H. O.; Schindler, J. L.; Kannewurf, C. R.; Liu, Y.-J.; Hirpo, W.; Kanatzidis, M. G. Redox Intercalative Polymerization of Aniline in V<sub>2</sub>O<sub>5</sub> Xerogel. The Postintercalative Intralamellar Polymer Growth in Polyaniline/Metal Oxide Nanocomposites Is Facilitated by Molecular Oxygen. *Chem. Mater.* **1996**, *8* (8), 1992–2004. <https://doi.org/10.1021/cm9600236>.
- (455) Chatterjee, K.; Mitra, M.; Kargupta, K.; Ganguly, S.; Banerjee, D. Synthesis, Characterization and Enhanced Thermoelectric Performance of Structurally Ordered Cable-like Novel Polyaniline–Bismuth Telluride Nanocomposite. *Nanotechnology* **2013**, *24* (21), 215703. <https://doi.org/10.1088/0957-4484/24/21/215703>.
- (456) Xu, X.; Chen, L.; Wang, C.; Yao, Q.; Feng, C. Template Synthesis of Heterostructured Polyaniline/Bi<sub>2</sub>Te<sub>3</sub> Nanowires. *J. Solid State Chem.* **2005**, *178* (6), 2163–2166. <https://doi.org/10.1016/j.jssc.2005.03.036>.
- (457) Zhao, X. B.; Hu, S. H.; Zhao, M. J.; Zhu, T. J. Thermoelectric Properties of Bi<sub>0.5</sub>Sb<sub>1.5</sub>Te<sub>3</sub>/Polyaniline Hybrids Prepared by Mechanical Blending. *Mater. Lett.* **2002**, *52* (3), 147–149. [https://doi.org/10.1016/S0167-577X\(01\)00381-0](https://doi.org/10.1016/S0167-577X(01)00381-0).
- (458) Wang, Y. Y.; Cai, K. F.; Yin, J. L.; An, B. J.; Du, Y.; Yao, X. In Situ Fabrication and Thermoelectric Properties of PbTe–Polyaniline Composite Nanostructures. *J. Nanoparticle Res.* **2011**, *13* (2), 533–539. <https://doi.org/10.1007/s11051-010-0043-y>.
- (459) Song, H.; Cai, K. Preparation and Properties of PEDOT:PSS/Te Nanorod Composite Films for Flexible Thermoelectric Power Generator. *Energy* **2017**, *125*, 519–525. <https://doi.org/10.1016/j.energy.2017.01.037>.
- (460) Liu, C.; Jiang, F.; Huang, M.; Lu, B.; Yue, R.; Xu, J. Free-Standing PEDOT-PSS/Ca<sub>3</sub>Co<sub>4</sub>O<sub>9</sub> Composite Films as Novel Thermoelectric Materials. *J. Electron. Mater.* **2011**, *40* (5), 948–952. <https://doi.org/10.1007/s11664-010-1465-0>.
- (461) Selvaganesh, S. V.; Mathiyarasu, J.; Phani, K.; Yegnaraman, V. Chemical Synthesis of PEDOT–Au Nanocomposite. *Nanoscale Res. Lett.* **2007**, *2* (11), 546. <https://doi.org/10.1007/s11671-007-9100-6>.
- (462) Zhang, B.; Sun, J.; Katz, H. E.; Fang, F.; Opila, R. L. Promising Thermoelectric Properties of Commercial PEDOT:PSS Materials and Their Bi<sub>2</sub>Te<sub>3</sub> Powder Composites. *ACS Appl. Mater. Interfaces* **2010**, *2* (11), 3170–3178. <https://doi.org/10.1021/am100654p>.
- (463) Du, Y.; Cai, K. F.; Chen, S.; Cizek, P.; Lin, T. Facile Preparation and Thermoelectric Properties of Bi<sub>2</sub>Te<sub>3</sub> Based Alloy Nanosheet/PEDOT:PSS Composite Films. *ACS Appl. Mater. Interfaces* **2014**, *6* (8), 5735–5743. <https://doi.org/10.1021/am5002772>.
- (464) Ao, W. Q.; Wang, L.; Li, J. Q.; Pan, F.; Wu, C. N. Synthesis and Characterization of Polythiophene/Bi<sub>2</sub>Te<sub>3</sub> Nanocomposite Thermoelectric Material. *J. Electron. Mater.* **2011**, *40* (9), 2027. <https://doi.org/10.1007/s11664-011-1664-3>.
- (465) Du, Y.; Cai, K. F.; Shen, S. Z.; An, B.; Qin, Z.; Casey, P. S. Influence of Sintering Temperature on Thermoelectric Properties of Bi<sub>2</sub>Te<sub>3</sub>/Polythiophene Composite Materials. *J. Mater. Sci. Mater. Electron.* **2012**, *23* (4), 870–876. <https://doi.org/10.1007/s10854-011-0509-4>.

- (466) Toshima, N.; Imai, M.; Ichikawa, S. Organic–Inorganic Nanohybrids as Novel Thermoelectric Materials: Hybrids of Polyaniline and Bismuth(III) Telluride Nanoparticles. *J. Electron. Mater.* **2011**, *40* (5), 898–902. <https://doi.org/10.1007/s11664-010-1403-1>.
- (467) See, K. C.; Feser, J. P.; Chen, C. E.; Majumdar, A.; Urban, J. J.; Segalman, R. A. Water-Processable Polymer–Nanocrystal Hybrids for Thermoelectrics. *Nano Lett.* **2010**, *10* (11), 4664–4667. <https://doi.org/10.1021/nl102880k>.
- (468) Toshima, N.; Jiravanichanun, N.; Marutani, H. Organic Thermoelectric Materials Composed of Conducting Polymers and Metal Nanoparticles. *J. Electron. Mater.* **2012**, *41* (6), 1735–1742. <https://doi.org/10.1007/s11664-012-2041-6>.
- (469) Hu, X.; Zhang, K.; Zhang, J.; Wang, S.; Qiu, Y. Thermoelectric Properties of Conducting Polymer Nanowire–Tellurium Nanowire Composites. *ACS Appl. Energy Mater.* **2018**, *1* (9), 4883–4890. <https://doi.org/10.1021/acsaem.8b00909>.
- (470) Barbe, E. J. W. *Prehistoric Textiles : The Development of Cloth in the Neolithic and Bronze Ages with Special Reference to the Aegean*; Princeton University Press: Princeton, N.J., 1991.
- (471) Shao, H.; Wei, S.; Jiang, X.; Holmes, D. P.; Ghosh, T. K. Bistable Polymer Actuators: Bioinspired Electrically Activated Soft Bistable Actuators (*Adv. Funct. Mater.* 35/2018). *Adv. Funct. Mater.* **2018**, *28* (35).
- (472) Savage, N. Thermoelectric Coolers. *Nat. Photonics* **2009**, *3* (9), 541–542. <https://doi.org/10.1038/nphoton.2009.158>.
- (473) Zhao, D.; Tan, G. *A Review of Thermoelectric Cooling: Materials, Modeling and Applications*; 2014; Vol. 66. <https://doi.org/10.1016/j.applthermaleng.2014.01.074>.
- (474) Wu, Q.; Hu, J. A Novel Design for a Wearable Thermoelectric Generator Based on 3D Fabric Structure. *Smart Mater. Struct.* **2017**, *26* (4), 45037. <https://doi.org/10.1088/1361-665X/aa5694>.
- (475) Wu, Q.; Hu, J. Waterborne Polyurethane Based Thermoelectric Composites and Their Application Potential in Wearable Thermoelectric Textiles. *Compos. Part B* **2016**, *107* (Journal Article), 59–66. <https://doi.org/10.1016/j.compositesb.2016.09.068>.
- (476) Du, Y.; Cai, K.; Chen, S.; Wang, H.; Shen, S. Z.; Donelson, R.; Lin, T. Thermoelectric Fabrics: Toward Power Generating Clothing. *Sci. Rep.* **2015**, *5* (1), 6411. <https://doi.org/10.1038/srep06411>.
- (477) Du, Y.; Xu, J.; Wang, Y.; Lin, T. Thermoelectric Properties of Graphite-PEDOT:PSS Coated Flexible Polyester Fabrics. *J. Mater. Sci. Mater. Electron.* **2017**, *28* (8), 5796–5801. <https://doi.org/10.1007/s10854-016-6250-2>.
- (478) Park, K. T.; Choi, J.; Lee, B.; Ko, Y.; Jo, K.; Lee, Y. M.; Lim, J. A.; Park, C. R.; Kim, H. High-Performance Thermoelectric Bracelet Based on Carbon Nanotube Ink Printed Directly onto a Flexible Cable. *J. Mater. Chem. A* **2018**, *6* (40), 19727–19734. <https://doi.org/10.1039/C8TA08170K>.
- (479) Mohammadi, A.; Valipouri, A.; Salimian, S. Nanoparticle-Loaded Highly Flexible Fibrous Structures Exhibiting Desirable Thermoelectric Properties. *Diam. Relat. Mater.* **2018**, *86* (Journal Article), 54–62. <https://doi.org/10.1016/j.diamond.2018.04.018>.
- (480) Darian-Smith, I.; Johnson, Kenneth O. THERMAL SENSIBILITY AND THERMORECEPTORS. *J. Invest. Dermatol.* **1977**, *69* (1), 146–153. <https://doi.org/10.1111/1523-1747.ep12497936>.

- (481) C. Stevens Kenneth K. Choo, J. Temperature Sensitivity of the Body Surface over the Life Span. *Somatosens. Mot. Res.* **1998**, *15* (1), 13–28.  
<https://doi.org/10.1080/08990229870925>.
- (482) Tollefson, J. The hard truths of climate change — by the numbers  
<http://www.nature.com/articles/d41586-019-02711-4> (accessed Mar 30, 2020).
- (483) Suarez, F.; Parekh, D. P.; Ladd, C.; Vashae, D.; Dickey, M. D.; Öztürk, M. C. Flexible Thermoelectric Generator Using Bulk Legs and Liquid Metal Interconnects for Wearable Electronics. *Appl. Energy* **2017**, *202*, 736–745.  
<https://doi.org/10.1016/j.apenergy.2017.05.181>.
- (484) Hyland, M.; Hunter, H.; Liu, J.; Veety, E.; Vashae, D. Wearable Thermoelectric Generators for Human Body Heat Harvesting. *Appl. Energy* **2016**, *182*, 518–524.  
<https://doi.org/10.1016/j.apenergy.2016.08.150>.
- (485) Yazawa, K.; Shakouri, A. Cost-Efficiency Trade-off and the Design of Thermoelectric Power Generators. *Environ. Sci. Technol.* **2011**, *45* (17), 7548–7553.  
<https://doi.org/10.1021/es2005418>.
- (486) Madan, D.; Wang, Z.; Wright, P. K.; Evans, J. W. Printed Flexible Thermoelectric Generators for Use on Low Levels of Waste Heat. *Appl. Energy* **2015**, *156*, 587–592.  
<https://doi.org/10.1016/j.apenergy.2015.07.066>.
- (487) Kim, C. S.; Lee, G. S.; Choi, H.; Kim, Y. J.; Yang, H. M.; Lim, S. H.; Lee, S.-G.; Cho, B. J. Structural Design of a Flexible Thermoelectric Power Generator for Wearable Applications. *Appl. Energy* **2018**, *214*, 131–138.  
<https://doi.org/10.1016/j.apenergy.2018.01.074>.
- (488) Eom, Y.; Wijethunge, D.; Park, H.; Park, S. H.; Kim, W. Flexible Thermoelectric Power Generation System Based on Rigid Inorganic Bulk Materials. *Appl. Energy* **2017**, *206*, 649–656. <https://doi.org/10.1016/j.apenergy.2017.08.231>.
- (489) Wang, X.; Meng, F.; Tang, H.; Gao, Z.; Li, S.; Jin, S.; Jiang, Q.; Jiang, F.; Xu, J. Design and Fabrication of Low Resistance Palm-Power Generator Based on Flexible Thermoelectric Composite Film. *Synth. Met.* **2018**, *235*, 42–48.  
<https://doi.org/10.1016/j.synthmet.2017.11.010>.
- (490) Gayner, C.; Kar, K. K. Recent Advances in Thermoelectric Materials. *Prog. Mater. Sci.* **2016**, *83* (Journal Article), 330–382. <https://doi.org/10.1016/j.pmatsci.2016.07.002>.
- (491) Zhu, T.; Liu, Y.; Fu, C.; Heremans, J. P.; Snyder, J. G.; Zhao, X. Compromise and Synergy in High-Efficiency Thermoelectric Materials. *Adv. Mater.* **2017**, *29* (14), 1605884. <https://doi.org/10.1002/adma.201605884>.
- (492) Nakai, Y.; Honda, K.; Yanagi, K.; Kataura, H.; Kato, T.; Yamamoto, T.; Maniwa, Y. Giant Seebeck Coefficient in Semiconducting Single-Wall Carbon Nanotube Film. *Appl. Phys. Express* **2014**, *7* (2), 025103. <https://doi.org/10.7567/APEX.7.025103>.
- (493) Freeman, D. D.; Choi, K.; Yu, C. N-Type Thermoelectric Performance of Functionalized Carbon Nanotube-Filled Polymer Composites. *PLOS ONE* **2012**, *7* (11), e47822.  
<https://doi.org/10.1371/journal.pone.0047822>.
- (494) Meng, C.; Liu, C.; Fan, S. A Promising Approach to Enhanced Thermoelectric Properties Using Carbon Nanotube Networks. *Adv. Mater.* **2010**, *22* (4), 535–539.  
<https://doi.org/10.1002/adma.200902221>.
- (495) Hsu, K. F.; Loo, S.; Guo, F.; Chen, W.; Dyck, J. S.; Uher, C.; Hogan, T.; Polychroniadis, E. K.; Kanatzidis, M. G. Cubic AgPbmSbTe<sub>2+m</sub>: Bulk Thermoelectric Materials with

- High Figure of Merit. *Science* **2004**, *303* (5659), 818–821.  
<https://doi.org/10.1126/science.1092963>.
- (496) Fan, S.; Zhao, J.; Guo, J.; Yan, Q.; Ma, J.; Hng, H. H. P-Type Bi<sub>0.4</sub>Sb<sub>1.6</sub>Te<sub>3</sub> Nanocomposites with Enhanced Figure of Merit. *Appl. Phys. Lett.* **2010**, *96* (18), 182104.  
<https://doi.org/10.1063/1.3427427>.
- (497) Fu, C.; Zhu, T.; Liu, Y.; Xie, H.; Zhao, X. Band Engineering of High Performance P-Type FeNbSb Based Half-Heusler Thermoelectric Materials for Figure of Merit  $ZT > 1$ . *Energy Environ. Sci.* **2015**, *8* (1), 216–220. <https://doi.org/10.1039/C4EE03042G>.
- (498) Korkosz, R. J.; Chasapis, T. C.; Lo, S.; Doak, J. W.; Kim, Y. J.; Wu, C.-I.; Hatzikraniotis, E.; Hogan, T. P.; Seidman, D. N.; Wolverton, C.; Dravid, V. P.; Kanatzidis, M. G. High ZT in P-Type (PbTe)<sub>1–2x</sub>(PbSe)<sub>x</sub>(PbS)<sub>x</sub> Thermoelectric Materials. *J. Am. Chem. Soc.* **2014**, *136* (8), 3225–3237. <https://doi.org/10.1021/ja4121583>.
- (499) Liu, F.; Wagterveld, R. M.; Gebben, B.; Otto, M. J.; Biesheuvel, P. M.; Hamelers, H. V. M. Carbon Nanotube Yarns as Strong Flexible Conductive Capacitive Electrodes. *Colloid Interface Sci. Commun.* **2014**, *3*, 9–12. <https://doi.org/10.1016/j.colcom.2015.02.001>.
- (500) Ma, W.; Song, L.; Yang, R.; Zhang, T.; Zhao, Y.; Sun, L.; Ren, Y.; Liu, D.; Liu, L.; Shen, J.; Zhang, Z.; Xiang, Y.; Zhou, W.; Xie, S. Directly Synthesized Strong, Highly Conducting, Transparent Single-Walled Carbon Nanotube Films. *Nano Lett.* **2007**, *7* (8), 2307–2311. <https://doi.org/10.1021/nl070915c>.
- (501) Piao, M.; Alam, M. R.; Kim, G.; Dettlaff-Weglikowska, U.; Roth, S. Effect of Chemical Treatment on the Thermoelectric Properties of Single Walled Carbon Nanotube Networks. *Phys. Status Solidi B* **2012**, *249* (12), 2353–2356. <https://doi.org/10.1002/pssb.201200101>.
- (502) Wu, G.; Gao, C.; Chen, G.; Wang, X.; Wang, H. High-Performance Organic Thermoelectric Modules Based on Flexible Films of a Novel n-Type Single-Walled Carbon Nanotube. *J. Mater. Chem. A* **2016**, *4* (37), 14187–14193.  
<https://doi.org/10.1039/C6TA05120K>.
- (503) Shim, M.; Javey, A.; Shi Kam, N. W.; Dai, H. Polymer Functionalization for Air-Stable n-Type Carbon Nanotube Field-Effect Transistors. *J. Am. Chem. Soc.* **2001**, *123* (46), 11512–11513. <https://doi.org/10.1021/ja0169670>.
- (504) Mistry, K. S.; Larsen, B. A.; Bergeson, J. D.; Barnes, T. M.; Teeter, G.; Engtrakul, C.; Blackburn, J. L. N-Type Transparent Conducting Films of Small Molecule and Polymer Amine Doped Single-Walled Carbon Nanotubes. *ACS Nano* **2011**, *5* (5), 3714–3723.  
<https://doi.org/10.1021/nn200076r>.
- (505) Ryu, Y.; Freeman, D.; Yu, C. High Electrical Conductivity and N-Type Thermopower from Double-/Single-Wall Carbon Nanotubes by Manipulating Charge Interactions between Nanotubes and Organic/Inorganic Nanomaterials. *Carbon* **2011**, *49* (14), 4745–4751. <https://doi.org/10.1016/j.carbon.2011.06.082>.
- (506) Wang, L.; Jia, X.; Wang, D.; Zhu, G.; Li, J. Preparation and Thermoelectric Properties of Polythiophene/Multiwalled Carbon Nanotube Composites. *Synth. Met.* **2013**, *181*, 79–85.  
<https://doi.org/10.1016/j.synthmet.2013.08.011>.
- (507) Guo, J.; Li, G.; Reith, H.; Jiang, L.; Wang, M.; Li, Y.; Wang, X.; Zeng, Z.; Zhao, H.; Lu, X.; Schierning, G.; Nielsch, K.; Liao, L.; Hu, Y. Doping High-Mobility Donor–Acceptor Copolymer Semiconductors with an Organic Salt for High-Performance Thermoelectric Materials. *Adv. Electron. Mater.* **2020**, *6* (3), 1900945.  
<https://doi.org/10.1002/aelm.201900945>.

- (508) Linseis, V.; Völklein, F.; Reith, H.; Woias, P.; Nielsch, K. Platform for In-Plane ZT Measurement and Hall Coefficient Determination of Thin Films in a Temperature Range from 120 K up to 450 K. *J. Mater. Res.* **2016**, *31* (20), 3196–3204. <https://doi.org/10.1557/jmr.2016.353>.
- (509) Xu, F.; Wei, B.; Liu, W.; Zhu, H.; Zhang, Y.; Qiu, Y. In-Plane Mechanical Properties of Carbon Nanotube Films Fabricated by Floating Catalyst Chemical Vapor Decomposition. *J. Mater. Sci.* **2015**, *50* (24), 8166–8174. <https://doi.org/10.1007/s10853-015-9395-0>.
- (510) Li, M.; Kang, J. S.; Hu, Y. Anisotropic Thermal Conductivity Measurement Using a New Asymmetric-Beam Time-Domain Thermoreflectance (AB-TDTR) Method. *Rev. Sci. Instrum.* **2018**, *89* (8), 084901. <https://doi.org/10.1063/1.5026028>.
- (511) Aouraghe, M. A.; Xu, F.; Liu, X.; Qiu, Y. Flexible, Quickly Responsive and Highly Efficient E-Heating Carbon Nanotube Film. *Compos. Sci. Technol.* **2019**, *183*, 107824. <https://doi.org/10.1016/j.compscitech.2019.107824>.
- (512) Liu, J.; Zhu, J.; Tian, M.; Gu, X.; Schmidt, A.; Yang, R. Simultaneous Measurement of Thermal Conductivity and Heat Capacity of Bulk and Thin Film Materials Using Frequency-Dependent Transient Thermoreflectance Method. *Rev. Sci. Instrum.* **2013**, *84* (3), 1–12. <https://doi.org/10.1063/1.4797479>.
- (513) Jiang, P.; Huang, B.; Koh, Y. K. Accurate Measurements of Cross-Plane Thermal Conductivity of Thin Films by Dual-Frequency Time-Domain Thermoreflectance (TDTR). *Rev. Sci. Instrum.* **2016**, *87* (7), 1–23. <https://doi.org/10.1063/1.4954969>.
- (514) Cahill, D. G. Analysis of Heat Flow in Layered Structures for Time-Domain Thermoreflectance. *Rev. Sci. Instrum.* **2004**, *75* (12), 5119–5122. <https://doi.org/10.1063/1.1819431>.
- (515) Zhu, J.; Tang, D.; Wang, W.; Liu, J.; Holub, K. W.; Yang, R. Ultrafast Thermoreflectance Techniques for Measuring Thermal Conductivity and Interface Thermal Conductance of Thin Films. *J. Appl. Phys.* **2010**, *108* (9), 094315. <https://doi.org/10.1063/1.3504213>.
- (516) Cahill, D. G.; Watanabe, F. Thermal Conductivity of Isotopically Pure and Ge-Doped Si Epitaxial Layers from 300 to 550 K. *Phys. Rev. B* **2004**, *70* (23), 235322. <https://doi.org/10.1103/PhysRevB.70.235322>.
- (517) Costescu, R. M.; Wall, M. A.; Cahill, D. G. Thermal Conductance of Epitaxial Interfaces. *Phys. Rev. B* **2003**, *67* (5), 054302. <https://doi.org/10.1103/PhysRevB.67.054302>.
- (518) Subramanyan, H.; Kim, K.; Lu, T.; Zhou, J.; Liu, J. On the Importance of Using Exact Full Phonon Dispersions for Predicting Interfacial Thermal Conductance of Layered Materials Using Diffuse Mismatch Model. *AIP Adv.* **2019**, *9* (11), 115116. <https://doi.org/10.1063/1.5121727>.
- (519) Kaur, S.; Raravikar, N.; Helms, B. A.; Prasher, R.; Ogletree, D. F. Enhanced Thermal Transport at Covalently Functionalized Carbon Nanotube Array Interfaces. *Nat. Commun.* **2014**, *5* (1), 3082. <https://doi.org/10.1038/ncomms4082>.
- (520) Mai, C. K.; Liu, J.; Evans, C. M.; Segalman, R. A.; Chabinyk, M. L.; Cahill, D. G.; Bazan, G. C. Anisotropic Thermal Transport in Thermoelectric Composites of Conjugated Polyelectrolytes/Single-Walled Carbon Nanotubes. *Macromolecules* **2016**, *49* (13), 4957–4963. <https://doi.org/10.1021/acs.macromol.6b00546>.
- (521) Erickson, K. J.; Léonard, F.; Stavila, V.; Foster, M. E.; Spataru, C. D.; Jones, R. E.; Foley, B. M.; Hopkins, P. E.; Allendorf, M. D.; Talin, A. A. Thin Film Thermoelectric Metal–Organic Framework with High Seebeck Coefficient and Low Thermal Conductivity. *Adv. Mater.* **2015**, *27* (22), 3453–3459. <https://doi.org/10.1002/adma.201501078>.

- (522) Hopkins, P. E.; Kaehr, B.; Phinney, L. M.; Koehler, T. P.; Grillet, A. M.; Dunphy, D.; Garcia, F.; Brinker, C. J. Measuring the Thermal Conductivity of Porous, Transparent SiO<sub>2</sub> Films With Time Domain Thermoreflectance. *J. Heat Transf.* **2011**, *133* (6). <https://doi.org/10.1115/1.4003548>.
- (523) Liu, J.; Yoon, B.; Kuhlmann, E.; Tian, M.; Zhu, J.; George, S. M.; Lee, Y.-C.; Yang, R. Ultralow Thermal Conductivity of Atomic/Molecular Layer-Deposited Hybrid Organic–Inorganic Zincone Thin Films. *Nano Lett.* **2013**, *13* (11), 5594–5599. <https://doi.org/10.1021/nl403244s>.
- (524) Shin, J.; Sung, J.; Kang, M.; Xie, X.; Lee, B.; Lee, K. M.; White, T. J.; Leal, C.; Sottos, N. R.; Braun, P. V.; Cahill, D. G. Light-Triggered Thermal Conductivity Switching in Azobenzene Polymers. *Proc. Natl. Acad. Sci.* **2019**, *116* (13), 5973–5978. <https://doi.org/10.1073/pnas.1817082116>.
- (525) Liu, J.; Wang, X.; Li, D.; Coates, N. E.; Segalman, R. A.; Cahill, D. G. Thermal Conductivity and Elastic Constants of PEDOT:PSS with High Electrical Conductivity. *Macromolecules* **2015**, *48* (3), 585–591. <https://doi.org/10.1021/ma502099t>.
- (526) He, X.; Wang, X.; Nanot, S.; Cong, K.; Jiang, Q.; Kane, A. A.; Goldsmith, J. E. M.; Hauge, R. H.; Léonard, F.; Kono, J. Photothermoelectric p–n Junction Photodetector with Intrinsic Broadband Polarimetry Based on Macroscopic Carbon Nanotube Films. *ACS Nano* **2013**, *7* (8), 7271–7277. <https://doi.org/10.1021/nn402679u>.
- (527) Pradhan, N. R.; Duan, H.; Liang, J.; Iannacchione, G. S. The Specific Heat and Effective Thermal Conductivity of Composites Containing Single-Wall and Multi-Wall Carbon Nanotubes. *Nanotechnology* **2009**, *20* (24), 245705. <https://doi.org/10.1088/0957-4484/20/24/245705>.
- (528) Zhang, W.; Liu, H.; Sun, C.; Drage, T. C.; Snape, C. E. Capturing CO<sub>2</sub> from Ambient Air Using a Polyethyleneimine–Silica Adsorbent in Fluidized Beds. *Chem. Eng. Sci.* **2014**, *116*, 306–316. <https://doi.org/10.1016/j.ces.2014.05.018>.
- (529) Peirce, F. T. The Geometry of Cloth Structure. *J. Text. Inst. Trans.* **1937**, *28* (3), T4–T96. <https://doi.org/10.1080/19447023708658809>.
- (530) Jeon, B. S.; Chun, S. Y.; Hong, C. J. Structural and Mechanical Properties of Woven Fabrics Employing Peirce’s Model. *Text. Res. J.* **2003**, *73* (10), 929–933. <https://doi.org/10.1177/004051750307301014>.
- (531) Ng, W. S.; Hu, H. Woven Fabrics Made of Auxetic Plied Yarns. *Polymers* **2018**, *10* (2), 226. <https://doi.org/10.3390/polym10020226>.
- (532) Shahabi, N. E.; Mousazadegan, F.; Varkiyani, S. M. H.; Saharkhiz, S. Crimp Analysis of Worsted Fabrics in the Terms of Fabric Extension Behaviour. *Fibers Polym.* **2014**, *15* (6), 1211–1220. <https://doi.org/10.1007/s12221-014-1211-y>.

**APPENDICES**

## Appendix A

**Supplementary Information: In-Plane Thermoelectric Properties of Flexible and Room Temperature Doped Carbon Nanotube Films**

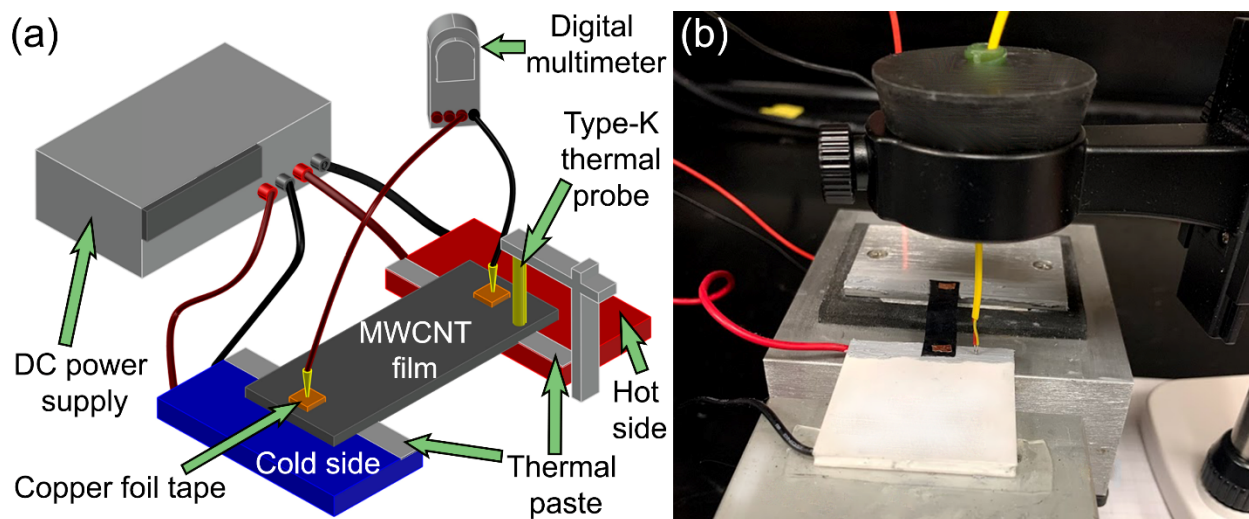


**Figure S30:** (a) Schematic diagram of the setup to measure Seebeck coefficient with the image in (b) showing the setup with the MWCNT film places across the hot and cold sides. While in (b) the temperature probe has been moved aside to show a better view of the film, during measurement the probe is placed on the film as in (a) to measure thermal gradient and Seebeck voltages on the same side of the film.

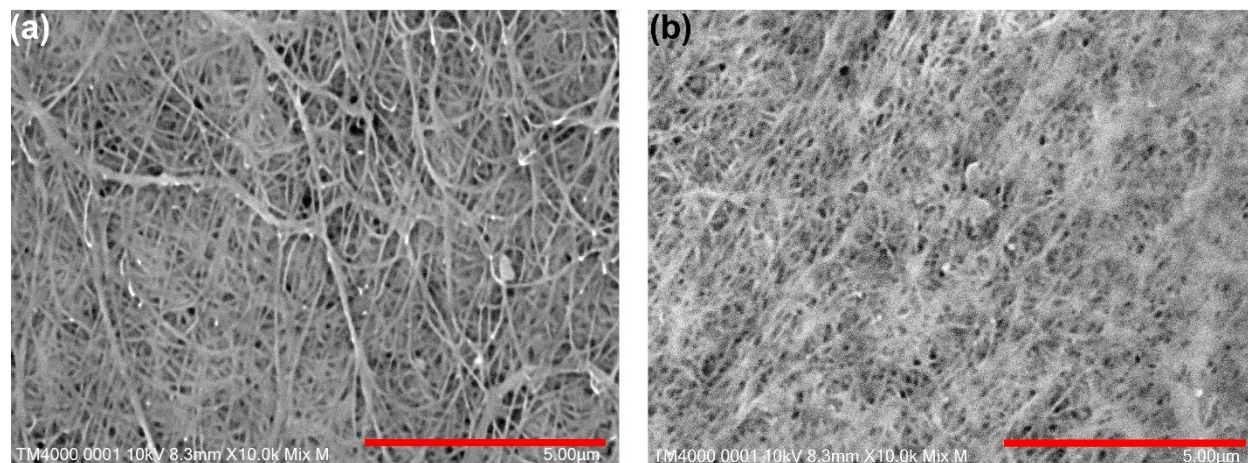


**Figure S31:** SEM images at 10000X magnification for (a) pristine MWCNT film and (b) 5-MWCNT/PEI film. Both scale bars are 5  $\mu\text{m}$ .

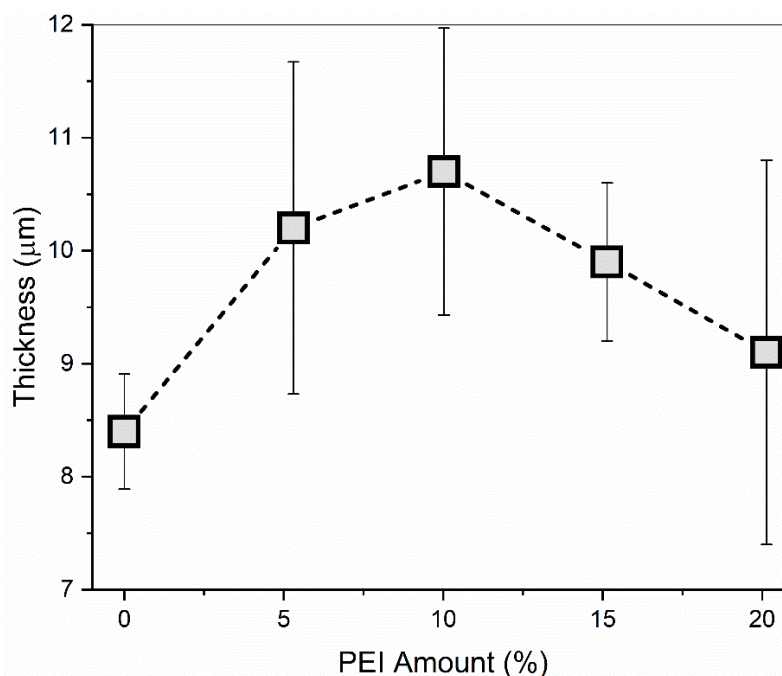


**Figure S32:** Thickness variation as a function of concentration of PEI in ethanol. Table S1. Thermoelectric properties of pristine and n-type MWCNT films. ZT for the films is calculated by assuming that the thermal conductivities of the PEI doped films remain constant as the concentration varies from 5 to 20 wt.% PEI.

**Table S2:** Overall TE performance of MWCNT materials

Film Type	Thickness (μm)	Seebeck Coefficient (μV/K)	Electrical Conductivity (S/m)	Power Factor (μW/mK <sup>2</sup> )	Thermal Conductivity (W/mK)	ZT (at 300 K)
p-type MWCNT	8.4 ± 0.5	56.19 ± 0.002	107977.61 ± 0.01	340.94 ± 0.02	5.5 ± 0.8	<b>0.019</b>
5- MWCNT/PEI	10.2 ± 1.5	- 54.29 ± 0.004	134238.78 ± 30036.18	395.59 ± 62.53	8.1 ± 1.2	<b>0.015</b>
10- MWCNT/PEI	10.7 ± 1.3	- 50.72 ± 3.07	166084.83 ± 8365.31	429.36 ± 51.79	8.1 ± 1.2	<b>0.016</b>
15- MWCNT/PEI	9.9 ± 0.7	- 50.60 ± 1.25	203003.99 ± 28278.62	521.66 ± 69.33	8.1 ± 1.2	<b>0.019</b>
20- MWCNT/PEI	9.1 ± 1.7	- 43.82 ± 11.10	211463.31 ± 34596.35	402.21 ± 97.04	8.1 ± 1.2	<b>0.015</b>

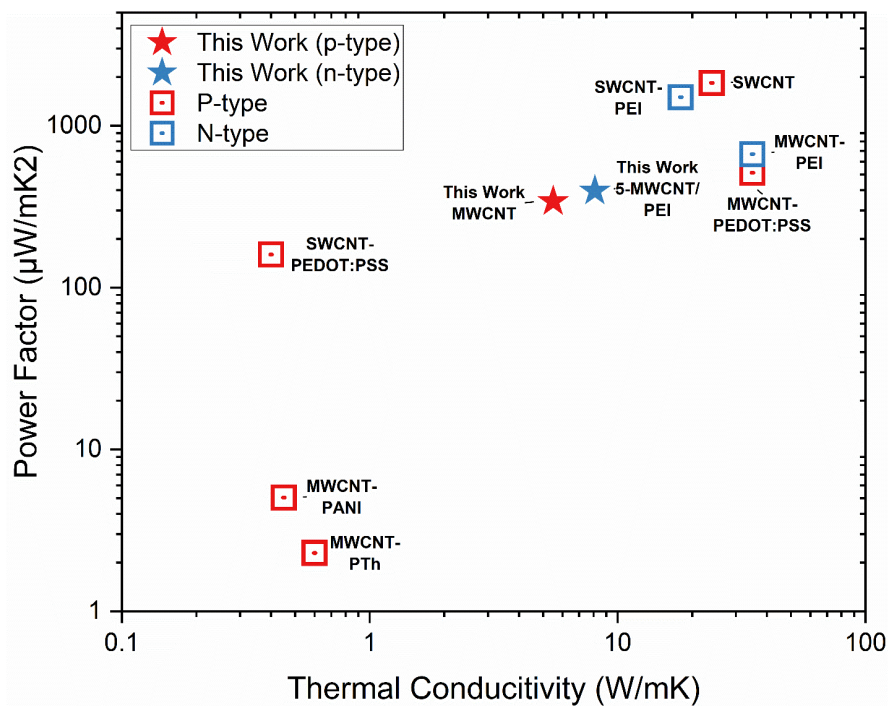


**Figure S33:** Comparison of  $\kappa$  and PF for various reported TE materials containing CNTs (cited work indicated by  $\square$  with red for p-type and blue for n-type). Data for the materials are from the cited sources: MWCNT-PANI,<sup>494</sup> MWCNT-PTh,<sup>506</sup> SWCNT-PEDOT:PSS,<sup>248</sup> SWCNT-PEI,<sup>255</sup> SWCNT,<sup>255</sup> MWCNT-PEI,<sup>437</sup> and MWCNT-PEDOT:PSS.<sup>437</sup> This work (indicated by  $\star$ ) shows high PF with lower  $\kappa$  than other reported materials.

## Appendix B

**Supplementary Information: Design and Evaluation of a Woven Thermoelectric  
Heating/Cooling Fabric for On-Body Thermal Comfort**

## I. Projected Area Calculation

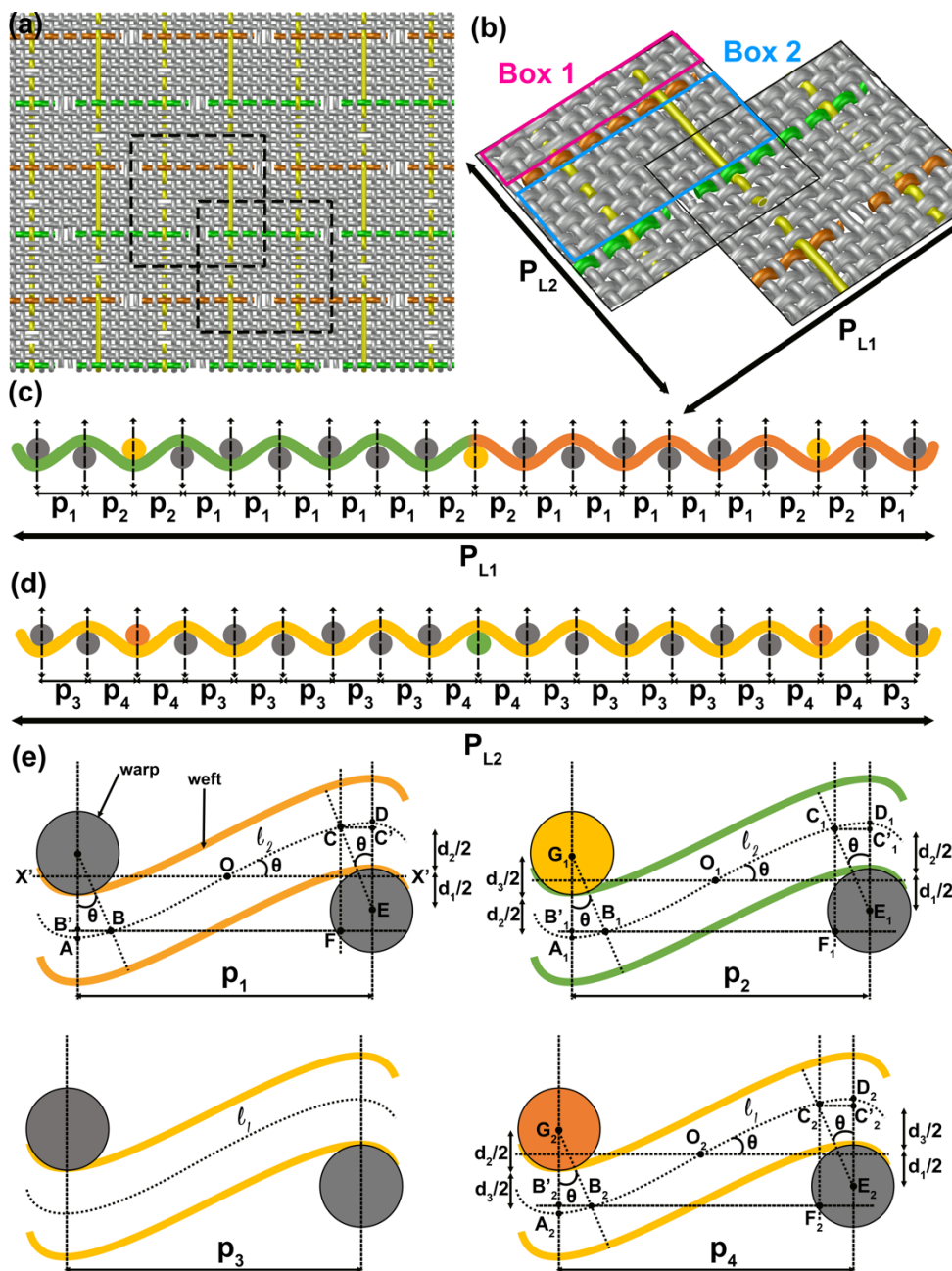


**Figure S34:** FabTEC modeling for TE performance. (a) Overall fabric design with disconnects. (b) Repeat unit with symmetry. (c) Projected length in the  $XX'$  plane. (d) Projected length in the  $YY'$  plane. (e) Calculation of projected lengths.

Important Variables:

- Spacing between warp support yarns =  $p_1$
- Modular length of TE yarn (weft yarn) =  $l_2$
- Modular length of interconnect (warp yarn) =  $l_1$
- Diameter of support yarns =  $d_1$
- Diameter of TE yarn =  $d_2$
- Diameter of interconnect =  $d_3$
- Weave angle =  $\theta$
- Total length of either P or N-type TE yarn in a single junction =  $L_{TE}$
- Aspect ratio of single TE yarn in a single junction =  $L_{TE} / d_2$
- Assumptions:
- All weave angles are assumed to be the same
- All yarns are assumed to be of circular cross-section

**Derivation of  $p_1$ :**

$$DE = CE = d_1/2 + d_2/2 = 0.5(d_1 + d_2)$$

$$\text{Curve length of CD} = \text{Curve length of AB} = CE \times \theta = 0.5(d_1 + d_2)\theta$$

$$CC' = BB' = CE \times \sin \theta = 0.5(d_1 + d_2) \sin \theta$$

$$BC = AD - AB - CD = l_2 - (d_1 + d_2)\theta$$

$$BF = BC \times \cos \theta = \{l_2 - (d_1 + d_2)\theta\} \cos \theta$$

$$p_1 = BB' + BF + CC' = 0.5(d_1 + d_2) \sin \theta + \{l_2 - (d_1 + d_2)\theta\} \cos \theta + 0.5(d_1 + d_2) \sin \theta$$

$$\mathbf{p_1 = (d_1 + d_2) \sin \theta + \{l_2 - (d_1 + d_2)\theta\} \cos \theta}$$

Similarly, we can derive  $p_3$  as:

$$\mathbf{p_3 = (d_1 + d_3) \sin \theta + \{l_1 - (d_1 + d_3)\theta\} \cos \theta}$$

For  $p_2$ , we have the following:

$$D_1E_1 = C_1E_1 = 0.5(d_1 + d_2) \text{ and } G_1A_1 = G_1B_1 = 0.5(d_2 + d_3)$$

$$C_1D_1 = 0.5(d_1 + d_2)\theta \text{ and } A_1B_1 = 0.5(d_2 + d_3)\theta$$

$$C_1C'_1 = C_1E_1 \times \sin \theta = 0.5(d_1 + d_2) \sin \theta$$

$$B_1B'_1 = G_1B_1 \times \sin \theta = 0.5(d_2 + d_3) \sin \theta$$

$$B_1C_1 = A_1D_1 - A_1B_1 - C_1D_1 = l_2 - 0.5(d_1 + d_2)\theta - 0.5(d_2 + d_3)\theta$$

$$B_1C_1 = l_2 - \{d_2\theta + 0.5(d_1 + d_2)\theta\}$$

$$B_1F_1 = B_1C_1 \times \cos \theta = [l_2 - \{d_2\theta + 0.5(d_1 + d_2)\theta\}] \cos \theta$$

$$p_2 = B_1B'_1 + B_1F_1 + C_1C'_1 = l_2 \cos \theta + d_2(\sin \theta - \theta \cos \theta) + 0.5(d_1 + d_3)(\sin \theta - \theta \cos \theta)$$

$$p_2 = l_2 \cos \theta + d_2(\sin \theta - \theta \cos \theta) + 0.5(d_1 + d_3)(\sin \theta - \theta \cos \theta)$$

Similarly, we can write  $p_4$  as:

$$p_4 = l_1 \cos \theta + d_3(\sin \theta - \theta \cos \theta) + 0.5(d_1 + d_2)(\sin \theta - \theta \cos \theta)$$

The projected length in the  $XX'$  plane,  $P_{L1}$  can be written as,

$$P_{L1} = 12p_1 + 6p_2$$

$$P_{L1} = 12[(d_1 + d_2) \sin \theta + \{l_2 - (d_1 + d_2)\theta\} \cos \theta] + 6[l_2 \cos \theta + d_2(\sin \theta - \theta \cos \theta) + 0.5(d_1 + d_3)(\sin \theta - \theta \cos \theta)]$$

The projected length in the  $YY'$  plane,  $P_{L2}$  can be written as,

$$P_{L2} = 12p_3 + 6p_4$$

$$P_{L2} = 12[(d_1 + d_3) \sin \theta + \{l_1 - (d_1 + d_3)\theta\} \cos \theta] + 6[l_1 \cos \theta + d_3(\sin \theta - \theta \cos \theta) + 0.5(d_1 + d_2)(\sin \theta - \theta \cos \theta)]$$

The projected area of a single repeat unit =  $A_p = P_{L1} \times P_{L2}$

$$A_p = [12[(d_1 + d_2) \sin \theta + \{l_2 - (d_1 + d_2)\theta\} \cos \theta] + 6[l_2 \cos \theta + d_2(\sin \theta - \theta \cos \theta) + 0.5(d_1 + d_3)(\sin \theta - \theta \cos \theta)]] \times [12[(d_1 + d_3) \sin \theta + \{l_1 - (d_1 + d_3)\theta\} \cos \theta] + 6[l_1 \cos \theta + d_3(\sin \theta - \theta \cos \theta) + 0.5(d_1 + d_2)(\sin \theta - \theta \cos \theta)]]$$

## II. Thermoelectric Equations

Thermoelectric equations used for calculating total heating and cooling have been adapted from literature.<sup>336</sup>

$$\text{In the cooling mode, } Q_c = n\alpha T_c I - \frac{I^2 R_{elec-TEC}}{2} - \frac{(T_h - T_c)}{R_{therm-TEC}}$$

where  $Q_c$  = total TE cooling = Peltier cooling – Joule Heating – Thermal Leak between hot and cold sides

$n$  = number of junctions,  $\alpha$  = device Seebeck coefficient,  $T_c$  = target temperature of cold side (side close to skin),  $I$  = current supplied to TEC,  $R_{elec-TEC}$  = electrical resistance of TEC device,  $R_{therm-TEC}$  = thermal resistance of TEC device,  $T_h$  = Hot side temperature, heat rejection side

On the cool side, the term  $(\frac{I^2 R_{elec-TEC}}{2} + \frac{T_h - T_c}{R_{therm-TEC}})$  has to be minimized to enable higher amount of cooling

$$\text{Device electrical resistance} = R_{elec-TEC} = n \left\{ \frac{L_{TE}}{a_{TE}} \left( \frac{1}{\sigma_n} + \frac{1}{\sigma_p} \right) + \frac{L_{In}}{a_{In}} \left( \frac{1}{\sigma_{In}} \right) \right\}$$

Where  $n$  = number of junctions

$L_{TE}$ ,  $a_{TE}$  = total modular length, cross-sectional area of the TE leg (p or n) in a single junction,  $\sigma_n$ ,  $\sigma_p$  and  $\sigma_{In}$  = electrical conductivity of n-type, p-type and interconnect yarns, respectively,  $L_{in}$ ,  $a_{in}$  = length, cross-sectional area of interconnect yarn in single junction

$$\text{Device thermal resistance} = R_{therm-TEC} = \frac{1}{n} \left\{ \frac{L_{TE}}{a_{TE}} \left( \frac{1}{\kappa_n} + \frac{1}{\kappa_p} \right) + \frac{L_{In}}{a_{In}} \left( \frac{1}{\kappa_{In}} \right) \right\}$$

Where  $\kappa_p$ ,  $\kappa_n$  = thermal conductivities of p and n-type TE yarns

$$\text{In the heating mode, } Q_h = n\alpha T_h I + \frac{I^2 R_{elec-TEC}}{2} - \frac{T_h - T_c}{R_{therm-TEC}}$$

Where  $Q_h$  = total TE heating = Peltier heating + Joule Heating – Thermal Leak between hot and cold sides

Hence, the cooling density is defined as: Cooling/Area of Fabric

$$\text{Cooling Density} = Q_c / A_p$$

$$\text{Cooling Density} = \frac{\left\{ n\alpha T_c I - \frac{I^2 R_{elec-TEC}}{2} - \frac{(T_h - T_c)}{R_{therm-TEC}} \right\}}{\left[ \begin{aligned} &12[(d_1 + d_2) \sin \theta + \{l_2 - (d_1 + d_2)\theta\} \cos \theta] + \\ &6[l_2 \cos \theta + d_2(\sin \theta - \theta \cos \theta) + \\ &0.5(d_1 + d_3)(\sin \theta - \theta \cos \theta)] \times \\ &12[(d_1 + d_3) \sin \theta + \{l_1 - (d_1 + d_3)\theta\} \cos \theta] \\ &+ 6[l_1 \cos \theta + d_3(\sin \theta - \theta \cos \theta) \\ &+ 0.5(d_1 + d_2)(\sin \theta - \theta \cos \theta)] \end{aligned} \right]}$$

### III. FabTEC Modeling Assumptions and Data

Assumptions for the modeling data for effect of AR on the cooling density of FabTEC:

- Number of junctions = 4
- Weave angle = 2 °
- No contact resistance
- Hot side temperature = 21 °C
- ZT of p-type and n-type = 0.002
- Length of interconnect yarn = 2.4 mm
- Constant current value set as = 10 mA

For each aspect ratio, the parameters used are:

**Table S3:** Modeling Parameters for AR Effect on FabTEC Cooling Density

Modular Length ( $l_2$ ) (mm)	Leg Length ( $L_{TE} = 12 \times l_2$ ) (mm)	Diameter of yarn ( $d_2$ ) (mm)	Aspect Ratio (AR)
0.0083	0.1	0.2	0.5
0.02	0.24	0.2	1.2
0.04	0.48	0.2	2.4
0.06	0.72	0.2	3.6
0.08	0.96	0.2	4.8
0.1	1.2	0.2	6
0.12	1.44	0.2	7.2
0.14	1.68	0.2	8.4
0.16	1.92	0.2	9.6
0.18	2.16	0.2	10.8
0.20	2.4	0.2	12
0.22	2.64	0.2	13.2

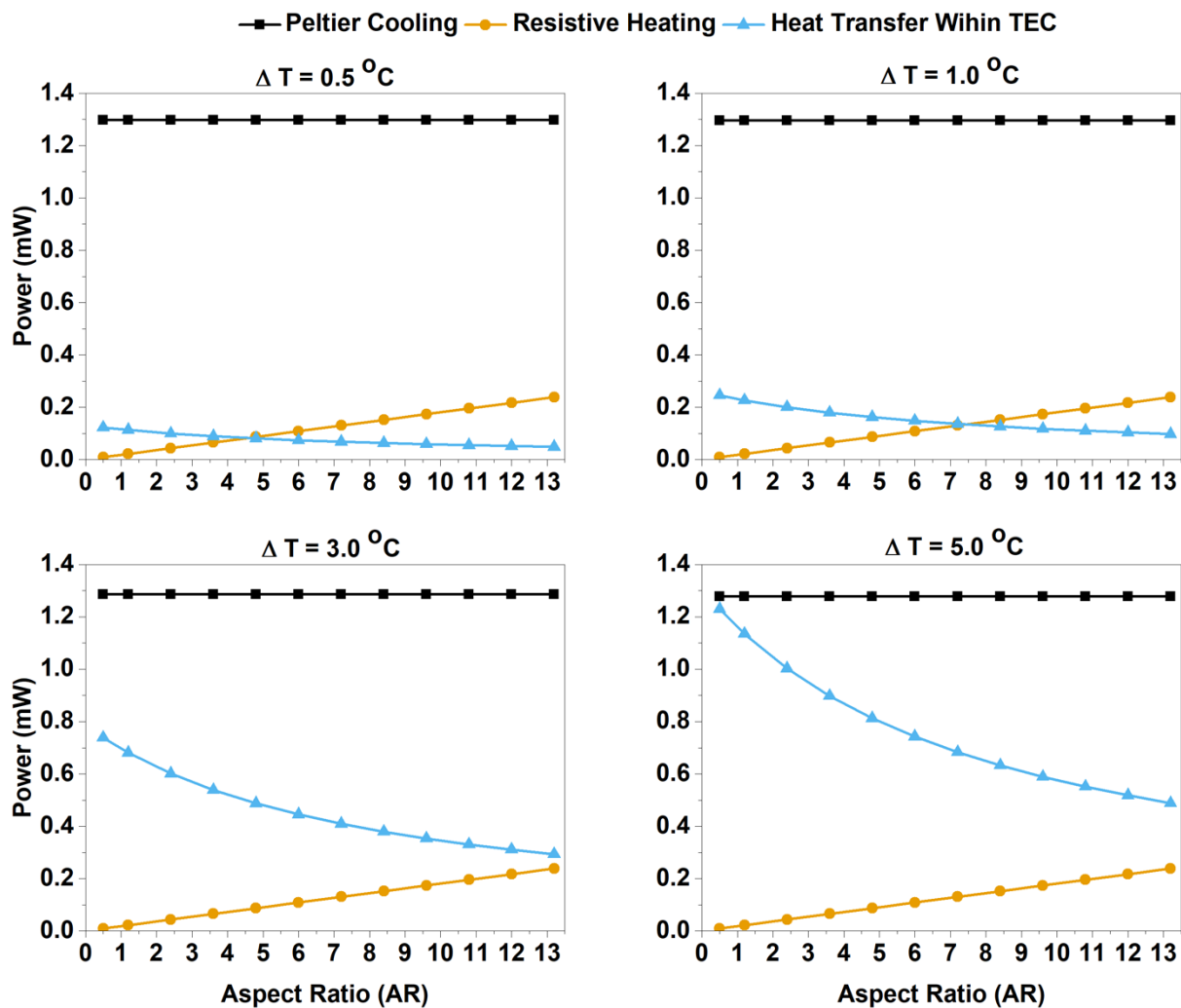


**Figure S35:** Peltier cooling, resistive heating, and heat transfer within the TEC as a function of the AR for various cooling gradients.

#### IV. Junction Density Calculation

From *Figure S34(b)* we can see that there are two junctions in the geometric repeat unit of this fabric. The TE repeat unit, however, would consist of just a single junction that could either be a heating or a cooling junction, i.e., either PN or NP in *Figure S34(a)*. Junction density will be defined as the number of junctions per meter of fabric. For calculating the junction density, we need to take into account the total number of support yarns needed in the warp and weft direction for a single junction, defined as ends (warp yarns) per inch and picks (weft yarns) per inch. In a typical textile fabric, the ends and picks per inch range from 30-120 ends/picks per inch i.e. from 1200-4700 ends/picks per meter. Hence, we will consider three cases for junction density: (i) 1200 ends/picks per meter (30 ends per inch), (ii) 2400 ends/picks per meter (60 ends per inch), and (iii) 4000 ends/picks per meter (100 ends per inch) to calculate the junction density.

Considering the single PN junction in *Figure S34(a)* we see that there are 12 weft ends (this includes 10 grey support yarn and 2 TE yarns) and 18 warp ends (16 grey support yarns to support the two TE yarns, and 2 interconnect yarns) required for each junction. Due to the symmetry of the structure, the same number of yarns are required for the NP junction as well. Hence, we can say that

- 18 warp ends and 12 weft ends are required for 1 junction
- For every 2 PN or NP junction pairs, we need: 36 warp ends and 24 weft ends

We can now calculate the resultant number of junctions per square meter for the three cases:

Case 1: 1200 ends and 1200 picks per meter:

$$\text{Number of junctions per meter}^2 \text{ of fabric} = 1200/36 \times 1200/24 = 33.33 \times 50$$

$$\text{Number of junctions per meter}^2 \text{ of fabric} = 1,666 \text{ junctions}$$

Case 2: 2400 ends and 2400 picks per meter:

Number of junctions per meter<sup>2</sup> of fabric =  $2400/36 \times 2400/24 = 66.67 \times 100$

Number of junctions per meter<sup>2</sup> of fabric = 6,666 junctions

Case 3: 4000 ends and 4000 picks per meter:

Number of junctions per meter<sup>2</sup> of fabric =  $4000/36 \times 4000/24 = 111.11 \times 166.67$

Number of junctions per meter<sup>2</sup> of fabric = 18,518 junctions

For each of these three cases, while the number of junctions seem high it is important to understand that this is for a square meter of fabric which usually includes a high number of ends and picks, due to the small size of the yarns.

Hence the junction densities that would be considered for modeling are: 1666 junctions/m<sup>2</sup>, 6666 junctions/m<sup>2</sup> and 18518 junctions/m<sup>2</sup>.

Assumptions for the modeling data for junction density on the cooling density of FabTEC:

- Weave angle = 2°
- Aspect ratio = 24
- No contact resistance
- Hot side temperature = 21 °C
- ZT of p-type and n-type = 0.002

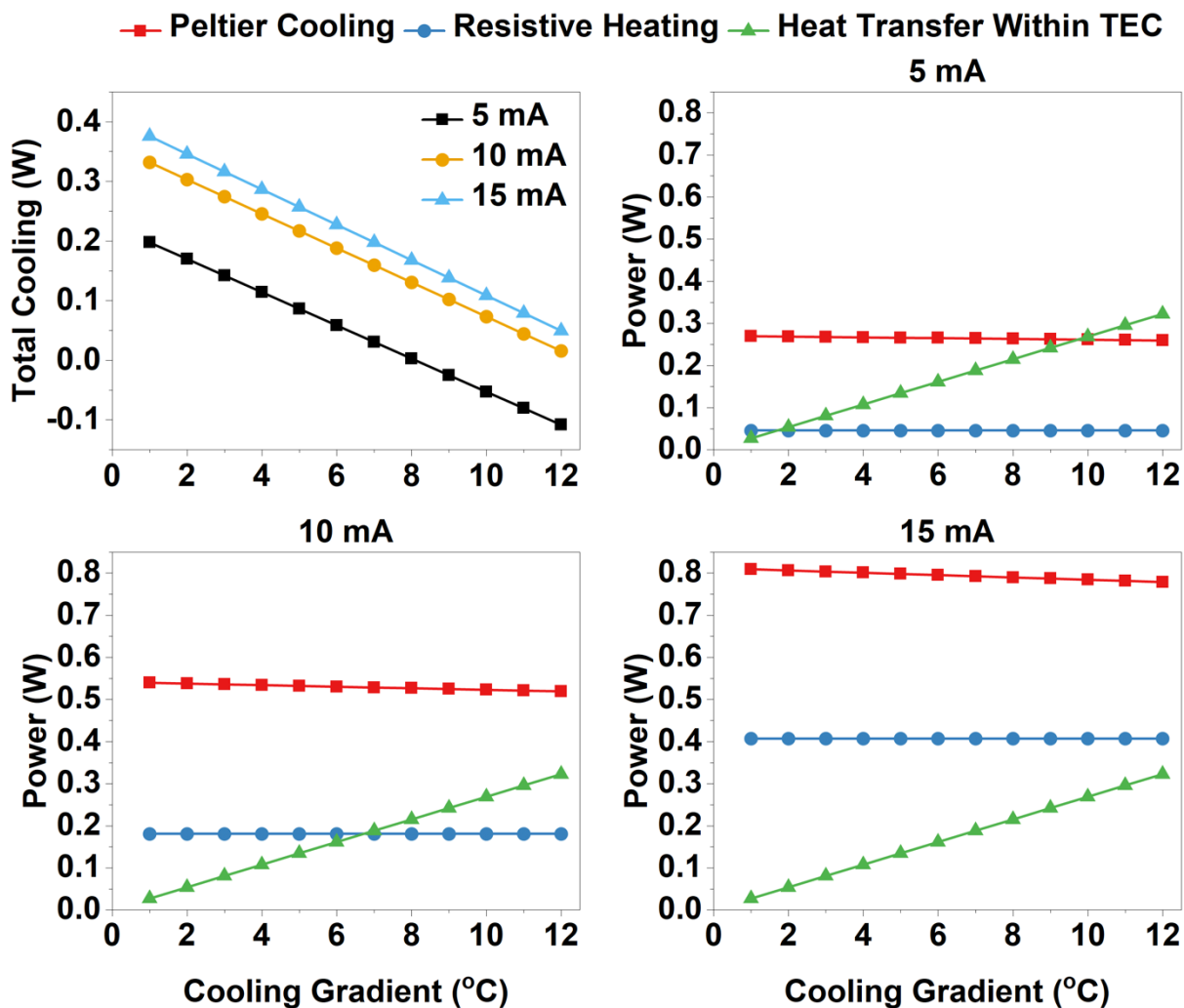


**Figure S36:** Peltier cooling, resistive heating and heat transfer within the FabTEC for 1666 junctions/m<sup>2</sup> density.

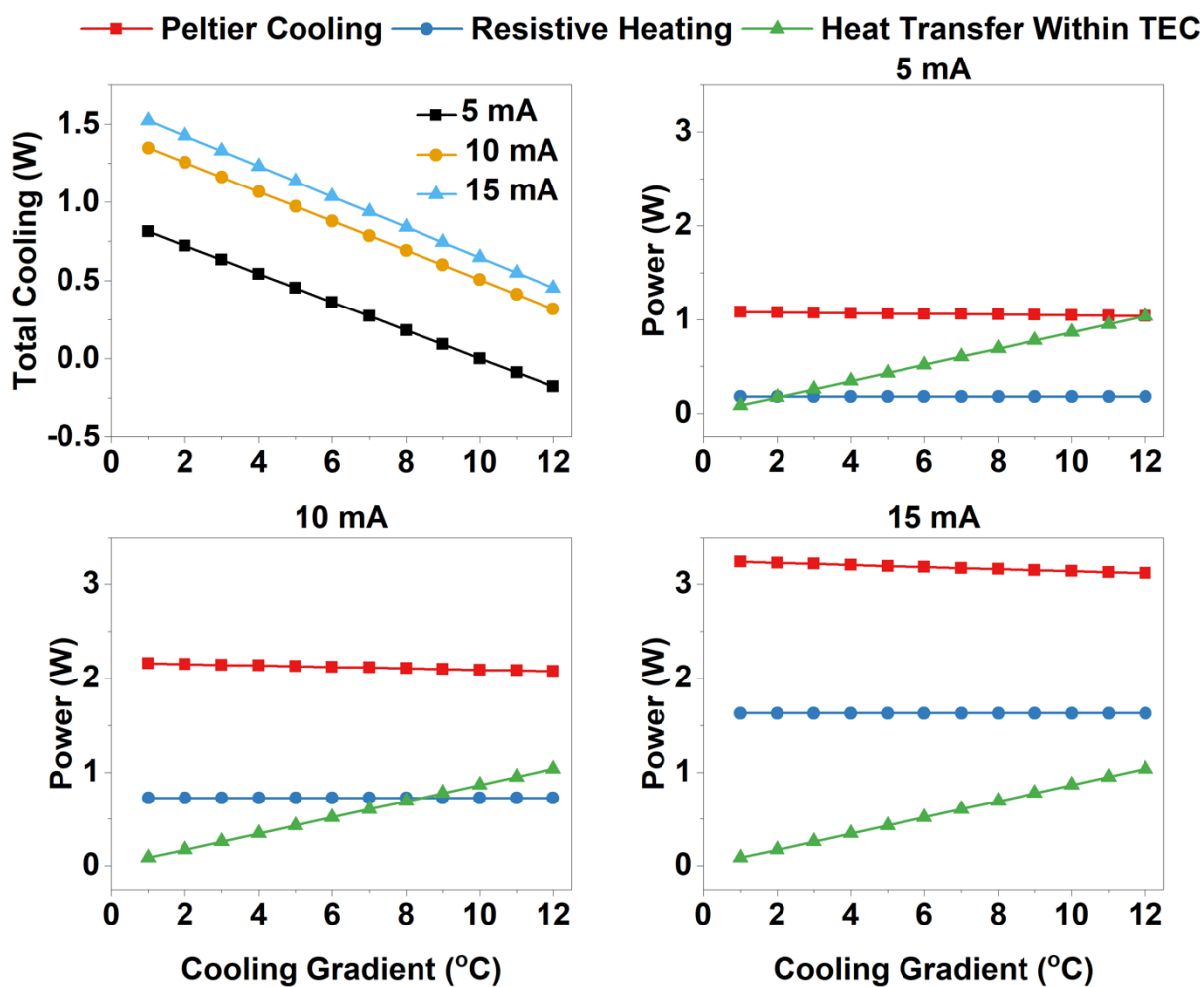


*Figure S37:* Peltier cooling, resistive heating and heat transfer within the FabTEC for 6666 junctions/m<sup>2</sup> density.

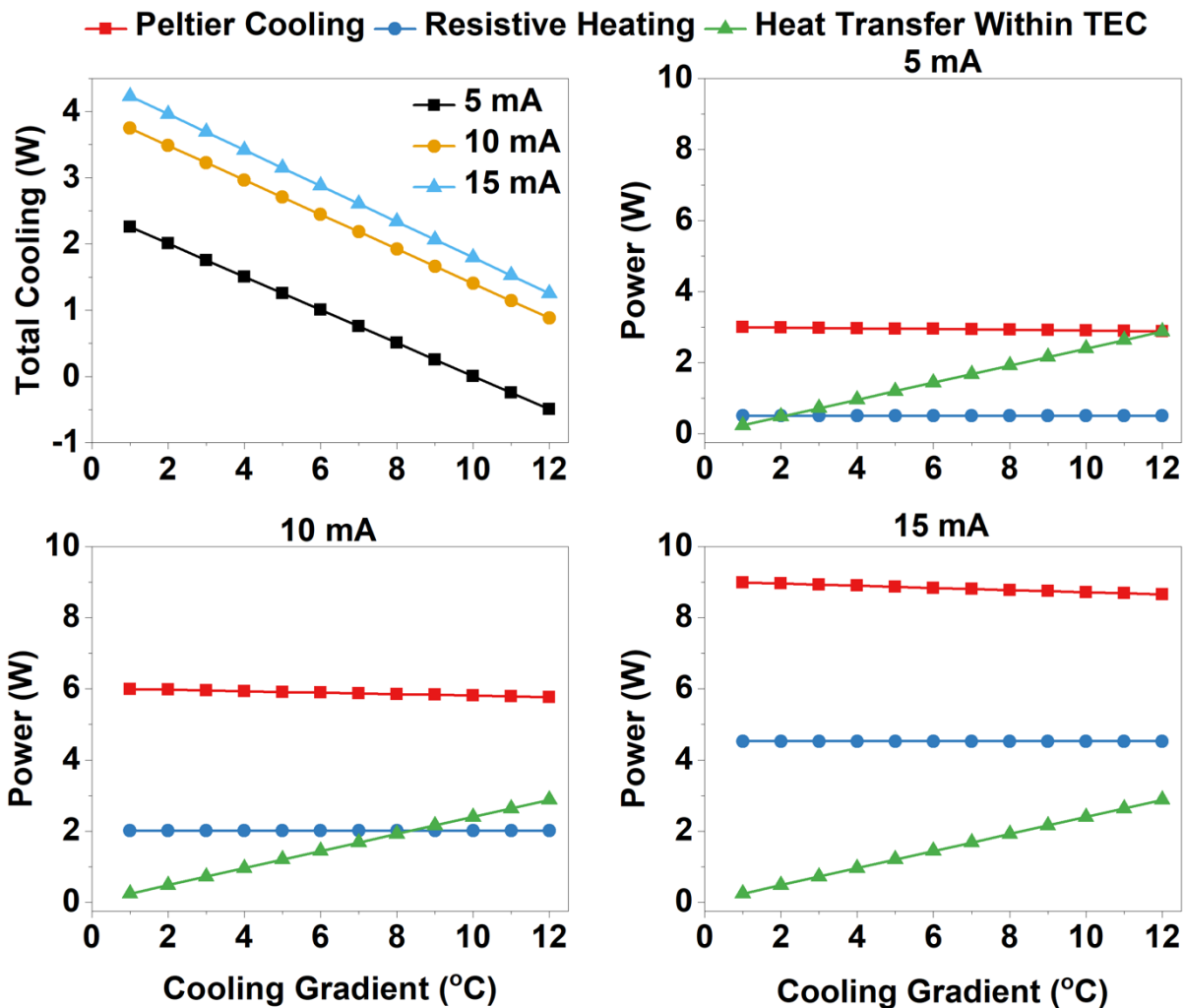


**Figure S38:** Peltier cooling, resistive heating and heat transfer within the FabTEC for 18518 junctions/m<sup>2</sup> density.